



Delft University of Technology

Structure and supramolecular assembly in multi-component organogels

Ghanbari, E.

DOI

[10.4233/uuid:bdc47b1e-68dd-40a9-ad36-abe8537e9f90](https://doi.org/10.4233/uuid:bdc47b1e-68dd-40a9-ad36-abe8537e9f90)

Publication date

2023

Document Version

Final published version

Citation (APA)

Ghanbari, E. (2023). *Structure and supramolecular assembly in multi-component organogels*. [Dissertation (TU Delft), Delft University of Technology]. <https://doi.org/10.4233/uuid:bdc47b1e-68dd-40a9-ad36-abe8537e9f90>

Important note

To cite this publication, please use the final published version (if applicable).
Please check the document version above.

Copyright

Other than for strictly personal use, it is not permitted to download, forward or distribute the text or part of it, without the consent of the author(s) and/or copyright holder(s), unless the work is under an open content license such as Creative Commons.

Takedown policy

Please contact us and provide details if you believe this document breaches copyrights.
We will remove access to the work immediately and investigate your claim.

Structure and supramolecular assembly in multi-component organogels

Dissertation
for the purpose of obtaining the degree of doctor
at Delft University of Technology
by the authority of the Rector Magnificus, Prof.dr.ir. T.H.J.J. van der Hagen,
chair of the Board of Doctorates
to be defended publicly on Tuesday
24 October 2023 at 15:00

by

Elmira GHANBARI

Master of Science in Biomedical Engineering-Biomaterials,
Amirkabir University of Technology, Iran

born in Tehran, Iran

This dissertation has been approved by the promotores.

Composition of the doctoral committee:

Rector Magnificus	chairperson
Prof. dr. J. H. van Esch	Delft University of Technology, promotor
Prof. dr. S. J. Picken	Delft University of Technology, co-promotor

Independent members:

Prof. F. Grozema	Delft University of Technology
Prof. D.J. Adams	University of Glasgow
Dr. hab. E. Mendes	Delft University of Technology
Dr. P.H.J. Kouwer	Radboud University
Prof. dr. A. Urakawa	Delft University of Technology, reserve member

The work described in this dissertation was carried out in the Advanced Soft Matter (ASM) group, Department of Chemical Engineering, Faculty of Applied Science, Delft University of Technology. The research was funded by Arkema company, multi-national manufacturer of specialty materials (headquartered in Colombes, France), and Delft University of Technology.



Printed by: Gildeprint

Copyright ©2023 by Elmira Ghanbari

ISBN 978-94-6419-947-5

An electronic version of this dissertation is available
at <http://repository.tudelft.nl/>.

To all people who strive
for cultivating awareness
and harvesting freedom

Contents

Chapter 1	1
Introduction	
1.1 Background.....	1
1.2 From serendipity to rational design of gelators	1
1.3 Why multi-component gels	2
1.4 Research goals.....	3
1.5 Thesis outline	4
1.6 References.....	6
Chapter 2	11
From molecular assembly to gel formation via crystallization: what is going on behind the scenes of supramolecular gel formation	
Introduction	11
2.1 Classical nucleation	15
2.2 Non-classical nucleation.....	17
2.3 Crystal growth	18
2.3.1 Equilibrium growth	19
2.3.2 Non-equilibrium growth	20
2.4 Network formation.....	25
2.4.1 Network formation via different modes of assembly	25
2.4.2 How do different network structures develop via different growth/branching modes?	26
2.4.3 How do different network morphologies impact the rheological properties?.....	30
2.5 References.....	39
Chapter 3	49
Molecular arrangement and thermal properties of bisamide organogelators in the solid state	
Abstract	49

3.1 Introduction	50
3.2 Materials and methods	52
3.2.1 Materials	52
3.2.2 Synthesis and characterization	53
3.2.3 Proton-Nuclear magnetic resonance spectroscopy (^1H NMR).....	53
3.2.4 Differential Scanning Calorimetry (DSC)	54
3.2.5 $\text{DSC}_N(T)$ analytical model and curve fitting	54
3.2.6 Powder X-ray diffraction (XRD) and molecular modelling	55
3.2.7 Fourier transform infrared spectroscopy (ATR-FTIR).....	56
3.3 Results and discussion.....	56
3.3.1 Synthesis of bisamide gelators.....	56
3.3.2 Thermal analysis	56
3.3.3 Crystal structure.....	61
3.3.4 Fourier transform infrared spectroscopy (ATR-FTIR).....	72
3.4 Conclusions	74
3.5 References.....	77
3.6 Supplementary Information.....	81
3.6.1 Preparation of bisamide gelators.....	81
3.6.2 Crystal structure of odd BAs	84
Chapter 4	101
Supramolecular arrangement and rheological properties of bisamide gels	
Abstract	101
4.1 Introduction	101
4.2 Materials and methods	103
4.2.1 Materials	103
4.2.2 Gel preparation	104
4.2.3 Differential Scanning Calorimetry (DSC)	104
4.2.4 $\text{DSC}_N(T)$ analytical model and curve fitting	105
4.2.5 X-ray diffraction (XRD)	106
4.2.6 Scanning Electron Microscopy (SEM).....	106
4.2.7 Rheology	106

4.3 Results and discussion.....	107
4.4 Conclusions	123
4.5 References.....	125
4.6 Supplementary information	125
4.6.1 DSC thermogram of 5BA gel (20 wt%)	129
4.6.2 FHM model development	130
4.6.3 Solubility curves of nBA gels	131
4.6.4 Microstructure evolution of gels with change in the concentration ...	134
4.6.5 FHM model fitted to the solubility curves of nBA gels (20 wt%)	135
4.6.6 XRD patterns of nBA gels (20 wt%) in comparison with their gelators in the solid state	136
Chapter 5.....	137
Analysis of differential scanning calorimetry (DSC): Determining the transition temperatures, and enthalpy and heat capacity changes in multi-component systems by analytical model fitting	
Abstract	137
5.1 Introduction	138
5.2 Materials and methods	140
5.2.1 Differential Scanning Calorimetry (DSC) measurement.....	140
5.2.2 Theoretical principles and calculation of the analytical model (DSC _N (T))	142
5.2.3 Experimental error and fitting residuals	150
5.3 Validation of the analytical method for different types of materials.....	151
5.3.1 Indium as a metal calibration sample	151
5.3.2 Stearic acid as an organic compound.....	154
5.3.3 Phase transitions in a liquid crystal compound	155
5.3.4 Low molecular weight bisamide gelators with different number of methylene spacers between the amide groups.....	157
5.3.5 Binary systems (binary mixtures of low molecular weight gelators) ...	158
5.3.6 Semi-crystalline polymer (PHBVH) with glass transition, cold crystallization, and melting peaks.....	160
5.4 Conclusion	162
5.5 References.....	163

5.6 Supplementary information	165
Chapter 6	173
Design rules for binary bisamide gelators: towards gels with tailor-made structures and properties	
Abstract	173
6.1 Introduction	174
6.2 Materials and methods	175
6.2.1 Binary mixtures of nBA gelators	175
6.2.2 Gel preparation	176
6.2.3 Differential Scanning Calorimetry (DSC)	177
6.2.4 DSC _N (T) analytical model and curve fitting	177
6.2.5 X-ray diffraction (XRD)	179
6.2.6 Scanning Electron Microscopy (SEM).....	179
6.2.7 Rheology	179
6.3 Results and discussion.....	180
6.3.1 Binary gelators in the solid state.....	180
6.3.2 Phase diagram.....	187
6.3.3 Binary bisamides in the gel state	190
6.3.4 Rheological properties	196
6.4 Conclusions	198
6.5 References.....	200
6.6 Supplementary Information.....	203
Summary	219
Samenvatting.....	221
Acknowledgment.....	223
Curriculum Vitae.....	226
List of Publications.....	227

Chapter 1

Introduction

1.1 Background

Supramolecular gels are receiving significant attention due to their versatile applications as biomaterials ^{1–4}, sensors and catalysts ^{5–8}, and in electronics ⁹. Supramolecular gels form as a result of the non-covalent self-assembly of small molecules, also known as low molecular weight gelators (LMWG), in a solvent medium. LMWGs consist of a diverse range of chemical structures including simple alkanes, sugars, modified amino acids, oligopeptides, dendrimers, bola-amphiphiles, peptide-amphiphiles, nucleobases, and C3-symmetric molecules in a solvent medium ^{10–16}.

The assembly of these molecules into primary structures- particularly long one-dimensional objects such as fibers, tapes, tubes and helical structures- occur under specific conditions. These primary structures are not able to efficiently entrap the solvent or simply form a gel unless their interactions, entanglements, or branching lead to a sample-spanning network. In fact, structural features like the size of primary structures and their spatial arrangements, the number of junctions or entanglements between these structures and their strength ultimately determine the gel properties such as reversibility and the associated rheological properties ¹⁷.

1.2 From serendipity to rational design of gelators

Since the mid-90s when the first attempts were made to design LMWGs, a substantial effort has been dedicated to move from fortuitous discovery towards scientific engineering of the required molecular structure: the first generation of LMWGs were purely the result of trial-and-error processes ^{18,19}. For instance, one of the key characteristics of LMWGs, which was found to be crucial for design is anisotropy. Anisotropic intermolecular interaction directs assembly into forming

one-dimensional primary structures ²⁰. The anisotropy can be created by the incorporation of specific functional moieties into the backbone structure of the gelators ²¹. Some of the known moieties which can guide anisotropy via hydrogen bonds are amides, ureas, and urethanes ²². Many gelators entailing amide groups have been developed ^{23–31} since amide groups are one of the effective motifs due to their self-complementarity, directionality, and ability to form thermodynamically favorable hydrogen bonds in a variety of solvents ³².

During the course of developing diverse LMWGs, most of the attention was dedicated to boost the design parameters, so as to improve the gelling capacity of these gelators, optimize the gel production, and predict the structure-properties correlations. This approach paved the way to produce the next generation of LMWGs which are the outcome of exploring the conventional structures, understanding the underlying principles to deduct the design rules, and ultimately incorporating the desired structural features to obtain functional gels for the target applications ^{10,33–43}.

1.3 Why multi-component gels

While versatile single-component LMWG systems for different applications have been explored for decades, recent research in this field has focused on alternative approaches to produce gels with tailored properties. One of the main approaches in this regard is to add other molecular compounds so as to have more freedom of formulation and have the ability to create new functionalities ^{44–50}; for instance, one way is the careful design or selection of an additive which is added to the gelator/gel that can influence the gelation process itself, or can modify the gel functional properties ^{51,52}. Multi-component LMWG gels can also be designed based on two non-gelling agents which cannot form a gel on their own but their complementary self-assembly yields the gel with desired properties ⁵³. Another example is when a second gelator is added to a parent gelator system which can modify the rheological properties of the final gel through encouraging co-assembly or self-sorting of these molecules into specific primary structures or networks with a diverse range of gel properties. The question which arises in this realm is whether we can control the gels spatially in terms of co-assembly and self-sorting of gelators. The answer to this question facilitates the fabrication of gels with diverse yet well-defined morphologies that are dedicated to the application at hand.

1.4 Research goals

To understand the assembly pattern in binary systems, our approach is to blend a homologous series of bisamide gelators, that act as model systems, to investigate their mixing behavior in the solid and gel state and to assess the subsequent impact it has on the final gel properties. The odd and even number of methylene groups in the bridging spacer between amide groups affecting the properties, the so-called “odd-even effect”, is the prominent design feature of these gelators which has been widely observed in LMWGs and has been extensively studied⁵⁴⁻⁵⁹. Sumiyoshi et al.⁶⁰ examined how the odd and even spacer lengths control the self-complementary assembly of diamides (bisamides) forming gels with woven- and ribbon structures (Figure 1.1). In fact, the parity of the spacer length controls the spatial arrangement of the amide groups in these gelators which is proposed to dictate the parallel and antiparallel direction of hydrogen bonding⁶¹. Based on these investigations, the positioning and self-complementarity of hydrogen bonding between the bisamides with odd and even spacer length make bisamide systems ideal to study their assembly patterns in binary mixtures.

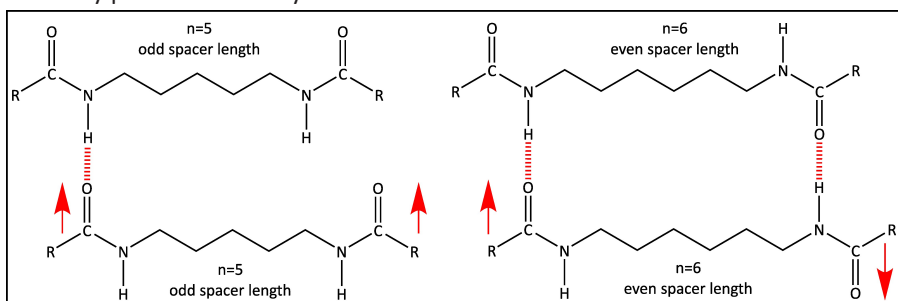


Figure 1.1 The parallel and antiparallel positions (shown by red arrows) of amide groups in bisamide molecules with odd-numbered and even-numbered spacer length respectively leading to different hydrogen bonding patterns between the amide moieties.

A fundamental study of single LMWG gels requires the full characterization of the gels across all length-scales which still remains quite challenging⁶². This complexity arises in multi-component gel systems due to the introduction of new variables into the system. A simple example of this complexity is investigating the assembly pattern across primary structures in bi-component systems: in the binary systems consisting of odd and even bisamides, molecules can conceptually assemble in three different ways (Figure 1.2):

- a. Odd and even molecules co-assemble to form a new alternating primary structures.
- b. Random interaction of odd and even molecules form stochastic primary structures consisting of a random amount of each group.
- c. Odd and even molecules self-sort to discrete structures where each entity consists of either odd or even molecules.

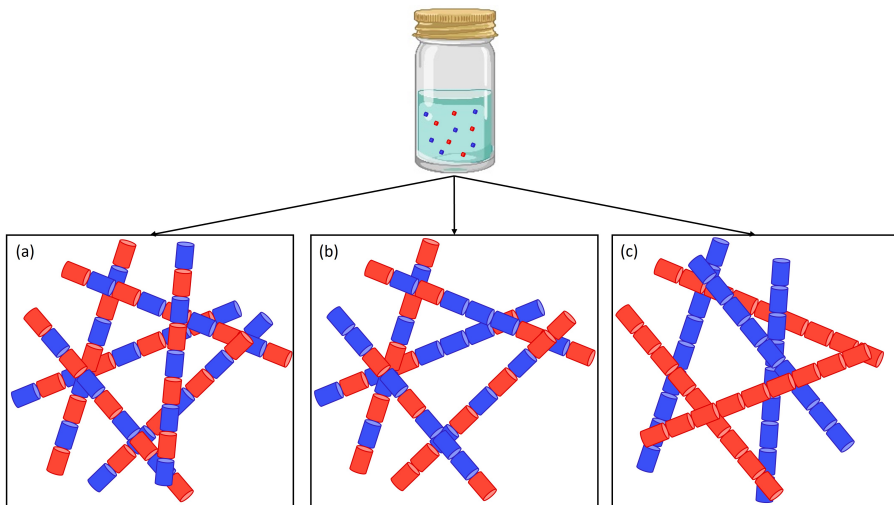


Figure 1.2 Simple classification of assembly behavior in bi-component LMWG gels: a) co-assembly, b) random assembly, and c) self-sorting.

In the context of this research, we also aim at addressing the above-mentioned problem by improving the quantitative description of phase behavior in multi-component systems by accessible methods like differential scanning calorimetry (DSC).

1.5 Thesis outline

This thesis reports on the “**structure and supramolecular assembly in multi-component organogels**”. It guides readers how the aim of this research has been achieved by division of the main question into subgoals in different chapters. This introduction chapter gives a brief overview on the research theme, it is followed by the second chapter extracted from our literature review on “From molecular assembly to gel formation: what is going on behind the scenes of supramolecular gel formation”. This tutorial review discusses three different assembly mechanisms in molecular gels namely: supramolecular polymerization, crystallization, and

spinodal decomposition. The second chapter of this thesis is based on the section on the crystallization mechanism from the larger tutorial review paper, since crystallization is found to be the dominant mechanism of gel formation in bisamide systems throughout our research. It provides a general background on molecular gels followed by how crystallization can lead to the order in the gel network. The third chapter elaborates the study of single bisamide gelators in the solid state. It aims at understanding how odd-even spacer length in the chemical structure affects the complementarity of hydrogen bonding which determines the molecular structure and gelator properties. The fourth chapter describes the supramolecular arrangement and rheological properties of single bisamide gels. In the fifth chapter of this thesis, we explain how we developed and validated the $DSC_N(T)$ analytical model. This model empowered our research toolkit to quantitatively analyze the experimental data obtained from DSC. This reliable analysis enabled us to understand the phase behavior of bisamide molecules in the solid state (chapter 3), gel state (chapter 4), and binary systems (both solid and gel state in the subsequent chapter). The last chapter (chapter 6) focuses on the ultimate goal of this thesis: to develop design rules to control the supramolecular assembly pattern in the solid and gel state of multi-component systems. In the course of this phase of research, we made an attempt to understand how compound formation/ co-assembly and phase separation/ self-sorting impact the rheological properties of bisamide gels. The summary of this scientific journey is provided at the end of this thesis.

1.6 References

- [1] M. C. Branco and J. P. Schneider, "Self-assembling materials for therapeutic delivery", *Acta Biomater.*, 2009.
- [2] J. B. Matson, R. H. Zha, and S. I. Stupp, "Peptide self-assembly for crafting functional biological materials", *Curr. Opin. Solid State Mater. Sci.*, 2011.
- [3] D. M. Ryan, B. L. Nilsson, D. M. Ryan, and B. L. Nilsson, "Self-assembled amino acids and dipeptides as noncovalent hydrogels for tissue engineering", *Polym. Chem.*, 2012.
- [4] P. R. A. Chivers and D. K. Smith, "Shaping and structuring supramolecular gels", *Nat. Rev. Mater.*, 2019.
- [5] B. Escuder, F. Rodríguez-Llansola, and J. F. Miravet, "Supramolecular gels as active media for organic reactions and catalysis", *New J. Chem.*, 2010.
- [6] C. Berdugo Gumbau, B. Escuder, J. F. Miravet, C. Berdugo, B. Escuder, and J. F. Miravet, "Structural insight into the aggregation of L-prolyl dipeptides and its effect on organocatalytic performance", *Organic & Biomolecular Chemistry*, 2015.
- [7] J. F. Miravet and B. Escuder, "Molecular Gels as Containers for Molecular Recognition, Reactivity and Catalysis", *Funct. Mol. Gels*, 2014.
- [8] X. Cao, A. Gao, J. Hou, and T. Yi, "Fluorescent supramolecular self-assembly gels and their application as sensors: A review", *Coord. Chem. Rev.*, 2021.
- [9] A. R. Hirst, B. Escuder, J. F. Miravet, and D. K. Smith, "High-tech applications of self-assembling supramolecular nanostructured gel-phase materials: From regenerative medicine to electronic devices", *Angew. Chemie - Int. Ed.*, 2008.
- [10] P. Terech and R. G. Weiss, "Low molecular mass gelators of organic liquids and the properties of their gels," *Chem. Rev.*, vol. 97, no. 8, pp. 3133–3160, 1997.
- [11] M. De Loos, B. L. Feringa, and J. H. van Esch, "Design and application of self-assembled low molecular weight hydrogels," *European J. Org. Chem.*, vol. 2005, no. 17, pp. 3615–3631, 2005.
- [12] P. Chen, "Self-assembly of ionic-complementary peptides: a physicochemical viewpoint", *Colloids Surfaces A Physicochem. Eng. Asp.*, 2005.
- [13] N. Zweep and J. H. Van Esch, "Functional Molecular Gels", The Royal Society of Chemistry, 2014.
- [14] D. K. Smith, "Dendritic supermolecules—towards controllable nanomaterials", *Chem.*

Commun., 2006.

- [15] J. D. Hartgerink, E. Beniash, and S. I. Stupp, “Peptide-amphiphile nanofibers: a versatile scaffold for the preparation of self-assembling materials”, *Proc. Natl. Acad. Sci.*, 2002.
- [16] D. J. Adams and P. D. Topham, “Peptide conjugate hydrogelators”, *Soft Matter*, 2010.
- [17] L. Petraru and W. H. Binder, “Rheological properties of supramolecular gels”, *Polymer Preprints*, 2006.
- [18] J. H. Van Esch and J. H. van Esch, “We can design molecular gelators, but do we understand them?”, *Langmuir*, 2009.
- [19] N. Lin, X. Y. Liu, R. Yu, N. Lin, W. Yu, and X. Y. Liu, “Crystal networks in supramolecular gels: formation kinetics and mesoscopic engineering principles”, *CrystEngComm*, 2015.
- [20] N Zweep, et al., “Balancing hydrogen bonding and van der waals interactions in cyclohexane-based bisamide and bisurea organogelators”, *Langmuir*, 2009.
- [21] D. R. Nunes et al., “Organogel formation rationalized by Hansen solubility parameters: Shift of the gelation sphere with the gelator structure”, *Langmuir*, 2019.
- [22] G. A. Jeffrey and G. A. Jeffrey, “An introduction to hydrogen bonding”, Oxford university press New York, 1997.
- [23] K. Hanabusa et al., “L-Lysine based gemini organogelators: their organogelation properties and thermally stable organogels”, *Org. Biomol. Chem.*, 2003.
- [24] J. Van Esch, S. De Feyter, R. M. Kellogg, F. De Schryver, and B. L. Feringa, “Self-assembly of bisurea compounds in organic solvents and on solid substrates”, *Chem. Eur. J.*, vol. 3, 1997.
- [25] K. Hanabusa, K. Shimura, K. Hirose, M. Kimura, and H. Shirai, “Formation of organogels by intermolecular hydrogen bonding between ureylene segment”, *Chem. Lett.*, 1996.
- [26] M. De Loos et al., “Cyclohexane bis-urea compounds for the gelation of water and aqueous solutions”, *Org. Biomol. Chem.*, 2005.
- [27] M. De Loos et al., “Remarkable stabilization of self-assembled organogels by polymerization”, *J. Am. Chem. Soc.*, 1997.
- [28] D. D. Di et al., “‘Click’ chemistry in a supramolecular environment: stabilization of organogels by Copper (I)-catalyzed azide– alkyne (3+ 2) cycloaddition”, *J. Am. Chem. Soc.*, 2006.

- [29] K. Hanabusa, A. Kawakami, M. Kimura, and H. Shirai, "Small molecular gelling agents to harden organic liquids: Trialkyl cis-1, 3, 5-cyclohexanetricarboxamides", *Chem. Lett.*, 1997.
- [30] Y. Yasuda, "Novel low-molecular-weight organic gels: N, N' - tristearyltrimesamide/organic solvent system", *Chem. Lett.*, 1996.
- [31] J. J. Van Gorp, J. A. J. M. Vekemans, and E. W. Meijer, "C 3-symmetrical supramolecular architectures: Fibers and organic gels from discotic trisamides and trisureas", *J. Am. Chem. Soc.*, 2002.
- [32] F. Fages, F. Vögtle, M. Žinić, and M. Žinic, "Systematic design of amide-and urea-type gelators with tailored properties", *Top. Curr. Chem.*, 2005.
- [33] S. Shinkai and K. Murata, "Cholesterol-based functional tectons as versatile building-blocks for liquid crystals, organic gels and monolayers", *J. Mater. Chem.*, 1998.
- [34] S. Banerjee, R. K. Das, and U. Maitra, "Supramolecular gels 'in action'", *J. Mater. Chem.*, vol. 19, no. 37, pp. 6649–6687, 2009.
- [35] J. Esch et al., "Low Molecular Weight Gelators for Organic Solvents: From serendipity towards design". Springer, 1999.
- [36] . Gronwald, E. Snip, S. S. U, and S. Shinkai, "Gelators for organic liquids based on self-assembly: a new facet of supramolecular and combinatorial chemistry", *Curr. Opin. Colloid Interface Sci.*, 2002.
- [37] K. J. C. Van Bommel, A. Friggeri, and S. Shinkai, "Organic templates for the generation of inorganic materials", *Angew. Chemie Int. Ed.*, 2003.
- [38] T. Ishi-i and S. Shinkai, "Dye-based organogels: Stimuli-responsive soft materials based on one-dimensional self-assembling aromatic dyes", *Supramolecular Dye Chem.*, 2005.
- [39] D. J. Abdallah and R. G. Weiss, "Organogels and low molecular mass organic gelators", *Adv. Mater.*, 2000.
- [40] N. M. Sangeetha and U. Maitra, "Supramolecular gels: Functions and uses", *Chem. Soc. Rev.*, 2005.
- [41] M. George and R. G. Weiss, "Molecular organogels. Soft matter comprised of low-molecular-mass organic gelators and organic liquids", *Acc. Chem. Res.*, 2006.
- [42] A. Ajayaghosh and V. K. Praveen, "π-Organogels of self-assembled p-phenylenevinylenes: soft materials with distinct size, shape, and functions", *Acc. Chem. Res.*, 2007.

- [43] D. K. Smith, "Lost in translation? Chirality effects in the self-assembly of nanostructured gel-phase materials", *Chem. Soc. Rev.*, 2009.
- [44] V. Jayawarna et al., "Nanostructured hydrogels for three-dimensional cell culture through self-assembly of fluorenylmethoxycarbonyl-dipeptides", *Adv. Mater.*, 2006.
- [45] J. A. Foster et al., "Blending gelators to Tune gel structure and probe anion-induced disassembly", *Chem. Eur. J.*, 2014.
- [46] K. V. Rao and S. J. George, "Supramolecular Alternate Co-Assembly through a Non-Covalent Amphiphilic Design: Conducting Nanotubes with a Mixed D–A Structure", *Chem. Eur. J.*, 2012.
- [47] A. Das and S. Ghosh, "A generalized supramolecular strategy for self-sorted assembly between donor and acceptor gelators", *Chem. Commun.*, 2011.
- [48] B. Karwowski et al., "Chiral recognition in bis-urea-based aggregates and organogels through cooperative interactions", *Angew. Chemie*, 2001.
- [49] R. J. Swanekamp, J. T. M. DiMaio, C. J. Bowerman, and B. L. Nilsson, "Coassembly of enantiomeric amphipathic peptides into amyloid-inspired rippled β -sheet fibrils", *J. Am. Chem. Soc.*, 2012.
- [50] R. Afrasiabi and H. H. Kraatz, "Small-Peptide-Based Organogel Kit: Towards the Development of Multicomponent Self-Sorting Organogels", *Chem. Eur. J.*, 2013.
- [51] A. M. Brizard et al., "Self-assembled interpenetrating networks by orthogonal self-assembly of surfactants and hydrogelators", *Faraday Discuss.*, 2009.
- [52] A. Brizard, M. Stuart, K. van Bommel, A. Friggeri, M. de Jong, and J. van Esch, "Preparation of Nanostructures by Orthogonal Self-Assembly of Hydrogelators and Surfactants", *Angew. Chemie*, 2008.
- [53] A. R. Hirst and D. K. Smith, "Two-Component Gel-Phase Materials—Highly Tunable Self-Assembling Systems", *Chem. Eur. J.*, 2005.
- [54] V. Kocasoy et al., "Influence of odd–even effect and intermolecular interactions in 2D molecular layers of bisamide organogelators", *RSC Adv.*, 2018.
- [55] F. Tao and S. L. Bernasek, "Understanding odd– even effects in organic self-assembled monolayers", *Chem. Rev.*, 2007.
- [56] K. Aoki, M. Kudo, and N. Tamaoki, "Novel odd/even effect of alkylene chain length on the photopolymerizability of organogelators", *Org. Lett.*, 2004.
- [57] T. Wang, Y. Li, and M. Liu, "Gelation and self-assembly of glutamate bolaamphiphiles with hybrid linkers: effect of the aromatic ring and alkyl spacers", *Soft Matter*, 2009.

- [58] J. Schneider et al., "Odd-even effects in supramolecular assemblies of diamide bolaamphiphiles", *Langmuir*, 2000.
- [59] H. D. Burrows, "Studying odd-even effects and solubility behavior using α [alpha], ω [omega]-dicarboxylic acids", *J. Chem. Educ.*, 1992.
- [60] T. Sumiyoshi, K. Nishimura, M. Nakano, T. Handa, Y. Miwa, and K. Tomioka, "Molecular Assembly of C 2-Symmetric Bis-(2 S)-2-methyldodecanoylamides of α , ω -Alkylidenediamines into Coiled Coil and Twisted Ribbon Aggregates", *J. Am. Chem. Soc.*, 2003.
- [61] K. Tomioka, T. Sumiyoshi, and S. Narui, "Molecular Assembly and Gelating Behavior of Didodecanoylamides of α , ω -Alkylidenediamines", *Journal of the American Chemical Society*, 2001.
- [62] E. R. Draper and D. J. Adams, "How should multicomponent supramolecular gels be characterised?", *Chem. Soc. Rev.*, 2018.

Chapter 2

From molecular assembly to gel formation via crystallization: what is going on behind the scenes of supramolecular gel formation

Introduction

Gels and gel-like substances have been in use for thousands of years. For instance, Arabic gum has been applied by ancient Egyptians as a binder for inorganic pigments to produce coatings or as a glue for wood ¹, while Irish moss and carrageenan have been used in southern Ireland as a thickener for food already since 400 AC. ². Nowadays, there is a variety of applications for gels in many fields, such as the food industry ³, biomedical applications, including drug delivery systems ^{4,5}, tissue engineering ⁶, sensors and other electronics ^{7,8}, cosmetics ⁹, art conservation ^{10,11}, and photography ¹².

Despite the diversity of gels and the difficulty to give a general definition of gels- as stated by Jordan Lloyd, “The colloidal condition, the gel, is one which is easier to recognize than to define.” ¹³, all definitions agree on a major rule: a gel consists of a liquid component (solvent) as the predominant content and a solid component, a gelator, in the minor portion which ultimately constructs a network with viscoelastic properties. Small organic molecules, surfactants, peptides, micelles, and globular proteins are groups of materials which can act as gelators in polymer and colloid gels ¹⁴⁻²⁰. A particular interesting class of gelators are the Low Molecular Weight Organic Gelators (LMWGs), which are organic compounds with low molecular mass (molecular weights <2000 Da ²¹) and are very efficient gelling agents for a wide variety of solvents, including water. These LMWG gelling agents have the distinctive property that they form so-called supramolecular gels. In a supramolecular gel a three dimensional network is a result of non-covalent intermolecular interactions between gelator molecules such as van der Waals interactions, $\pi-\pi$ stacking,

hydrogen bonding, metal coordination, or donor–acceptor interactions. These weak interactions endow supramolecular gels with reversibility, in contrast to the permanent covalent linkages in cross-linked polymeric gels^{22,23} (Figure 2.1).

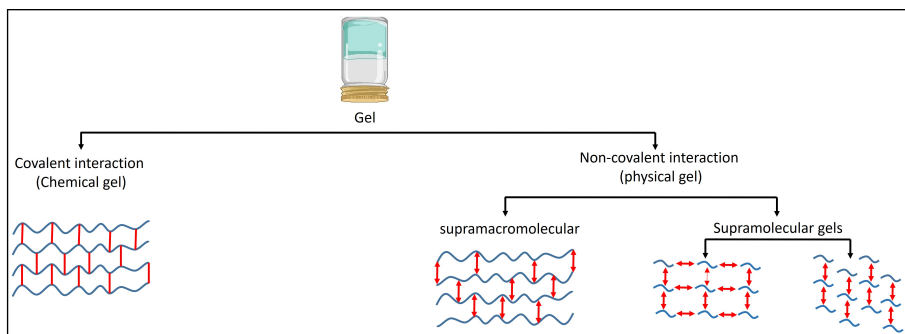


Figure 2.1 Gels categorized based on the nature of the interaction bonds between the gelators as building blocks of gels.

As a result of the reversible intermolecular interactions, the transformation from a sol state (fluid) to a gel state (non-fluid) or vice versa, gelation or dissolution can respectively occur. These interactions are induced via stimuli such as pH, light, heat, sound, mechanical stress, magnetic or electric fields, anions, metal cations, enzymes, or other chemicals depending on the molecular structure of the gelator and solvent components^{24–33}.

One of the main characteristics of supramolecular gels are their viscoelastic properties which means they possess both viscous properties of the entrapped solvent and elastic properties of the network^{34,35}; in rest or when a small scale of stress is applied, they behave as elastic solids but when stress exceeds a certain threshold value, the yield stress, they turn into viscoelastic fluid. The instant method to test if a gel has formed qualitatively is ‘tube inversion test’ in which the tube containing the sample to be examined is turned over³⁶. If the sample does not flow over a long period of time, it is considered to be a gel, and if the sample flows it is a viscous fluid. However, the viscoelastic properties of gels encompasses a broad spectrum, ranging from highly dynamic viscoelastic liquid to static viscoelastic solids³⁷. Therefore, a quantitative rheological test is required to determine whether the sample has truly gelled or not, and where a supramolecular gel stands in this spectrum^{38,39}. The most common rheology test measures the elastic (storage) modulus G' and the viscous (loss) modulus G'' as functions of frequency ω . When G' reaches a plateau and is greater than G'' over a reasonably accessible frequency

range (mostly agreed on 10^{-3} rad.s $^{-1}$ to 10^2 rad.s $^{-1}$), the sample is considered to exhibit the gel-like behavior⁴⁰.

From the first attempts to design supramolecular gels, characterization of structural properties has been the dominant strategy to engineer the microstructure and achieve the required functionalities for specific applications^{16,41-48}. In one approach, considerable focus has been given to understanding of the supramolecular chemistry of the main constituents, the gelator and solvent, to reach a recipe with certain chemical structures^{47,49-59}. The success of the recipe was evaluated by studying the manifestation of the chemical features at gel microstructure and at the next level, their macroscopic behavior, particularly rheological properties^{16,41,43,60,61}. In the course of these investigations, much attention has been paid to *why* do gels form, i.e. the driving forces for gelator-gelator and gelator-solvent interaction, but much less attention has been paid to *how* gels form, the mechanisms of assembly which lead to the formation of a gel network⁶². However, it is the driving force for the assembly of the gelator molecules in conjunction with the mechanism directing the assembly towards the gel formation, which are the main gearwheels that relate the chemical structure with the final gel properties (Figure 2.2).

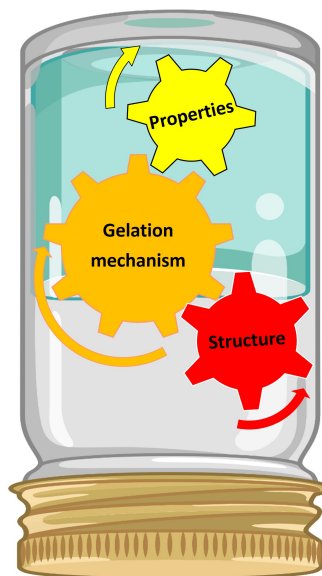


Figure 2.2 Gelation mechanisms, the physical-chemical mechanisms bridging the structure and properties of supramolecular gels.

To address the mechanism of gelation and network formation, first one needs to understand what is the driving force for the aggregation of the gelator molecules, how they assemble to supramolecular, often fibrous assemblies, and finally how these assemblies can develop a gel network. In our tutorial review ⁶³, we focus on the mechanism of supramolecular assembly and the subsequent network formation. We explicitly distinguish three dominant assembly mechanisms in supramolecular gel systems, namely supramolecular polymerization ^{64–68}, crystallization ^{69–71}, and spinodal decomposition ^{72–74}. In this chapter, the part of the review dealing with the crystallization mechanism is discussed because it is the dominant mechanism of assembly in LMWG systems and bisamide LMWGs are central to this research, appeared to form gels through the crystallization mechanism. In the following discussion on the gel formation through crystallization, the basic stages of nucleation, growth, and the formation of multi-level crystal networks are explained. Accordingly, the effect of the developed microstructural features on the macroscopic properties of some supramolecular gels as examples will be described.

In the classic method, thermally-triggered gels are prepared from molecular gelators as follows: a solid gelator is fully dissolved in an appropriate liquid solvent upon heating until an apparent solution (sol) is obtained (Figure 2.3a). By cooling the solution, the concentration of the solute gelators exceeds the equilibrium solubility, known as supersaturation. When crystallization occurs from the melt state, supersaturation can be defined by use of the heat of fusion (Δf) in Equation 2.1:

$$\sigma = \frac{\Delta H_f}{R} \times \frac{\Delta T}{T_f} \quad \text{Equation 2.1}$$

This equation explains why cooling below the equilibrium temperature does not lead to an immediate precipitation. In fact, a considerable cooling (undercooling (ΔT)) with associated levels of supersaturation is the prerequisite to the emergence of a relatively opaque phase in the initially transparent mixture (Figure 2.3b). As a result, at a certain temperature (T_{sg}) where sufficient separation of the solutes from the solvent occurs, a new phase forms which might ultimately lead to the gel formation (Figure 2.3c) ⁷⁵.

The microstructure of the gel (Figure 2.3c) characterized using electron microscopy and X-ray experiments have evidenced the presence of crystalline structures such as 1D objects like fibers ^{76–84} and 2D objects like platelets ^{85–90} in a three-dimensional (3D) network ⁹¹. Therefore, the formation of crystalline structures and development of 3D network in a gel can be explained using the common model for crystallization, nucleation and growth. In fact, many of the self-assembly principles that have been

elegantly found by exploring crystalline materials are applicable to molecular gels^{92,93}.

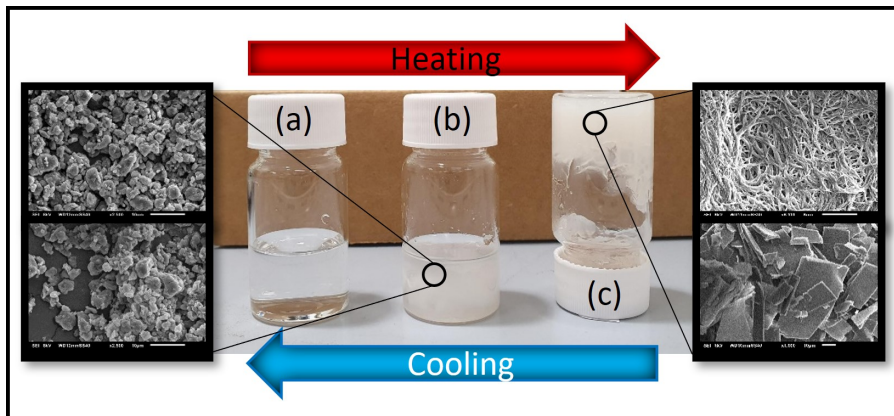


Figure 2.3 Classic gel preparation using the heat-cool process: a) macroscopically homogeneous solution mixture, b) the coexistence of precipitated phase in non-gelled liquid zones, insets showing some non-gelled microstructures due to the insufficient supersaturation, c) the whole sample volume is completely gelled upon considerable cooling reaching the required level of supersaturation, insets showing some possible microstructures of the fibrous or platelet-like network in the gel imaged by scanning electron microscopy.

2.1 Classical nucleation

According to the classical nucleation theory, in the solution state, entropic factors dominate the system, and therefore molecularly dissolved gelator molecules and solvent molecules are in equilibrium, and assembly of the molecules is negligible. Upon decreasing the temperature or increasing the concentration, enthalpic interactions becomes dominant over entropic factors, and this drives assembly of the gelator molecules once their concentration exceeds the solubility limit. In this stage, the molecules form clusters, driven by a reduction of the volume or bulk free energy contribution (ΔG_v) to the total free energy of the system (ΔG_T)^{94,95}. However, despite the intrinsic driving force for aggregation and emergence of many clusters in the early stage of cooling, only a fraction of them would become sufficiently large to successfully grow into nuclei. The reason for this is that the formation of clusters creates a new surface with the solution phase, which is associated with an unfavorable interfacial energy (ΔG_s). Hence, the balance between the volume free energy (ΔG_v) and the interfacial energy (ΔG_s) determines the total Gibbs free energy

of the system for nucleation (ΔG_T). The former describes how favorable it is to have a phase change and the latter is the amount of energy needed to create an interface.

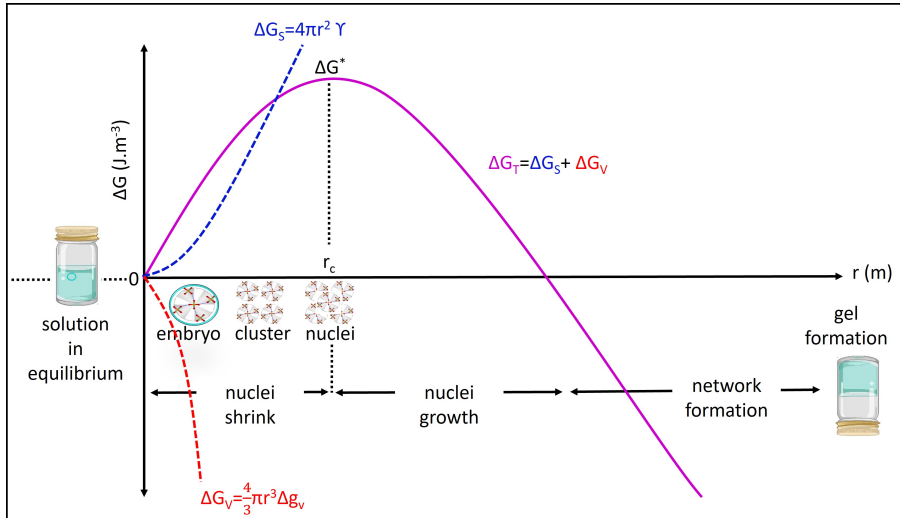


Figure 2.4 Energy contribution of the nucleation in the total Gibbs free energy, the embryos (clusters of a few molecules) are prone to dissociate. Above the solubility limit, the density of the clusters increases which increases the probability of these clusters to meet each other thereby exceeding the critical size at which the bulk energy overtakes the interfacial energy. These clusters reach a critical size and form nuclei. Initially the density of the clusters is low so that the rate at which nucleation appears is very small and when the density of the clusters become larger, the rate of cluster-cluster aggregation increases accordingly.

The mathematical expression of total energy of the system for spherical clusters is given in Equation 2.2 where Δg_v is the Gibbs free energy per unit of volume and r is the radius of spherical clusters. The optimization of ΔG_{total} in Equation 2.2 yields the critical radius in Equation 2.3:

$$\Delta G_{\text{total}} = \Delta G_v + \Delta G_s = -\frac{4}{3}\pi r^3 \Delta g_v + 4\pi r^2 \gamma \quad \text{Equation 2.2}$$

$$r_c = \frac{2\gamma}{\Delta g_v} \quad \text{Equation 2.3}$$

From Figure 2.4 it is apparent that only for clusters whose sizes exceed the critical radius (r_c), further growth leads to a further reduction of ΔG_{total} while clusters with $r < r_c$ can only decrease the Gibbs free energy by dissolving back in the solution.

Hence, only clusters with a radius $r > r_c$ have overcome the nucleation barrier $\Delta G^*(r_c)$ and are sufficiently stable for further growth driven by the decrease of ΔG_{total} ⁹⁶⁻¹⁰⁰.

In the kinetic formalism of Gibb's theory, the nucleation rate (J)- the number of nuclei formed per unit time per unit volume- is controlled by (ΔG^*) . The steady-state rate of nucleation is expressed in the form of Arrhenius reaction rate in Equation 2.4:

$$J = J_0 \cdot e^{-\frac{\Delta G^*}{k_B \cdot T}} \quad \text{Equation 2.4}$$

2

where k_B is the Boltzmann's constant and J_0 is the pre-exponential factor which is related to the rate of attachment of molecules to the critical nucleus. The rate of molecular attachment depends on the molecular mobility which is also sensitive to temperature (T).

2.2 Non-classical nucleation

The classic nucleation theory based on the thermodynamics description by Gibbs along with kinetic theories from the 1930s and 1940s has successfully addressed many aspects of nucleation particularly in the case of low supersaturation^{101,102}. The classical nucleation theory assumes that nuclei create constituents with sharp interfaces within the parent phase. It is also based on the assumption that the constituents have exactly the same arrangement as the final crystal (Figure 2.5a). In the last two decades, experiments have shown that many nucleation processes cannot be simply explained by classical nucleation theory. The classical nucleation theory can be extended by four major amendments¹⁰³:

1. Nucleation can occur in two steps where the formation of disordered precursors precedes the development of crystalline nuclei (Figure 2.5b)^{104,105}.
2. Single atoms or molecules can form nuclei if the nucleation barrier drops sufficiently at a given temperature (Figure 2.5c)¹⁰⁶.
3. Nuclei with non-equilibrium shapes form which have similar shape to the final crystal phase (Figure 2.5d)^{107,108}.
4. Another scenario goes beyond the classical and non-classical nucleation theory: it explains how the order parameter of a nucleus changes moving outwards from the core, consisting of one or a few atoms. Therefore, there is no sharp interface between the nucleus and its surrounding phase and it is changing over time as the nucleus grows (Figure 2.5e)¹⁰⁹.

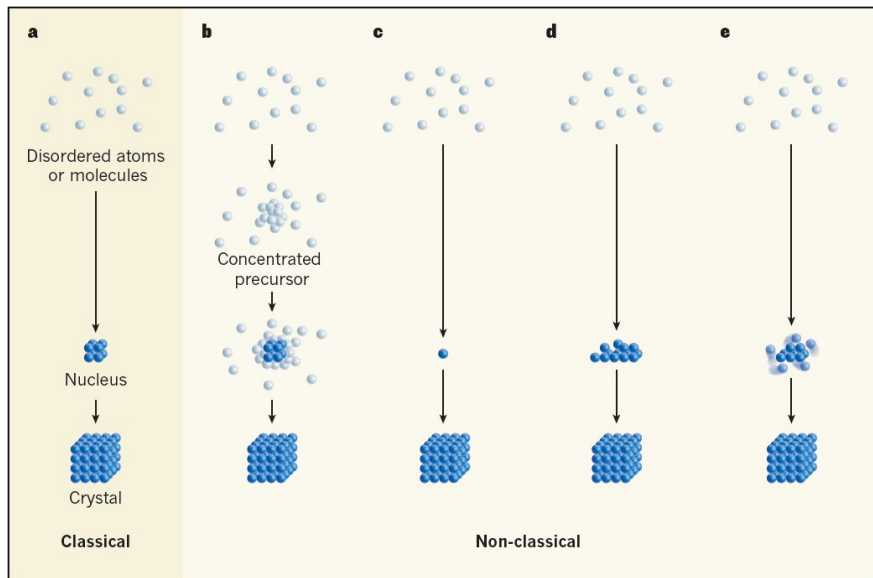


Figure 2.5 Classical versus non-classical nucleation theories: a) classical nucleation which explains how clusters of atoms or molecules which grow into nuclei with a particular shape, size, and sharp edges with the same crystal structure as the final crystal (dissolved molecules in the solution are in pale blue and ordered constituents of a nucleus are shown in dark blue), b) the non-classical two-step model proposes that initial precursors can form which are completely disordered and nuclei emerge in a separate step, c) in another non-classical theory, one atom or very few atoms can act as a nucleus, d) nuclei with the same lattice as the emerging crystal but not the ideal ‘equilibrium’ shape of the classical theory is expected, e) nuclei with non-equilibrium shapes emerge which can change over time, reprinted with permission from ref. ¹⁰³.

2.3 Crystal growth

After nucleation has occurred, the solution usually remains supersaturated thereby providing a driving force for further crystal growth. It should be noted that this growth is a dynamic process, in which the adsorption rates of molecules from the solution to the nuclei exceeds desorption rates of molecules from the nuclei into the solution. While desorption rates only depend on the interaction energy of the molecule with the surface, the adsorption rates increase with increasing the solute concentration, and hence, crystal growth rates increase with increasing supersaturation.

2.3.1 Equilibrium growth

Nuclei grow over time until they reach a state of equilibrium, where the rate of crystal growth is equal to the rate of the dissolution, which can be explained to some extent by Gibbs–Curie–Wulff theorem¹¹⁰: the equilibrium state is reached when the crystal is in a thermodynamically stable state and has the minimum level of surface energy. In fact based on Gibbs theory about heterogeneous phase equilibria, crystals grow at equilibrium such that the total surface area times the surface free energy is at a minimum. This form of crystal is called the equilibrium crystal shape (Figure 2.6), which is exclusive to a constant temperature and pressure. The normal growth rates of crystal faces are proportional to the surface free energies as proposed by Curie. In the equilibrium crystal shape, the relative areas of the different faces are inversely related to the ratio of the interfacial free energies as suggested by the Wulff theorem¹¹⁰. Based on Wulff theory, the central distances of the crystal faces from a point within the crystal (Wulff point) are proportional to the corresponding specific surface free energies of these faces (Figure 2.6b). In other words, the crystal faces with the highest interfacial free energy have the smallest interfacial area, conversely, those with the lowest interfacial free energy have the largest interfacial area. Crystal faces with the highest interfacial energy (or attachment energies) grow the fastest, as a result of this growth mode, the interfacial area of the adjacent faces increases. Therefore, as long as the growth rates of the crystal faces are sufficiently slow to allow the growing crystal to equilibrate towards a minimal interfacial energy via interfacial migration and annealing, the ratio between the interfacial areas of the various crystal faces remains preserved and an equilibrium crystal shape is obtained.

Although Gibbs–Curie–Wulff theory can explain many aspects of crystallization, the lack of concrete experimental proof makes the theory imperfect to some degree. Moreover, there is little quantitative evidence to support this theorem in the field of supramolecular gels, which are mainly based on organic materials: for inorganic materials, the crystal-forming components (atoms or ions) are spherical (ball shape). Therefore, the orientation of atoms/ions do not matter when they are transported to the crystal phase during the crystal growth. However, for organic materials like molecular gels, the crystal-forming components (gelator molecules) are composed of more than one atom which makes them anisometric. This feature of (many) organic molecules make their crystal growth processes more complex than that of the inorganic materials and brings new questions, e.g., what is the orientation of the molecules approaching the crystal interface?

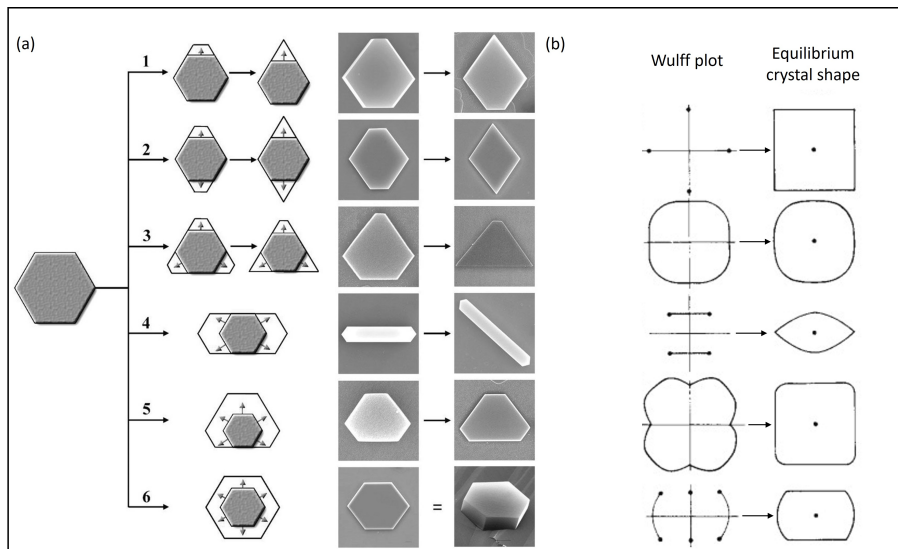


Figure 2.6 Equilibrium shapes of crystals: a) lateral growth and resulting crystal shapes according to Gibbs-Curie-Wulff theory, b) some equilibrium shapes corresponding to Wulff plots, reprinted with permission from ref. ^{110,111}.

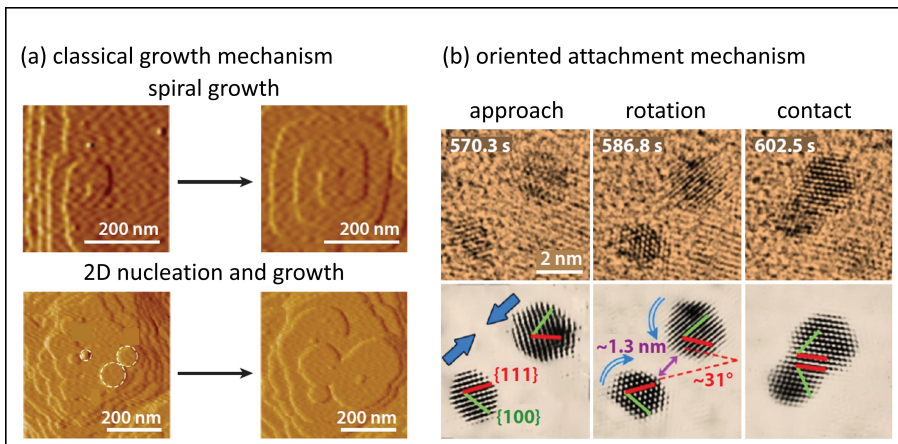


Figure 2.7 Illustration of the growth theories: a) classical growth mechanisms in the forms of spiral growth and 2D island nucleation-growth, b) non-classical growth via oriented attachment which occurs in three steps for gold nano particles, approach, rotation, and contact, reprinted with permission from ref. ¹¹².

In a solution, nuclei of gelator molecules grow into larger crystals by migration of primary constituents (atoms, molecules, etc.) and their attachments to the pre-existing nuclei to form a layer. This process is driven by the minimization of the interfacial free energy manifested by the multiple intermolecular interactions at the

edges as compared to single interaction for isolated adsorbed molecules and further attachment/migration to the layer edges to grow the layer (Figure 2.7).

2.3.2 Non-equilibrium growth

At larger supersaturations, the rate of attachment of the molecules exceeds the rate of migration or annealing of the growing edge. Hence, the growth rate of one or more crystal faces may become too large to maintain the equilibrium shape. Depending on the degree of supersaturation, different growth modes may occur each leading to different morphologies, each with their own characteristics deviating from the equilibrium shapes. Non-equilibrium growth encompasses a wide range of growth processes that occur far from thermodynamic equilibrium. The first growth mode may occur when the rate of the crystal growth is no longer governed by the relative interfacial energies (i.e. desorption rates), but become limited by the rate of molecular diffusion to the grown interfaces. In the diffusion-limited growth, the diffusion rate (flux) of molecules towards the crystal face increases with the local curvature of the front tip: at regions of high curvature, the diffusion rate is typically higher due to the increased concentration gradient, which results in a larger driving force for diffusion. In general, these will be the crystal faces with the highest interfacial free energy that were already growing fast. Thus, diffusion-limited growth will favor the growth of the already fastest growing interfaces, leading to crystal shapes that are more elongated along their fastest growing axis, compared to the equilibrium shape. The diffusion rate is even larger towards the crystal edges because of the larger local curvature, and this may lead to stronger growth of the edges, also known as tip growth. Tip growth has the tendency to become a self-amplifying process as a growing tip has an even larger local curvature, and hence diffusion towards such a tip becomes faster thereby even more accelerating its growth.

2.3.2.1 Small-angle tip splitting (side branching)

These diffusion-controlled growth modes are often mingled with the growth modes that are more related to the local annealing of defects by interfacial migration, which is driven by a local minimization of the interfacial free energy. At high supersaturation, the adsorption rates may become too fast, thus there is insufficient time for the local defects to be annealed by short-range diffusion. Therefore, such a defect at the growing tip becomes a tip by itself. It starts to grow independently from the growing tip via molecular deposition in a different direction, resulting in splitting of the tip, known as tip-splitting (Figure 2.8a). Tip splitting is a phenomenon

that occurs during the growth of fibers where the growing fiber splits into two or more separate fibers at the tip which forms branched or bifurcated fibers. This type of tip splitting, i.e. the occurrence of defects leading to tip-splitting is also known as non-crystallographic mismatch or small-angle branching. Generally, tip splitting occurs at high supersaturation or due to other factors like variations in the chemical composition of the growth medium, changes in the temperature or flow rate of the growth medium, changes in the direction or rate of growth of the fiber.

Defects which are not annealed may also occur at the lateral face of growing crystal rather than at the edges or tips. In such cases the defect often becomes the nucleus for the growth of a new crystal, a so-called daughter crystal, that is merged to the lateral face of the parent crystal (known as side-merging which is shown in the inset of Figure 2.8a). This growth mode is caused by secondary or heterogeneous nucleation leading to the formation of daughter crystals. The growth of the daughter crystal in this growth mode is typically faster than that of the parent crystal face which is due to its larger associated diffusion front.

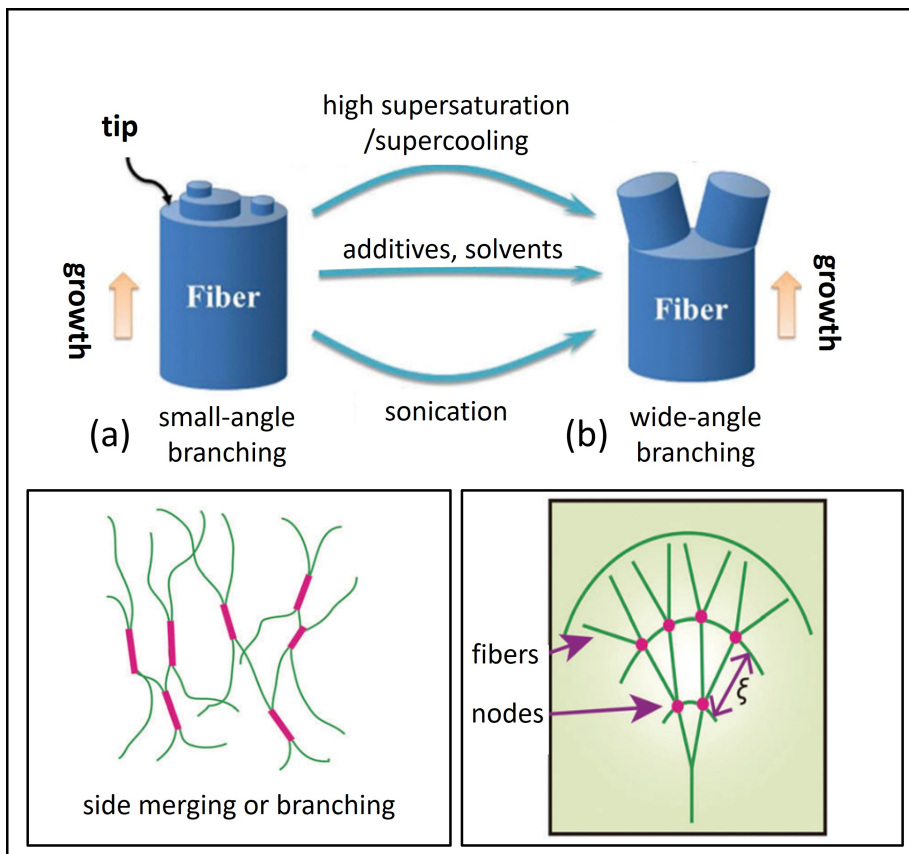


Figure 2.8 Illustration of fiber growth modes: a) small angle (non-crystallographic mismatch), b) wide-angle branching (crystallographic mismatch) which occurs at relatively higher supersaturation level compared to small-angle branching, reprinted with permission from ref. ¹¹³.

2.3.2.2 Wide-angle tip branching (crystallographic mismatch)

Another form of splitting can occur when the crystallographic alignment between the adjacent crystallites may be lost by an abrupt increase in supersaturation ¹¹⁴⁻¹¹⁷. This is known as wide-angle branching which occurs at relatively higher supersaturation than the small-angle tip splitting (Figure 2.8b). In fact, the crystallographic orientation of the branches (daughter crystals) significantly deviates from the main growing crystal (the parent crystal), thus, a new crystal domain forms. The anisotropy between the interface of daughter branches and their parent results in this different growth pattern, known as a wide-angle crystallographic mismatch or a non-crystallographic branching ¹¹⁸. This mode of

growth occurs in 3D where the parent fiber acts as a substrate for the radial growth of the crystals developing a Cayley tree structure.

In systems where the supersaturation is the only driving force for the growth, the above mentioned modes of growth can be explained via different terminologies. The deposition of a thin layer of atoms/molecules on the top of the crystal substrate is called epitaxial growth if the crystal structure of the deposited layer matches with the substrate. The term “epitaxial” comes from the Greek words “*epi*” which means “on top of” and “*taxis*” meaning arrangement. If the deposited layer is aligned with the underlying substrate and follows the orientation of the substrate crystal, the lattice parameters of the substrate and the deposited material will be similar, thereby epitaxial growth occurs. Self-epitaxial growth is dominant in the systems where growth is not mediated by external means like impurities. Thus, a thin layer of material on top of the substrate from the same material deposits. In this case, the term “self” refers to the fact that the substrate and the deposited layer are made of the same material. Figure 2.9 summarizes how the mode of self-epitaxial growth can change with the degree of supersaturation: at low supersaturation where the nucleation energy barrier (ΔG^*) is too high, a complete self-epitaxial match is dominant whereas increasing the supersaturation encourages the mismatch of the daughter crystals from the parent crystals ¹¹³.

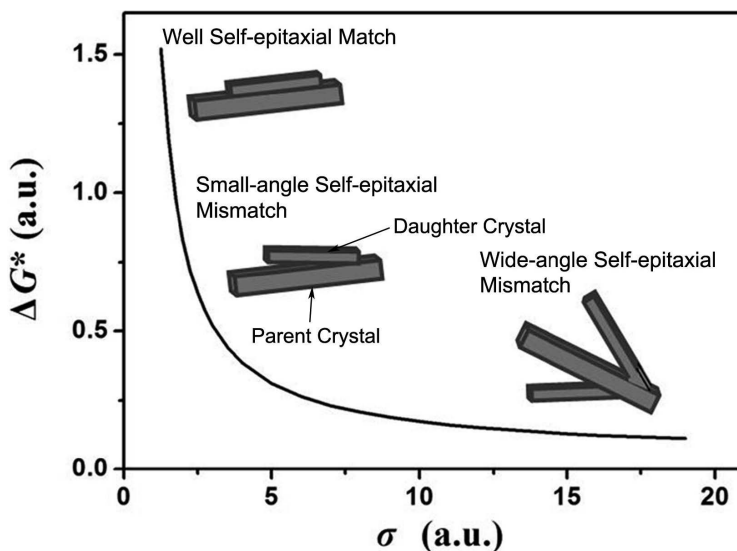


Figure 2.9 Energy barrier change (ΔG^*) with supersaturation (σ), reprinted with permission from ref. ¹¹⁹.

2.4 Network formation

Nucleation and growth can lead to the gel formation if the self-assembly of gelator molecules ultimately forms the three dimensional gel network permeating the solvent. From a hierarchical perspective, the assembly of gelator molecules builds primary structures (microscale) which grow further to form secondary structures (mesoscale). The interconnection of individual secondary structures leads to the tertiary structure, i.e., the gel network (macroscopic scale)¹⁵.

2.4.1 Network formation via different modes of assembly

The network formation in a gel driven by the above-mentioned growth modes can occur via different assembly-modes in supramolecular gels.

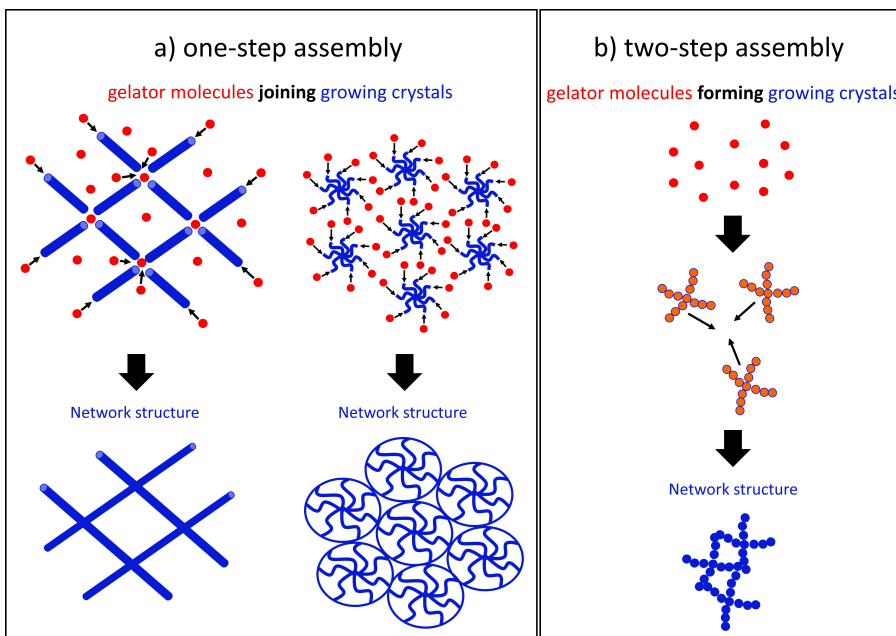


Figure 2.10 The crystal network formation in a gel can occur with different modes of assemblies: (a) one-step process of assembly, (b) two-step process of assembly.

These assembly modes have been very well explained by Liu et al. and are briefly summarized here¹²⁰:

a) One-step assembly

Gelator molecules can directly participate in the crystal network formation without the formation of intermediate crystal entities. This mode of

assembly is known as the one-step assembly process. In fact, in this mode of assembly, nucleation and growth occur at the same time (Figure 2.10a).

b) Two-step assembly

Compared to the direct one-step assembly mode, the network formation occurs in two stages: first, the assembly of the molecules to form crystalline entities, then growth/network formation occurs via coalescence of the growing crystallites (Figure 2.10b).

c) Hybrid modes of assembly (simultaneous one-step and two-steps assemblies)

It is also possible that the crystal network develops by the co-occurrence of the one-step and two-step assembly processes.

The tip splitting/branching and the side branching belong to the one-step process and mixed mode of assembly while two-step crystallization occurs mainly at nano/mesoscale and is mainly the dominant mechanism in typical atomic systems ¹²¹.

2.4.2 How do different network structures develop via different growth/branching modes?

Different modes of growth occurred via different pathways can construct gel network patterns with their characteristic rheological properties. One of the well-known patterns which occurs in nature are dendrites (Figure 2.11). For example, when water supersaturates and starts to crystallize, the nuclei grow and star-shaped snowflakes form ¹²².

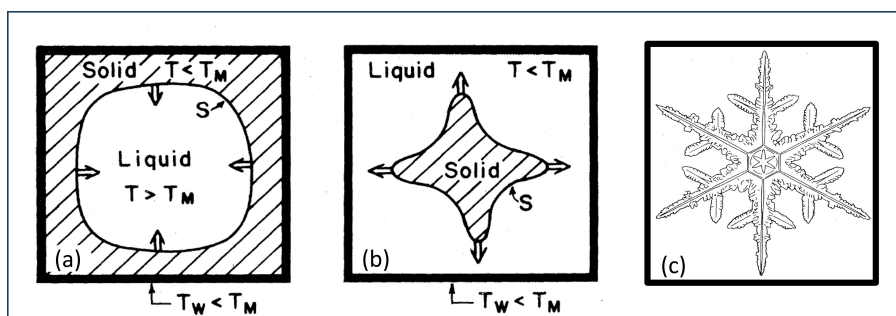


Figure 2.11 schematic illustration of the solidification of a liquid in a vessel whose walls are at a temperature (T_w) below the melting temperature of a pure substance (T_m), thus the generated latent heat is eliminated through the walls: a) the solidifying front S starts to form from the walls, b) the liquid is undercooled below the melting temperature, c) dendritic growth, reprinted with permission from ref. ¹²³.

In classic epitaxial growth, the daughter crystals form with well-defined orientation with respect to the parent crystals which can develop dendritic structures ¹²⁴. The relative orientation of the new crystalline layer with respect to the parent substrate differentiates epitaxial growth pattern from multi-crystalline or random amorphous structures. As mentioned previously, in self-epitaxial growth, the parent substrate is a growing surface of the same type of crystallites which is a dominant growth mode at low supersaturation levels. This growth pattern forms periodic zigzag branches where there is a strong anisotropy. In fact, the microscopic interfacial anisotropy is essential to stabilize the dendritic growth (Figure 2.12a) while an insufficient or a weak anisotropy encourages the development of fractal patterns (Figure 2.12b).

Dendrites and fractal patterns have the same origin: in dendrites, continuous annealing reduces the tip splitting frequency by removing local tips. Gel networks with dendritic morphologies form when the rate of growth is not yet very fast, for example at a low supersaturation level while gel networks with fractal morphology form at higher supersaturation levels where there is a wide-angle mismatch between the crystallographic orientation of daughter crystals and of the parent crystal. At high supersaturations where the mismatch nucleation barrier is overcome, fiber branching indeed occurs at the tip of fibers growing one-dimensionally. Thereby, the frequency of tip splitting increases leading to the formation of fractals (Figure 2.12b). Fractal patterns embody self-similar parts representing the properties of the whole pattern. Therefore, their geometric properties are independent of the length scale ¹²⁵. In this pattern, there is a symmetrical relationship between the daughter and parent crystals; they are from the same structure but with different crystallographic orientations.

The fractal pattern transforms via self-epitaxial nucleation and growth which can develop a Cayley tree network by going through a cycle of branching-growth-branching.

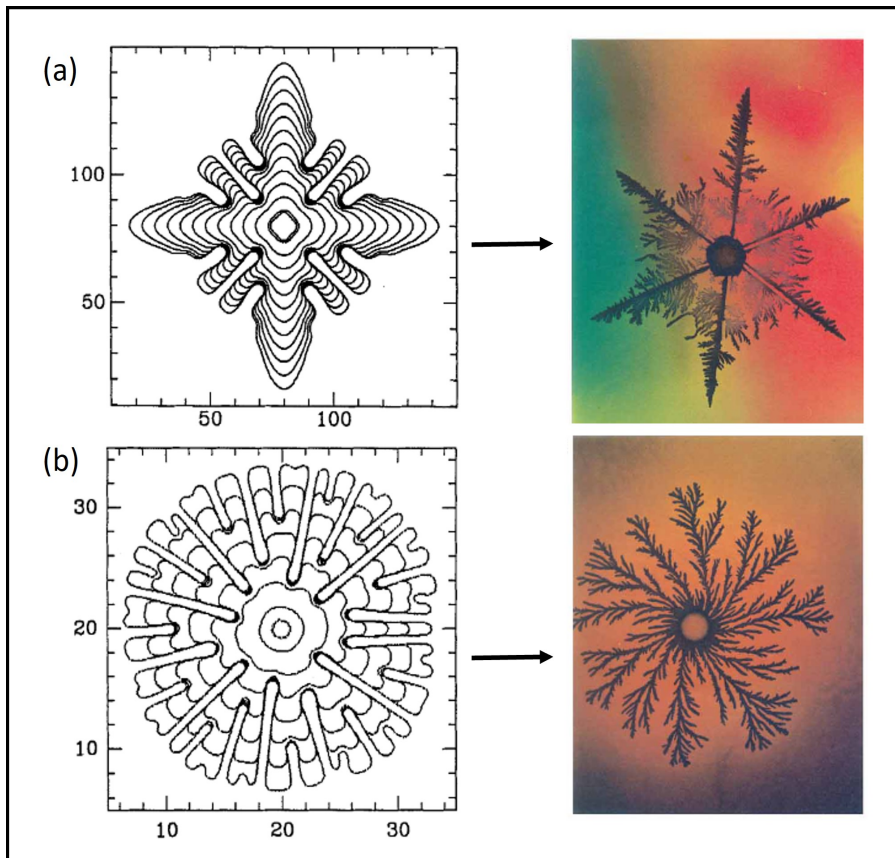
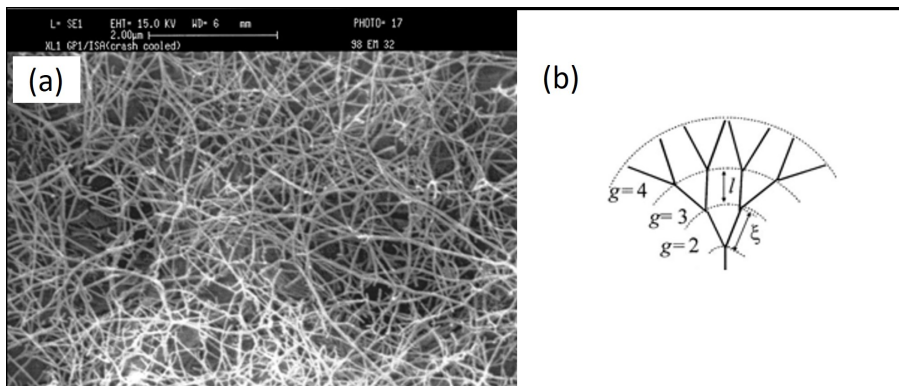


Figure 2.12. Simulated model and microscopic morphologies of two different network patterns in molecular gels: fractal versus dendritic morphologies; a) the dendritic growth when sufficient anisotropy is included, b) tip splitting growth leading to a densely branched pattern in the absence of anisotropy or presence of weak anisotropy, reprinted with permission from ref. ¹²⁴.

This structure is defined using three main parameters (Figure 2.13):

1. the length of the branches which is also known as correlation length (ζ), the length of the fiber between two neighboring branching points.
2. the branching rate (z)
3. the activity of the growth sites

In the course of the development of the usual Cayley tree with fractal mode of growth, the parameters z and ζ are constant and the branching takes place on all sites simultaneously ¹²⁵.



2

Figure 2.13 Fractal Cayley tree structure: a) the microstructure image of fiber networks in the GP-1 gel, b) schematic illustration of Cayley fractal tree where branching growth has started via branching from a single branch. The correlation length (ξ) is the length of branches along the tree which is not equal to the Euclidean distance l within the embedding space, reprinted with permission from ref. ¹²⁵.

Liu and Sawant explained the growth of fractal nanofiber networks in organogels using the Avrami relation ¹²⁵. The Avrami relation (Equation 2.5) describes the nucleation and growth of bulk crystals where k is a rate constant, t is time, and X_{cr} is the crystallinity.

$$X_{cr} = 1 - e^{-k \cdot t^n} \quad \text{Equation 2.5}$$

The parameter D represents the dimension of growing bulk crystals: for the one-dimensional such as rod-like growth ($D=1$), the two-dimensional such as sheet-like growth ($D=2$), and the three-dimensional or spherical growth ($D=3$). For fractal growth, the expression is given in Equation 2.6 where the length of bulk crystals as a function of t (in Equation 2.5) is substituted by the radius of gyration of fiber networks and the dimension D is replaced by the fractal dimension D_f .

$$\ln(1 - X_{cr}(t)) = -K(t - t_g)^{D_f} \quad \text{Equation 2.6}$$

The expression for fractal growth in Equation 2.6 is introduced to describe the growth of the three-dimensional network occurring after t_g . Thus, the parameter t in the Avrami equation is then replaced by $t-t_g$.

2.4.3 How do different network morphologies impact the rheological properties?

The flow behavior and deformation properties of gels are studied using rheology which provides information about the structure and dynamics of the assemblies. The rheological properties, particularly the viscoelastic behavior of molecular gels are governed by microstructural features of solid networks entrapping the viscose solvent. These structural characteristics in a fibrillar network include symmetry and crystallinity of fibers (for example the bending modulus of the individual fibers), the correlation length of fibers (network density and mesh size), the degree of branching, and the strength of the entanglements or interactions between the fibers.

Liu et al. have shown that the rheological properties of the gel is engineered via controlling the supersaturation of the system ¹²⁶. Dynamic rheological measurements of the microstructural evolution at different stages of nucleation and growth have shown that a permanent fiber network with a high G' can be formed by changing the architecture of a biocompatible organogel. This network can be produced by intensive entanglement or branching which reinforces the 3D solid network through reducing the mesh size of a network. Therefore, a network with an entangled or a sufficiently branched fibers forms smaller meshes which entrap the solvent more efficiently.

As discussed in previous sections, the degree of supersaturation controls the degree of crystallographic mismatch branching; at high supersaturation levels, the wide-angle mismatch branching occurs which can construct a denser network with better elasticity due to a shorter correlation length (Figure 2.14a). On the contrary, at low supersaturation levels, the good structural match between the growing daughter crystals and the parent phase develops the network with a larger correlation length (ζ) which has a larger mesh size.

Figure 2.14c shows the evolution of G' of N- lauroyl-L-glutamic acid di-n-butylamide system as a function of the degree of supersaturation in the system. Upon increasing supersaturation, G'_{\max} increases in the beginning due to the formation of more fibers with higher degree of branching.

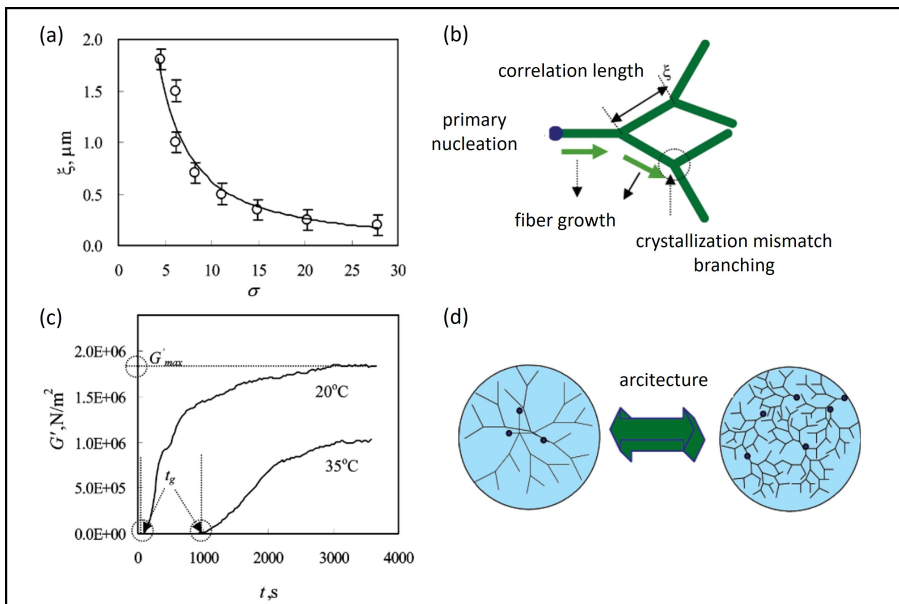


Figure 2.14 The crystal formation in N- lauroyl-L-glutamic acid di-n-butylamide system: a) the effect of supersaturation on the correlation length, b) the formation of fibrous network via nucleation-growth- crystallographic mismatch branching, c) change of G'_{\max} upon changing supersaturation, d) development of multi-domain networks from abundant nuclei due to high supersaturation, reprinted with permission from ref. ¹²⁶.

At very high concentrations, G'_{\max} reaches a plateau. Van Esch et al. described the correlation of G'_{\max} with the concentration difference from the equilibrium concentration in bis-ureas based organogels using Equation 2.7 ¹²⁷:

$$G'_{\max} = a \cdot (C - C_e)^b \quad \text{Equation 2.7}$$

In this power law equation, a and b are constants; C and C_e are respectively the gelator concentration at each temperature and the concentration at the equilibrium. However, this equation is valid at low supersaturation and cannot comprehensively explain the evolution of G'_{\max} at entire supersaturation range for this gel or other gels.

Weiss et al. studied the microstructures of fibrillar network in 5 α -Cholestan-3 β -yl N-(2 Naphthyl) carbamate/ n-Alkane organogel system ¹²⁸. They found that upon increasing the supersaturation, spherulitic structures form as a result of radial growth mode while the nucleation rate also increases at the same time. Therefore, the emergence of the spherulites from different nucleation centres leads to multiple

individual network domains in a gel system, a multi-domain structures. Multi-domain networks with transient junctions at domain-domain boundaries which are normally weaker than single domain of fibers with uniform junctions. In these systems, the degree of fiber branching determines the domain size of the spherulites. When it is intense, the individual fibers from one spherulite can overlap the fibers of adjacent spherulites, while a relatively milder degree of branching isolates the spherulites resulting in clear boundaries. Those boundaries separate spherulites from their neighbors. As a result, spherulitic gels with multi-domain networks develop where the size and the density of spherulites, and the strength of the domain-domain interactions (G'_{domain}) influence the rheological properties of the gels (schematically shown in Figure 2.15a) ^{113,129}.

Similar to the spherulitic structure, the degree of supersaturation regulates the size and number of fiber bundles in an interconnected fibrous networks ^{130–132}. In those systems, the fibers grow by side-branching (one-dimensionally alongside each other) and interact via transient junctions or entanglements. As a result of this specific growth mode caused by a relatively low degree of supersaturation, the bundling of the fibers occurs where individual fibers meet each other and fuse together within a certain angle and level of proximity, forming a single-domain interconnected network (Figure 2.15b); a higher degree of supersaturation, by increasing the gelator concentration for example, encourages the evolution from scattered bundles to larger 3D bundles. The rheological properties of the gel with a single domain depends on the strength of the individual fibers (G'_{fiber}), the density of the fibers, the thickness of the bundles, in addition to the strength of the transient junctions in the networks ¹³³.

The mechanical properties of the gels with different topologies, i.e. single and multi-domain networks, were compared by investigating the *in situ* formation of the gel networks in the N-lauroyl-L-glutamic acid di-n-butylamide (GP-1)/propylene glycol (PG) system and studying their rheological properties ¹³⁴. The results have shown that although the fibrillar network can possess higher elastic modulus in the first stage, spherulitic domain-domain interactions can show more resistance to the breakage compared to the transient junctions within the bundles. In other words, the breakage of the spherulitic network occurs at larger strains (Figure 2.16). The elastic modulus of the gel network can be tuned by the number of the spherulites (the density of the domain-domain interactions) and the strength of the junctions in spherulitic gels and via the average length of the fiber segments, mesh size, the aspect ratio of the fibers, and their stiffness in single domain networks.

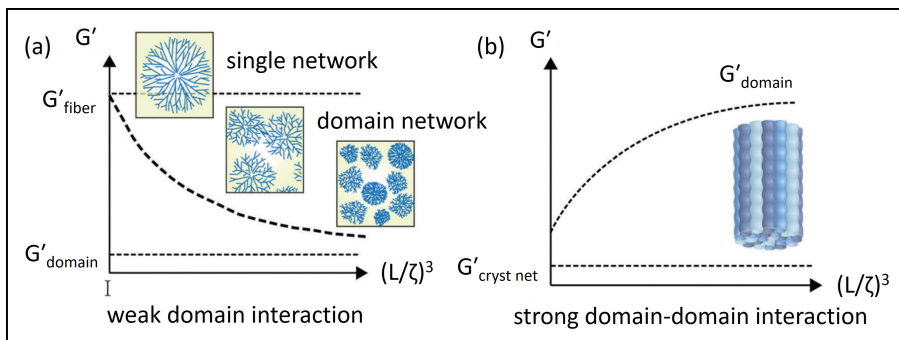


Figure 2.15 The schematic comparison of G' evolution in two different network morphologies: a) single and multi-domain spherulitic network, b) the network formed from fibrillar bundles, L is the length of the system, reprinted with permission from ref. ¹¹³.

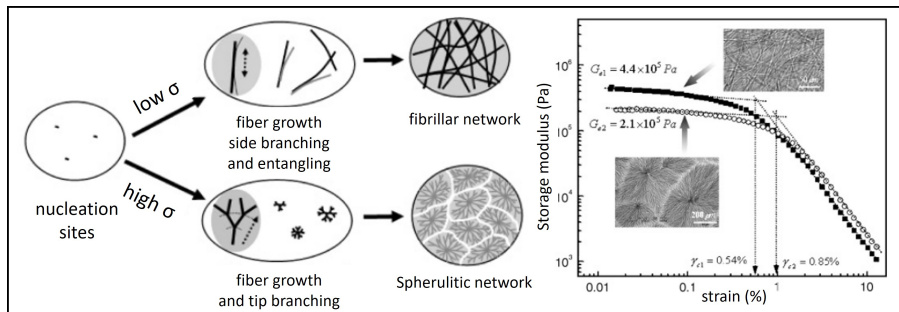


Figure 2.16 Two supersaturation-driven growth modes, the correlation of morphology and rheological properties in multi-domain spherulitic and fibrillar network, reprinted with permission from ref. ^{113,134}.

Figure 2.17 schematically shows how the elasticity of the gels can be tuned by the level of supersaturation. The gelation via crystallization at higher temperature reduces the supersaturation while the nucleation rate is also low. The presence of less nuclei leads to the formation of a network with better interpenetrating fibers within the domain-domain boundaries which can improve the gel elasticity. On the other hand, at higher temperature, i.e. less supersaturation, the fibers may form isolated and large spherulites with junctions susceptible to the breakage under shear stress ¹¹³.

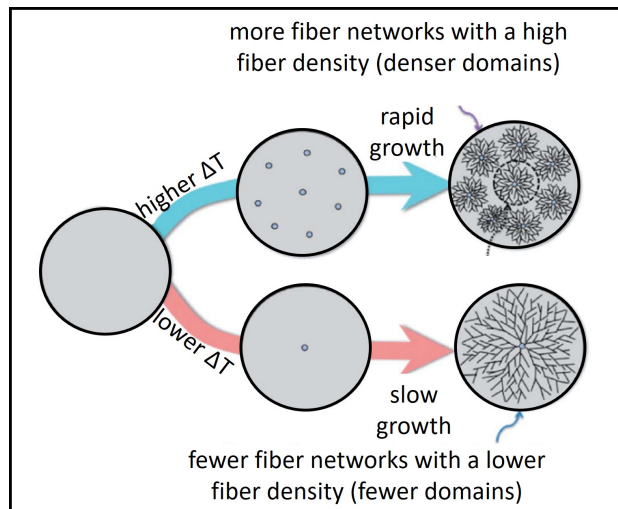


Figure 2.17 The effect of the degree of supercooling on the size of spherulites and joint densities, reprinted with permission from ref. ¹¹³.

The contribution of the strength of the domain-domain junctions in the network to the mechanical properties of multi-domain structures has been studied by Hanabusa et al. ¹³⁵. The gels prepared by the incubation of a sol at lower temperature have shown thixotropic behavior upon shear removal while the incubation at a higher temperature did not assist the recovery of the gel state. The progressive shear-recovery cycles reveal how the decrease in recovery time and reduced steady-state storage modulus are affected by the network morphology: depending on the packing degree of crystals in the network, the stress concentration on single and multi-domain networks can be expressed in different ways; in the spherulitic networks with less crystalline fibers, the network disintegration is limited to the domain-domain junctions. The stress accommodation occurs by disintegration of 3D network to 1D fibers which rather reform a network upon stress removal. However importantly, the sol obtained by applying shear does not have the required kinetics to reconstruct spherulites. Instead it appears that the molecules reassemble to lamellae-like structures driven by van der Waals interactions ¹³⁵. As Figure 2.18 shows, the gel state reformed after the breakage under shear has a different network morphology than the original 3D structure with overlapping spherulites. This is due to the fact that the junctions of spherulitic domains are less resistant to shear force and show signs of fatigue which finally results in gel disintegration; upon increasing the number of shear and

recovery cycles, the spherulitic structure transforms into a long fibrillar morphology which lacks thixotropic properties.

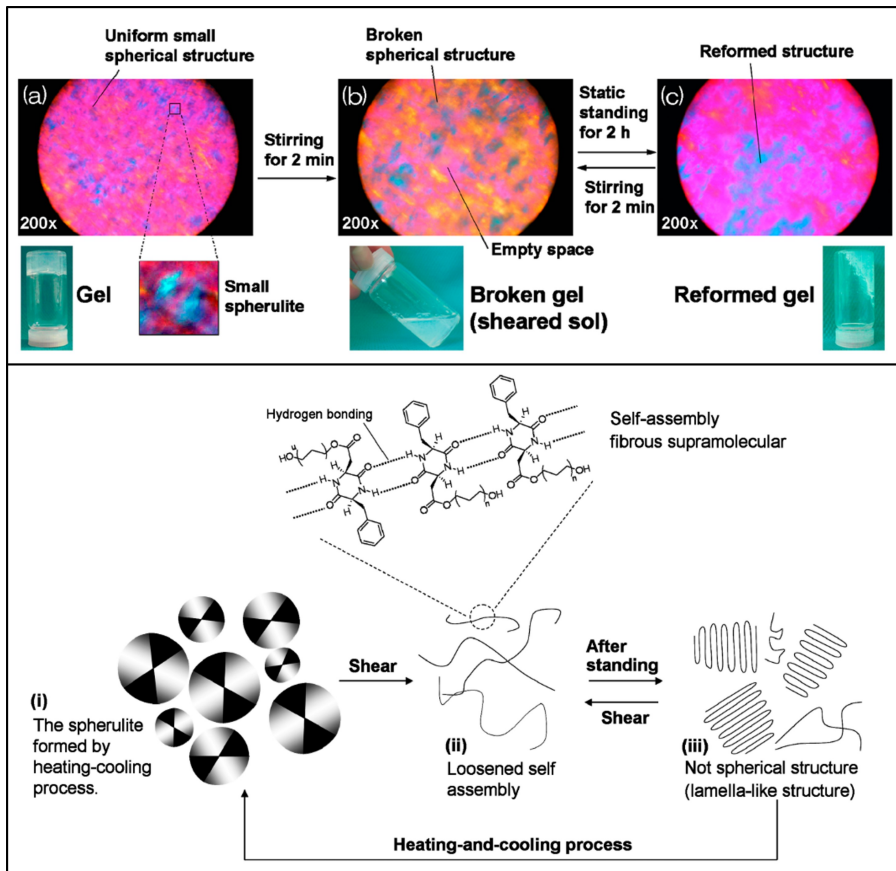


Figure 2.18 Polarized light microscope and schematic images of microstructures of a) the gel with spherulitic structure, b) the broken gel to sol-like structure under shear, c) reformed gel after standing, reprinted with permission from ref. ¹³⁵.

Heterogeneous network structures (in terms of morphology, mesh size, and spatial distribution of fiber networks) can originate from uncontrolled nucleation due to non-isothermal cooling processes in a gel preparation procedure (Figure 2.19a). Liu et al. have investigated that homogeneous fiber networks with uniform mesh sizes can be obtained by controlling the nucleation via the addition of polymer additives. They inhibited the early-stage nucleation of N-lauroyl-L-glutamic acid di-n-butylamide (GP-1) as the molecular gelling agent in benzyl benzoate (BB) using ethylene/vinyl acetate copolymer (EVACP) as the copolymer additive which is

strongly adsorbed on the surface of the fibers ¹³⁶. As a result, at the early cooling stage no intermediate fibrillar network forms (Figure 2.19b) which causes a uniform spherulitic network instead of a mixture of spherulites and interconnected fibers which can exclusively form at higher and lower levels of supercooling, respectively.

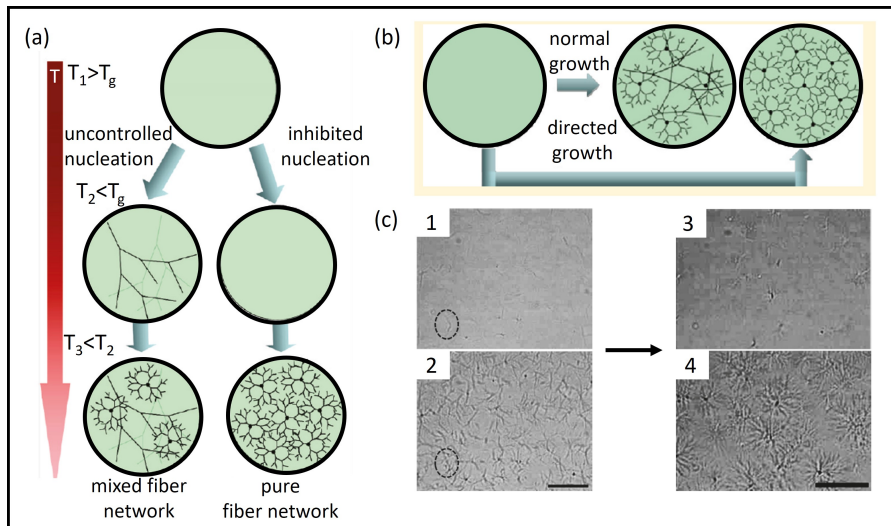


Figure 2.19 The evolution of nucleation and growth studied using real-time observation of the early stage GP-1 fiber formation in BB (1,2) in the absence of an additive EVACP and (3,4) in the presence of an additive EVACP: a) the effect of uncontrolled nucleation caused by non-isothermal cooling processes on the homogeneity of network structure, b) direct growth of uniform spherulitic using copolymer additives to avoid the formation of the mixture of spherulites and interconnected fibers, reprinted with permission from ref. ¹³⁶.

The elasticity of gels is governed by the strength of the individual fibers and their interactions in the network: in the fibrillar network structure with well-interconnected fibers, the gel behaves like a single uniform network. To encourage this mode of fiber growth, Liu et al. used the non-ionic surfactant Tween 80 which is effectively adsorbed on the surface of the growing tips of fibers in gels from N-lauroyl-L-glutamic acid di-n- butylamide (GP-1) and lanosterol (LS). In the presence of the surfactant, the elasticity of the gels was found to increase significantly followed by a constant level with increasing the surfactant concentration. Introduction of Tween 80 to these gel systems has evolved the network structure from transient entanglement of individual fibers to a well-interconnected fibrous network. As a result, the storage modulus of the gels has enhanced in the order of 30%-266% ¹¹⁶.

In spherulitic structures, the strength of the junctions among spherulites determines the strength and the integrity of the network. Indeed, the domain-domain junctions at the boundaries of spherulites can act as mechanically weak regions under shear stress ¹³⁷. The stiffness of these gels can be increased by increasing the polymer additive concentration. The polymer additive retards the nucleation rate in the solution. As a result, larger spherulites grow which form less number of weak junctions at the boundary zones.

The elastic properties of spherulitic structures can be weakened or improved by reconstruction of the network's topology. One example is the microstructural evolution in gels from N-lauroyl-L-glutamic acid di-n-butylamide in propylene glycol by adjusting the concentration of Span 20 as the additive ¹³⁸: at the lower concentration, the lateral adsorption of the surfactant molecules on the surface of the parent fibers encourages a transverse nucleation and growth of the new fibers. By increasing the concentration above a critical micelle concentration, radial fibers grow from the nucleation sites. The rheological properties of the gels change by structural transformation from spherulitic to comb-like and subsequent spherulitic topology with smaller length-scales (Figure 2.20); the latter growth pattern forms spherulitic domains with a higher elastic modulus compared to the former comb-like structure.

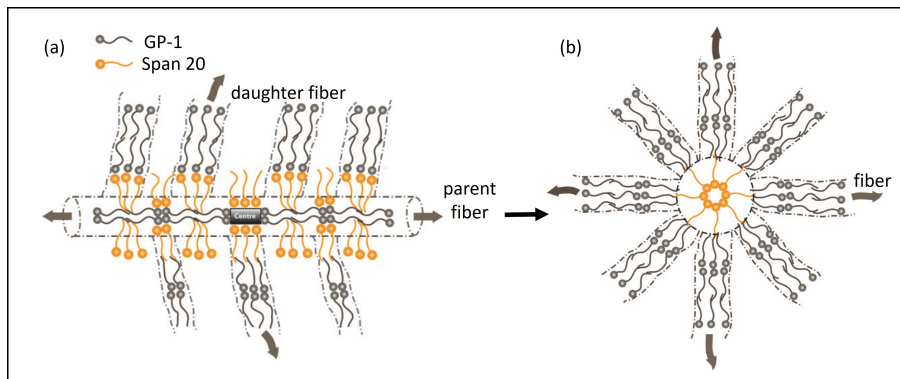


Figure 2.20 The transformation of the lateral growth mode to the comb-like structure in the presence of Span 20 additive, reprinted with permission from ref. ¹³⁸.

Another approach to improve the viscoelasticity of gels is to combine these two methods: thermal supersaturation with the addition of suitable additives which can impede the nucleation process of gelators in the solvent. As an example, Poly(methyl methacrylate co-methacrylic acid) was added in small amounts (0.01-

0.06%) to N-lauroyl-L-glutamic acid di-n-butylamide (GP-1) system. The results have shown that the polymer molecules adsorbed on the surface of the fibers of GP-1 in propylene glycol (PG) impede the fiber growth from the formation of an integrated fibrillar network. The higher the concentration of the polymer additives, the larger the size of the spherulites (Figure 2.21) which could dramatically increase the viscosity of the gel up to 3.5 times ¹³⁷.

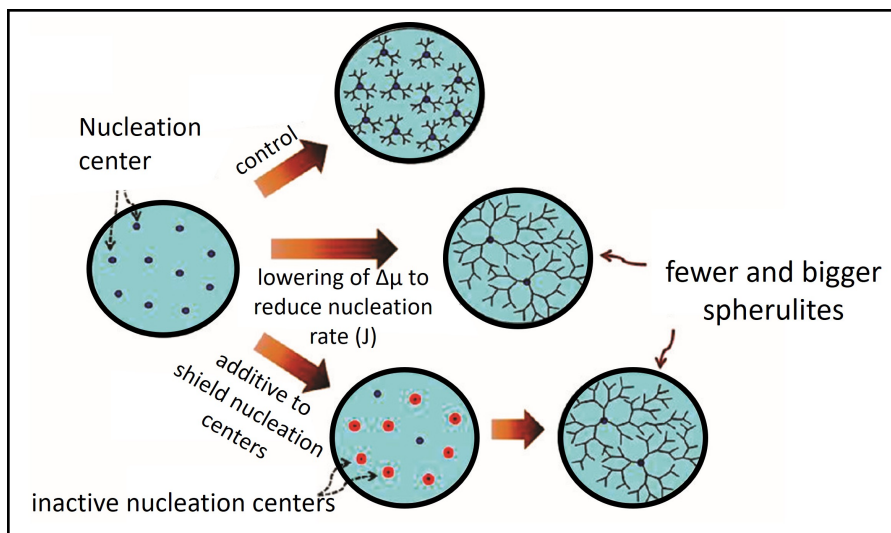


Figure 2.21 Engineering of the fiber network using additives to control the gel morphology by decreasing the joint density at the boundaries between spherulites which act as mechanically weak areas in the network, reprinted with permission from ref. ¹³⁷.

2.5 References

- [1] D. A. Scott, "A review of ancient Egyptian pigments and cosmetics", *Stud. Conserv.*, 2016.
- [2] K. Hock and K. H. Chew, "Relations between composition and physical properties of carrageenan gums", University of New South Wales, 1980.
- [3] M. Pernetti, K. van Malssen, D. Kalnin, and E. Flöter, "Structuring edible oil with lecithin and sorbitan tri-stearate", *Food Hydrocoll.*, 2007.
- [4] L. Kang, X. Y. Liu, P. D. Sawant, P. C. Ho, Y. W. Chan, and S. Y. Chan, "SMGA gels for the skin permeation of haloperidol", *J. Control. release*, 2005.
- [5] P. F. C. Lim, X. Y. Liu, L. Kang, P. C. L. Ho, and S. Y. Chan, "Physicochemical effects of terpenes on organogel for transdermal drug delivery", *Int. J. Pharm.*, 2008.
- [6] L. E. Buerkle, H. A. von Recum, and S. J. Rowan, "Toward potential supramolecular tissue engineering scaffolds based on guanosine derivatives", *Chem. Sci.*, 2012.
- [7] A. R. Hirst, B. Escuder, J. F. Miravet, and D. K. Smith, "High-tech applications of self-assembling supramolecular nanostructured gel-phase materials: from regenerative medicine to electronic devices", *Angew. Chemie Int. Ed.*, 2008.
- [8] D. Astruc, E. Boisselier, and C. C. Ornelas, "Dendrimers designed for functions: from physical, photophysical, and supramolecular properties to applications in sensing, catalysis, molecular electronics, photonics, and nanomedicine", *Chem. Rev.*, vol. 110, 2010.
- [9] D. Tripathy, A. S. Gadtya, and S. Moharana, "Supramolecular Gel, Its classification, preparation, properties, and applications: A review", *Polym. Technol. Mater.*, 2022.
- [10] P. Baglioni, L. Dei, E. Carretti, and R. Giorgi, "Gels for the conservation of cultural heritage", *Langmuir*, 2009.
- [11] E. Carretti et al., "New frontiers in materials science for art conservation: Responsive gels and beyond", *Acc. Chem. Res.*, 2010.
- [12] E. Carretti, L. Dei, and R. G. Weiss, "Soft matter and art conservation. Rheoreversible gels and beyond", *Soft Matter*, 2005.
- [13] W. J. Merz and P. J. Flory, "Introductory lecture", *Faraday Discuss. Chem. Soc.*, 1974.
- [14] P. Terech and R. G. Weiss, "Low molecular mass gelators of organic liquids and the properties of their gels", *Chem. Rev.*, 1997.
- [15] L. A. Estroff and A. D. Hamilton, "Water gelation by small organic molecules", *Chem.*

- Rev., 2004.
- [16] N. M. Sangeetha and U. Maitra, "Supramolecular gels: Functions and uses," *Chem. Soc. Rev.*, 2005.
 - [17] W. H. Binder and O. W. Smrzka, "Self-Assembly of Fibers and Fibrils", *Angew. Chemie Int. Ed.*, 2006.
 - [18] Y. E. Shapiro, "Structure and dynamics of hydrogels and organogels: An NMR spectroscopy approach", *Prog. Polym. Sci.*, 2011.
 - [19] Y. Osada, J. P. Gong, Y. Tanaka, J. Ping Gong, and Y. Tanaka, "Polymer gels," *J. Macromol. Sci. Part C Polym. Rev.*, 2004.
 - [20] S. R. Raghavan and J. F. Douglas, "The conundrum of gel formation by molecular nanofibers, wormlike micelles, and filamentous proteins: gelation without cross-links?", *Soft Matter*, 2012.
 - [21] B. O. Okesola and D. K. Smith, "Applying low-molecular weight supramolecular gelators in an environmental setting—self-assembled gels as smart materials for pollutant removal", *Chem. Soc. Rev.*, 2016.
 - [22] K. Hanabusa and M. Suzuki, "Physical gelation by low-molecular-weight compounds and development of gelators", *Bull. Chem. Soc. Jpn.*, 2016.
 - [23] K. Hanabusa and M. Suzuki, "Development of low-molecular-weight gelators and polymer-based gelators", *Polym. J.*, 2014.
 - [24] A. R. Hirst et al., "Low-molecular-weight gelators: elucidating the principles of gelation based on gelator solubility and a cooperative self-assembly model", *J. Am. Chem. Soc.*, 2008.
 - [25] M. H.-Y. Y. Chan and V. W.-W. W. Yam, "Toward the Design and Construction of Supramolecular Functional Molecular Materials Based on Metal–Metal Interactions", *J. Am. Chem. Soc.*, 2022.
 - [26] F. Allix, P. Curcio, Q. N. Pham, G. Pickaert, B. Jamart-Grégoire, and B. Jamart-Grégoire, "Evidence of intercolumnar π – π stacking interactions in amino-acid-based low-molecular-weight organogels", *Langmuir*, 2010.
 - [27] M. Suzuki, Y. Nakajima, M. Yumoto, M. Kimura, H. Shirai, and K. Hanabusa, "Effects of hydrogen bonding and van der Waals interactions on organogelation using designed low-molecular-weight gelators and gel formation at room temperature", *Langmuir*, 2003.
 - [28] C. Maity, W. E. Hendriksen, J. H. Van Esch, and R. Eelkema, "Spatial structuring of a supramolecular hydrogel by using a visible-light triggered catalyst", *Angew. Chemie*

- Int. Ed., 2015.
- [29] T. Suzuki, S. Shinkai, and K. Sada, "Supramolecular crosslinked linear poly(trimethylene iminium trifluorosulfonimide) polymer gels sensitive to light and thermal stimuli", *Adv. Mater.*, 2006.
 - [30] W. Fang, Y. Zhang, J. Wu, C. Liu, H. Zhu, and T. Tu, "Recent advances in supramolecular gels and catalysis", *Chem. Asian J.*, 2018.
 - [31] K. Lalitha, Y. S. Prasad, V. Sridharan, C. U. Maheswari, G. John, and S. Nagarajan, "A renewable resource-derived thixotropic self-assembled supramolecular gel: magnetic stimuli responsive and real-time self-healing behavior", *RSC Adv.*, 2015.
 - [32] W. H. Binder et al., "Magnetic and temperature-sensitive release gels from supramolecular polymers", *Adv. Funct. Mater.*, 2007.
 - [33] Z. Sun, Q. Huang, T. He, Z. Li, Y. Zhang, and L. Yi, "Multistimuli-Responsive Supramolecular Gels: Design Rationale, Recent Advances, and Perspectives", *ChemPhysChem*, 2014.
 - [34] A. Noro, M. Hayashi, and Y. Matsushita, "Design and properties of supramolecular polymer gels", *Soft Matter*, 2012.
 - [35] A. L. Motyka, "An introduction to rheology with an emphasis on application to dispersions", *J. Chem. Educ.*, 1996.
 - [36] P. Science and K. Nishinari, "Some thoughts on the definition of a gel", in *Gels: Structures, properties*, Springer, 2009.
 - [37] P. Terech, "Fibers and wires in organogels from low-mass compounds: Typical structural and rheological properties", *Berichte der Bunsengesellschaft für Phys. Chemie*, 1998.
 - [38] D. T. N. N. Chen, Q. Wen, P. A. Janmey, J. C. Crocker, and A. G. Yodh, "Rheology of soft materials", *Annu. Rev. Condens. Matter Phys.*, 2010.
 - [39] S. B. R.-M. GAYNOR M. RAVANAGH, "Characterization Polymer Gels", *Prog. Polym. Sci.*, 1998.
 - [40] C. Yan and D. J. Pochan, "Rheological properties of peptide-based hydrogels for biomedical and other applications", *Chem. Soc. Rev.*, 2010.
 - [41] G. Yu, X. Yan, C. Han, and F. Huang, "Characterization of supramolecular gels," *Chem. Soc. Rev.*, 2013.
 - [42] J. W. Steed, "Supramolecular gel chemistry: developments over the last decade", *Chem. Commun.*, 2011.

- [43] A. Dawn and H. Kumari, “Low molecular weight supramolecular gels under shear: Rheology as the tool for elucidating structure–function correlation”, *Chem. Eur. J.*, 2018.
- [44] L. E. Buerkle, S. J. Rowan, L. Zhang, X. Wang, T. Wang, and M. Liu, “Tuning soft nanostructures in self-assembled supramolecular gels: from morphology control to morphology-dependent functions”, *Small*, 2015.
- [45] Y. Liang et al., “Low-molecular-weight supramolecular adhesives based on non-covalent self-assembly of a small molecular gelator”, *Mater. Horizons*, 2022.
- [46] K. J. Skilling, F. Citossi, T. D. Bradshaw, M. Ashford, B. Kellam, and M. Marlow, “Insights into low molecular mass organic gelators: a focus on drug delivery and tissue engineering applications”, *Soft Matter*, 2014.
- [47] G. C. Maity, “Low molecular mass gelators of organic liquids”, *J. Phys. Sci.*, 2007.
- [48] D. Pasini and A. Kraft, “Supramolecular self-assembly of fibres”, *Curr. Opin. Solid State Mater. Sci.*, 2004.
- [49] X. Yu, L. Chen, M. Zhang, and T. Yi, “Low-molecular-mass gels responding to ultrasound and mechanical stress: towards self-healing materials”, *Chem. Soc. Rev.*, 2014.
- [50] P. Duan, Y. Li, J. Jiang, T. Wang, and M. Liu, “Towards a universal organogelator: a general mixing approach to fabricate various organic compounds into organogels”, *Sci. China Chem.*, 2011.
- [51] G. Zhu and J. S. Dordick, “Solvent effect on organogel formation by low molecular weight molecules”, *Chem. Mater.*, 2006.
- [52] L. E. Buerkle and S. J. Rowan, “Supramolecular gels formed from multi-component low molecular weight species”, *Chem. Soc. Rev.*, 2012.
- [53] Y. Wang, L. Tang, and J. Yu, “Investigation on the assembled structure–property correlation of supramolecular hydrogel formed from low-molecular-weight gelator”, *J. Colloid Interface Sci.*, 2008.
- [54] P. Dastidar, “Designing supramolecular gelators: challenges, frustrations, and hopes”, *Gels*, 2019.
- [55] M. Yamanaka, “Urea derivatives as low-molecular-weight gelators”, *J. Incl. Phenom. Macrocycl. Chem.*, 2013.
- [56] X. Yang, G. Zhang, D. Zhang, and J. W. Steed, “Stimuli responsive gels based on low molecular weight gelators”, *J. Mater. Chem.*, 2012.

- [57] M. George and R. G. Weiss, “Molecular organogels. Soft matter comprised of low-molecular-mass organic gelators and organic liquids”, *Acc. Chem. Res.*, 2006.
- [58] P. Dastidar, “Supramolecular gelling agents: can they be designed?”, *Chem. Soc. Rev.*, 2008.
- [59] M. Liu, G. Ouyang, D. Niu, and Y. Sang, “Supramolecular gelatons: towards the design of molecular gels”, *Org. Chem. Front.*, 2018.
- [60] Y. Sang and M. Liu, “Nanoarchitectonics through supramolecular gelation: formation and switching of diverse nanostructures”, *Mol. Syst. Des. Eng.*, 2019.
- [61] Fabiana Meijon Fadul, S. R. Raghavan, and B. H. Cipriano, “Gel formation: phase diagrams using tabletop rheology and calorimetry in Molecular gels”, Springer, 2006.
- [62] M. M. Huda and N. Rai, “Probing Early-Stage Aggregation of Low Molecular Weight Gelator in an Organic Solvent”, *J. Phys. Chem. B*, 2020.
- [63] E. Ghanbari, A. Roshanasan, S. J. Picken, and J. Van Esch, “From molecular assembly to gelation : What is going on behind the scenes of supramolecular gels formation”, to be submitted, 2023.
- [64] S. R. Raghavan and J. F. Douglas, “The conundrum of gel formation by molecular nanofibers, wormlike micelles, and filamentous proteins: gelation without cross-links?”, *Soft Matter*, 2012.
- [65] T. Takata, L. Brunsved, B. J. B. Folmer, E. W. Meijer, and R. P. Sijbesma, “Supramolecular polymers” *Chem. Rev.*, 2001.
- [66] T. Aida, E. W. Meijer, and S. I. Stupp, “Functional supramolecular polymers”, *Science*, 2012.
- [67] T. F. A. A. De Greef, M. M. J. J. Smulders, M. Wolffs, A. P. H. J. H. J. Schenning, R. P. Sijbesma, and E. W. Meijer, “Supramolecular polymerization”, *Chem. Rev.*, 2009.
- [68] M. M. J. J. Smulders, M. M. L. L. Nieuwenhuizen, T. F. A. A. de Greef, P. van der Schoot, A. P. H. J. H. J. Schenning, and E. W. à W. Meijer, “How to distinguish isodesmic from cooperative supramolecular polymerisation”, *Chem. Eur. J.*, 2010.
- [69] R. Yu, N. Lin, W. Yu, and X. Y. Liu, “Crystal networks in supramolecular gels: formation kinetics and mesoscopic engineering principles”, *CrystEngComm*, 2015.
- [70] J. L. Li, B. Yuan, X. Y. Liu, R. Y. Wang, and X. G. Wang, “Control of crystallization in supramolecular soft materials engineering”, *Soft Matter*, 2013.
- [71] D. K. Kumar and J. W. Steed, “Supramolecular gel phase crystallization: orthogonal self-assembly under non-equilibrium conditions”, *Chem. Soc. Rev.*, 2014.

- [72] S. Manley et al., "Glasslike arrest in spinodal decomposition as a route to colloidal gelation", *Phys. Rev. Lett.*, 2005.
- [73] E. Bokusoglu, S. K. Pal, J. J. de Pablo, and N. L. Abbott, "Colloid-in-liquid crystal gels formed via spinodal decomposition", *Soft Matter*, 2014.
- [74] N. A. M. M. Verhaegh, D. Asnaghi, H. N. W. W. Lekkerkerker, M. Giglio, and L. Cipelletti, "Transient gelation by spinodal decomposition in colloid-polymer mixtures", *Phys. A Stat. Mech. its Appl.*, 1997.
- [75] X. Y. Liu, "Gelation with Small Molecules: from Formation Mechanism to NanostructureArchitecture", *Low Mol. mass gelator*, 2005.
- [76] K. K. Kartha, S. S. Babu, S. Srinivasan, and A. Ajayaghosh, "Attogram sensing of trinitrotoluene with a self-assembled molecular gelator", *J. Am. Chem. Soc.*, 2012.
- [77] P. Terech, J. J. Allegraud, and C. M. Garner, "Thermoreversible gelation of organic liquids by arylcyclohexanol derivatives: a structural study", *Langmuir*, 1998.
- [78] V. Ajay Mallia, R. G. Weiss, V. A. Mallia, and R. G. Weiss, "Self-assembled fibrillar networks and molecular gels employing 12-hydroxystearic acid and its isomers and derivatives", *J. Phys. Org. Chem.*, 2014.
- [79] Nonappa, M. Lahtinen, B. Behera, E. Kolehmainen, and U. Maitra, "Unraveling the packing pattern leading to gelation using SS NMR and X-ray diffraction: direct observation of the evolution of self-assembled fibers", *Soft Matter*, 2010.
- [80] M. George and R. G. Weiss, "Low molecular-mass gelators with diyne functional groups and their unpolymerized and polymerized gel assemblies", *Chem. Mater.*, 2003.
- [81] E. R. Draper et al., "Using small-angle scattering and contrast matching to understand molecular packing in low molecular weight gels", *Matter*, 2020.
- [82] M. George, G. Tan, V. T. John, and R. G. Weiss, "Urea and Thiourea Derivatives as Low Molecular-Mass Organogelators", *Chem. Eur. J.*, 2005.
- [83] D. J. Abdallah and R. G. Weiss, "Organogels and low molecular mass organic gelators," *Adv. Mater.*, vol. 12, no. 17, pp. 1237–1247, 2000.
- [84] K. Hanabusa, M. Matsumoto, M. Kimura, A. Kakehi, and H. Shirai, "Low molecular weight gelators for organic fluids: gelation using a family of cyclo (dipeptide)", *J. Colloid Interface Sci.*, 2000.
- [85] D. J. Abdallah, S. A. Sirchio, and R. G. Weiss, "Hexatriacontane organogels. The first determination of the conformation and molecular packing of a low-molecular-mass organogelator in its gelled state", *Langmuir*, 2000.

- [86] A. R. Hirst, D. K. Smith, and J. P. Harrington, “Unique Nanoscale Morphologies Underpinning Organic Gel-Phase Materials”, *Chem. Eur. J.*, 2005.
- [87] D. Bordignon et al., “Wet spinning of a library of carbohydrate low molecular weight gels”, *J. Colloid Interface Sci.*, 2021.
- [88] A. Bernet, M. Behr, and H.-W. W. Schmidt, “Supramolecular nanotube-based fiber mats by self-assembly of a tailored amphiphilic low molecular weight hydrogelator”, *Soft Matter*, 2011.
- [89] S. Bhattacharya, S. N. Ghanashyam Acharya, and S. N. G. Acharya, “Impressive gelation in organic solvents by synthetic, low molecular mass, self-organizing urethane amides of L-phenylalanine”, *Chem. Mater.*, 1999.
- [90] T. Sumiyoshi, K. Nishimura, M. Nakano, T. Handa, Y. Miwa, and K. Tomioka, “Molecular Assembly of C 2-Symmetric Bis-(2 S)-2-methylundecanoylamides of α , ω -Alkylidenediamines into Coiled Coil and Twisted Ribbon Aggregates”, *J. Am. Chem. Soc.*, 2003.
- [91] R. G. Weiss, “The past, present, and future of molecular gels. What is the status of the field, and where is it going?”, *J. Am. Chem. Soc.*, 2014.
- [92] I. Kuzmenko et al., “Design and characterization of crystalline thin film architectures at the air- liquid interface: Simplicity to complexity”, *Chem. Rev.*, 2001.
- [93] . Design, G. R. D. Copyright, J. Wiley, and G. DESIRAJU, “Crystal design: structure and function”, Wiley, 2003.
- [94] X. Y. Liu, “Interfacial effect of molecules on nucleation kinetics”, *J. Phys. Chem. B*, 2001.
- [95] A. You, M. A. Y. Be, I. In, and X. Y. Liu, “Heterogeneous nucleation or homogeneous nucleation?”, *J. Chem. Phys.*, 2000.
- [96] M. A. Rogers and A. G. Marangoni, “Non-isothermal nucleation and crystallization of 12-hydroxystearic acid in vegetable oils”, *Cryst. Growth Des.*, 2008.
- [97] A. You et al., “Ordering of self-assembled nanobiominerals in correlation to mechanical properties of hard tissues”, *Appl. Phys. Lett.*, 2005.
- [98] A. A. Chernov, “Modern crystallography III: crystal growth”, Springer Science & Business Media, 2012.
- [99] O. S. L. Bruinsma and J. P. van der Eerden, “Science and technology of crystal growth”, Kluwer academic publishers, 1995.
- [100] N. DU and X. Y. Liu, “Controlled ice nucleation in microsized water droplet”, *Appl.*

- Phys. Lett., 2002.
- [101] M. Volmer and W. Schultze, "Kondensation an kristallen", Zeitschrift für Phys. Chemie, 1931.
 - [102] E. Behandlung, R. Becker, and W. Döring, "Kinetische behandlung der keimbildung in übersättigten dämpfen", Ann. Phys., 1935.
 - [103] P. G. Vekilov, "Crystallization tracked atom by atom", Nature Publishing Group UK London, 2019.
 - [104] P. G. Vekilov, "The two-step mechanism of nucleation of crystals in solution," Nanoscale, 2010.
 - [105] D. Erdemir, A. Y. Lee, and A. S. Myerson, "Nucleation of crystals from solution: classical and two-step models", Acc. Chem. Res., 2009.
 - [106] D. Kashchiev, "Nucleation: basic theory with applications. 1^a edição", Butterworth Heinemann. Grã-Britânia, 2000.
 - [107] U. Gasser, E. R. Weeks, A. Schofield, P. N. Pusey, and D. A. Weitz, "Real-space imaging of nucleation and growth in colloidal crystallization", Science, 2001.
 - [108] S.-T. T. Yau, P. G. Vekilov, and P. G. Vekilov, "Quasi-planar nucleus structure in apoferritin crystallization", Nature, 2000.
 - [109] J. Zhou et al., "Observing crystal nucleation in four dimensions using atomic electron tomography", Nature, 2019.
 - [110] R. Li, X. Zhang, H. Dong, Q. Li, Z. Shuai, and W. Hu, "Gibbs-Curie-Wulff Theorem in Organic Materials: A Case Study on the Relationship between Surface Energy and Crystal Growth", Adv. Mater., 2016.
 - [111] T. L. Einstein and V. Beijeren, "Equilibrium shape of crystals", in Handbook of Crystal Growth, Elsevier, 2015.
 - [112] Y.-S. Jun et al., "Classical and nonclassical nucleation and growth mechanisms for nanoparticle formation", Annu. Rev. Phys. Chem., 2022.
 - [113] N. Lin and X. Y. Liu, "Correlation between hierarchical structure of crystal networks and macroscopic performance of mesoscopic soft materials and engineering principles", Chem. Soc. Rev., 2015.
 - [114] X. Y. Liu, P. D. Sawant, W. B. Tan, I. B. M. Noor, C. Pramesti, and B. H. Chen, "Creating new supramolecular materials by architecture of three-dimensional nanocrystal fiber networks", J. Am. Chem. Soc., 2002.
 - [115] X. Y. Liu and S. W. Lim, "Templating and supersaturation-driven anti-templating:

- Principles of biomineral architecture”, J. Am. Chem. Soc., 2003.
- [116] J. L. Li, X. Y. Liu, C. S. Strom, and J. Y. Xiong, “Engineering of small molecule organogels by design of the nanometer structure of fiber networks”, *Adv. Mater.*, 2006.
- [117] X. Y. Liu and P. D. Sawant, “Mechanism of the formation of self-organized microstructures in soft functional materials”, *Adv. Mater.*, 2002.
- [118] J. Li and X. Liu, “Architecture of supramolecular soft functional materials: From understanding to micro-/nanoscale engineering”, *Adv. Funct. Mater.*, 2010.
- [119] Z. Wang, G. Ma, and X. Y. Liu, “Will fluoride toughen or weaken our teeth? Understandings based on nucleation, morphology, and structural assembly”, *J. Phys. Chem. B*, 2009.
- [120] N. Lin, X. Y. Liu, N. Lina, and X. Y. Liu, “Correlation between hierarchical structure of crystal networks and macroscopic performance of mesoscopic soft materials and engineering principles1”, *Chem. Soc. Rev.*, 2015.
- [121] T. H. Zhang, X. Y. Liu, H. Z. Tian, and Y. L. Xiang, “How does a transient amorphous precursor template crystallization”, *J. Am. Chem. Soc.*, 2007.
- [122] S.-C. C. Huang and M. E. Glicksman, “Overview 12: Fundamentals of dendritic solidification—I. Steady-state tip growth”, *Acta Metall.*, 1981.
- [123] J. S. Langer, “Instabilities and pattern formation in crystal growth”, *Rev. Mod. Phys.*, 1980.
- [124] E. Ben-Jacob, “From snowflake formation to growth of bacterial colonies”, *Contemp. Phys.*, 1993.
- [125] X. Y. Liu and P. D. Sawant, “Formation kinetics of fractal nanofiber networks in organogels”, *Appl. Phys. Lett.*, 2001.
- [126] J.-L. Li, X.-Y. Liu, R.-Y. Wang, and J.-Y. Xiong, “Architecture of a biocompatible supramolecular material by supersaturation-driven fabrication of its fiber network”, *J. Phys. Chem. B*, 2005.
- [127] J. Brinksma, B. L. Feringa, R. M. Kellogg, R. Vreeker, and J. van Esch, “Rheology and thermotropic properties of bis-urea-based organogels in various primary alcohols”, *Langmuir*, 2000.
- [128] Y. Jeong et al., “Solvent/gelator interactions and supramolecular structure of gel fibers in cyclic bis-urea/primary alcohol organogels”, *Langmuir*, 2005.
- [129] J. H. Shi, X. Y. Liu, J. L. Li, C. S. Strom, and H. Y. Xu, “Spherulitic networks: from structure to rheological property”, *J. Phys. Chem. b*, 2009.

- [130] A. T. Nguyen, Q. Huang, Z. Yang, N. Lin, G. Xu, and X. Y. Liu, "Crystal networks in silk fibrous materials: from hierarchical structure to ultra performance", *Small*, 2015.
- [131] N. Du, Z. Yang, X. Y. Liu, Y. Li, and H. Y. Xu, "Structural origin of the strain-hardening of spider silk", *Adv. Funct. Mater.*, 2011.
- [132] G. Xu, L. Gong, Z. Yang, and X. Y. Liu, "What makes spider silk fibers so strong? From molecular-crystallite network to hierarchical network structures", *Soft Matter*, 2014.
- [133] C. E. B. M. Dei L, "Berrie BH Angelova LV Baglioni P", *Weiss RG Acc. Chem. Res*, 2010.
- [134] R. Wang, X.-Y. Y. Liu, J. Xiong, and J. Li, "Real-time observation of fiber network formation in molecular organogel: supersaturation-dependent microstructure and its related rheological property", *J. Phys. Chem. b*, 2006.
- [135] H. Hoshizawa, Y. Minemura, K. Yoshikawa, M. Suzuki, and K. Hanabusa, "Thixotropic hydrogelators based on a cyclo (dipeptide) derivative", *Langmuir*, 2013.
- [136] J.-L. Li, B. Yuan, X.-Y. Liu, X. Wang, and R. Wang, "Kinetically controlled homogenization and transformation of crystalline fiber networks in supramolecular materials", *Cryst. Growth Des.*, 2011.
- [137] J.-L. L. Li, X.-Y. Y. Liu, B. Yuan, X.-Y. Y. Liu, and H.-Y. Xu, "Microengineering of supramolecular soft materials by design of the crystalline fiber networks", *Cryst. Growth Des.*, 2010.
- [138] S. Tang, X. Y. Liu, and C. S. Strom, "Producing supramolecular functional materials based on fiber network reconstruction", *Adv. Funct. Mater.*, 2009.

Chapter 3

Molecular arrangement and thermal properties of bisamide organogelators in the solid state

Abstract

To shed light on the gelation behavior of bisamide organogelators, it is essential to investigate the properties of the main components, the gelator compounds themselves. In this study the crystal structure and phase behavior of bisamide gelator molecules are investigated using DSC, FTIR, XRD and molecular modelling. A homologous series of bisamide model compounds (nBAs) was prepared with $(\text{CH}_2)_n$ spacer between the two amide groups, where n varies from 5 to 10, and with two symmetric C17 alkyl tails. With increasing the spacer length the thermal properties show a clear odd-even effect which was reliably detected using our newly developed $\text{DSC}_N(T)$ analytical model, determining the melting transition measured by DSC and allowing accurate calculation of the enthalpy of fusion and the change in heat capacity of nBA compounds. Using XRD, all studied nBA compounds show 001 reflections, the characteristic of layer-like structures with a highly defined layer spacing. The XRD patterns of the odd BA series are very similar, but show marked differences compared to the XRD patterns of the even series, which in turn are very similar. Crystal structure analysis shows that the odd-membered 5BA molecules are nearly perpendicular to the stacked layers, as described by a pseudo orthorhombic unit cell, whereas the even-membered 6BA molecules are tilted at an angle with respect to the layer normal, as described by a triclinic unit cell. In both the odd and even series the inter-layer interaction is the Van der Waals interaction. The intra-layer packing of molecules in the 6BA structure not only differs from that of 5BA in terms of tilting, but also in terms of H-bonding: the 6BA hydrogen-bonding scheme is very similar to that of Nylon 6,10 α , unlike the 5BA H-bonding scheme. The packing

of the C17 alkyl tails in the 5BA layers has a pseudo-orthorhombic $Z = 2$ projection cell, similar to the orthorhombic cell of polyethylene and unlike 6BA. The 6BA gelator has a slightly higher crystalline density (1.038 g.cm^{-3}) than 5BA (1.018 g.cm^{-3}). This is in agreement with its higher melting point and the presence of N-H bands at higher wave numbers observed by FTIR. The XRD reflections of 5BA and 6BA disappear around 132°C and 145°C respectively, which is in reasonable agreement with the melting temperatures obtained from $\text{DSC}_\text{N}(T)$. The structural differences observed between the odd and even BA series reflect the different structure-directing effect of parallel versus anti-parallel amide hydrogen bonding motifs. These differences underly the odd-even effects observed in the thermal properties.

3.1 Introduction

Low molecular weight organic gelators (LMWGs) are low molecular mass gelling agents that are able to form supramolecular gels ¹. They can construct gels via self-assembly leading to the formation of micrometer-long crystals in various morphologies which entangle into an overall three-dimensional network and entrap the solvent in the network ²⁻⁴. The self-assembly of LMWGs occurs through non-covalent reversible bonds such as π -stacking, hydrogen-bonding, and Van der Waals interactions ⁵⁻⁷.

As most of the LMWGs used as additives to increase the viscosity of liquid products were discovered fortuitously ⁸⁻¹⁰, there was little theoretical understanding on their mechanisms of gel formation. Finding and screening numerous compounds has directed research toward the systematic study of gelator structure, their interaction with solvents, and the correlation to the rheological properties of their final gels ¹¹⁻¹³. New LMWGs are designed rationally by stepwise modification of the molecular structure of the former gelators to optimize the rheological properties of the final gels ^{9,14}.

The efficiency of LMWGs is determined by the tendency to form a stable gel at the lower gelator concentrations ^{15,16}. LMWGs with long aliphatic chains or aromatic groups with a large surface combined with moieties such as ureas, urethanes, carbamates, and amides forming three dimensional networks via strong intermolecular hydrogen bonds have shown efficient immobilization of a variety of organic solvent ¹⁷⁻²². Hanabusa et al. designed LMWGs which gelate a wide variety of organic liquids via thermoreversible intermolecular hydrogen bonds between the N-H and C=O groups of both the amide and urethane bonds ²³.

Among these structures, amide groups are effective structural units for the formation of supramolecular gels since the formation of hydrogen bonds (H-bonding) between amides is thermodynamically favored in a variety of solvents¹⁹. Therefore, low molecular weight gelators which contain single^{24,25} or multiple amide groups²⁶⁻²⁸ can act as efficient gelators due to inducing directional intermolecular H-bonding for self-assembly.

Thermal properties such as melting of these gels were found to be associated with the strength of intermolecular H-bonding and Van der Waals interactions²⁹. One of the main challenges in the rational design of these molecules has been understanding the degree of intermolecular interactions and their inherent characteristics. So far some attempts have been made to correlate the position of amide groups in the molecular structure to the conformation of H-bonding in the network, i.e. in the presence of different solvents, but still an elaborate study on the structure and properties of the solid LMWGs as the main building units of these gel networks is required. In fact, the first step toward successful gel design and preparation is to fully characterize the structure and properties of the gelator molecules themselves.

Here, we study solely the thermal properties and molecular arrangement of bisamide LMWGs in the solid state as they are the main active components of the gels. Understanding the structure can best be achieved by a systematic study of the structure-properties relations of a homologous series of such molecules. Therefore, a series of bisamide compounds (nBA) was synthesized with two linear alkyl tails attached to bisamide groups bridged with n carbon spacer length. Both odd and even linear spacers were prepared with length n increasing from 5 to 10. These can be considered as simple model compounds for bisamide LMWGs. The properties of bisamide gelators with this generic structure, i.e. bisamides with the same tails, different tails, different tail lengths, or a different core structure have been studied so far for different applications such as injectable gels, drug delivery systems, tissue engineering, and rheological modifiers in coating applications³⁰⁻³⁶.

Tomioka et al. studied the effect of spacer length in the bisamide structure with a series of 10-didodecanoyleamides on the gelability which has shown significantly different morphologies in the gel state³⁷. The dodecanoyl tails of the molecules interact with Van der Waals forces of these bisamides. The zigzag arrangement of an odd spacer directs the two amide carbonyl groups into a parallel position and an even spacer would appear to dictate an antiparallel alignment of amide groups. As a result of the spatial arrangement of amide groups in these two groups of bisamides, even bisamides form two pairs of hydrogen bonds with two other molecules in a

single plane while bisamide molecules with odd spacer length can potentially form four independent hydrogen bonds with four other molecules not in one plane. This however would require a substantial change in the molecular conformation. By analogy, the different H-bonding patterns may cause specific self-assembly behavior for odd and even bisamides in the gel state. In fact, in the presence of appropriate organic solvents, this class of bisamide gelators can form gels with different morphologies and microstructural properties ^{38,39}. The gelation process and final morphology of a series of α,ω -polymethylene bisamides, with the two amide groups bridged by even or odd numbers of spacer carbons, has been studied in a variety of solvents ⁴⁰. It was found that the odd-even effect has a determining role on the gelability and the final properties of the gels; the bisamide gelators with even spacer length have shown the ability to gelate Mesitylene. However, the longer the bridging spacer, the poorer the efficiency of gelation due to the formation of ribbon-like structures. In contrast, gelators with odd spacer length exhibited efficient immobilization of Mesitylene via a fine woven fibrous network.

The present study is limited to linear symmetric bisamide gelators with a simple structure in order to understand the relation of H-bonding via amide groups with packing of these molecules in the solid state. It seems not only logical but also necessary to obtain information on the relationships between spacer length parity and the spatial arrangement of two amide groups of molecules in the solid state to be able to understand their effects on the microscopic structures in the gel state. The thermal properties and crystal structure of the molecules in the solid state have been addressed for further systematic experiments due to the fact that both the solubility and the rate of crystallization are influenced by the regularity of the H-bonding pattern ^{41,42}. In fact, the analysis of structural evolution of bisamide compounds at elevated temperature is of great importance to complement our understanding of the stability of these gelators in the presence of usually poor solvents, the thermodynamics of gelation, and intermolecular interaction i.e. dissolution or recrystallization of these compounds during the self-assembly process.

3.2 Materials and methods

3.2.1 Materials

Diamines varying in the number of methylene groups (n) between amine groups from 5 to 10, i.e. 1,5-Diaminopentane ($\text{NH}_2(\text{CH}_2)_5\text{NH}_2$), 1,6-Diaminohexane ($\text{NH}_2(\text{CH}_2)_6\text{NH}_2$), 1,7-Diaminoheptane ($\text{NH}_2(\text{CH}_2)_7\text{NH}_2$), 1,8-Diaminoctane ($\text{NH}_2(\text{CH}_2)_8\text{NH}_2$), 1,9-Diaminononane ($\text{NH}_2(\text{CH}_2)_9\text{NH}_2$), 1,10-Diaminodecane

($\text{NH}_2(\text{CH}_2)_{10}\text{NH}_2$), and stearic acid ($\text{CH}_3(\text{CH}_2)_{16}\text{COOH}$), Sigma Aldrich (95-97% analytically pure), Hypophosphorous acid solution, H_3PO_2 (50 wt. % in H_2O), were used as received for the synthesis of bisamide molecules. Dimethyl sulfoxide- d_6 (DMSO D_6) (^1H NMR reference standard grade) was used as a solvent for the analysis by nuclear magnetic resonance (^1H NMR).

3.2.2 Synthesis and characterization

A series of bisamide compounds was produced with $(\text{CH}_2)_n$ spacer between the amide groups, where $n = 5$ to 10, and with C17 alkyl tails at each side of the amide groups. The bisamides were notated according to the number of carbon atoms in the spacer (n) with 'BA' as the suffix for 'bisamide compound'. The general chemical structure of nBA compounds is shown in Figure 3.1, using 5BA as example.

The nBA series was synthesized by condensation of stearic acid and a series of diamines. 2 moles of stearic acid and 1 mole of the appropriate N,N'-diamine were heated above their melting points and mixed via a mechanical stirrer. The synthesis was done in a neutral environment provided with N_2 purge (99 % purity). H_3PO_2 in negligible amounts was added as an anti-oxidizing agent. As a result of an amidification reaction, the bisamide compounds were synthesized in the melt state. A homogeneous yellowish white compound was produced upon cooling of the molten product.

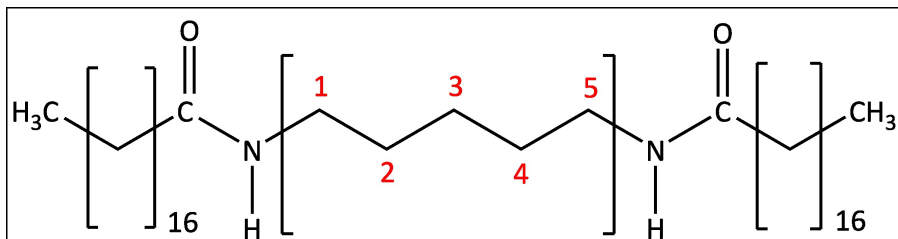


Figure 3.1 Chemical structure of synthesized bisamides (nBAs) with $(\text{CH}_2)_n$ spacer between the amide groups ($n = 5$ in this example) and with C17 alkyl tails.

3.2.3 Proton-Nuclear magnetic resonance spectroscopy (^1H NMR)

Proton NMR spectroscopy was used for all nBA compounds to check the successful synthesis of the compounds with the formation of amide groups. ^1H NMR spectra were recorded on an Agilent 400-MR DD₂ NMR spectrometer equipped with a 5 mm ONE NMR Probe. The nBA compounds were dissolved in Dimethyl sulfoxide d_6 (5 wt%) at 80 °C. Tetramethylsilane (TMS) was used as an internal reference. The

resolution of the spectra was compromised due to the poor solubility of nBA compounds in almost any solvent.

3.2.4 Differential Scanning Calorimetry (DSC)

Differential Scanning Calorimetry (DSC) was employed to characterize the thermal behavior of nBA compounds. Perkin Elmer-Pyris Diamond differential scanning calorimeter with two 1 g-furnaces (working on the Power-compensation temperature null principle with accuracy $< \pm 1\%$ and precision $< \pm 0.1\%$). Nitrogen (99.99 % purity) was used to purge the thermal analysis system at a rate of 50 mL/min. Temperature and heat flow calibration were done before each measurement using the heating scan of indium, a highly pure metal provided by Perkin Elmer with accurately known enthalpies of fusion and melting point, $\Delta H_{\text{fusion}} = 28.47 \text{ J.g}^{-1}$ and $T_m^0 = 156.4 \text{ }^\circ\text{C}$, under the same condition as the to-be-measured samples. The onset of the melting transition and the area under the peak, calculated by PYRIS analytical software, were chosen respectively for the calibration of the melting temperature and the enthalpy of fusion.

A bisamide compound ($6 \pm 1 \text{ mg}$) was placed in a $40 \mu\text{L}$ aluminum sample pan and was weighed on a microbalance. The sample pan and a reference pan (an identical empty pan), both covered by aluminum lids, were placed in the furnaces of the DSC apparatus. Both pans were heated from room temperature to at least $30 \text{ }^\circ\text{C}$ above and below the temperature range of interest. Isothermal melting was followed by a fixed cooling cycle preceding a second heating cycle, all scans at the rate of 10 K.min^{-1} . In fact, the identical method was performed in order to eliminate the thermal history of the compounds which might have been caused during the compound synthesis and sample preparation processes. Therefore, the data recorded from the second heating cycle can be used for further analysis to obtain information solely on the effect of different spacer lengths of nBA on their thermal properties. Prior to the data collection for the analysis, the heat flow of the raw data (mW) was normalized per weight of the sample (mg) resulting in 'normalized heat flows' (W/g). The normalized data were transferred from the Perkin-Elmer computer into ASCII format. The data visualization was done by Python and the endothermic peaks were plotted in upward direction in all graphs.

3.2.5 $\text{DSC}_N(T)$ analytical model and curve fitting

Based on the thermodynamics of melting phenomena, an analytical DSC model $\text{DSC}_N(T)$ has been developed which fits the DSC experimental traces by capturing the

peak shape ⁴³. The model allows fitting of the DSC peaks taking an assumed Arrhenius crystal size distribution together with instrumental and sample-related peak broadening into account and yields a much more accurate determination of the equilibrium melting point, enthalpy of fusion, and change in heat capacity of nBA compounds. The non-linear curve fitting of $DSC_N(T)$ to the experimental DSC traces has been done using the Python 3 programming language. The non-linear least squares (NLLS) function from the `scipy.optimize.curve_fit` module was used, which takes the independent variable and the function parameters and optimizes the parameters within defined lower and upper bounds to minimize the sum of squares of nonlinear functions. The curve fitting consisted of the entire temperature range on the x-axis, which is broad enough to cover the peak region and to precisely determine the baseline on the tails at both sides of the peak minimum. This method improves the reproducibility of the fitting process and the precision of the fitted parameters.

To extract accurate information from DSC measurements, at least three nBA samples with nearly identical weight were measured under the same condition. The standard deviation of the melting temperature, enthalpy of fusion, and heat capacity change were obtained by fitting $DSC_N(T)$ analytical model to the three sets of raw data which contain the experimental error along with the fitting procedure error. The fitting deviation for each parameter was obtained from the residuals of NLLS. The reported error margins of the fit parameters in tables are the residuals of NLLS rounded to two digits.

3.2.6 Powder X-ray diffraction (XRD) and molecular modelling

X-Ray diffraction combined with molecular modelling was used to obtain information on the crystal structure of nBA compounds. X-ray diffraction patterns were recorded at room temperature with a Bruker D8 Advance ECO diffractometer in Bragg-Brentano geometry, equipped with a Cu X-ray source ($K_{\alpha 1} = 1.54060 \text{ \AA}$ and $K_{\alpha 2} = 1.54439 \text{ \AA}$) and LYNXEYE-XE-T position sensitive detector. A knife-edge has been used to reduce the background due to the scattering of the primary beam. The patterns were measured from $0.6^\circ(2\theta)$ to $50^\circ(2\theta)$ with a step size of 0.01° and measuring time of 0.5 s/step. The Cerius2 software package (version 4.2, from Accelrys, now owned by Biovia) was used to build the crystal structure models, employing the COMPASS force field. Simulated XRD patterns were calculated using the Cerius2 diffraction module and the GSAS-2 software system ⁴⁴. The Lorentz and polarization factors were included in the calculated reflection intensities. The crystallite sizes were chosen to match the observed diffraction patterns.

Temperature-dependent XRD measurements were performed with a Bruker D8 Advance in reflection mode equipped with a Co X-ray source ($K_{\alpha 1} = 1.78897 \text{ \AA}$ and $K_{\alpha 2} = 1.79285 \text{ \AA}$) and a LynxEYE-XE position sensitive detector. Variable divergence slits were used to achieve a constant footprint on the sample, itself located inside an Anton Paar XRD900. The sample was loaded into a Macor ceramic sample holder designed to minimize systematic errors on the data (i.e. shift in 2θ position) caused by the thermal expansion of the sample holder resulting in a different height of the sample. The measurements were performed by stepwise increasing the temperature at the rate of $10 \text{ K} \cdot \text{min}^{-1}$.

3.2.7 Fourier transform infrared spectroscopy (ATR-FTIR)

To study the supramolecular interaction of bisamide compounds, Fourier transform infrared (FTIR) spectroscopy with an attenuated total reflection (ATR) method was carried out. ATR-FTIR spectra were recorded on a FTIR spectrophotometer (Nicolet 6700 from Thermo Fisher Inc., USA) equipped with an ATR attachment with a diamond crystal. The appropriate amount of nBA compound was placed on the crystal, and then its FTIR spectrum was measured. The resolution of the spectra was 2 cm^{-1} . The final spectra were acquired as the average of 32 scans.

3.3 Results and discussion

3.3.1 Synthesis of bisamide gelators

Bisamide compounds nBA with spacer length $n = 5$ to 10 , and with C17 alkyl tails at both amide groups were synthesized. The ^1H NMR spectra show that the amidification reaction has occurred and the nBA compounds were produced in high yield (Table S3.1). The ^1H NMR spectra of all nBA compounds (Figure S3.1) were comparable with those reported in the literature.

3.3.2 Thermal analysis

The effect of spacer length on the phase behavior of nBA compounds was studied with DSC. Figure 3.2a shows the second heating DSC traces of nBA compounds scanned from $25 \text{ }^\circ\text{C}$ to $180 \text{ }^\circ\text{C}$. All nBA compounds exhibit transition peaks between $120 \text{ }^\circ\text{C}$ and $150 \text{ }^\circ\text{C}$. The melting points of the solid state bisamide gelators with even spacer lengths and C17 alkyl tails have been reported to be around $140 \text{ }^\circ\text{C}$ ^{45,46}. Therefore, the transition peaks in heat flow vs. temperature diagram (Figure 3.2a) are assigned to the melting transitions of the nBA compounds.

The thermodynamic melting point of a fully crystalline and 100 % pure compound is in theory an infinitely sharp peak in a DSC thermogram⁴⁷. However, in real nBA samples a distribution of crystal sizes exists which causes an asymmetric shape for the melting transitions in the DSC trace (Figure 3.2a). Other factors broadening the peak include limited instrumental resolution and thermal gradients in the sample. Moreover, the presence of impurities in the samples can cause additional broadening. As a result of these effects, the DSC signal would turn into a symmetric Gaussian distribution. The onset of the melting peak is usually considered as the onset of the melting transition where the extrapolated baseline and the tangent of the rising edge intersect; we find however that this method of analysis should be changed in the case of severely asymmetric peaks, as is the case for nBA compounds.

In case of a broad, crystal size-induced, asymmetric melting point depression, the convolution of a truncated Arrhenius base function with Gaussian broadening provides a convenient and rather versatile asymmetric melting peak function. Equation 3.1 gives $DSC_N(T)$ analytical model that we derived which yields the equilibrium melting temperature (T_m^0), the enthalpy of fusion (ΔH), and the change in heat capacity prior and after the transition ($\Delta C_{p,m}$) as described by Equation 3.2⁴³. The mathematical terms and physical attributions of the parameters of $DSC_N(T)$ are summarized in Table 3.1.

$$DSC_N(T) = \Delta H \cdot \frac{\alpha}{2} \cdot e^{\frac{\alpha^2}{4\beta}} \cdot e^{\alpha(T-T_m^0)} \cdot \operatorname{erfc} \left(\sqrt{\beta} \left(T - T_m^0 + \frac{\alpha}{2\beta} \right) \right) + \Delta C_p(T) + B + C(T - T_m^0) + D(T - T_m^0)^2 \quad \text{Equation 3.1}$$

$$\Delta C_p(T) = \Delta C_{p,m} \cdot \frac{1}{2} \cdot e^{\frac{-\alpha^2}{4\beta}} \cdot \left(e^{\frac{\alpha^2}{2\beta}} \cdot e^{\alpha(T-T_m^0)} \cdot \operatorname{erfc} \left(\sqrt{\beta} \left(T - T_m^0 + \frac{\alpha}{2\beta} \right) \right) + e^{\frac{\alpha^2}{4\beta}} \cdot (\operatorname{erf}(\sqrt{\beta}(T - T_m^0)) + 1) \right) \quad \text{Equation 3.2}$$

Figure 3.2a shows that the $DSC_N(T)$ analytical model fits the second experimental heating traces of all nBA compounds remarkably well ($R^2 > 0.99$) (Table S3.2). Shown by the dashed-blue line in the inset for 5BA as an example, the equilibrium melting point (T_m^0) obtained from the $DSC_N(T)$ model is at a different location than the onset of the peak. In fact, it occurs on the trailing edge of the DSC peak.

Calculated based on $DSC_N(T)$, Figure 3.2b manifests the odd-even alternation of the equilibrium melting temperature (T_m^0), enthalpy of fusion (ΔH) (Figure 3.2c), and change in heat capacity prior to and after transition ($\Delta C_{p,m}$) (Figure 3.2d) versus the spacer length of nBA compounds. We find that T_m^0 , ΔH , and $\Delta C_{p,m}$ of even nBAs are higher than those of the odd nBAs, where the not too dramatic difference refers to

the similarities in crystal structure and molecular arrangement that will be discussed in the XRD analysis section.

Figures 3.2b,c compare the melting temperature and enthalpy of fusion of nBA compounds calculated from the $DSC_n(T)$ analytical model and from the tentative values of enthalpy and entropy change of melting of methylene (CH_2) and amide groups ($CONH$) suggested by Van Krevelen et al.⁴⁸. All bisamides consist of 2 amide groups and $n+34$ methylene groups (n as spacer length and 17 in each tail) in their structures. The enthalpy of fusion of the bisamide increases upon increasing the spacer length since the length of the entire backbone increases which reinforces the Van der Waals interaction among these molecules. The calculation of enthalpy of fusion from the enthalpy per $CONH$ and CH_2 results in average values between odd and even converging to the enthalpy of Polyethylene where CH_2 groups are the only moieties in the backbone. Thus the Van der Waals force is the sole force controlling the interactions between these ‘infinite’ bisamide molecules, however the alternation in $DSC_n(T)$ values indicates that the H-bonding via amide moieties contributes to the enthalpy, which is known as the odd-even effect. The enthalpy of fusion for the contribution of the $CONH$ group for even bisamides and odd bisamides is $7.8\text{ kJ}\cdot\text{mol}^{-1}$ and $5.8\text{ kJ}\cdot\text{mol}^{-1}$ respectively, indicating that the odd-even alternation in properties results from the packing of the molecules in the solid state⁴⁹.

Table 3.1 The variables, functions, and parameters of $DSC_N(T)$.

parameter	power units	thermodynamic units	physical attributions and mathematical terms
T_m^0	°C	K	The equilibrium melting point of the phase transition
B	W.g ⁻¹	J.g ⁻¹ .K ⁻¹	Baseline offset
C	W.g ⁻¹ .K ⁻¹	J.g ⁻¹ .s ⁻¹	Linear baseline slope
D	W.g ⁻¹ .K ⁻²	J.g ⁻¹ .s ⁻¹ .K ⁻²	Second order baseline curvature
α	K ⁻¹	K ⁻¹	Strength of the linearized Arrhenius function ($\alpha = Ea/(R.(T_m^0)^2)$ describing the crystal size distribution.
β	K ⁻²	K ⁻²	The parameter in relation to the Gaussian distribution of the peak ($\beta = \frac{1}{2\sigma^2}$), describing the peak broadening in the declining edge.
$\Delta C_{p,m}$	W.g ⁻¹ .K ⁻¹	J. K ⁻¹	The difference between the heat capacity of the solid and liquid states.
$e^{\alpha(T-T_m^0)}$	-	-	The Arrhenius function determining the rising edge of the curve.
$erfc\left(\sqrt{\beta}(T-T_m^0 + \frac{\alpha}{2\beta})\right)$	-	-	Erfc, the complementary error function, describes the falling edge of the peak as it returns to the baseline.
ΔH	W.g ⁻¹	J.g ⁻¹	The coefficient of $DSC_N(T)$ function representing the change in the enthalpy associated with the phase transition.
R^2	-	-	The statistical measure for the goodness of fit in a regression function.

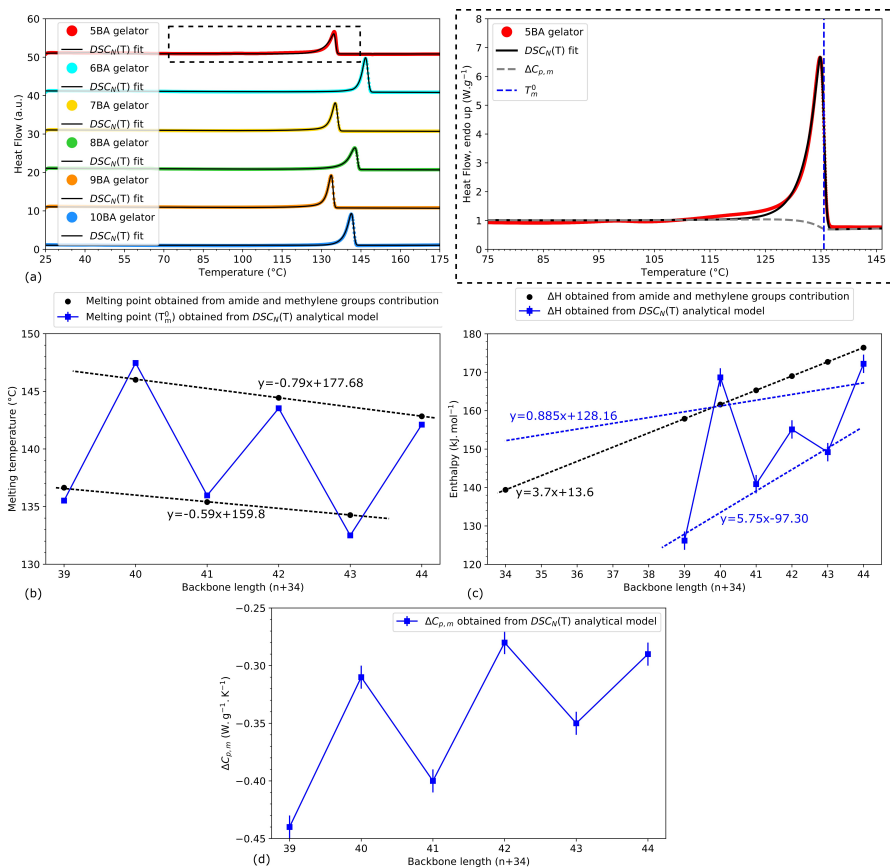


Figure 3.2 DSC thermogram of nBA compounds (curves were shifted vertically for clarity): a) $DSC_N(T)$ function fitted to the second heating traces (endo up) representing the melting transition of nBA compounds measured at 10 K.min⁻¹ after calibration at the onset for the given sample weight and scan rate, the thermal properties of nBA compounds showing the odd-even effect: b) melting temperatures (T_m^0) obtained from the $DSC_N(T)$ analytical model and calculated using tentative values of methylene and amide group contributions, c) the enthalpy of fusion obtained from the $DSC_N(T)$ analytical model and calculated using tentative values of methylene and amide group contributions, d) change in heat capacity obtained from $DSC_N(T)$ analytical model (the errors of change in enthalpy and heat capacity are the experimental errors obtained from measurements on three samples analyzed by $DSC_N(T)$ and for the melting points obtained from $DSC_N(T)$, the errors are the fitting residuals calculated using $DSC_N(T)$, SD= 0.00 °C).

3.3.3 Crystal structure

3.3.3.1 Room-temperature XRD

To investigate the molecular arrangement and crystal structure of the BA compounds in the solid state, XRD patterns of the synthesized nBA compounds were measured at ambient temperatures. Figure 3.7 displays the XRD patterns of the odd BAs and Figure 3.8 those of the even BAs (see also Figure S3.2). The 5BA and 6BA crystal structures were investigated in detail, as they represent odd and even BAs respectively.

5BA (odd nBAs)

An initial model for the crystal structure of 5BA was built and energy-minimized with free unit cell parameters using the Cerius2 software. Calculation of the XRD pattern based on this model allows indexing of the observed XRD pattern. Subsequently, unit cell refinement was carried out via least-squares refinement using a suitable set of observed 2θ peak positions (Figure S3.3). The final unit cell for the 5BA model is triclinic; parameters are given in Table 3.2. The calculated 2θ peak positions based on the refined unit cell are very close (within 0.8 %) to the observed values (Table 3.3), implying successful unit cell determination and refinement.

Table 3.2 Refined unit cell parameters of 5BA and 6BA respectively compared to polyethylene (PE) and Nylon 6,10 α (from literature^{50, 51}).

compound	5BA	PE	6BA	Nylon 6,10 α
unit cell	Triclinic (pseudo-orthorhombic)	orthorhombic	triclinic	triclinic
a (Å)	8.55	7.39	5.02	4.95
b (Å)	4.36	4.30	5.29	5.40
c (Å)	55.58	2.54	57.46	22.40
α (°)	90.0	90	48.7	49.0
β (°)	92.1	90	76.8	76.5
γ (°)	91.9	90	65.2	63.5
z	2	-	1	-
symmetry	P1	-	P-1	-
ρ (g.cm⁻³)	1.018	0.96	1.038	1.07-1.09

The refined unit cell was used as constraint in subsequent COMPASS energy minimizations to obtain the final 5BA crystal structure models. Two different models (see Figure 3.6) match the data, as will be discussed in more detail later: a sheet-like model and a bi-directionally hydrogen bonded model (2D H-bonding), sharing the same unit cell dimensions. Atomic coordinates are available in Table S3.3 and S3.4. The sheet-like model was used to produce the calculated intensities listed in Table 3.3, assuming random crystallite orientation in the powder. The $00l$ intensities are reproduced very well, including the near absence of the $00l$ reflections marked as very weak (vw) or weak (w). The presence of higher order $00l$ reflections up to $l = 20$ at $2\theta = 32.16^\circ$ indicates an exceptionally regular layer spacing. The observed non- $00l$ reflections show severe overlap, unlike the $00l$ reflections. They are weaker than calculated, indicating preferred orientation.

Figure 3.3a presents the calculated XRD pattern based on the sheet-like crystal structure model of 5BA, together with the observed XRD pattern of 5BA. The simulated pattern was calculated using the GSAS-2 software package ⁴⁴, taking preferred orientation into account via the March-Dollase model with unique reflection 001 . The simulated pattern (not shown) for the bi-directional H-bonding model of 5BA is very similar to that of the sheet-like model. Figure 3.3a shows that the simulated 5BA pattern matches the observed pattern very well, even the weak peaks in the high angle region are nicely reproduced. The observed pattern shows one extra peak (indicated in red in Table 3.3), which may be due to a different polymorph.

The 5BA crystal structure has a triclinic unit cell which is pseudo-orthorhombic since the angles are very close to 90° (Table 3.2). The 5BA molecular axes (in both models) are not completely parallel to the c -axis but show pronounced tilting in the ac -plane, referred to as axis tilting. The tilted axes are reasonably parallel to the $(-2\ 0\ 1)$ planes (indicated in red), as is clear from Figure 3.4. This contributes to the high intensity of the $-2\ 0\ 1$ reflection listed in Table 3.3.

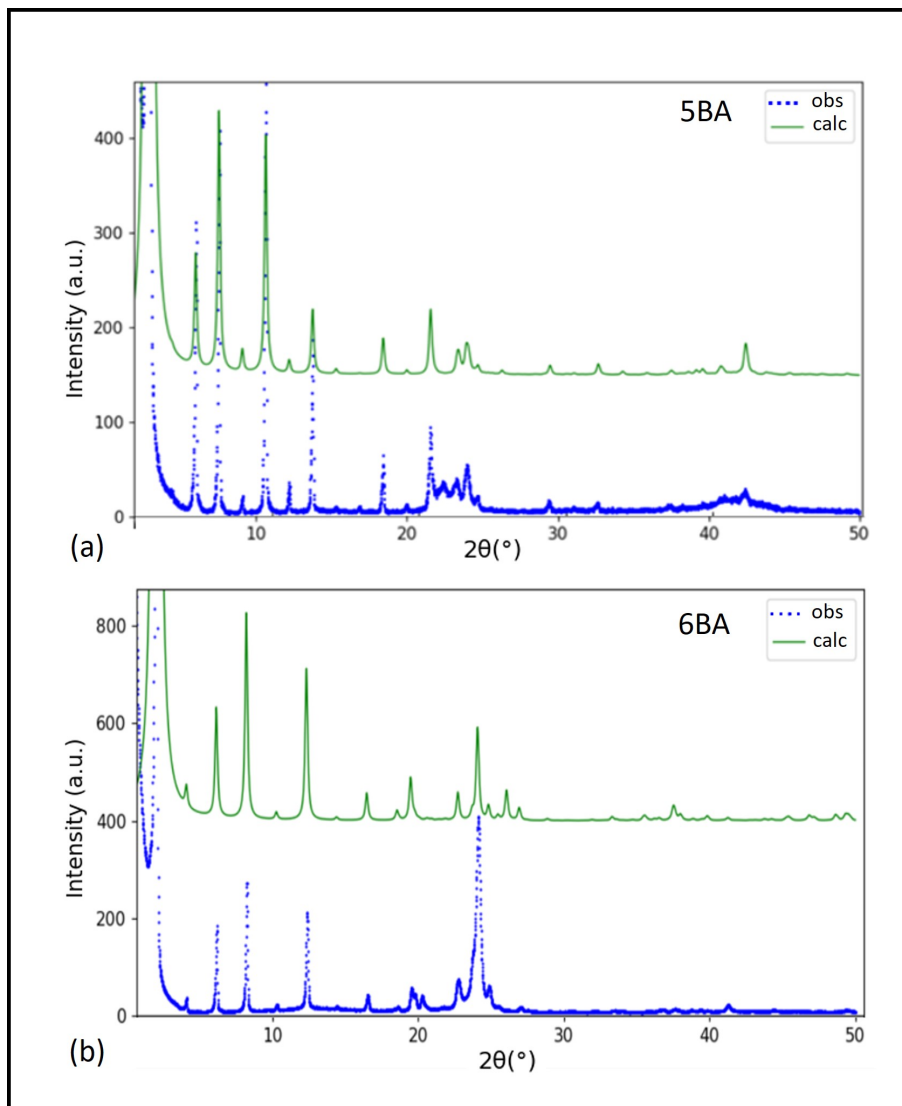


Figure 3.3 Calculated XRD pattern (upper curve) compared to the observed XRD pattern (lower curve) for: a) the sheet-like model of 5BA, b) 6BA (curves were shifted vertically for clarity). In the calculated patterns preferred orientation is taken into account.

Table 3.3 Observed versus calculated peak positions and intensities for the sheet-like 5BA model, assuming random orientation^[a].

d_{obs} (Å)	reflection positions		indexing			intensities	
	$2\theta_{obs}$ (°)	$2\theta_{calc}$ (°)	h	k	l	I_{obs}	I_{calc}
54.065	1.63	1.59	0	0	1	vs	1000
28.583	3.09	3.18	0	0	2	vw	0.3
18.382	4.81	4.77	0	0	3	s	13.1
13.821	6.40	6.36	0	0	4	s	30.0
11.087	7.97	7.96	0	0	5	w	2.6
9.233	9.58	9.55	0	0	6	s	27.4
7.923	11.17	11.15	0	0	7	w	1.5
6.934	12.77	12.75	0	0	8	m	7.4
6.176	14.34	14.35	0	0	9	vw	0.6
5.551	15.97	15.96	0	0	10	vw	<0.1
5.051	17.56	17.56	0	0	11	m	4.1
4.630	19.17	19.17	0	0	12	vw	0.5
4.275	20.78	20.79	0	0	13	m	3.4
		20.79	2	0	0		60.3
		20.80	-2	0	1		169.9
4.111	21.62						
3.938	22.58	22.58	1	-1	0		50.1
		22.62	-1	1	1		12.2
		22.67	1	-1	1		72.2
		22.76	-1	1	2		61.2
3.826	23.25	23.21	1	1	0		101.0
3.710	23.99	23.80	1	1	3		15.2
		23.82	-1	-1	4		12.7
3.474	25.64	25.66	0	0	16	vw	0.4
3.089	28.90	28.93	0	0	18	vw	0.9
2.925	30.57	30.58	0	0	19	vw	0.1
2.783	32.16	32.23	0	0	20	vw	1.0
2.142	42.20	42.24	2	0	22		8.2
		42.31	-2	0	23		13.5

[a] Intensities of $00l$ reflections are marked as very weak (vw), weak (w), medium (m), strong (s) or very strong (vs); the other reflections are not on the same intensity scale due to preferred orientation. The reflection indicated in red is not explained by the model and may point to polymorphy.

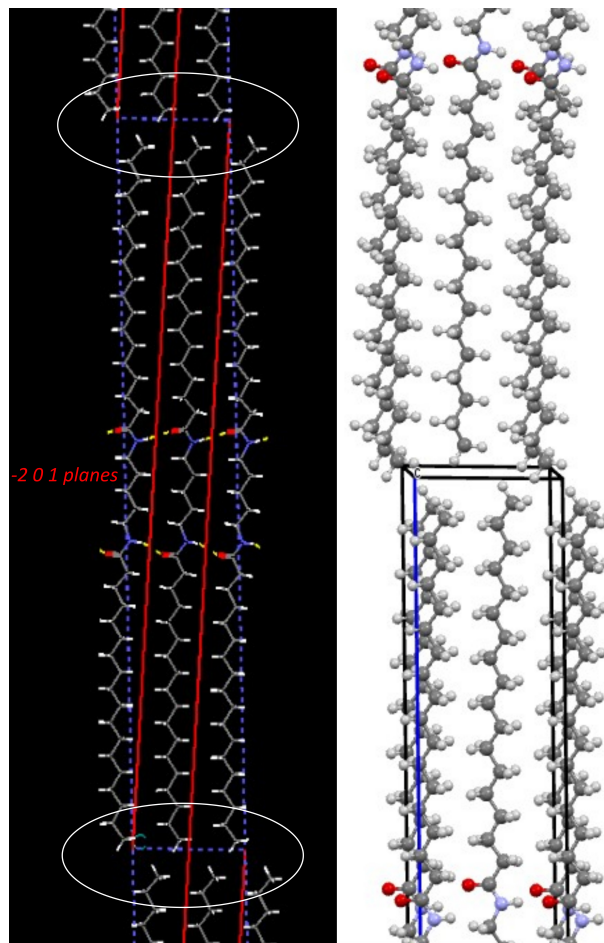


Figure 3.4 Molecular axis tilting of 5BA, tilting of molecules is in the ac-plane (blue-dashed lines) and white ellipses highlight the methyl groups which avoid each other to minimize steric hindrance. The red lines indicate the $(-2\ 0\ 1)$ planes.

Zooming out from a single unit cell to a 5BA crystallite, it is clear that the 5BA gelator molecules are packed in layers with the long axis of the molecules nearly perpendicular to the layers (Figure 3.5a). The interaction between the layers is governed by Van der Waals forces. In fact, the above mentioned tilting effect allows optimal packing of the methyl groups and adequately takes into account the influence of neighboring layers, or in other words the typical layer stacking. The layer stacking may, however, be influenced by a typical form of layer stacking polymorphy often seen in layer-like materials, i.e. by the particular polytype exhibited by the 5BA crystallites. The presented models are mono-layer models. Two-layer polytype models can be constructed simply by doubling the unit cell along

the *c*-axis and (e.g.) introducing inversion symmetry. This results in $Z = 4$, *P-1* models with the same unit cell parameters as the mono-layer models except for the *c*-axis, which is twice as long. Although it is good to be aware of the possibility of polytype polymorphism, such models are not explored here, since they are out of the scope of the present investigation.

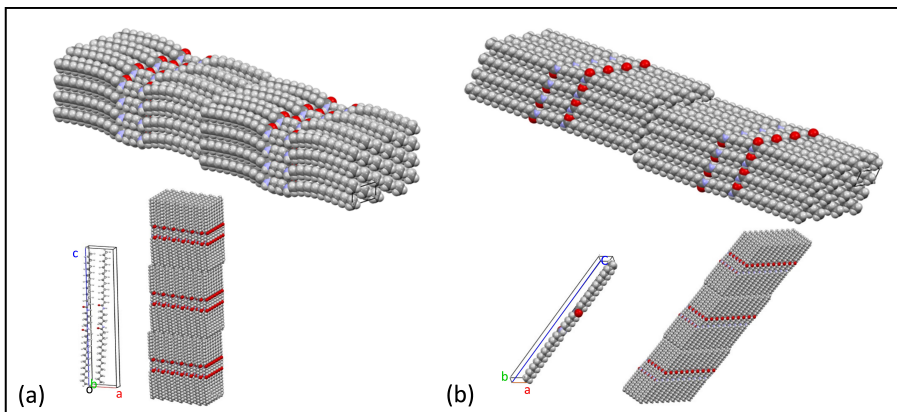


Figure 3.5 Crystal structure of 5BA and 6BA showing layer stacking: a) the long axes of the 5BA molecules are nearly perpendicular to the stacked layers as described by the pseudo-orthorhombic unit cell (with two molecules per cell), b) 6BA molecules are at an angle to the stacked layers as described by the triclinic unit cell. The 6BA unit cell has one molecule per cell and shows the molecular axis tilting effect, just like 5BA. Sheet-like H-bonding between 6BA molecules occurs along the (010) planes in the stacked layers.

The 5BA structural models show 1D and 2D H-bonding as schematically illustrated in Figure 3.6b and a, respectively. Clearly this intra-layer H-bonding interaction is stronger than the Van der Waals interaction between the stacked layers (i.e. the inter-layer interaction). The molecules are hydrogen bonded along the (110) diagonal planes for the sheet-like structure and along both (110) and $(1-10)$, for the bi-directionally hydrogen bonded structure. The sheet-like structure is lower in energy by $8.37\text{ kJ}\cdot\text{mol}^{-1}$. The actual structure may be a mixture of both hydrogen-bonding schemes.

Figures 3.6c,d show the sheet-like 5BA model viewed along two different diagonal directions, i.e. along the (110) and $(1 -1 0)$ crystallographic planes. The backbone of the two C17 alkyl tails (i.e. the “zig-zag”) is positioned in the crystal structure in such a way that the backbones of the two tails are in the two different diagonal planes, instead of only in one plane. This C17 alkyl tail rotation effect is attributed to the odd C5 spacer, which induces a rotation of the alkyl tail from one diagonal plane in

the pseudo-orthorhombic unit cell to the other. The C5 alkyl spacer backbone is parallel to the $(1 -1 0)$ planes. Compared to the polymer chain packing in polyethylene (PE), the packing of the C17 alkyl tails in the ab -plane of 5BA is similar, since they both have a pseudo-orthorhombic $Z = 2$ projection cell (exactly orthorhombic for PE as shown in Table 3.2). However, the molecular packing of 5BA is more dense than the polymer chain packing in PE, especially along the a axis. Moreover, the alkyl tails do not have a herringbone-like packing as in PE⁵⁰.

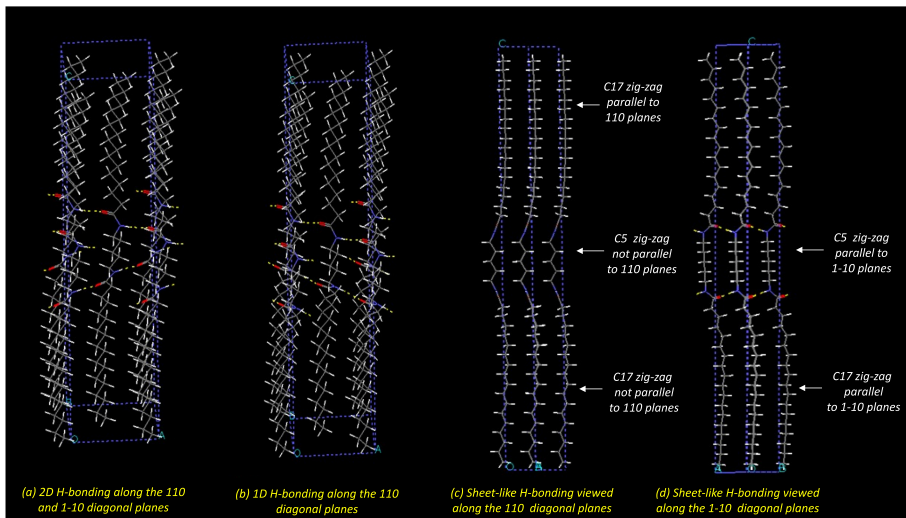


Figure 3.6 The 5BA structural models: a) 2D H-bonding in the bi-directionally hydrogen bonded structure, b) 1D H-bonding in the sheet-like structure, viewed along two different diagonal directions: c) along the (110) diagonal planes, d) along the $(1 -1 0)$ diagonal planes.

The observed XRD patterns of the three odd BAs are shown in Figure 3.7. The characteristic lamellar $00l$ reflections observed for 5BA (Table 3.3) are observed for 7BA and 9BA as well, indicating a highly defined layer spacing. The shift to lower angles with increasing spacer length from 5BA to 9BA is due to an increasing c -axis length. The reflections in the $20 - 25^\circ$ (2θ) range are very similar for all odd gelators, implying that the side-by-side packing of 7BA and 9BA molecules is very similar to that found for 5BA.

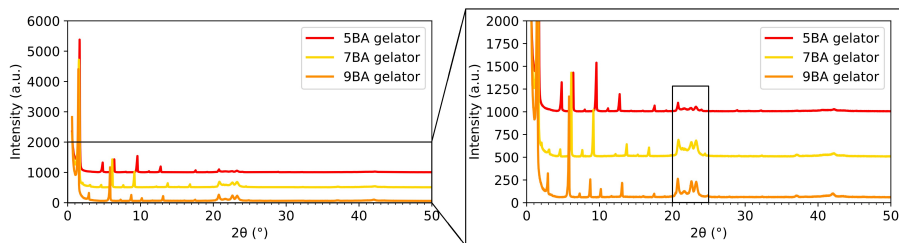


Figure 3.7 Observed XRD patterns of odd nBA gelators, including zoomed-in figure (curves were normalized to the highest intensity and shifted vertically for clarity). The $00l$ reflections shift to lower angles with increasing spacer length. The black box emphasizes reflections in the $20 - 25^\circ(2\theta)$ range, which are hardly influenced by the spacer length.

6BA (even nBAs)

3

An initial crystal structure model for 6BA was built using molecular modelling and diffraction pattern matching. The model allowed indexing of an inset of observed XRD peak positions (Figure S3.4), which was subsequently employed in a least squares refinement of the cell parameters. A zero-shift correction was applied, which refined to $-0.061^\circ(2\theta)$. The refined unit cell parameters are listed in Table 3.2. COMPASS energy minimization using the refined unit cell parameters as constraints produces the final model of which the atomic coordinates are listed in Table S3.5. The simulated XRD pattern based on the model, taking into account preferred orientation, shows a good match with the observed XRD pattern (Figure 3.3b). The calculated 2θ peak positions based on the refined unit cell are very close (within 0.8 %) to the observed values (Table 3.4), implying successful unit cell determination and refinement. The refined model was used to produce the calculated intensities listed in Table 3.4, assuming random orientation.

The refined model is a mono-layer model (Figure 3.5b), which exhibits similar layer stacking as found for 5BA, again with the Van der Waals interaction as inter-layer interaction. Also similar to 5BA, 6BA exhibits a molecular axis tilting effect, i.e. the molecular axes are tilted in the ac -plane, with respect to the c -axis, which ensures minimal steric hindrance between the methyl groups. However, 6BA has a triclinic unit cell with one molecule per cell ($Z = 1$), very different from the pseudo-orthorhombic unit cell of 5BA with $Z = 2$ (Table 3.2). The inversion symmetry of the 6BA molecules translates to $P-1$ space group symmetry, unlike 5BA, where the molecules do not have inversion symmetry and the space group symmetry is $P1$. There is no alkyl tail rotation effect in 6BA unlike in 5BA, where the odd C5 spacer

induces alkyl tail rotation. 6BA has a slightly higher crystalline density (1.038 g.cm^{-3}) as compared to 5BA (1.018 g.cm^{-3}). The long axes of the 6BA molecules are at an angle to the layers, as described by the triclinic unit cell.

Comparing the molecular packing of 6BA with that of nylons, the 6BA cell parameters are very close to those of Nylon 6,10 α ⁵¹, except for the *c*-axis, which is much longer for 6BA (Table 3.2). The 6BA molecules exhibit sheet-like H-bonding (Figure S3.6) in each stacked layer along the (010) planes, very similar to Nylon 6,10 α . In fact, the molecular backbones of the C6 spacer and C17 tails are in the plane of the hydrogen bonded sheets, which is similar to Nylon 6,10 α .

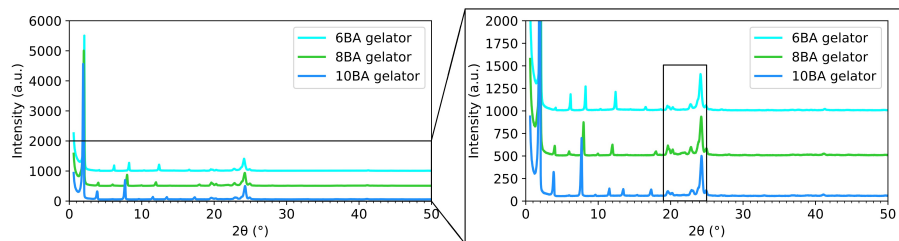


Figure 3.8 Observed XRD patterns of even bisamide gelators, including the zoomed-in figure (curves were normalized to the highest intensity and shifted vertically for clarity). The $00l$ reflections shift to lower angles with increasing spacer length. The black box emphasizes the reflections in the $19 - 25^\circ$ (2θ) range, which are hardly influenced by the spacer length.

The XRD patterns of the even BAs displayed in Figure 3.8 not only show $00l$ reflections for 6BA, but also for 8BA and 10BA. The *c*-axis length increases with increasing spacer length which leads to a low-angle shift of the $00l$ peaks. The reflections in the $19 - 25^\circ$ (2θ) range are very similar for the even gelators, implying that the side-by-side packing of 8BA and 10BA is very similar to that of 6BA.

Table 3.4 Observed versus calculated peak positions and intensities based on the 6BA model, assuming random orientation^[a].

reflection positions d_{obs} (Å)	$2\theta_{obs}$ (°)	$2\theta_{calc}$ (°)	indexing			intensities	
			<i>h</i>	<i>k</i>	<i>l</i>	I_{obs}	I_{calc}
42.657	2.07	2.05	0	0	1	vs	1000.0
21.394	4.13	4.11	0	0	2	w	2.8
14.280	6.19	6.16	0	0	3	s	14.5
10.707	8.26	8.22	0	0	4	s	27.4
8.562	10.33	10.28	0	0	5	w	1.0
7.140	12.40	12.34	0	0	6	s	20.1
6.125	14.46	14.41	0	0	7	w	0.4
5.356	16.55	16.48	0	0	8	m	3.6
4.762	18.63	18.51 18.56 18.71 18.75				0	2.3
		0 0 9 0 1 6 0 1 9				w	1.2
		19.48 19.52 19.66				-1 0 1 1 0 0 -1 0 2	7.1 116.2 14.4
4.538	19.56	19.79	1	0	1	226.0	
		20.29	-1	0	3	11.9	
4.077	21.80	21.90	1	1	3	8.0	
3.906	22.76	22.74	0	0	11	m	3.4
3.747	23.75	23.71	1	1	1		40.0
3.688	24.13	24.09	0	1	0		338.6
3.580	24.87	24.83	1	1	0		42.5
3.496	25.48	25.48	0	-1	1		14.7
2.187	41.29	41.26	0	2	23		9.8

[a] The intensities of $00l$ reflections are marked as very weak (vw), weak (w), medium (m), strong (s) or very strong (vs); the other reflections are not on the same intensity scale due to preferred orientation.

3.3.3.2 High-temperature XRD

To investigate the structural evolution of the nBA compounds and their phase behavior at high temperatures, their XRD patterns at elevated temperatures were measured. Inspecting the X-ray diffraction patterns (Figure 3.9a,b) at elevated temperatures it is clear that the crystalline peaks of these compounds disappear and turn into a very broad peak around 132.5 °C and 145 °C for 5BA and 6BA, respectively. These broad peaks are due to the amorphous structure of the liquid state formed

upon melting, which is in agreement with the melting transitions obtained from $DSC_N(T)$ ($T_m^0 = 135.52$ °C for 5BA and $T_m^0 = 147.46$ °C for 6BA). The melting transition detected by XRD differs from DSC measurement by a few degrees, which is due to the different measurement equipment and conditions.

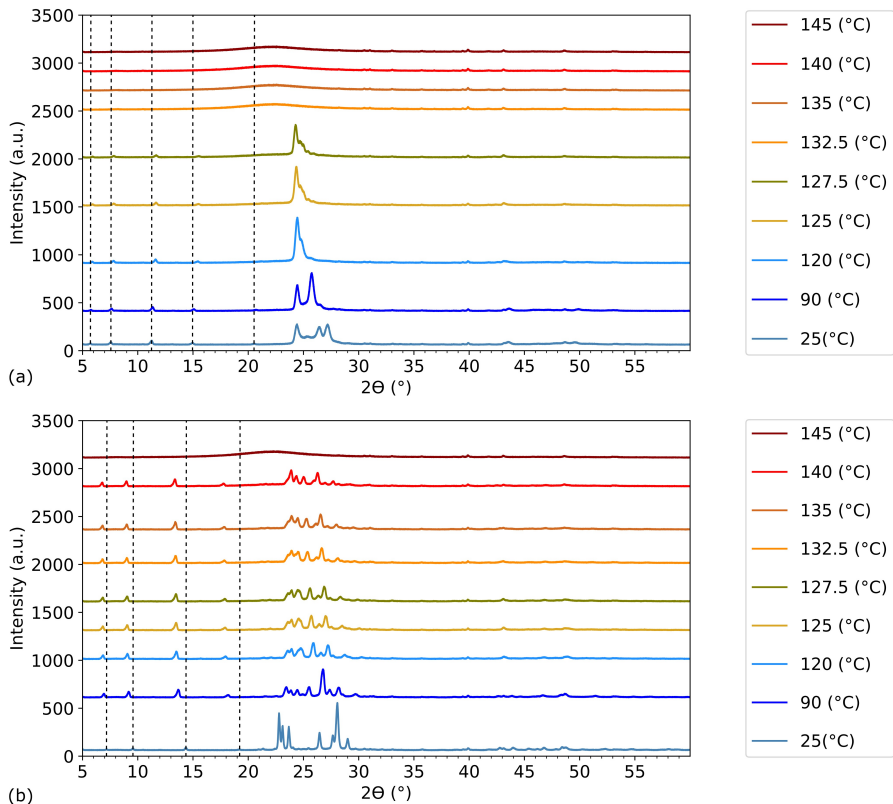


Figure 3.9 XRD patterns at different temperatures for a) 5BA, b) 6BA (curves were shifted vertically for clarity) showing that melting of 5BA and 6BA have occurred around 132.5 °C and 145 °C respectively, dashed lines show the shifting 001 reflections.

The XRD patterns in Figure 9 were measured with Co radiation, unlike the XRD patterns in Figures 3.7 and 3.8, which were measured with Cu radiation. Hence the patterns in Figure 3.9 are shifted to higher angles compared to the measurements with Cu radiation due the different wavelength (Bragg's law). With increasing temperature, the 001 peaks slightly shift to higher angles (Figure 3.9a), which is in agreement with thermal motion causing a slight contraction of the molecular axes. The reflections in the $25 - 28^\circ$ (2θ) range start to merge with increasing temperature

suggesting a gradual change to a somewhat higher symmetric structure, which may be a disordered phase.

The structural evolution of 6BA is quite different from that of 5BA. While for 5BA the $00l$ reflections indicate a small contraction of the molecular length, the $00l$ reflections for 6BA show a marked shift to lower angles (Figure 3.9b), indicating that the layer spacing increases. This points to a change in lattice angles leading to a smaller angle of the molecular axes with respect to the normal to the stacked layers. At the same time the reflections in the $23 - 30^\circ$ (2θ) range change considerably, but they do not gradually merge as in the case of 5BA. These changes point to a solid state transition to a very different high temperature structure occurring in the temperature range below 120°C . Remarkably this structure seems to be quite robust, since it remains intact up to melting.

3.3.4 Fourier transform infrared spectroscopy (ATR-FTIR)

FTIR spectroscopy was used to probe the H-bonding interactions where several absorption bands in the infrared region are related to the H-bonding pattern. ATR-FTIR spectra of the nBA compounds in the solid state are displayed in Figure 3.10. The symmetric and asymmetric stretching peaks of $-\text{CH}_2$ and $-\text{CH}_3$ groups were observed around 2844 cm^{-1} and 2918 cm^{-1} , respectively. As expected, the relative intensity of the $-\text{CH}_2$ peak increases with increasing spacer length. N-H (stretch), C=O (amide I), and N-H bending (amide II) are the characteristic bands involved in the H-bonding between nBA molecules, thus they are sensitive to changes in the H-bonding pattern. The C=O (amide I) band was found to be sensitive to molecular arrangement since an alternating shift was detected between the spectra of the odd and even series (Table 3.5), for instance the C=O (amide I) band shifts from 1635 cm^{-1} for 5BA to 1633 cm^{-1} for 6BA as can be seen most clearly from the inset on top of Figure 3.10.

Similarly, N-H (stretch) bands alternate significantly between the odd and even members of the series, for example the N-H (stretch) band is observed at 3291 cm^{-1} for 5BA and at 3309 cm^{-1} for 6BA. The change in N-H (stretch) is much more dramatic as compared to the C=O band since the hydrogen is more directly influenced by the H-bonding via the N-H bond than the C=O engaged in the H-bonding interaction. In fact, C=O is present in the BA molecule as a more stiff bond but the hydrogen in N-H is slightly close or slightly further away from the N, depending on the H-bonding network (Table 3.5).

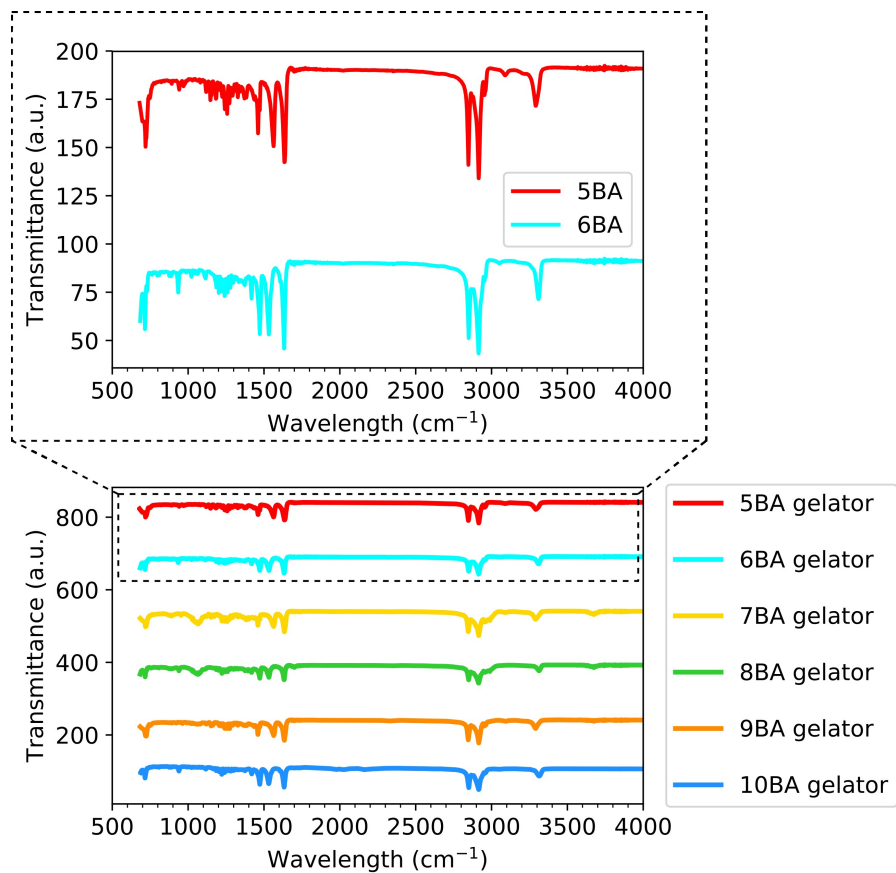


Figure 3.10 FTIR spectra of nBA compounds (curves were shifted vertically for clarity), the inset shows the shift in the positions of three characteristic FTIR bands for 5BA and 6BA compounds.

Table 3.5 The positions of FTIR bands for odd and even bisamide compounds: N-H (stretch) bands and amide II bands alternate between odd and even members but no significant shift observed between the members of odd or even nBA series.

compound	N-H stretch (cm ⁻¹)	C=O (Amide I) (cm ⁻¹)	N-H bending (Amide II) (cm ⁻¹)
5BA	3291	1635	1563
6BA	3309	1633	1533
7BA	3291	1634	1564
8BA	3313	1633	1532
9BA	3290	1634	1564
10BA	3314	1633	1531

The amide II band is another characteristic band for nBA compounds and is observed at 1563 cm^{-1} for 5BA, shifting to 1533 cm^{-1} for 6BA. The systematic alternation of N-H (stretch) bands and amide II bands between odd and even members, with no significant shift observed between the members of odd or even nBA series, is in agreement with the difference in the odd and even H-bonding patterns observed by XRD. The H-bonding network is confining the freedom of the motion of the molecules such that the molecules in odd bisamides feel slightly less constrained than the even molecules since the N-H bands have emerged at lower wave numbers. This systematic shift to higher frequencies for even bisamides compared with odd bisamides can be attributed to stronger H-bonding between N-H and C=O as the H-bond donor and acceptor respectively, which is in agreement with the observation of XRD showing a higher packing density for 6BA than 5BA⁴⁴.

3.4 Conclusions

This study provides insights into the effect of odd-even spacer length on the molecular arrangement of model bisamide gelators (nBA compounds) in the solid state and their thermal properties aimed at a better understanding of the gel systems based on nBA compounds. To this end, a homologous series of nBA compounds was designed with $(\text{CH}_2)_n$ spacer ($n = 5 - 10$) between the amide groups and with C17 alkyl tails. Thermal properties as a function of the spacer length n were measured by DSC and subsequently FTIR spectroscopy, X-ray diffraction analysis and molecular modelling were employed to investigate their structural origin. A new analytical model, $\text{DSC}_N(T)$, was developed to reliably investigate the odd-even alternation in melting temperatures, the change in enthalpy and in heat capacity of nBA compounds. The not too dramatic difference in thermal properties between the odd and even nBA series indicates that the crystal structures of these two groups of bisamides show both differences and similarities.

XRD analysis shows that the studied compounds consist of stacked layers of nBA molecules with highly defined layer spacings, since they exhibit a series of $00l$ reflections extending up to very high order ($l = 20$). The unit cell of the odd-membered 5BA gelator is pseudo-orthorhombic, whereas that of the even-membered BA6 gelator is triclinic. Their crystalline densities are 1.018 and 1.038 g.cm^{-3} respectively. The c -axis length increases with increasing the spacer length in both odd and even nBAs, and is close to the length of the gelator molecule, although the molecular axes are tilted somewhat with respect to the c -axis. The latter tilting ensures optimal packing of the methyl groups located at each layer surface; the inter-layer interaction is the Van der Waals interaction. The layer spacing of the odd-

membered 5BA gelator (54.06 Å) is close to the 5BA *c*-axis length (55.58 Å), as described by the pseudo-orthorhombic lattice. The layer spacing of the even-membered 6BA gelator (42.66 Å) however, is much smaller than its *c*-axis length (57.46 Å), and hence much smaller than the 6BA molecular length, due to the triclinic lattice. The very different crystal lattice of odd-membered BAs compared to even-membered BAs translates into a layer spacing close to the molecular length for the odd nBAs and with the long molecular axes almost perpendicular to the stacked layers. For the even nBAs the molecular axes are tilted at an angle with respect to the layer normal, which results in a layer spacing markedly smaller than the molecular length. As for the intra-layer structure, the XRD analysis shows that the side-by-side packing of molecules and the H-bonding pattern is similar within the odd/even series, but differs markedly between the series. The H-bonding pattern of 5BA can be either sheet-like or bi-directional (or both in different domains). It is different from that of 6BA, which exhibits sheet-like H-bonding very similar to that of Nylon 6,10 α . Moreover, the unit cell parameters of 6BA are remarkably close to those of Nylon 6,10 α (except of course for the *c*-axis length).

The latter observation lends support to the conclusion that the anti-parallel amide groups in the even-membered 6BA gelator exhibit a strong structure-directing effect: even though the number of amide groups in 6BA with its C17 alkyl tails is far lower than in Nylon 6,10 α , the 6BA amide groups are still capable of inducing a Nylon 6,10 α type packing and H-bonding scheme. In contrast with the even-membered 6BA, the unit cell parameters of the odd-membered 5BA are quite close to those of polyethylene (except for the *c*-axis length). The C17 alkyl tails of 5BA have a pseudo-orthorhombic $Z = 2$ *ab* projection cell, similar to the orthorhombic projection cell of polyethylene, and unlike the $Z = 1$ projection cell of 6BA. These differences in the packing of 5BA and 6BA nicely illustrate the different (i.e. lower) structure-directing influence of the parallel amide hydrogen bonding motif in the odd BA series as compared to the anti-parallel amide hydrogen bonding motif in the even BA series.

Upon increasing the temperature, melting of the nBA compounds is observed in the temperature range 120 - 150 °C. The melting temperatures obtained from XRD are in good agreement with the ones obtained from DSC_N(T). The structural evolution with temperature of the odd-membered 5BA is quite different from that of the even-membered 6BA. The 5BA crystal structure shows a change with temperature to a somewhat higher symmetric structure, which may be a disordered phase. The 6BA crystal structure shows a transition with temperature to a structure with a markedly larger layer spacing than that at ambient temperatures, indicating a reduction of the molecular tilt with respect to the layer normal. Moreover the high-

temperature 6BA structure seems to be quite robust, since it remains largely intact up to melting, again indicating the stronger structure-directing effect of anti-parallel amide groups, as compared to parallel amide groups. The N-H stretch bands observed using FTIR show an odd-even effect, with the N-H stretch bands of even BAs shifted to higher wavenumbers, pointing to stronger hydrogen bonding between the anti-parallel amide groups in the even series than between the parallel amide groups in the odd series. This is in agreement with the XRD results and with the higher melting points of the even BA series.

Summing up, the structural differences observed between the odd and even BA series reflect the different structure-directing effect of parallel versus anti-parallel amide hydrogen bonding motifs. These differences, together with the structural evolution with temperature as observed using high-temperature XRD, explain the odd-even effects observed via DSC.

3.5 References

- [1] P. Terech and R. G. Weiss, "Low molecular mass gelators of organic liquids and the properties of their gels", *Chem. Rev.*, 1997.
- [2] B. O. Okesola et al., "Supramolecular self-assembly to control structural and biological properties of multicomponent hydrogels", *Chem. Mater.*, 2019.
- [3] J. Becerril, B. Escuder, J. F. Miravet, R. Gavara, and S. V. Luis, "Understanding the Expression of Molecular Chirality in the Self-Assembly of a Peptidomimetic Organogelator", *European J. Org. Chem.*, 2005.
- [4] A. R. Hirst et al., "Low-molecular-weight gelators: Elucidating the principles of gelation based on gelator solubility and a cooperative self-assembly model", *J. Am. Chem. Soc.*, 2008.
- [5] D. B. Amabilino, D. K. Smith, and J. W. Steed, "Supramolecular materials", *Chem. Soc. Rev.*, 2017.
- [6] P. Duan, H. Cao, L. Zhang, and M. Liu, "Gelation induced supramolecular chirality: Chirality transfer, amplification and application", *Soft Matter*, vol. 10, 2014.
- [7] P. R. A. Chivers and D. K. Smith, "Shaping and structuring supramolecular gels", *Nat. Rev. Mater.*, 2019.
- [8] P. Terech, H. Bouas-Laurent, and J.-P. Desvergne, "Small molecular luminescent gelling agent 2, 3-bis-n-decyloxyanthracene: rheological and structural study", *J. Colloid Interface Sci.*, 1995.
- [9] J. H. van Esch and B. L. Feringa, "New functional materials based on self-assembling organogels: from serendipity towards design", *Angew. Chemie Int. Ed.*, 2000.
- [10] M. Moniruzzaman and P. R. Sundararajan, "Low molecular weight organogels based on long-chain carbamates", *Langmuir*, 2005.
- [11] X. Liu and P. D. Sawant, "Determination of the fractal characteristic of nanofiber-network formation in supramolecular materials", *ChemPhysChem*, 2002.
- [12] R. Wang, X.-Y. Y. Liu, J. Xiong, and J. Li, "Real-time observation of fiber network formation in molecular organogel: supersaturation-dependent microstructure and its related rheological property", *J. Phys. Chem. b*, 2006.
- [13] L. Wang, Y. Jiang, Y. Lin, J. Pang, and X. Y. Liu, "Rheological properties and formation mechanism of DC electric fields induced konjac glucomannan-tungsten gels", *Carbohydr. Polym.*, 2016.

- [14] X. Y. Liu, P. D. Sawant, W. B. Tan, I. B. M. M. Noor, C. Pramesti, and B. H. Chen, “Creating new supramolecular materials by architecture of three-dimensional nanocrystal fiber networks”, *J. Am. Chem. Soc.*, 2002.
- [15] J.-M. Lehn, “Perspectives in supramolecular chemistry: self-assembly in solution”, *J. Mol. Biol.*, 1995.
- [16] Ö. Demir-Ordu, H. Şimşir, and K. Alper, “Synthesis of bis[N-(p-aryl)-carbamoyloxy]alkanes as new low-molecular weight organogelators”, *Tetrahedron*, 2015.
- [17] L. A. Estroff and A. D. Hamilton, “Water gelation by small organic molecules”, *Chem. Rev.*, 2004.
- [18] K. Kim, K. E. Plass, and A. J. Matzger, “Structure of and competitive adsorption in alkyl dicarbamate two-dimensional crystals”, *J. Am. Chem. Soc.*, 2005.
- [19] F. Fages, F. Vögtle, and M. Žinić, “Systematic design of amide-and urea-type gelators with tailored properties”, *Top. Curr. Chem.*, 2005.
- [20] M. Suzuki, Y. Nakajima, M. Yumoto, M. Kimura, H. Shirai, and K. Hanabusa, “Effects of Hydrogen Bonding and van der Waals Interactions on Organogelation Using Designed Low-Molecular-Weight Gelators and Gel Formation at Room Temperature”, *Langmuir*, 2003.
- [21] K. Yabuuchi, E. Marfo-Owusu, and T. Kato, “A new urea gelator: Incorporation of intra- and intermolecular hydrogen bonding for stable 1D self-assembly”, *Org. Biomol. Chem.*, 2003.
- [22] J. Van Esch, R. M. Kellogg, and B. L. Feringa, “Di-urea compounds as gelators for organic solvents”, *Tetrahedron Lett.*, 1997.
- [23] K. Hanabusa, A. Kawakami, M. Kimura, and H. Shirai, “Small molecular gelling agents to harden organic liquids: Trialkyl cis-1,3,5-cyclohexanetricarboxamides”, *Chemistry Letters*, 1997.
- [24] U. Beginn, S. Sheiko, and M. Möller, “Self-organization of 3,4,5-tris(octyloxy)benzamide in solution and embedding of the aggregates into methacrylate resins”, *Macromol. Chem. Phys.*, 2000.
- [25] M. George, S. L. Snyder, P. Terech, C. J. Glinka, and R. G. Weiss, “N-alkyl perfluoroalkanamides as low molecular-mass organogelators”, *J. Am. Chem. Soc.*, 2003.
- [26] K. Hanabusa, M. Yamada, M. Kimura, and H. Shirai, “Prominent gelation and chiral aggregation of alkylamides derived from trans-1, 2-diaminocyclohexane”, *Angew.*

- Chemie Int. Ed. English, 1996.
- [27] J. G. Hardy, A. R. Hirst, and D. K. Smith, "Exploring molecular recognition pathways in one- and two-component gels formed by dendritic lysine-based gelators", *Soft Matter*, 2012.
 - [28] Y. Zhang and S. Jiang, "Fluoride-responsive gelator and colorimetric sensor based on simple and easy-to-prepare cyano-substituted amide", *Org. Biomol. Chem.*, 2012.
 - [29] N. Zweep, A. Hopkinson, A. Meetsma, W. R. Browne, B. L. Feringa, and J. H. van Esch, "Balancing hydrogen bonding and van der Waals interactions in cyclohexane-based bisamide and bisurea organogelators", *Langmuir*, 2009.
 - [30] C.-C. Tsou and S.-S. Sun, "New fluorescent amide-functionalized phenylethynylthiophene low molecular weight gelator", *Org. Lett.*, 2006.
 - [31] K. Hanabusa and M. Suzuki, "Physical gelation by low-molecular-weight compounds and development of gelators", *Bull. Chem. Soc. Jpn.*, 2016.
 - [32] N. Goyal, S. Cheuk, and G. Wang, "Synthesis and characterization of d-glucosamine-derived low molecular weight gelators", *Tetrahedron*, 2010.
 - [33] K. H. Kim, Y. G. Kim, and Y. Kwon, "The improvement of surface energy of bpda-eda polyimide by controlling molecular-level structure", *Mol. Cryst. Liq. Cryst.*, 2009.
 - [34] K. Hanabusa, C. Koto, M. Kimura, H. Shirai, and A. Kakehi, "Remarkable viscoelasticity of organic solvents containing trialkyl-1, 3, 5-benzenetricarboxamides and their intermolecular hydrogen bonding", *Chem. Lett.*, 1997.
 - [35] Y. Yasuda, Y. Takebe, M. Fukumoto, Y. Shirota, H. Inada, and Y. Shirota, "4, 4', 4 "-Tris (stearoylamo) triphenylamine as a novel material for functional molecular gels", *Adv. Mater.*, 1996.
 - [36] D. S. Tsekova, B. Escuder, and J. F. Miravet, "Solid-state polymorphic transition and solvent-free self-assembly in the growth of organic crystalline microfibers", *Cryst. Growth Des.*, 2008.
 - [37] K. Tomioka et al., "Molecular assembly and gelating behavior of didodecanoylamides of α , ω -alkylidenediamines", *J. Am. Chem. Soc.*, 2001.
 - [38] V. Kocasoy, B. Dedeoglu, O. Demir-Ordu, and V. Aviyente, "Influence of odd-even effect and intermolecular interactions in 2D molecular layers of bisamide organogelators", *RSC Adv.*, 2018.
 - [39] T. Sumiyoshi, K. Nishimura, M. Nakano, T. Handa, Y. Miwa, and K. Tomioka, "Molecular Assembly of C 2-Symmetric Bis-(2 S)-2-methyldodecanoylamides of α , ω -Alkylidenediamines into Coiled Coil and Twisted Ribbon Aggregates", *J. Am. Chem.*

- Soc., 2003.
- [40] H. D. Burrows, "Studying odd-even effects and solubility behavior using α [alpha], ω [omega]-dicarboxylic acids", *J. Chem. Educ.*, 1992.
 - [41] A. R. Hirst et al., "Low-molecular-weight gelators: elucidating the principles of gelation based on gelator solubility and a cooperative self-assembly model", *J. Am. Chem. Soc.*, 2008.
 - [42] J. F. Toro-Vazquez, J. Morales-Rueda, A. Torres-Martínez, M. A. Charó-Alonso, V. A. Mallia, and R. G. Weiss, "Cooling rate effects on the microstructure, solid content, and rheological properties of organogels of amides derived from stearic and (R)-12-hydroxystearic acid in vegetable oil", *Langmuir*, 2013.
 - [43] E. Ghanbari, S. J. Picken, and J. Van Esch, "Analysis of differential scanning calorimetry (DSC): Determining the transition temperatures , enthalpy and heat capacity changes in multicomponent systems by analytical model fitting", *J. Therm. Anal. Calorim.*, 2023.
 - [44] B. H. Toby and R. B. Von Dreele, "GSAS-II: The genesis of a modern open-source all purpose crystallography software package", *J. Appl. Crystallogr.*, 2013.
 - [45] K. D. Poopalam, L. Raghunanan, L. Bouzidi, S. K. Yeong, and S. S. Narine, "Solar Energy Materials and Solar Cells The anomalous behavior of aliphatic fatty diamides : Chain length and hydrogen bonding interactions", *Solar Energy Materials* , 2019.
 - [46] J. B. Williams, K. S. Geick, and J. A. Falter, "Structure/performance characteristics of bisamide lubricants in ABS", *J. Vinyl Addit. Technol.*, 1997.
 - [47] M. Raimo, "Kinetics of phase transformation of indium in the presence of polytetrafluoroethylene: implications for DSC measurements on polymers and their composites", *Int. J. Polym. Sci.*, 2015.
 - [48] D. W. W. Van Krevelen and K. Te Nijenhuis, "Polymer properties", *Prop. Polym.*, 1990.
 - [49] H. D. Burrows, "Studying odd-even effects and solubility behavior using α,ω -dicarboxylic acids", *Journol Chem. Educ.*, 1992.
 - [50] S. Kavesh and J. M. Schultz, "Lamellar and interlamellar structure in melt-crystallized polyethylene. I. Degree of crystallinity, atomic positions, particle size, and lattice disorder of the first and second kinds", *J. Polym. Sci. Part A-2 Polym. Phys.*, 1970.
 - [51] C. W. Bunn, E. V Garner, and W. L. Bragg, "The crystal structures of two polyamides ('nylons')", *Proc. R. Soc. London. Ser. A. Math. Phys. Sci.*, 1947.

3.6 Supplementary Information

Full details of the NMR spectra of the whole series of nBA compounds, the X-ray structure determination and X-ray crystallographic data are presented in this section.

3.6.1 Preparation of bisamide gelators

The resulting solid nBA compounds from the synthesis (described in the main text) were ground and recrystallized in ethanol (33 g.L^{-1}) which yielded yellowish white compounds. The melting points were measured by melting point apparatus and DSC, using the PYRIS analyzer software and $\text{DSC}_N(T)$ model as shown in the Table S3.1. The melting transition is already starting for the smaller crystals considerably earlier than the temperature identified as the melting point using the capillary because the melting point apparatus does not detect the melting point but it detects the point at which a substantial part of the sample has turned into a fluid, which is assessed by a visual observation. Therefore, the melting point measured by the capillary is only able to detect the final stage of melting phenomenon while by DSC the onset of melting can be detected as soon as the melting starts. However, the melting point obtained using a DSC analyzer software is inaccurate due to the asymmetric peak shape for nBA compounds, so the data from $\text{DSC}_N(T)$ model are more reliable to deduce the precise melting points of the compounds.

Table S3.1 Melting point (T_m) of recrystallized nBA compounds^[a].

nBA compounds	Yield (%)	T_m (°C) measured by melting apparatus	T_m (°C) measured by DSC	T_m (°C) obtained from the $\text{DSC}_N(T)$ model
5BA	91	132±1	135±1	135.49 ±0.00
6BA	89	143±1	147±1	147.46 ±0.00
7BA	86	132±1	135±1	135.97 ±0.00
8BA	83	140±1	143±1	143.53 ±0.00
9BA	94	129±1	134±1	132.50 ±0.00
10BA	85	138±1	141±1	139.60 ±0.00

[a] The melting points were measured by melting point apparatus (MP apparatus) and DSC (the errors are experimental errors for the melting points measured by melting apparatus and from DSC measurements and obtained by Pyris software while the melting points obtained from $\text{DSC}_N(T)$ model are the errors from the fitting residuals).

Table S3.2 Fitted parameters of the DSC_N(T) for experimental curves of 6±1 mg of odd and even nBA compounds heated at 10 K.min⁻¹ after calibration at the onset for the given weight and rate (the error margins are errors from the nonlinear fitting, excluding errors from the instrument calibration).

gelators	5BA	6BA	7BA	8BA	9BA	10BA
ΔH (J.g ⁻¹)	126.18±0.04	168.66±0.07	140.88±0.09	155.12±0.12	149.21±0.08	172.20±0.06
T _m ° (°C)	135.49±0.00	147.46±0.00	135.97±0.00	143.53±0.00	132.50±0.00	142.11±0.00
α (K ⁻¹)	0.39±0.00	0.63±0.00	0.52±0.00	0.31±0.00	0.52±0.00	0.48±0.00
β (K ⁻²)	3.01±0.04	1.19±0.02	1.50±0.03	1.69±0.04	2.68±0.05	1.40±0.02
$\Delta C_{p,m}$ (W.g ⁻¹ .K ⁻¹)	-0.44±0.01	-0.31±0.01	-0.40±0.01	-0.28±0.01	-0.35±0.01	-0.29±0.01
B (W.g ⁻¹)	1.12±0.00	1.12±0.01	1.04±0.01	0.94±0.01	1.07±0.01	1.19±0.01
C (W.g ⁻¹ .K ⁻¹)	0.00±0.00	0.00±0.00	0.00±0.00	0.00±0.00	0.00±0.00	0.01±0.00
D (W.g ⁻¹ .K ⁻²)	0.00±0.00	0.00±0.00	0.00±0.00	0.00±0.00	0.00±0.00	0.00±0.00
R ²	0.99	0.99	0.99	0.99	0.99	0.99

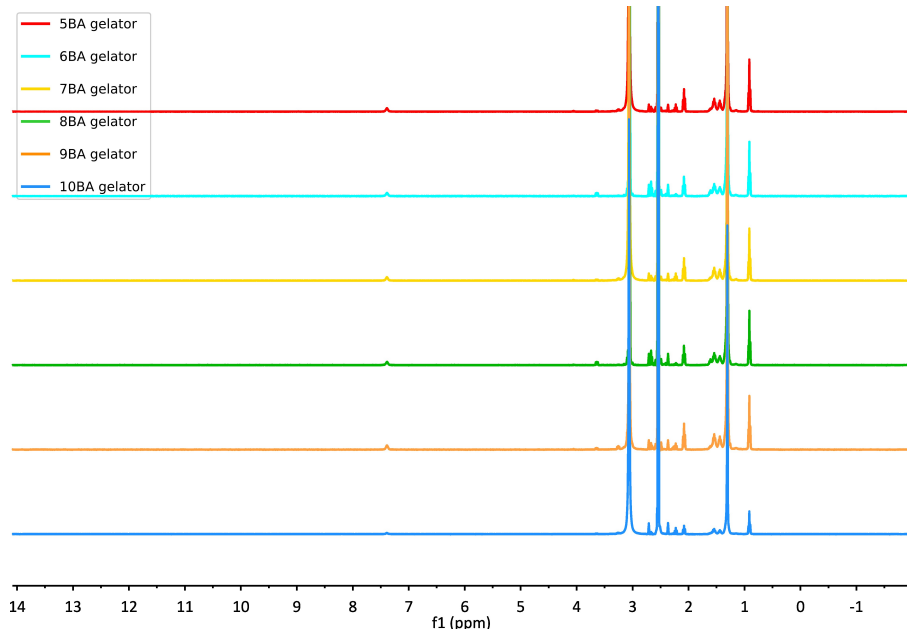
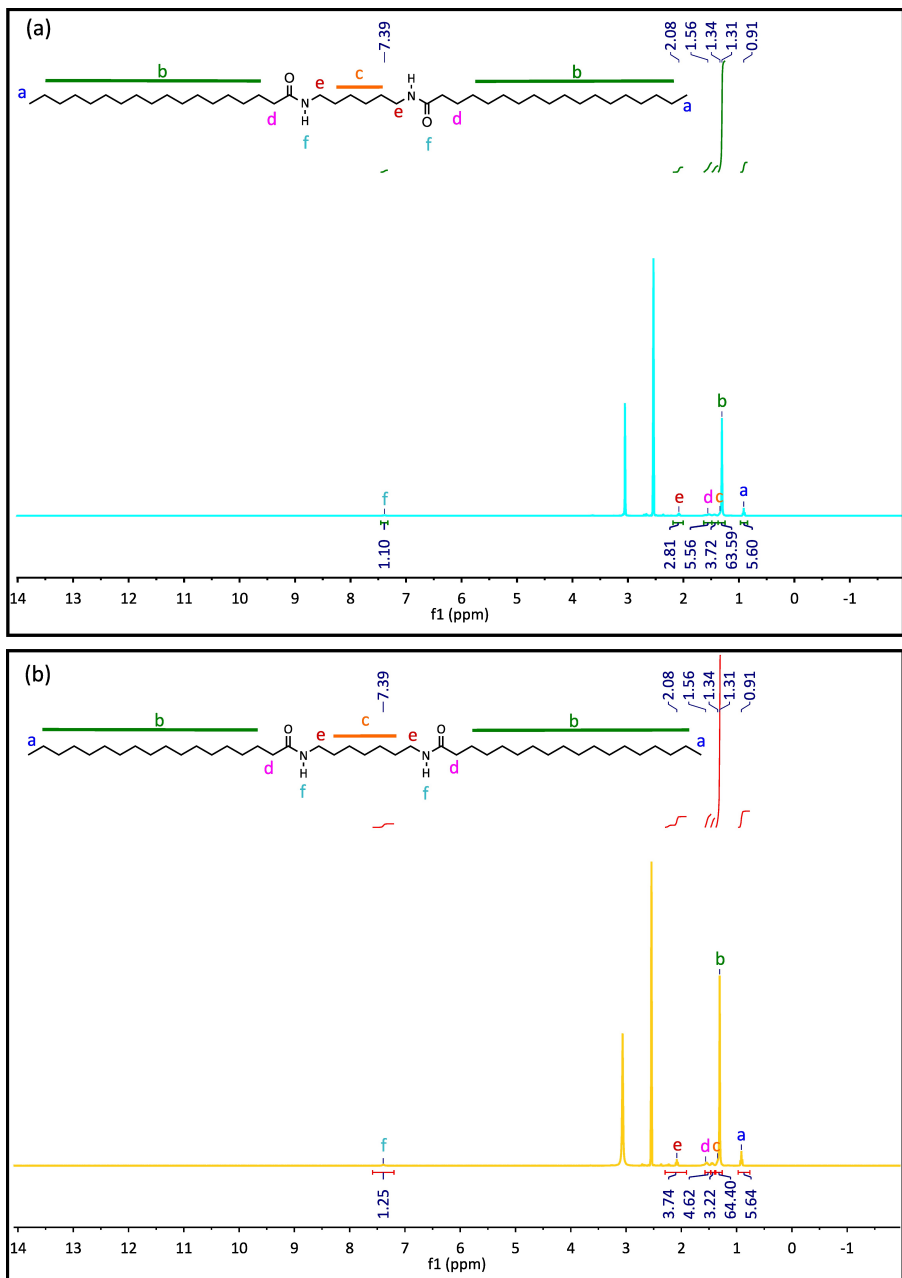


Figure S3.1 NMR spectra of nBA compounds in DMSO-d₆ (5 wt%) at 80 °C where DMSO signal on the spectra is at 2.5 ppm and water is at 3.3 ppm ^[a].



[a] The zoomed-in subsets are: a) 6BA representing even series, b) 7BA representing odd series.

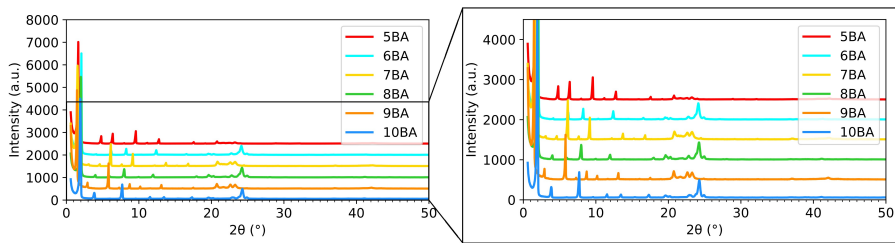


Figure S3.2 XRD patterns of synthesized nBA compounds (curves were normalized to the highest intensity and shifted vertically for clarity).

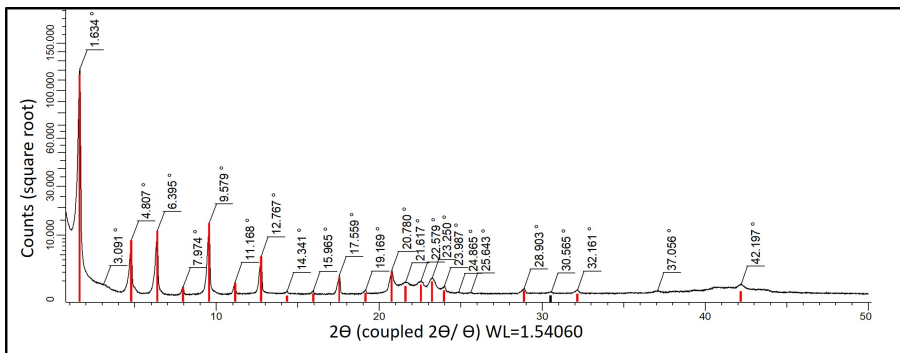


Figure S3.3 Observed 2θ positions of the XRD diffraction pattern of 5BA.

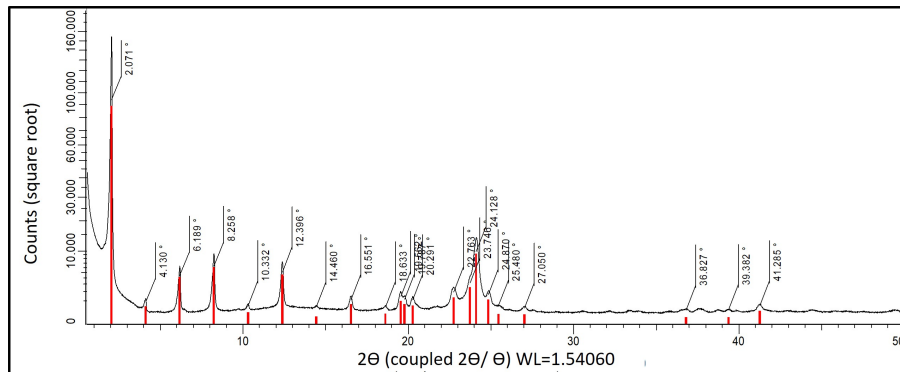


Figure S3.4 Observed 2θ positions of the XRD diffraction pattern of 6BA.

3.6.2 Crystal structure of odd BAs

The peak at $2\theta=42.20^\circ$ (Figure 3.7) is invariant within the odd series, although 5BA indexing shows that it has a very high l index (Table 3.3). For 5BA the latter peak is

indexed as $(-2\ 0\ 23)$ and $(2\ 0\ 22)$. Figure S3.5 shows the $(-2\ 0\ 23)$ planes, suitably shifted and all atoms in the unit cell are located in the $(-2\ 0\ 23)$ planes (to good approximation). Therefore the diffracted X-rays from these planes are all (nearly) in phase, which explains why the $(-2\ 0\ 23)$ reflection is relatively strong. A similar figure applies to 7BA, but with the $(-2\ 0\ 23)$ planes replaced by the $(-2\ 0\ 24)$ planes, since the 7BA spacer has two extra CH_2 groups, i.e. one extra zig-zag. Likewise, a similar figure also applies for 9BA, with two extra zig-zags and therefore with the $(-2\ 0\ 23)$ planes replaced by the $(-2\ 0\ 25)$ planes. Clearly, with increasing the odd spacer length, the crystal structure remains the same, except for a c -axis length increase by one or two zig-zags, then the indexing of the 42.20° peak will change from $(-2\ 0\ 23)$ (5BA) to $(-2\ 0\ 24)$ for 7BA and $(-2\ 0\ 25)$ for 9BA, in order to accommodate the extra CH_2 groups, while the spacings of these reflections remains the same. Therefore, the position of the $42.20^\circ(2\theta)$ peak will be invariant within the odd series.

3

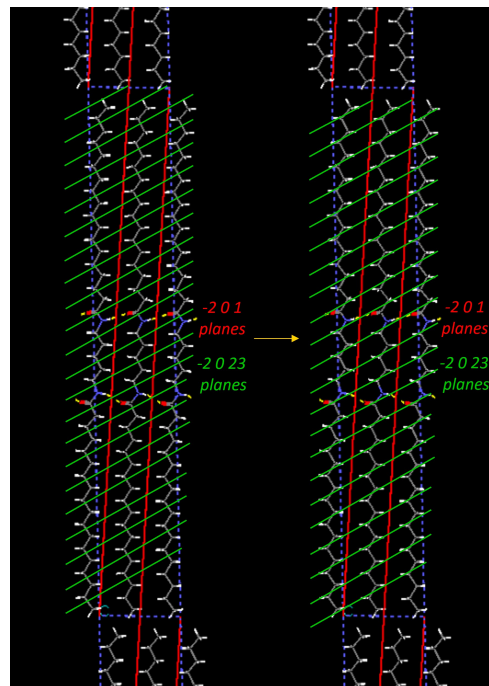


Figure S3.5 Crystal structure of 5BA showing the $(-2\ 0\ 23)$ planes suitably shifted (which is allowed, since the origin of the unit cell is arbitrary).

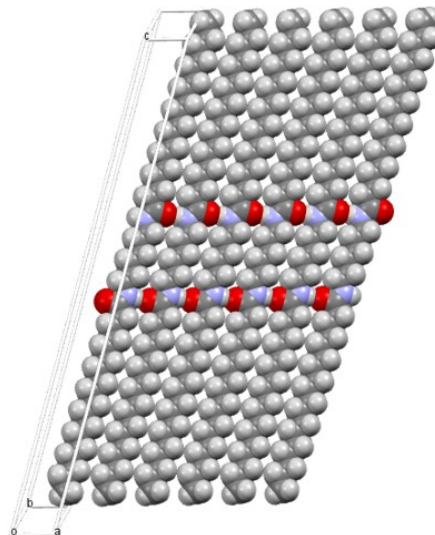


Figure S3.6 Sheet-like H-bonding between 6BA molecules along the (010) planes in the stacked layers.

Table S3.3 Fractional atomic coordinates of 5BA (1D-H bonding model).

Atom	x	y	z
C1	0.3123	0.5215	0.0888
C2	0.8116	0.0230	0.0886
H3	0.3114	0.4521	1.0038
H4	0.8120	-0.0501	1.0035
C5	0.3972	0.5725	0.0653
C6	0.8978	0.0684	0.0651
C7	0.2983	0.4743	0.0429
C8	0.7983	-0.0261	0.0426
C9	-0.1145	0.0216	0.0193
C10	0.3844	0.5266	0.0195
C11	0.4122	0.6168	0.1112
C12	0.9126	0.1119	0.1110
C13	0.4460	0.6914	0.2032
C14	0.9467	0.1758	0.2030
C15	0.3275	0.5667	0.1348
C16	0.8260	0.0719	0.1345
C17	0.4655	0.7058	0.2492
C18	0.9660	0.1789	0.2490
C19	0.4884	0.6832	0.2952
C20	0.9879	0.1470	0.2948
C21	0.4284	0.6580	0.1572
C22	0.9289	0.1498	0.1570
C23	0.3436	0.6092	0.1807
C24	0.8410	0.1203	0.1804
C25	0.3796	0.6582	0.2727
C26	0.8782	0.1739	0.2725
C27	0.3606	0.6436	0.2267
C28	0.8578	0.1601	0.2264
O29	0.3280	0.4888	0.4107
O30	0.8345	1.0110	0.4111
C31	0.4596	0.4003	0.4079
C32	0.9610	0.9010	0.4079
C33	0.5655	0.2267	0.4699
C34	1.0648	0.7298	0.4698
C35	0.4360	0.5494	0.3645
C36	0.9373	0.0487	0.3644
C37	0.4037	0.6336	0.3188
C38	0.9043	0.1418	0.3187

C39	0.4683	0.1446	0.4470
C40	0.9659	-0.3531	0.4471
N41	0.5398	0.2462	0.4249
N42	1.0373	-0.2623	0.4247
C43	0.5170	0.6026	0.3406
C44	1.0153	0.0683	0.3400
C45	0.5502	0.4549	0.3848
C46	1.0488	-0.0677	0.3843
C47	0.4826	0.1294	0.4928
C48	0.9823	0.6349	0.4929
O49	0.3711	0.4562	0.5755
O50	0.8714	-0.0423	0.5755
C51	-0.0001	-0.1514	0.5785
C52	0.4996	0.3474	0.5785
C53	0.0753	0.7110	0.5163
C54	0.5748	0.2075	0.5163
C55	0.0006	0.9949	0.6221
C56	0.5006	0.4948	0.6220
C57	-0.0047	1.0913	0.6679
C58	0.4953	0.5916	0.6679
C59	0.4868	0.1072	0.5387
C60	0.9873	0.6100	0.5386
N61	0.0683	0.6906	0.5613
N62	0.5679	0.1888	0.5613
C63	0.0899	0.9938	0.6465
C64	0.5899	0.4941	0.6464
C65	0.1000	0.8740	0.6020
C66	0.5998	0.3736	0.6020
C67	0.1637	1.0201	0.8747
C68	0.6638	0.5201	0.8747
C69	0.1138	1.0722	0.7831
C70	0.6137	0.5727	0.7831
C71	0.0601	1.1080	0.8528
C72	0.5602	0.6080	0.8528
C73	0.0965	1.0756	0.7374
C74	0.5964	0.5763	0.7374
C75	0.0881	1.0540	0.6918
C76	0.5881	0.5545	0.6917
C77	0.1372	1.0519	0.8289
C78	0.6372	0.5521	0.8289
C79	0.0349	1.1360	0.8068
C80	0.5348	0.6362	0.8068

C81	0.0000	1.1377	0.7142
C82	0.4999	0.6381	0.7142
C83	0.0140	1.1487	0.7606
C84	0.5138	0.6491	0.7606
C85	0.0868	1.0699	0.8987
C86	0.5870	0.5698	0.8987
H87	0.1612	0.9599	0.9832
H88	0.6616	0.4590	0.9832
C89	0.1908	0.9801	0.9205
C90	0.6910	0.4799	0.9205
C91	0.1138	1.0241	0.9446
C92	0.6141	0.5237	0.9446
C93	0.2192	0.9316	0.9660
C94	0.7195	0.4308	0.9660
H95	0.2036	0.6515	0.0883
H96	0.7054	0.1601	0.0880
H97	0.2762	0.2769	0.0903
H98	0.7715	0.7806	0.0900
H99	-0.0639	0.3117	0.0635
H100	0.4324	0.8175	0.0637
H101	0.0052	0.9347	0.0658
H102	0.5064	0.4442	0.0659
H103	0.2634	0.2292	0.0444
H104	0.7607	0.7302	0.0442
H105	0.1890	0.6020	0.0422
H106	0.6905	0.1065	0.0418
H107	-0.0078	0.8870	0.0195
H108	0.4927	0.3969	0.0196
H109	-0.0796	0.2649	0.0170
H110	0.4166	0.7712	0.0172
H111	0.0177	0.9715	0.1117
H112	0.5206	0.4861	0.1118
H113	-0.0453	0.3530	0.1094
H114	0.4487	0.8612	0.1097
H115	0.0384	1.0033	0.2035
H116	0.5508	0.5502	0.2035
H117	0.0077	0.4021	0.2017
H118	0.4884	0.9328	0.2020
H119	0.2198	0.6994	0.1343
H120	0.7230	0.2182	0.1340
H121	0.2899	0.3227	0.1362
H122	0.7805	0.8326	0.1358

H123	0.0412	0.3892	0.2484
H124	0.5152	0.9426	0.2487
H125	0.0449	0.9837	0.2489
H126	0.5654	0.5520	0.2491
H127	0.0529	0.9337	0.2932
H128	0.5793	0.5107	0.2939
H129	0.0759	0.3380	0.2950
H130	0.5499	0.9098	0.2957
H131	0.0293	0.9970	0.1577
H132	0.5356	0.5237	0.1576
H133	-0.0218	0.3861	0.1554
H134	0.4669	0.9014	0.1557
H135	0.3027	0.3669	0.1819
H136	0.7853	0.8888	0.1815
H137	0.2379	0.7478	0.1805
H138	0.7453	0.2841	0.1801
H139	0.2866	0.8267	0.2738
H140	0.8100	0.3833	0.2738
H141	0.3206	0.4289	0.2724
H142	0.7930	0.9780	0.2723
H143	0.2593	0.7936	0.2268
H144	0.7744	0.3476	0.2266
H145	0.3130	0.4052	0.2274
H146	0.7874	0.9434	0.2269
H147	0.0911	-0.0208	0.4701
H148	0.5906	0.4765	0.4703
H149	0.1782	0.6176	0.4692
H150	0.6797	0.1169	0.4694
H151	0.3764	0.7595	0.3694
H152	0.8945	0.2758	0.3692
H153	0.3450	0.3654	0.3619
H154	0.8344	0.8895	0.3627
H155	0.3251	0.8247	0.3216
H156	0.8504	0.3647	0.3216
H157	0.3289	0.4227	0.3173
H158	0.8079	0.9669	0.3178
H159	0.4455	-0.1063	0.4464
H160	0.9403	0.3968	0.4469
H161	0.3528	0.2472	0.4481
H162	0.8516	-0.2452	0.4481
H163	0.1393	-0.3581	0.4207
H164	0.6457	0.1650	0.4211

H165	0.1123	0.2417	0.3411
H166	0.5946	0.8093	0.3422
H167	0.0684	0.8461	0.3365
H168	0.5929	0.4081	0.3373
H169	0.1506	0.0919	0.3869
H170	0.6415	0.6358	0.3881
H171	0.0931	0.7096	0.3787
H172	0.6088	0.2463	0.3792
H173	0.3683	0.2399	0.4930
H174	0.8686	-0.2525	0.4931
H175	0.4567	-0.1204	0.4922
H176	0.9552	0.3855	0.4922
H177	0.1892	0.5996	0.5163
H178	0.6890	0.0974	0.5164
H179	0.1013	-0.0398	0.5173
H180	0.6001	0.4570	0.5172
H181	0.3938	0.3473	0.6233
H182	0.8938	0.8475	0.6233
H183	0.4627	0.7284	0.6177
H184	0.9628	0.2286	0.6178
H185	-0.0392	0.3315	0.6656
H186	0.4607	0.8317	0.6656
H187	0.3859	0.4506	0.6683
H188	0.8858	0.9505	0.6683
H189	0.3710	0.2108	0.5381
H190	0.8715	-0.2861	0.5381
H191	0.4637	-0.1436	0.5380
H192	0.9640	0.3593	0.5379
H193	0.1728	0.5960	0.5651
H194	0.6725	0.0948	0.5651
H195	0.1311	0.7597	0.6499
H196	0.6312	0.2601	0.6498
H197	0.1958	0.1443	0.6455
H198	0.6957	0.6447	0.6455
H199	0.1439	0.6480	0.6074
H200	0.6440	0.1480	0.6074
H201	0.2026	0.0284	0.5994
H202	0.7024	0.5283	0.5993
H203	0.1939	0.7767	0.8731
H204	0.6940	0.2768	0.8731
H205	0.2753	0.1547	0.8745
H206	0.7753	0.6548	0.8744

H207	0.2260	0.2043	0.7828
H208	0.7259	0.7051	0.7828
H209	0.1430	0.8276	0.7825
H210	0.6431	0.3281	0.7825
H211	0.4481	0.4752	0.8532
H212	0.9481	0.9752	0.8532
H213	0.5312	0.8521	0.8542
H214	1.0311	0.3520	0.8542
H215	0.1274	0.8316	0.7377
H216	0.6275	0.3324	0.7376
H217	0.2081	0.2098	0.7371
H218	0.7080	0.7108	0.7371
H219	0.1232	0.8130	0.6933
H220	0.6233	0.3137	0.6933
H221	0.1976	0.1949	0.6913
H222	0.6975	0.6957	0.6913
H223	0.2492	0.1848	0.8286
H224	0.7492	0.6851	0.8286
H225	0.1666	0.8078	0.8277
H226	0.6666	0.3080	0.8277
H227	0.5065	0.8810	0.8077
H228	1.0067	0.3809	0.8077
H229	0.4224	0.5049	0.8072
H230	0.9224	1.0049	0.8072
H231	0.3884	0.5036	0.7144
H232	0.8884	1.0035	0.7145
H233	-0.0304	0.3815	0.7135
H234	0.4693	0.8819	0.7134
H235	0.4014	0.5178	0.7609
H236	0.9014	1.0177	0.7609
H237	0.4853	0.8940	0.7608
H238	0.9855	0.3937	0.7608
H239	0.5568	0.8129	0.9004
H240	1.0566	0.3130	0.9004
H241	0.4755	0.4349	0.8989
H242	0.9754	0.9349	0.8989
H243	0.2221	0.7377	0.9187
H244	0.7223	0.2375	0.9186
H245	0.3017	0.1169	0.9204
H246	0.8020	0.6166	0.9204
H247	0.5829	0.7657	0.9466
H248	1.0826	0.2661	0.9466

H249	0.5033	0.3867	0.9447
H250	1.0031	0.8870	0.9447
H251	0.3287	0.0721	0.9669
H252	0.8290	0.5713	0.9668
H253	0.2505	0.6895	0.9645
H254	0.7508	0.1888	0.9645

Table S3.4 Fractional atomic coordinates of 5BA (2D-H bonding model).

unit cell: $a = 8.55$ (Å) $b = 4.36$ (Å) $c = 55.58$ (Å) $\alpha = 90.00$ (°) $\beta = 92.09$ (°) $\gamma = 91.92$ (°)			
C1	0.3088	0.4120	0.0810
C2	0.8088	-0.0880	0.0810
H3	0.3249	0.4140	0.9960
H4	0.8249	-0.0860	0.9960
C5	0.3987	0.4820	0.0582
C6	0.8987	-0.0180	0.0582
C7	0.3044	0.4002	0.0350
C8	0.8044	-0.0998	0.0350
C9	-0.1045	-0.0289	0.0124
C10	0.3955	0.4711	0.0124
C11	0.4020	0.4967	0.1042
C12	0.9020	-0.0033	0.1042
C13	0.4059	0.5107	0.1962
C14	0.9059	0.0107	0.1962
C15	0.3113	0.4248	0.1269
C16	0.8113	-0.0752	0.1269
C17	0.4118	0.5040	0.2421
C18	0.9118	0.0040	0.2421
C19	0.4248	0.4907	0.2879
C20	0.9248	-0.0093	0.2879
C21	0.4037	0.5079	0.1503
C22	0.9037	0.0079	0.1503
C23	0.3130	0.4314	0.1729
C24	0.8130	-0.0686	0.1729
C25	0.3261	0.4165	0.2650
C26	0.8261	-0.0835	0.2650
C27	0.3168	0.4285	0.2189
C28	0.8168	-0.0715	0.2189
O29	0.3021	0.2166	0.4041
O30	0.8021	0.7166	0.4041
C31	0.4307	0.3404	0.4022

C32	0.9308	0.8405	0.4022
C33	0.5890	0.3548	0.4661
C34	1.0890	0.8548	0.4661
C35	0.3822	0.3765	0.3574
C36	0.8822	-0.1235	0.3574
C37	0.3454	0.3985	0.3112
C38	0.8453	-0.1016	0.3112
C39	0.4792	0.2694	0.4446
C40	0.9792	-0.2306	0.4446
N41	0.5292	0.3850	0.4214
N42	1.0292	-0.1151	0.4214
C43	0.4503	0.4748	0.3334
C44	0.9503	-0.0252	0.3334
C45	0.4967	0.4580	0.3784
C46	0.9967	-0.0420	0.3784
C47	0.5189	0.2497	0.4898
C48	1.0189	0.7497	0.4898
O49	0.4182	0.5842	0.5715
O50	0.9182	0.0842	0.5715
C51	0.0467	-0.0239	0.5747
C52	0.5467	0.4761	0.5747
C53	0.1166	0.8322	0.5127
C54	0.6166	0.3322	0.5127
C55	0.0439	1.1312	0.6180
C56	0.5439	0.6312	0.6180
C57	0.0318	1.2334	0.6636
C58	0.5317	0.7334	0.6636
C59	0.5343	0.2247	0.5354
C60	1.0343	0.7248	0.5354
N61	0.1155	0.8133	0.5579
N62	0.6155	0.3133	0.5579
C63	0.1301	1.1351	0.6426
C64	0.6301	0.6351	0.6426
C65	0.1456	1.0079	0.5983
C66	0.6456	0.5079	0.5983
C67	0.1699	1.0803	0.8701
C68	0.6699	0.5802	0.8701
C69	0.1295	1.1842	0.7790
C70	0.6295	0.6842	0.7790
C71	0.0665	1.1771	0.8485
C72	0.5665	0.6771	0.8485
C73	0.1201	1.2064	0.7334

C74	0.6201	0.7064	0.7334
C75	0.1203	1.1955	0.6878
C76	0.6203	0.6955	0.6878
C77	0.1468	1.1401	0.8246
C78	0.6468	0.6401	0.8246
C79	0.0464	1.2326	0.8026
C80	0.5464	0.7326	0.8026
C81	0.0278	1.2748	0.7099
C82	0.5278	0.7748	0.7099
C83	0.0330	1.2691	0.7563
C84	0.5330	0.7691	0.7563
C85	0.0917	1.1091	0.8943
C86	0.5917	0.6091	0.8943
H87	0.1723	0.9432	0.9782
H88	0.6723	0.4432	0.9782
C89	0.1968	1.0079	0.9156
C90	0.6968	0.5079	0.9156
C91	0.1209	1.0320	0.9400
C92	0.6209	0.5321	0.9400
C93	0.2283	0.9255	0.9607
C94	0.7283	0.4255	0.9607
H95	0.1987	0.5375	0.0803
H96	0.6987	0.0375	0.0803
H97	0.2750	0.1655	0.0814
H98	0.7750	0.6655	0.0814
H99	-0.0666	0.2282	0.0579
H100	0.4334	0.7282	0.0579
H101	0.0083	0.8548	0.0588
H102	0.5083	0.3548	0.0588
H103	0.2696	0.1542	0.0352
H104	0.7696	0.6542	0.0352
H105	0.1950	0.5276	0.0344
H106	0.6950	0.0276	0.0344
H107	0.0026	0.8380	0.0122
H108	0.5026	0.3380	0.0122
H109	-0.0699	0.2163	0.0116
H110	0.4301	0.7163	0.0116
H111	0.0123	0.8720	0.1050
H112	0.5123	0.3720	0.1050
H113	-0.0647	0.2435	0.1040
H114	0.4354	0.7435	0.1040
H115	0.0170	0.8886	0.1966

H116	0.5170	0.3886	0.1966
H117	-0.0622	0.2582	0.1965
H118	0.4378	0.7582	0.1965
H119	0.2009	0.5494	0.1262
H120	0.7009	0.0494	0.1262
H121	0.2780	0.1779	0.1271
H122	0.7780	0.6779	0.1271
H123	-0.0571	0.2518	0.2426
H124	0.4429	0.7518	0.2426
H125	0.0233	0.8834	0.2420
H126	0.5233	0.3834	0.2420
H127	0.0369	0.8730	0.2871
H128	0.5369	0.3730	0.2871
H129	-0.0454	0.2390	0.2884
H130	0.4546	0.7390	0.2884
H131	0.0145	0.8848	0.1509
H132	0.5145	0.3848	0.1509
H133	-0.0639	0.2552	0.1502
H134	0.4361	0.7552	0.1502
H135	0.2799	0.1844	0.1728
H136	0.7799	0.6844	0.1728
H137	0.2026	0.5557	0.1723
H138	0.7026	0.0557	0.1723
H139	0.2150	0.5380	0.2654
H140	0.7150	0.0380	0.2654
H141	0.2946	0.1689	0.2645
H142	0.7946	0.6689	0.2645
H143	0.2061	0.5519	0.2187
H144	0.7061	0.0519	0.2187
H145	0.2842	0.1813	0.2186
H146	0.7842	0.6813	0.2186
H147	0.1107	0.1055	0.4665
H148	0.6107	0.6055	0.4665
H149	0.2036	0.7514	0.4639
H150	0.7036	0.2514	0.4639
H151	0.2700	0.4886	0.3598
H152	0.7700	-0.0114	0.3598
H153	0.3570	0.1266	0.3571
H154	0.8570	0.6266	0.3571
H155	0.2336	0.5162	0.3123
H156	0.7336	0.0162	0.3123
H157	0.3159	0.1500	0.3108

H158	0.8159	0.6500	0.3108
H159	0.4638	0.0169	0.4438
H160	0.9638	0.5169	0.4438
H161	0.3627	0.3598	0.4479
H162	0.8627	-0.1403	0.4479
H163	0.1374	-0.0199	0.4195
H164	0.6374	0.4801	0.4195
H165	-0.0230	0.2243	0.3339
H166	0.4770	0.7243	0.3339
H167	0.0634	0.8634	0.3316
H168	0.5634	0.3634	0.3316
H169	0.0174	0.2090	0.3792
H170	0.5174	0.7090	0.3792
H171	0.1099	0.8537	0.3753
H172	0.6099	0.3538	0.3753
H173	0.4028	0.3512	0.4912
H174	0.9028	-0.1489	0.4912
H175	0.4974	-0.0014	0.4892
H176	0.9974	0.4986	0.4892
H177	0.2323	0.7288	0.5121
H178	0.7323	0.2288	0.5121
H179	0.1382	0.0827	0.5136
H180	0.6382	0.5827	0.5136
H181	0.4373	0.4829	0.6191
H182	0.9373	0.9829	0.6191
H183	0.5059	0.8638	0.6134
H184	1.0060	0.3638	0.6134
H185	-0.0024	0.4736	0.6612
H186	0.4976	0.9736	0.6612
H187	0.4222	0.5925	0.6636
H188	0.9222	1.0925	0.6636
H189	0.4159	0.3171	0.5351
H190	0.9159	-0.1829	0.5351
H191	0.5171	-0.0274	0.5348
H192	1.0171	0.4726	0.5348
H193	0.2203	0.7209	0.5618
H194	0.7203	0.2209	0.5618
H195	0.1718	0.9022	0.6464
H196	0.6718	0.4022	0.6464
H197	0.2357	0.2869	0.6419
H198	0.7356	0.7869	0.6419
H199	0.1903	0.7840	0.6041

H200	0.6903	0.2840	0.6041
H201	0.2478	0.1634	0.5957
H202	0.7478	0.6634	0.5957
H203	0.2033	0.8402	0.8676
H204	0.7033	0.3402	0.8676
H205	0.2798	0.2206	0.8705
H206	0.7798	0.7206	0.8706
H207	0.2409	0.3196	0.7795
H208	0.7409	0.8196	0.7795
H209	0.1607	0.9411	0.7777
H210	0.6607	0.4411	0.7777
H211	0.4561	0.5386	0.8481
H212	0.9561	1.0386	0.8481
H213	0.5343	0.9182	0.8508
H214	1.0343	0.4182	0.8508
H215	0.1520	0.9629	0.7333
H216	0.6520	0.4629	0.7333
H217	0.2313	0.3425	0.7338
H218	0.7313	0.8425	0.7338
H219	0.1560	0.9549	0.6894
H220	0.6560	0.4549	0.6894
H221	0.2296	0.3378	0.6879
H222	0.7296	0.8378	0.6879
H223	0.2574	0.2783	0.8250
H224	0.7574	0.7783	0.8250
H225	0.1793	0.8986	0.8226
H226	0.6793	0.3986	0.8226
H227	0.5157	0.9754	0.8042
H228	1.0157	0.4754	0.8042
H229	0.4350	0.5972	0.8021
H230	0.9350	1.0972	0.8021
H231	0.4160	0.6407	0.7095
H232	0.9160	1.1407	0.7095
H233	-0.0023	0.5188	0.7094
H234	0.4977	1.0188	0.7094
H235	0.4208	0.6363	0.7559
H236	0.9208	1.1362	0.7559
H237	0.5036	1.0134	0.7571
H238	1.0036	0.5134	0.7571
H239	0.5589	0.8491	0.8970
H240	1.0589	0.3491	0.8970
H241	0.4817	0.4693	0.8939

H242	0.9817	0.9693	0.8939
H243	0.2299	0.7684	0.9127
H244	0.7299	0.2684	0.9127
H245	0.3067	0.1481	0.9160
H246	0.8067	0.6481	0.9160
H247	0.5889	0.7715	0.9431
H248	1.0889	0.2715	0.9431
H249	0.5107	0.3930	0.9397
H250	1.0107	0.8930	0.9397
H251	0.3381	0.0647	0.9618
H252	0.8381	0.5647	0.9618
H253	0.2588	0.6846	0.9582
H254	0.7588	0.1846	0.9582

Table S3.5 Fractional atomic coordinates of 6BA.

unit cell: a= 5.02 (Å) b=5.29 (Å) c=57.46 (Å) $\alpha=48.65$ (°) $\beta=76.80$ (°) $\gamma=65.17$ (°)			
Atom	x	y	z
C1	-0.2030	0.0149	0.1029
C2	-0.3744	0.0462	0.1054
C3	-0.1795	-0.0056	0.1074
C4	-0.3480	0.0278	0.1099
C5	-0.1521	-0.0245	0.1119
C6	-0.3210	0.0137	0.1143
C7	-0.1252	-0.0385	0.1164
C8	-0.2950	0.0027	0.1188
C9	-0.0996	-0.0492	0.1209
C10	-0.2698	-0.0064	0.1232
C11	-0.0741	-0.0575	0.1253
C12	-0.2433	-0.0148	0.1277
C13	-0.0465	-0.0640	0.1297
C14	-0.2139	-0.0223	0.1321
C15	-0.0160	-0.0671	0.1341
C16	-0.1810	-0.0270	0.1365
C17	0.0194	-0.0654	0.1385
C18	-0.1632	-0.0255	0.1408
C19	-0.1643	0.0238	0.1447
C20	0.0440	-0.0212	0.1466
C21	-0.1065	0.0212	0.1491
O1	-0.4183	-0.0038	0.1412
N1	-0.0135	-0.0243	0.1425

H1	-0.0238	-0.2517	0.1041
H2	-0.3461	0.0482	0.1015
H3	-0.1046	0.2235	0.1014
H4	-0.4793	-0.1568	0.1068
H5	-0.5540	0.3141	0.1042
H6	-0.0004	-0.2740	0.1086
H7	-0.0735	0.1964	0.1060
H8	-0.4545	-0.1737	0.1113
H9	-0.5267	0.2966	0.1087
H10	0.0255	-0.2942	0.1132
H11	-0.0438	0.1752	0.1105
H12	-0.4981	0.2839	0.1131
H13	-0.4297	-0.1855	0.1158
H14	0.0512	-0.3092	0.1177
H15	-0.0154	0.1596	0.1150
H16	-0.4049	-0.1952	0.1203
H17	-0.4713	0.2736	0.1176
H18	0.0764	-0.3203	0.1221
H19	0.0108	0.1482	0.1194
H20	-0.4458	0.2647	0.1220
H21	-0.3799	-0.2040	0.1247
H22	0.0359	0.1403	0.1238
H23	0.1020	-0.3284	0.1266
H24	-0.4201	0.2556	0.1264
H25	-0.3525	-0.2133	0.1292
H26	0.1309	-0.3340	0.1310
H27	0.0619	0.1353	0.1282
H28	-0.3922	0.2470	0.1309
H29	-0.3210	-0.2229	0.1336
H30	0.0898	0.1349	0.1326
H31	0.1634	-0.3355	0.1353
H32	-0.3619	0.2401	0.1353
H33	-0.2821	-0.2334	0.1381
H34	0.1201	0.1411	0.1369
H35	0.1998	-0.3329	0.1397
H36	0.1923	-0.0213	0.1420
H37	-0.2713	-0.1762	0.1463
H38	-0.3414	0.2940	0.1435
H39	0.1503	0.1794	0.1451
H40	0.2221	-0.2899	0.1478
H41	-0.2852	0.2900	0.1479
H42	-0.2116	-0.1805	0.1507

Chapter 4

Supramolecular arrangement and rheological properties of bisamide gels

Abstract

We report a systematic study of the gelation behavior of nBA gelators in xylene, with odd and even n-methylene spacers between the amide groups (n=5-10) and 17 carbons at each end.

The melting temperature (T_m^0) of nBA gels are obtained from fitting our $DSC_N(T)$ model to the experimental DSC data. The found T_m^0 of nBA gels are about 35°C lower than T_m^0 of the pure nBA gelators. This is reasonably explained by a simple model combining theories of Flory-Huggins and Gibbs free energy of melting (FHM model). We attribute this depression to an increase in entropy upon melting of the gel due to mixing with the solvent.

The odd-even alternation in T_m^0 of nBA gels, which was also found for the nBA gelators, indicates the solid structures inside the gels are somewhat similar. This was studied using XRD: similar $00l$ reflections were found in the XRD patterns of all nBA gels and their nBA gelators. For even nBA gels, the same reflections in the 19-25° (2θ) region confirms that the sheet-like supramolecular structure of the gels is analogous to the lamellar structure of the solid gelators. For odd nBA gels, a slight difference in the reflections around 20-25° (2θ) implies a somewhat different side-by-side packing of odd nBA gels compared to the solid state. This variation is found for all the odd gels, and indeed they show distinctly different morphologies compared to the even nBA gels. The possible effect of this on the rheological properties is discussed using some inspiration from the Halpin-Tsai model for composites where nBA gels are considered to be analogous to composite materials. The change of the storage modulus (G') with the shape factor of woven fibers and

sheets in nBA gels (20wt%) indicates a rheological odd-even effect might indeed be present.

4.1 Introduction

Low molecular weight gelators (LMWGs) are small organic compounds (molecular weight ≤ 3000 Da)¹ which can transform different types of organic liquids into solid-like viscoelastic gels²⁻⁷. In recent years, such gel systems have found many potential applications in a variety of fields⁸⁻¹¹ such as biomedicine¹²⁻¹⁸, cosmetics, and food industry¹⁹⁻²¹. LMWGs can form physical gels via specific non-covalent intermolecular interactions such as hydrogen bonding, Van der Waals, π - π stacking etc.²²⁻²⁴ and, hence, the gel formation is reversible, which makes this type of gelators an excellent subject for studies into supra-molecular chemistry²⁵.

Thermally triggered LMWG gels usually form via dissolution in a suitable solvent to obtain sol and cooling to a certain temperature where the sol-to-gel transition occurs²⁶⁻²⁸. In fact, heating to elevated temperatures assists overcoming intermolecular interaction forces among the gelator molecules in the crystalline solid state and dissolution of the gelators leading to the sol formation. Upon cooling to below the gel transition temperature, molecules reassemble into a (new) crystalline state at a lower free energy²⁹⁻³¹. The assembly of gelator molecules into an interconnected solid-like three-dimensional (3D) network can immobilize the organic solvent which results in the formation of a strong or weak gel depending on the gelator-gelator interactions as well as the solvent properties³²⁻³⁴.

Due to a large structural diversity, gelators cannot be categorized into a single group representing their abilities to form a gel. However, some features such as anisotropy in intermolecular interactions between the LMWGs is known as the driving force for their unidirectional assembly. As a result, they form fibers with large aspect ratios (length to cross-sectional diameter) which are able to efficiently immobilize a large quantity of the solvent due to surface tension^{35,36}. A general requirement for a gel regardless of the solvent and gelator chemistry and their specific applications is the stability of the network on the time scale of observation, showing solid-like rheological properties³².

The production of a gel with desirable rheological properties for a certain application necessitates a good understanding of how rheological properties are governed by the microstructure and network properties³⁷. There is a need for a comparative study of molecular arrangement of gelators in the solid and

supramolecular assembly of molecules in the gel state which can probe the link between the microscopic interactions between the constituent crystals of the gel network and the rheological properties of gels^{38,39}. Moreover, the formation of LMWG gels has been usually studied at relatively low mass fractions of LMWGs. A clear fundamental understanding of the physical properties of these gels at higher concentrations and how this impacts their rheological properties can provide essential information for potential applications and the optimization of the production processes.

For this purpose, LMWGs that contain amide groups are among the best candidates to be studied. They have the most effective structural units for the formation of supramolecular gels due to their thermodynamically-favored directional hydrogen bonding in a variety of solvents⁴⁰. Recently, in our research group, model bisamide gelators (nBAs) with the simplest structure were synthesized: linear aliphatic bisamides with two symmetric C17 alkyl tails, where the $(CH_2)_n$ spacer connecting the two amide groups was systematically varied from $n = 5$ to 10, see Figure 4.1. These were studied so as to determine their molecular arrangement and thermal properties in the solid state⁴¹, and to compare the corresponding gels state as we report here. Here, in this study, the effect of the spatial arrangement of amide groups on the supramolecular arrangement in the gel state and its influence on the microstructure and rheological properties is the topic of interest. The similarities and differences in molecular and supramolecular arrangement of the nBA gelators were investigated using calorimetry and X-ray diffraction. The differences in thermal properties of gels compared to the solid gelator state can be reasonably well explained by our Flory Huggins-melting (FHM) model, as described here. Finally, the implication of the odd-even effect on the microstructure and rheological properties of nBA gels is discussed using some inspiration from the Halpin-Tsai model.

4.2 Materials and methods

4.2.1 Materials

Xylene ($(CH_3)_2C_6H_4$, analytical reagent grade, CAS:1330-20-7, purchased from Fisher Scientific) and a series of bisamide compounds (nBA) where n is the spacer length between amide groups (varying from 5 to 10) with 17 carbons at each side of the amide groups (C17) were used. The synthesis and characterization of the nBA gelators have been described in chapter 3⁴¹. The general chemical structure of nBA compounds is shown in Figure 4.1, using 5BA as an example:

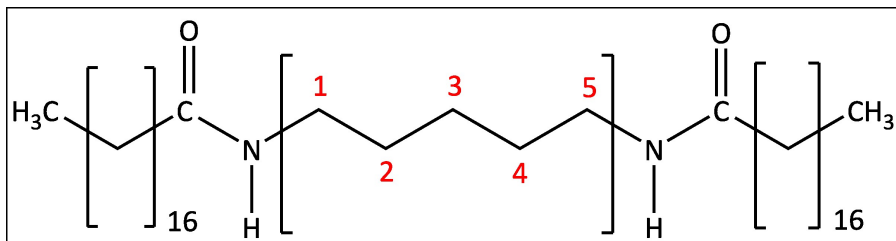


Figure 4.1 Chemical structure of synthesized nBAs with $(CH_2)_n$ spacer between the amide groups and with C17 alkyl tails ($n = 5$ in this example).

4.2.2 Gel preparation

A certain amount of the synthesized nBA gelator was ground, weighed, and dispersed in the required weight of xylene in a vial. The mixture was used to prepare the nBA gel at different concentrations (5 wt%, 10 wt%, 20 wt%, 40 wt%) by mechanical stirring using a magnetic stir bar at 500 rpm and heating up to around 120 °C to dissolve the nBA gelator in the solvent using a heating block. Once the mixture became transparent, the vial was taken out and allowed to cool down to ambient temperature. A tube inversion test was conducted as a quick assessment of the gel formation immediately after cooling down, and after 72 hours.

4

4.2.3 Differential Scanning Calorimetry (DSC)

The thermal behavior of nBA gels was determined using a Perkin Elmer-Pyris Diamond Differential scanning calorimeter with two 1(g)- furnaces (working on the Power-compensation temperature null principle). Nitrogen (99.99% purity) was used to purge the thermal analysis system at the rate of 50 (mL/min). The calibration of temperature and heat flow was done before each measurement using a heating scan of indium, a highly pure metal provided by Perkin Elmer with accurately known enthalpy of fusion and melting point, $\Delta H_{\text{fusion}} = 28.47 \text{ J. g}^{-1}$ and $T_m = 156.4 \text{ }^\circ\text{C}$, under the same condition as the to-be-measured samples. A nBA gel ($8 \pm 1 \text{ mg}$) was placed in a 40 μL stainless steel sample pan by weighing on a microbalance. The sample pan and a reference pan (identical in terms of geometry and weight), both covered by stainless steel lids, were placed in the furnaces of the DSC apparatus. Both the pans were heated to 130 °C, cooled to 25 °C, and subsequently followed the same heating cycle at a constant rate of 5 K.min⁻¹. The samples were kept isothermally for 2 minutes at the end of each scan.

4.2.4 $DSC_N(T)$ analytical model and curve fitting

$DSC_N(T)$ function recently developed in our research group was fitted to the DSC traces of nBA gels ⁴¹.

$$DSC_N(T) = \Delta H \cdot \frac{\alpha}{2} \cdot e^{\frac{\alpha^2}{4\beta}} \cdot e^{\alpha(T-T_m^0)} \cdot \operatorname{erfc} \left(\sqrt{\beta} \left(T - T_m^0 + \frac{\alpha}{2\beta} \right) \right) + \Delta C_p(T) + B + C(T - T_m^0) + D(T - T_m^0)^2 \quad \text{Equation 4.1}$$

This model captures the shape of the experimental DSC peaks taking an assumed Arrhenius crystal size distribution, together with instrumental and sample-related Gaussian peak broadening, into account. Relying on $DSC_N(T)$, a much more accurate determination of the equilibrium melting point (T_m^0), enthalpy of fusion, and change in heat capacity of nBA gels has become possible. The non-linear curve fitting of $DSC_N(T)$ to the experimental DSC traces was done using a Python 3 script ⁴¹, and yields optimized values for the following parameters: ΔH (the coefficient of $DSC_N(T)$ function representing the change in enthalpy associated with the phase transition), T_m^0 (the equilibrium temperature of the phase transition), α (the strength of the linearized Arrhenius function ($\alpha = \frac{E_a}{R \cdot (T_m^0)^2}$) describing the crystal size distribution, roughly proportional to the steepness of the rising edge of the peak), β (the parameter in relation to the Gaussian broadening of the peak ($\beta = \frac{1}{2\sigma^2}$), describing the peak broadening in the declining edge of the peak), and $\Delta C_{p,m}$ (the difference between the heat capacity of the pre- and post-transition states). The parameters B, C, and D respectively correct for baseline offset, a linear baseline slope, and a second order baseline curvature.

To assure the accuracy of the thermal properties obtained from DSC measurements, at least three nBA samples with a similar weight were measured under the same condition and the data were analyzed after the normalization per weight of the sample. The standard deviation of the thermal properties, melting temperature, enthalpy of fusion, and heat capacity change, and the other fit parameters were obtained by fitting $DSC_N(T)$ analytical model to the three sets of raw data which contains the experimental error along with the fitting procedure error. The experimental errors for the thermal properties of all nBA samples were less than 1%. The fitting deviation for each parameter was obtained from the residuals of non-linear least squares (NLLS). The reported errors margins of the fit parameters are the residuals of the NLLS rounded to two digits.

4.2.5 X-ray diffraction (XRD)

X-Ray diffraction was used to obtain information on the crystal structure of nBA gels. X-ray diffraction patterns were recorded at room temperature with a Bruker D8 Advance ECO diffractometer in Bragg-Brentano geometry, equipped with a Cu X-ray source ($K_{\alpha 1}=1.54060$ Å and $K_{\alpha 2}=1.54439$ Å) and LYNXEYE-XE-T position sensitive detector. A knife-edge has been used to reduce the background due to the scattering of the primary beam. The patterns were measured from 0.6° to $50^\circ(2\theta)$ with a step size of 0.01° and measuring time of 0.5 s per step. The intensity of reflections was recorded in $\text{counts} \cdot \text{s}^{-1}$ which is then normalized with respect to the reflection with the highest intensity, the reflection of (001). This method of normalization enables us to compare the low-intensity reflections of the gels with their respective reflections of the gelators which have higher intensities.

4.2.6 Scanning Electron Microscopy (SEM)

The microstructure of nBA gels was observed by using a JEOL JSM 6010LA scanning electron microscope. A SEM sample was prepared by taking a small amount of a freshly made gel gently placed on aluminum foil covering a microscope slide. All samples were dried in a VT6025 vacuum oven (Thermo Electron Corporation) for 3 hours at 60°C . This temperature has been chosen safely below the melting point of the gel and its constituents to avoid any morphological change in the samples. Subsequently, the prepared sample was coated with gold particles at 20 mA for 30 s to increase conductivity for better image quality. The images were recorded using the following setting: secondary electron images (SEI) mode, 8 kV, WD10 mm, and SS40 at different magnifications (500x, 1000x, and 2500x). The dimensions of the fibers and sheets in the SEM images from the microstructures of the gels were measured. At least, ten SEM images were collected from different parts of the gel sample to assess its structure and the dimension of crystalline entities more accurately.

4.2.7 Rheology

The rheological properties of the nBA gels were assessed by DISCOVERY HR-3 hybrid rheometer (TA Instrument). The used geometry was 40 mm parallel steel plate Peltier plate steel-999580. The temperature was set at 25°C and the gap was set to 500 μm . The inertia, friction and rotational mapping were calibrated. Zero gap was determined after the calibration of the geometry. Around 1.0 ± 0.2 g of a freshly prepared nBA gel sample was placed evenly on the bottom plate. The upper parallel

plate was lowered to the geometry gap. To avoid solvent evaporation during the measurement, a few drops of xylene was added to the solvent trap covering the gap prior to each measurement. The linear viscoelastic region was found by conducting a strain sweep from 0.001 % to 1 % strain. The strain was set to 0.01 % selected from the linear viscoelastic region. The angular frequency was set from 0.1 rad.s⁻¹ to 100 rad.s⁻¹ and the strain 0.01 % was applied to measure the storage modulus (G'), as a measure of the solid-like, and the loss modulus (G''), as a measure of the liquid-like characteristics of viscoelastic gels. To ensure the reliability and reproducibility of the experiments, three independent samples of each nBA gel were prepared under the same condition and frequency sweep tests were performed on them using the same protocol.

4.3 Results and discussion

The nBA gelators (5BA, 6BA, 7BA, 8BA, 9BA, and 10BA) were dissolved in xylene at different concentrations (5 wt%, 10 wt%, 20 wt%, and 40 wt%) by heating to obtain homogeneous and transparent solution without any clear supramolecular features remaining. After cooling down to the room temperature, gels with more turbid appearance were produced. It was observed that the solubility of the nBA gelators is remarkably low at room temperature which is a common feature among similar low molecular weight gelators ¹. The gelling capacity of the nBA gelators was qualitatively assessed by macroscopic observation of nBA gels upon tube inversion (Figure 4.2). In the odd series, 5BA and 7BA have formed stable gels at all given concentrations while 9BA can only form gel at 20 wt% and 40 wt%. In the even series, 6BA gels were stable at all of the concentrations. Similar to the odd series, upon increasing the spacer length of gelators in the even group, the gelling capacity of the gelators decreases; 8BA and 10BA at low concentrations (5 wt% and 10 wt%) form gels that are less stable against gravity. Screening the macroscopic appearance of the gels after 72 hours did not show disintegration or a change of colour. Further characterizations on the gels, described below, were carried out within 24 hours of gel preparation.

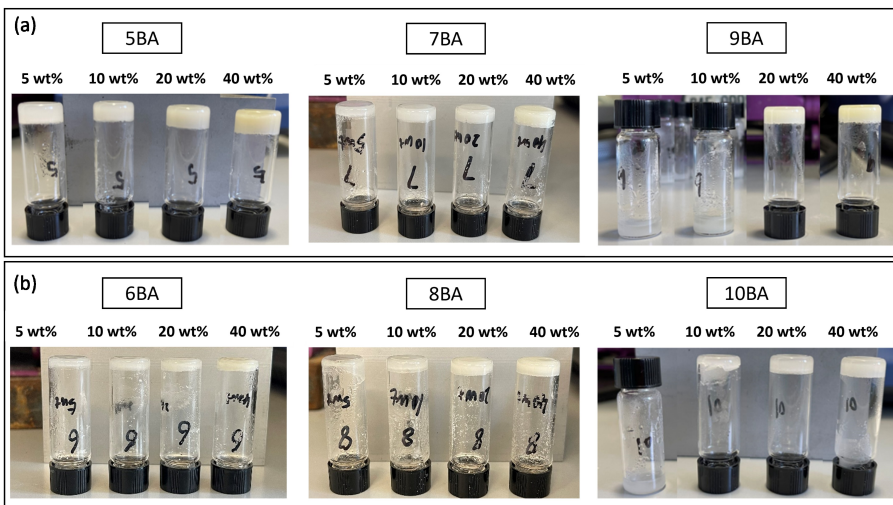


Figure 4.2 nBA gels at different concentrations (wt%) : a) odd nBA gels: 5BA gel, 7BA gel (all gels at different concentrations remain stable against the gravity), 9BA (gels at (5 wt%) and (10 wt%) start to flow as soon as the vial was inverted), b) even nBA gels : 6BA gel (all concentrations remained stable against gravity), 8BA gel (at low concentrations (5 wt% and 10 wt%) partially flowed), 10BA gel (5 wt% gel was too fluidic and could not bear the gravity upon inversion and 10 wt% gel partially flowed).

The nBA gels at 20 wt% were chosen for further analysis mainly because 20 wt% was the lowest concentration where all nBA gelators form stable gels as assessed by the vial inversion test. To identify the phase behavior of nBA gels 20 wt%, DSC measurements were conducted. Figure 4.3a shows a single endothermic transition in the second heating traces of the nBA gels which were heated from 25 °C to 130 °C (the first heating trace of 5BA gel (20 wt%) shows a double peak as seen in Figure S4.1 in supplementary Information section). Compared to the thermogram of the nBA gelators in the solid state (Figure 4.3b and 4.3c), those endothermic transitions can be attributed to the melting of the nBA gels ⁴¹. Similar to the DSC traces of nBA gelators, the DSC_n(T) function fits the second heating traces of all nBA gels (20 wt%) rather well ($R^2 > 0.95$) yielding melting temperature (T_m^0) of the gels as listed in Table 4.1 (Figure S4.2 shows the fit features in more details and all the fit parameters of all nBA gels are available in Table S4.1, in the supplementary information section).

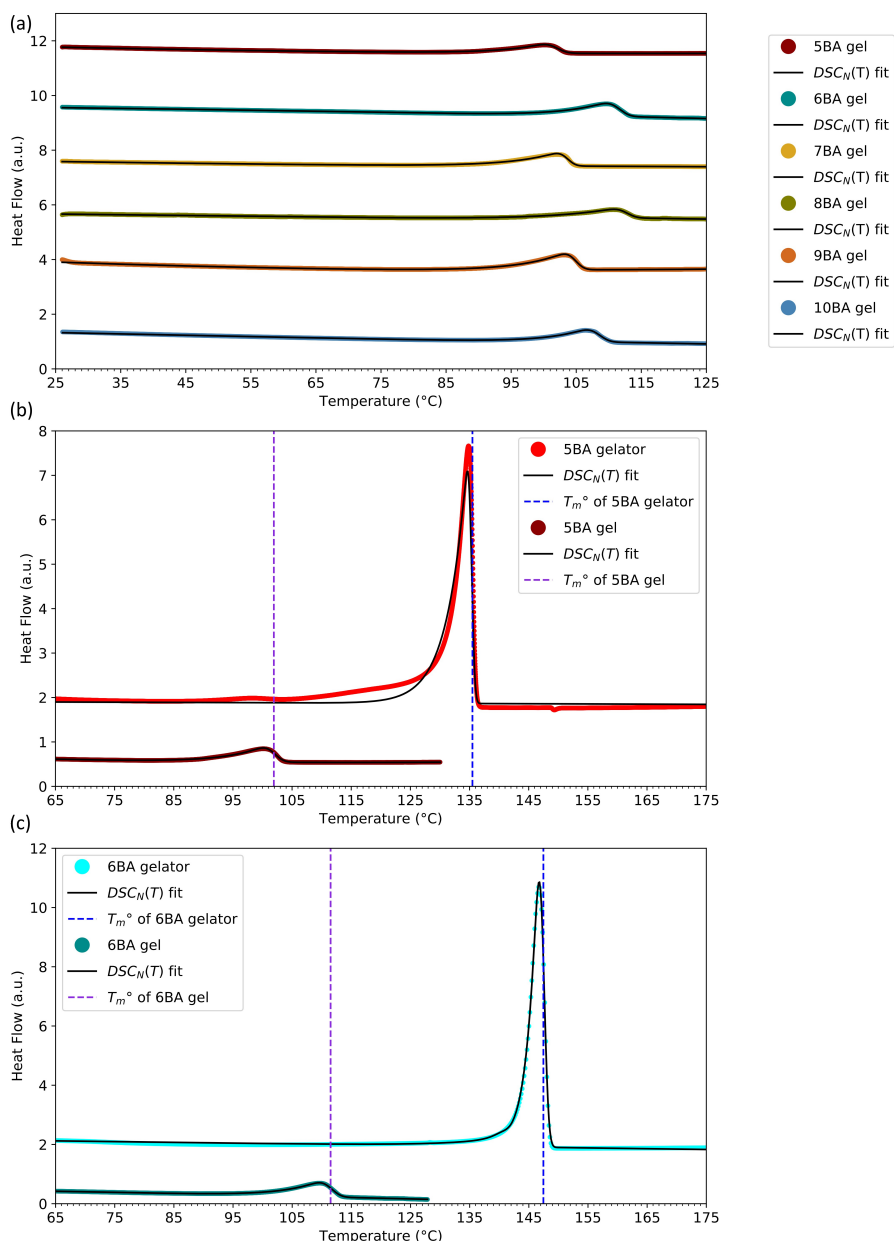


Figure 4.3 DSC thermogram of nBA gels (20 wt%) (curves were shifted vertically for clarity): a) DSC_N(T) function fitted to the second heating traces (endo up) measured at 5 K.min⁻¹ after calibration at the onset for the given sample weight and the scan rate, the second heating traces, fits, and T_m^0 of b) 5BA (as an example of the odd series), c) 6BA (as an example of the even series) were compared in the gelator and gel states, the results in the gelator solid state are from chapter 3⁴¹.

Table 4.1 Melting temperature (T_m^0) and the statistical coefficient (R^2) obtained from $DSC_N(T)$ model fit on the experimental curves of nBA gels^[a].

nBA gels (20 wt%)	T_m^0 (°C)	R^2
5BA	101.92±0.02	0.97
6BA	111.49±0.03	0.96
7BA	103.60±0.01	0.98
8BA	112.71±0.01	0.96
9BA	104.82±0.01	0.98
10BA	108.42±0.04	0.95

[a] All gels are 20 wt% heated at 5 K.min⁻¹ after calibration at the onset for the given weight and rate (the error margins are the errors from the non-linear fitting).

As Figure 4.3b,c show, the melting temperatures of 5BA and 6BA, as examples from odd and even series respectively, are somewhat lower than the melting temperatures of their respective gelators in the solid state (approximately 35 °C lower). To gain more insight into the dissolution behavior of these gelators, we determined the solubility curves of these gelators. The solubility curve can be derived from DSC experiments via the following two methods:

1. The first approach is to plot the curve based on the T_m^0 obtained from $DSC_N(T)$ model fit to the second heating traces of the gels at different concentrations which were measured by DSC (Figure S4.3).
2. The second approach is obtaining the curve from the cumulative integration of the melting transition in the second heating DSC trace of the gels (20 wt%). This method is described in more details in the supplementary information (Figure S4.4).

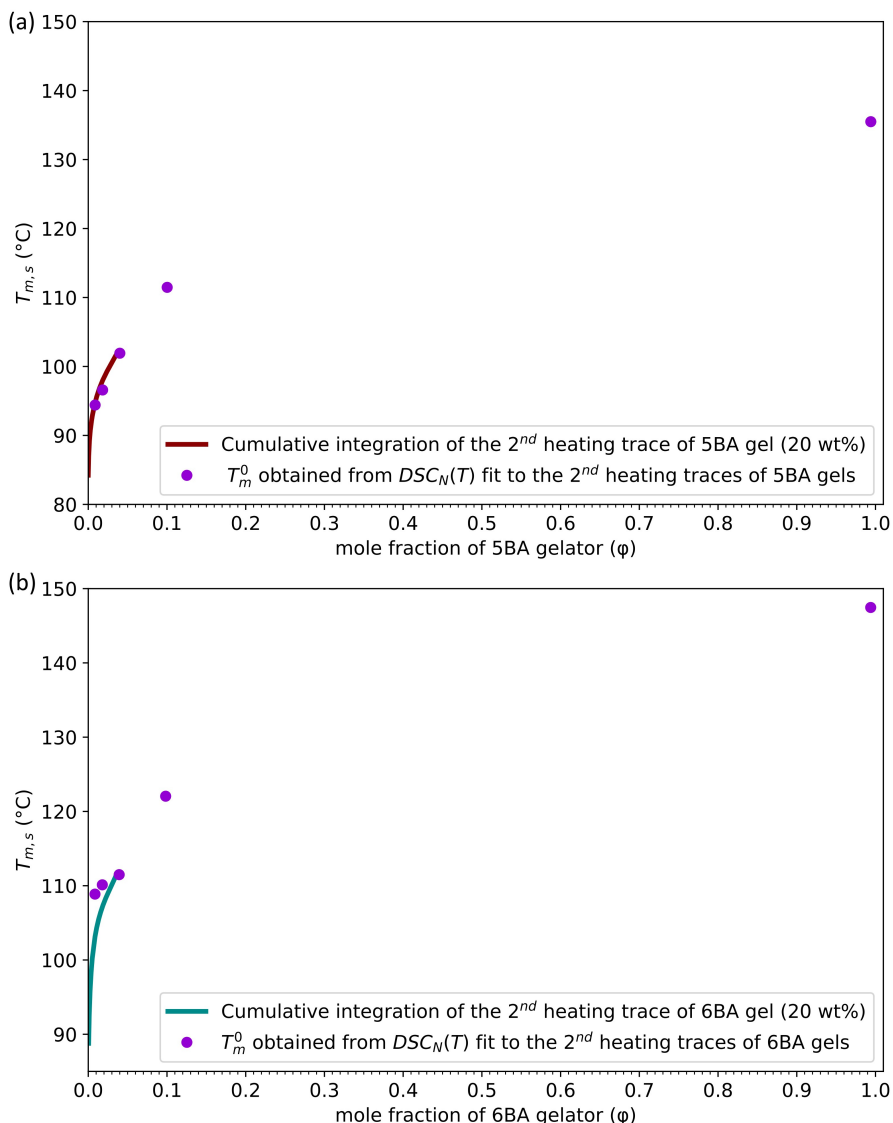


Figure 4.4 Solubility curves obtained from two different methods for: a) 5BA, b) 6BA gelators showing the melting temperature of the systems versus the mole fraction of the gelators present in xylene as solvent (in the case of both gelators, the mole fraction $\phi=1$ is pure gelator). The unit of temperature in FHM model is (K), however, the curves were plotted based on (°C) scale to be consistent with DSC thermogram in Figure 4.3.

Figure 4.4 shows the solubility curves for 5BA and 6BA gelators which are obtained from two different methods. The T_m^0 of 5BA and 6BA gels at different concentrations

fit to the solubility curve obtained from the cumulative integration of their gels (20 wt%) up to $\varphi=0.040$ and $\varphi=0.039$, which are respectively the mole fraction of 5BA and 6BA in their 20 wt% gels.

To gain insight into the mechanism of dissolution of nBA systems, we combined the well-known Flory-Huggins theory for mixing with the thermodynamics of melting, briefly FHM model, as described by Equation 4.2 (the route we took to develop FHM model is described in the supplementary information section).

$$T_{m,s} = \frac{\varphi \cdot \frac{\Delta H_m}{R} + \frac{\varphi \cdot (1 - \varphi) \cdot W_{12}}{R}}{\varphi \cdot \frac{\Delta S_m}{R} - \left(\frac{\varphi}{X_1} \cdot \ln \varphi + (1 - \varphi) \cdot \ln (1 - \varphi) \right)} \quad \text{Equation 4.2}$$

FHM model combines the theories of melting, describing the thermodynamics of the phase behavior in the solid crystalline or melt state, and Flory-Huggins, which originally elaborates the thermodynamics of polymer solutions, explains the thermodynamics of nBA gelators melting in the presence of solvent. FHM model is based on thermodynamic parameters which describe how the melting point of a nBA gel ($T_{m,s}$) changes with the volume fraction of the gelator (φ) (accordingly, $(1-\varphi)$ is the volume fraction of the solvent). The change in enthalpy and entropy of melting for a solid gelator are notated as ΔH_m and ΔS_m respectively. These two values are known from our previous research on the nBA gelators ⁴¹: the thermal properties of nBA gelators in the solid state, ΔH_m and T_m^0 , were obtained via fitting $DSC_N(T)$ to the second heating DSC traces where the melting transition occurs. Given ΔH_m and T_m^0 of the gelators, ΔS_m is calculated from $\Delta S_m = \Delta H_m / T_m^0$ for each nBA gelator (since ΔG is zero at the equilibrium). Therefore, the only adjustable parameters in Equation 4.2 are W_{12} and X_1 : the enthalpy of dissolution (W_{12}) is used to describe the interactions between the solvent and nBA gelator molecules. The parameter X_1 is the degree of association of the molecules after melting.

FHM model fits to the solubility curves of 5BA and 6BA gels obtained from the first method quite well (Figure 4.5 a,b). However, the second method provides the solubility curve with more data points. Figure 4.5 c,d shows that FHM model fits the melting-dissolution curve obtained from the latter method very well ($R^2 > 0.99$ according to Table 4.2). At room temperature the gelators dissolve negligibly in xylene, after raising the temperature to close to their melting points (T_m^0), 101.92 ± 0.02 °C and 111.49 ± 0.03 °C for 5BA and 6BA gels (20 wt%) respectively, more fraction of gelators start to melt and above T_m^0 all the melted gelators start mixing with the solvent.

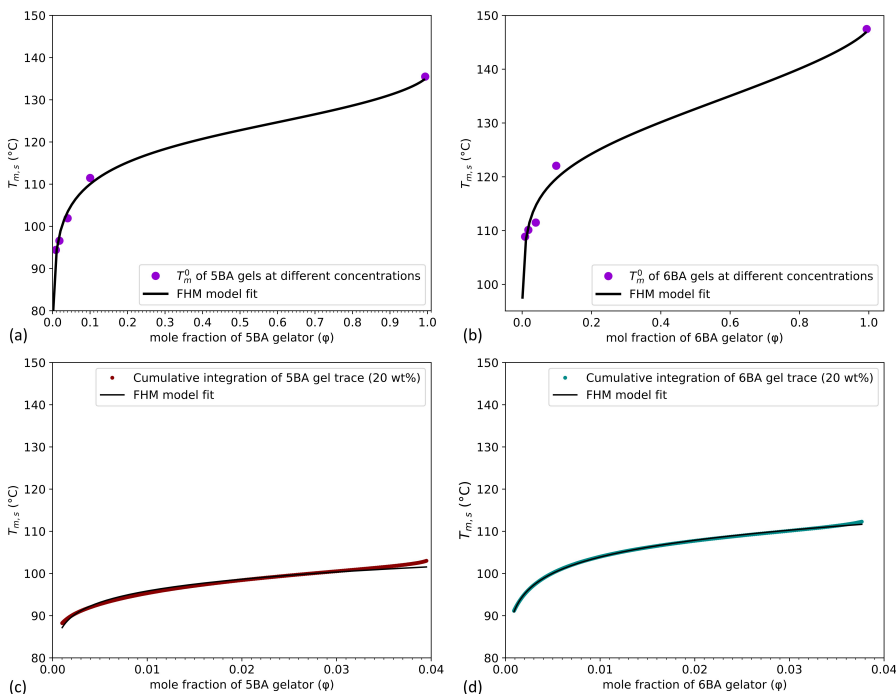


Figure 4.5 FHM model fitted to the solubility curves obtained from a, b) T_m^0 obtained from $DSC_N(T)$ model fit to the second heating traces of the gels at different concentrations for 5BA and 6BA respectively, c, d) from the cumulative integration of the second heating DSC traces of the 5BA and 6BA gels (20 wt%) respectively (the melting-dissolution curves for the rest of the gels can be found in the supplementary information (Figure S4.6)). The unit of temperature in FHM model is (K), however, the curves were plotted based on (°C) scale to be consistent with DSC thermogram in Figure 4.3.

Table 4.2 Fitted parameters and the statistical coefficient (R^2) of the FHM model fitted to the cumulative integration curves of second heating DSC traces of nBA gels^[a].

nBA gels (20 wt%)	$W_{12} (\text{J} \cdot \text{mol}^{-1})$	X_1	R^2
5BA	-870.50 ± 9.28	1.96 ± 0.00	0.99
6BA	-939.10 ± 29.31	3.72 ± 0.03	0.99
7BA	-620.33 ± 9.04	2.69 ± 0.04	0.99
8BA	-155.33 ± 33.65	2.09 ± 0.01	0.99
9BA	-814.19 ± 17.29	3.13 ± 0.01	0.99
10BA	-1512.64 ± 33.51	2.11 ± 0.01	0.99

[a] All gels are 20 wt% heated at $5 \text{ K} \cdot \text{min}^{-1}$ after calibration at the onset for the given weight and rate (the error margins are the errors from the non-linear fitting).

W_{12} is negative and less than 2% of ΔH_m for all nBA gels (Table 4.2). It indicates that after melting of the gelators, there is a small affinity between nBA gelators and xylene to interact. In fact, W_{12} term allows the fine-tuning of the initial slope of the solubility curves. X_1 is larger than 1 for all nBA gelators which indicates that after melting, there is still some degree of association between these molecules.

FHM model basically says that nBA gelators with a rather large ΔH_m are not inclined to dissolve because there is a ΔH penalty, thus below the melting point only a small concentration of the nBA gelator is dissolved in xylene solvent. Once the gelator solid crystal melts, the gelator molecules mix with the solvent which increases the entropy via the entropy of mixing. Therefore, the melting point of the system decreases. As Figure 4.6 shows, the melting points of the pure nBA gelators are generally about 35 °C higher than their melting-dissolution temperatures in the presence of xylene which is in agreement with FHM model theory. Other than that, the transition temperatures show a remarkably similar odd-even effect.

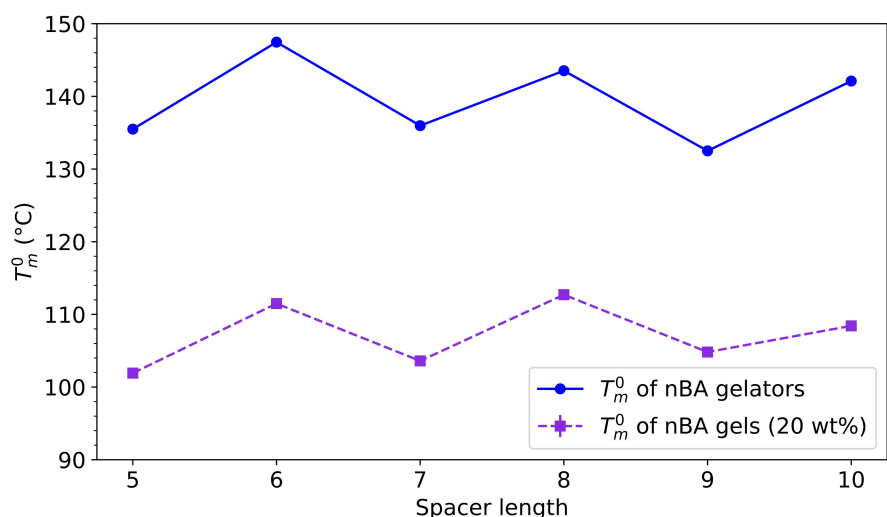


Figure 4.6 The melting temperature (T_m^0) of nBA gelators⁴¹ and the melting-dissolution temperature (T_m^0) of nBA gels (20 wt%) obtained from $DSC_N(T)$ fit to their second heating DSC traces.

Like the solid nBA gelators, the nBA gels also show a clear odd-even effect in T_m^0 upon increasing the spacer length from 5 to 10 (Figure 4.6). T_m^0 of even nBA gels is generally higher than the odd ones, similar to the trend in nBA gelators, which is attributed to their molecular arrangement⁴¹. In fact, odd nBA gelator molecules are in less favorable conformations, i.e. not at their lowest conformational energy to

allow the H-bonding network to develop [38]. Therefore, the odd members are under more internal stress. The even nBA gelators have higher melting points because the H-bonding is more regular as is achieved while keeping conformations close to the optimum lowest energy state. The question now arises whether the underlying crystal structures of the gels are actually similar to those of the pure gelator crystals? Figure 4.6 already indicates that this might be the case.

To investigate the supramolecular arrangement of the nBA molecules in the gel state, XRD patterns of gels (20 wt%) were measured at ambient temperatures under the same conditions as the nBA gelators in the solid state (Figure 4.7). In chapter 3, the XRD patterns of 5BA and 6BA gelators in the solid state were fully indexed which revealed a pseudo-orthorhombic lattice for odd and a triclinic one for even nBA gelators ⁴¹. Unfortunately, the XRD patterns of gel samples could not be indexed independently due to a relatively low resolution of the reflections, and therefore they were analyzed more globally by comparing them with the XRD patterns of the gelators in the solid state (Figure S4.7).

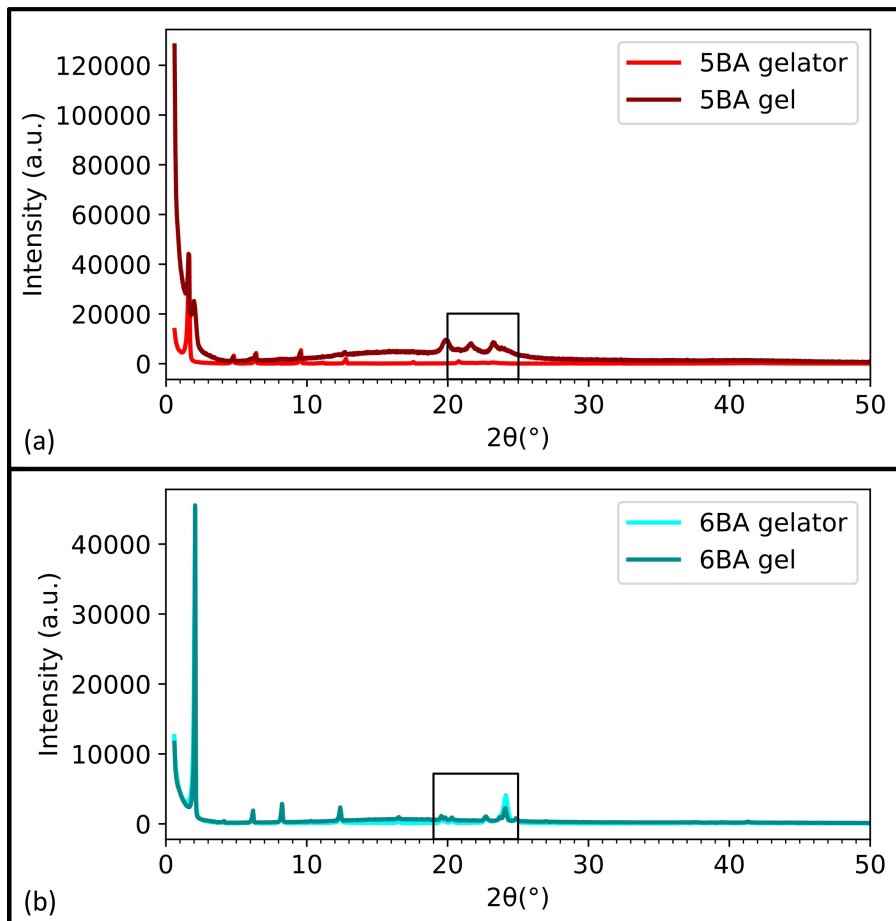


Figure 4.7 Observed XRD patterns of nBA gelators in the solid state and nBA gels (20 wt%): (a) 5BA, (b) 6BA, curves were normalized to the highest intensity and shifted vertically for clarity and solid boxes were added to guide eyes.

The general diffraction pattern of 5BA gel (20 wt%) is somewhat analogous to the 5BA gelator (Figure 4.7a), the characteristic lamellar $00l$ reflections are observed for both states, except for an extra reflection at $1.99^\circ(2\theta)$ which is due to polymorphism¹. More notably though, the pattern of the 5BA gel (20 wt%) shows a much higher background intensity and all reflections are strongly attenuated in intensity indicating substantially less crystallinity in the 5BA gel. Moreover, the reflections in the $20-25^\circ(2\theta)$ region of 5BA in the gelator and gel states are quite different which suggests that the side-by-side packing of the 5BA molecules in the gel state is actually different than that in the solid state. The observed XRD patterns

of the three odd nBA gels are shown in Figure S4.7d. The characteristic lamellar $00l$ reflections observed for the 5BA gel are observed for 7BA and 9BA gels as well, indicating a highly defined layer spacing. The shift to lower angles with increasing the spacer length from 5BA to 9BA is due to an increasing *c*-axis length. The reflections in the 20-25°(2θ) range are different among odd gels, implying a slightly different lateral packing for odd nBA gels.

The diffraction patterns of 6BA gel (20 wt%) shows many similarities with the pattern of the pure 6BA compound in the solid state (Figure 4.7b). The larger background and lower intensity of the reflections observed for 5BA gel (20 wt%) are also observed for the 6BA gel (20 wt%) compared to the 6BA pure gelator, but to a much lesser extent. The reflections of 6BA gel and solid gelators in the 1-19°(2θ) low angle and 19-25°(2θ) wide angle range are identical. This similarity suggests that the supramolecular arrangement of 6BA molecules in the 20 wt% gel is very similar to the molecular arrangement in the pure compound. The XRD patterns of the even nBA gels in Figure S4.7b show $00l$ reflections for all even nBA gels. The *c*-axis length increases with increasing the spacer length which leads to a low-angle shift of the $00l$ peaks. The reflections in the 19-25°(2θ) range are very similar for the even gels, implying that the lateral packing of 8BA and 10BA is very similar to that of 6BA.

The similarity in XRD patterns of nBA gels and their gelators facilitates their analysis using the indexing of nBA gelators in the solid state ⁴¹; like the XRD pattern of nBA gelators, the $00l$ reflections are present in both odd and even nBA gels which indicates regular layer spacing even though some higher order reflections have relatively lower intensities. The gel state patterns also show a clear odd-even difference suggesting the less favorable molecular conformation of odd molecules in the gel state. SEM was used to investigate the effect of the supramolecular structure on the gel morphology. As SEM images of nBA gels (20 wt%) in Figure 4.8 show, even nBA gels exhibit sheet-like crystals which are clearly distinguishable from the woven fibrous-like structure of odd nBA gels. This can be attributed to the packing model proposed for the even nBA molecules in the solid state ⁴¹; the stacking of several layers of molecules with the tilted lamellar geometry can self-assemble as sheet-like microcrystals observed for all even nBA gels. Odd nBA gels show three rather distinct morphologies which might be in line with their different XRD reflections in the 20-25°(2θ) region (Figure S4.7d); the 5BA gel shows a combination of woven fibers and spherical structures which is in agreement with the first two $00l$ reflections in its XRD pattern while 7BA and 9BA gels show a more uniform woven fibrillar structure. This variation in the microstructures of odd nBA gels is in reasonable agreement with the different microstructures as displayed by

their XRD patterns. A question might be whether these microstructural differences between odd and even nBA gels are reflected in their rheological properties?

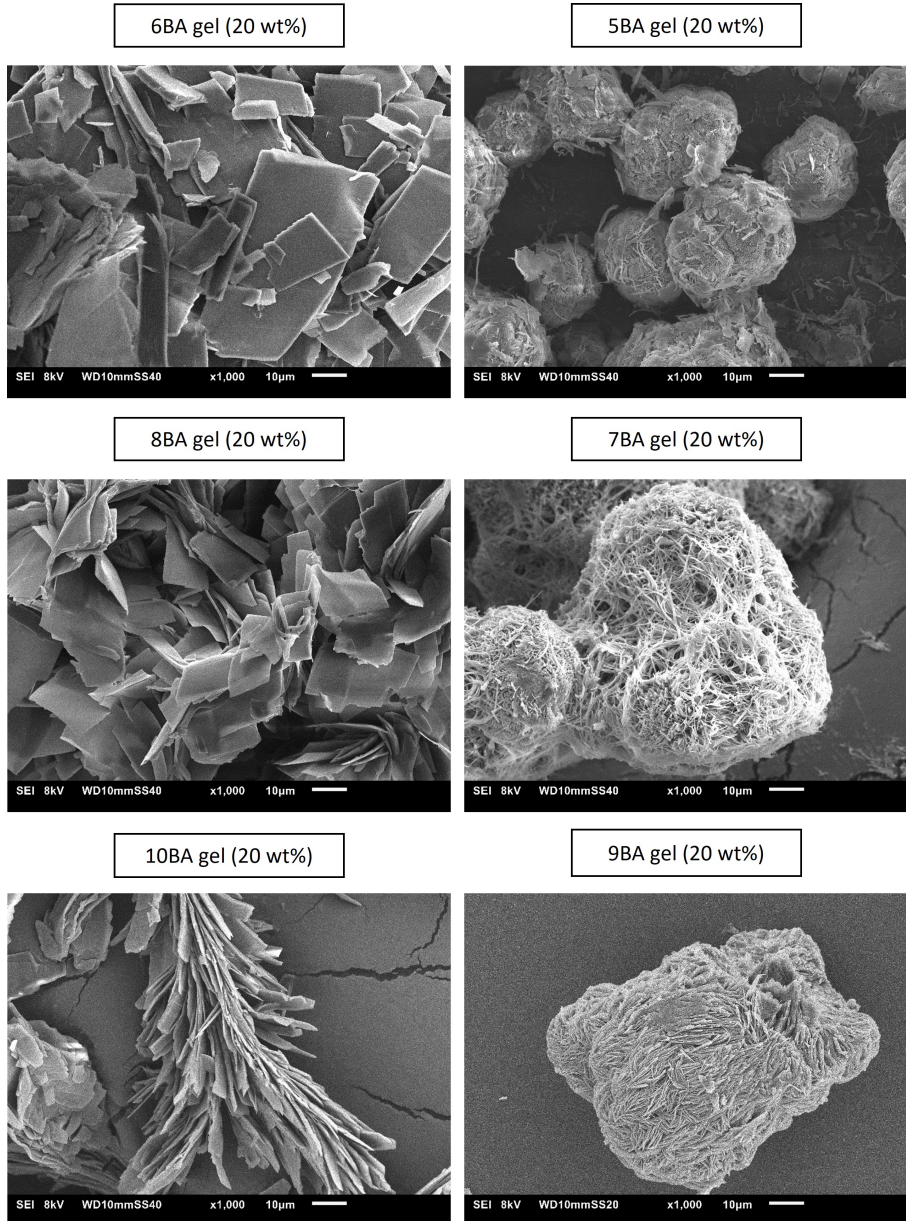


Figure 4.8 SEM images of nBA gels (20 wt%) depicting sheet-like structure of even gels versus woven fibrous morphology of odd gels.

To study the flow and deformation properties of nBA gels, initially, oscillatory rheological measurements (amplitude-sweep tests) were conducted on nBA gels (20 wt%). For all these gels, the elastic component (G') dominates over the viscous component (G'') at small applied shear and reaches a plateau in the linear response viscoelastic region (LVR). As shown in Figure 4.9a, the yield strain is independent of the spacer length and for all nBA gels, it is below 1 % resulting in a much smaller LVR compared to hydrogels in general ⁴². The nBA gels are remarkably strain-sensitive compared to many cross-linked gels and other supramolecular and complex fluid systems, that can often withstand strains 10–100 % strain if not more. This observation in itself may indicate that bisamide organogelator gels might be highly sensitive to strain and strain history, which makes reliable rheological characterization quite challenging. Note that even at strains around 10⁻³ % there is still some, admittedly mild, amplitude dependence, a strain of 1 part in 100,000 would normally be considered totally safe within the linear region.

Once LVR for every nBA gel was established, at the low strain of 0.01 % in the LVR, frequency sweep experiments were conducted to evaluate the storage and loss moduli of the nBA gels (Figure 4.9b). Under this condition, the storage modulus of nBA gels increases only very slightly with frequency, so the gel does not have any appreciable internal dynamics. Clearly, at the probed timescales, the gel network fails to rearrange and show an elastic behavior. At all frequencies, $G' > G''$ which indicates the gel behavior for all nBA gels (20 wt%). Interestingly, G'' decreases slightly with increasing ω while one could anticipate an increasing trend based on $G'' = \eta \cdot \omega$.

The relation between storage modulus and angular frequency can be explained by the simplified power law equation below:

$$G' = S\omega^n \text{ } ^{43} \quad \text{Equation 4.3}$$

In Equation 4.3, S is a material-specific constant, ω is the angular frequency, n is the viscoelastic exponent. In our test, n is close to 0 for all nBA gels which confirms their solid-like behavior where G' is invariant of the measured frequency while depending on the material-specific constant (S); the higher the S value, the higher the gel network modulus.

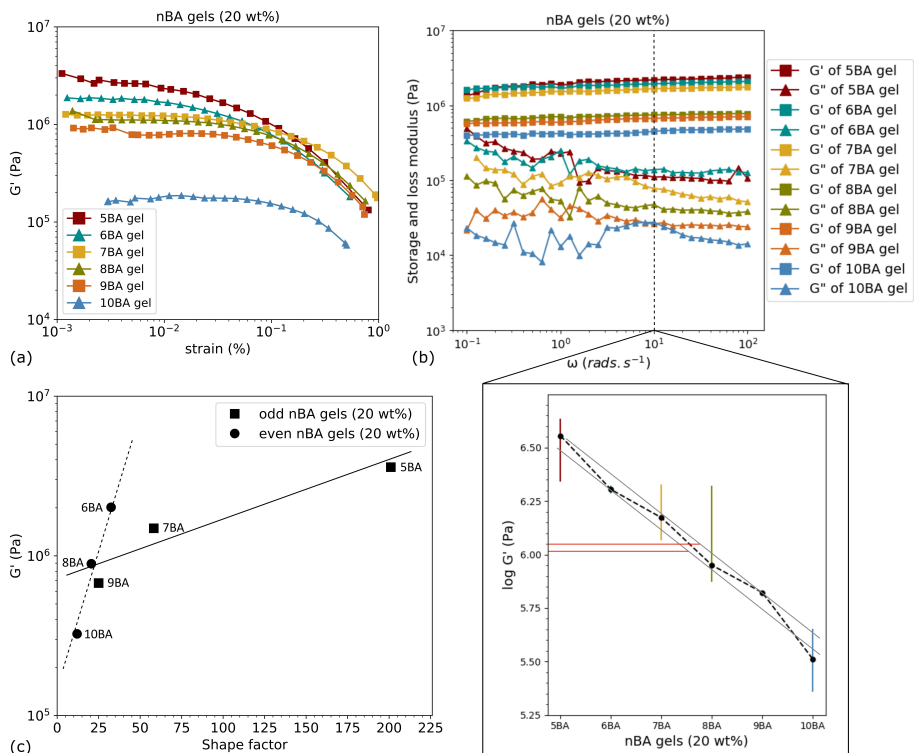


Figure 4.9 Rheological measurements on nBA gels (20 wt%): a) amplitude-sweep measurements from 0.001 % to 1 % strain rate at the constant frequency of 1 Hz, b) evolution of G' and G'' as a function of angular frequency (ω): the inset shows the change in storage modulus (G') with spacer length in nBA gels (20 wt%), the red solid lines were added to guide eyes for odd-even alternation amounting to about 25 % deviation from the overall (between the grey guidelines), c) the change of G' with the shape factor of woven fibers and sheets in odd and even nBA gels (20 wt%) respectively.

To compare the moduli of nBA gels, the values of G' at the constant frequency ($\omega=10$ rad·s⁻¹) for all gels were selected (Figure 4.9b). The storage modulus (G') of nBA gels (20 wt%) decreases by increasing the spacer length which is in a good agreement with the table-top rheology trend as observed from inverting the vials. Quantitative rheological measurements show that this decrease is not linearly related to the spacer length, but a slight odd-even alternation is observed, which is amounting to about 25 % deviation from the overall trendline.

The relation between gel morphology and rheological properties can be explained with inspiration from Halpin-Tsai model which discusses the effect of particle aspect ratio on the modulus of a composite material ⁴⁴. The Halpin-Tsai model is based on

the work by Hill, Kerner, and Hermans. It is often considered as a semi-empirical model. However, it has some unique features, such as taking the geometry of the filler in a composite into account, that are absent in other models⁴⁵. Although applying this model to the nBA gel systems is not fully justified, we found the model valuable to investigate the effect of particle geometry on the rheological properties of the gels. It is reasonable to surmise that a nBA gel is a type of composite material which consists of two components, a space filling 3D gel network and the solvent matrix with some molecularly dissolved gelator at a low concentration. To justify the application of the Halpin-Tsai model, the matrix would be required to have a sufficient stiffness for stress transfer, and the gel fibrils or sheets should act as a reinforcement, without taking any effect of fibril or sheet crosslinking into account. This evidently is not quite what we imagine an organogel to look like, because the matrix might be a viscous fluid and the crosslinks are the essence of what we might consider a required feature for a gel. The Halpin-Tsai model is given in Equation 4.4:

$$E_c = E_m \cdot \frac{(1 + \zeta \eta V_f)}{(1 - \eta V_f)} \quad \text{Equation 4.4}$$

$$\eta = \frac{(E_f - E_m)}{(E_f + \zeta E_m)} \quad \text{Equation 4.5}$$

Where E_c refers to the storage modulus of the composite material, E_f refers to the modulus of the fiber and E_m refers to the modulus of the matrix material. V_f is the fiber volume fraction and ζ is the reinforcing efficiency or the shape factor. The shape factor (ζ) is determined by the fiber geometry, molecular arrangement, packing fraction and loading conditions⁴⁶.

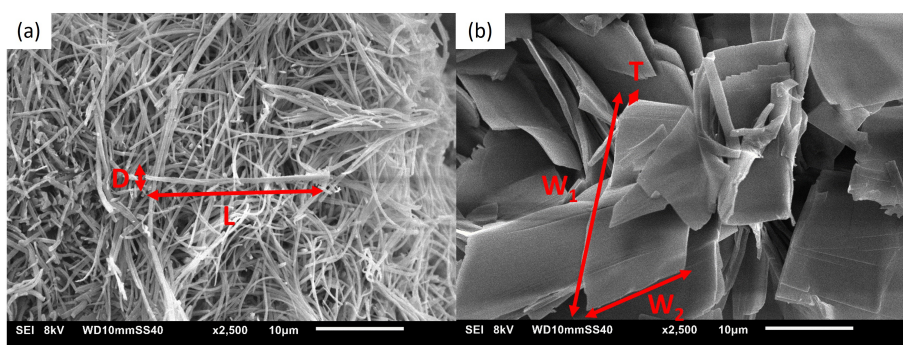


Figure 4.10 Schematic assignment of dimensions of: a) woven fibers in odd nBA gels ($L \gg D$), b) sheets in even nBA gels ($W_1 \approx W_2$ and $W \gg T$).

The stress-partitioning factor η is obtained from Equation 4.5. Assuming that the reinforcement only happens along the principal fiber direction, the formula of ζ_0 for fibers with circular or rectangular cross-section is given as Equation 4.6:

$$\zeta_0 = 2 \frac{L}{D} \quad \text{Equation 4.6}$$

Where L is the length of the fiber in its elongated direction and D is the diameter of the circular or width of the rectangular cross section in the rod-like fibers (Figure 4.10a). The shape factor for a sheet-like structure (ζ_E) is given by Equation 4.7, where W refers to the average width (W) of the sheets and T refers to the thickness of the sheets (Figure 4.10b):

$$\zeta_E = \frac{2W}{3T} \quad \text{Equation 4.7}$$

If we substantially simplify the Halpin-Tsai in Equation 4.4 for $E_f \gg E_m$ at a low filler fraction, the stiffness of the composite is obtained from Equation 4.8:

$$E_C = E_m \cdot (1 + (1 + \zeta) \cdot V_f) \quad \text{Equation 4.8}$$

As a result, the storage modulus of the composite material is linearly proportional to the aspect ratio of the fillers at the same gel concentration based on the Equation 4.8. It is worth observing that this equation is actually similar to the Einstein law for viscosity (Equation 4.9).

$$\mu = \mu_0(1 + 2.5\phi) \quad \text{Equation 4.9}$$

Where μ is the viscosity of the homogeneous suspension fluid, the Einstein coefficient is 2.5 which is related to the spherical shape of the particles, μ_0 is the liquid viscosity and ϕ is the particle volume fraction.

Figure 4.9c shows that the storage modulus of even and odd nBA gels are indeed linearly proportional to the shape factor of sheets and fibers respectively (ζ_E and ζ_0), albeit with a rather different slope. Because the Halpin Tsai model is only partially applicable to the gel system at hand, due to the physically crosslinked network, it should not be expected to give a very accurate prediction of the gel behavior. However, it does serve to underline the effect of the morphology on the gel properties which obviously deserves a more extensive analysis^{47,48}.

Another approach we considered was to estimate whether the organogels could be modelled as an open or closed cell foam, where the stiffness is wholly due to the 'sponge' of solid gelator and the solvent/solution contribution would be negligible (Equation 4.10). For a closed-cell foam the modulus is linear with the volume

fraction, whereas for an open-cell foam the modulus is proportional to the square of the volume fraction, i.e. $p = 1$ and $p = 2$ respectively^{49,50}.

$$E_{\text{foam}} = E_{\text{solid}} \cdot \phi^p \quad \text{Equation 4.10}$$

If we fill this in using E_{solid} is about 3 GPa and $f = 0.2$, we end up with gel moduli in the 120–600 MPa regime which is far too high. Some reduction to these values due to some Brownian motion of the gel fibrils and sheets might improve things slightly but it is clear quite more work needs to be done which is outside the scope of the current chapter.

4.4 Conclusions

To study the gelation behavior of bisamide gels, nBA gelators with simple structure where n is the spacer length between amide groups (varying from 5 to 10) with 17 carbons at each side of the amide groups (C17) were used. The relatively simple chemical structure of these gelators makes them ideal as model compounds to study their supramolecular assembly, gelation, and the gel properties of bisamide molecules in general. The spatial arrangement of gelator molecules in the gel state has been compared with the molecular arrangement in the solid state. The microscopic properties of the gels and their impacts on the final gel rheological properties have been investigated.

The instant table-top tube inversion test indicated that gellability of nBA gelators decreases upon increasing the spacer length in both odd and even gels; as a result, around at least 20 wt% gelators is required for the formation of homogeneous stable gels suitable for the further analysis. T_m^0 obtained from fitting of $DSC_N(T)$ to the DSC traces of nBA gels is about 35 °C lower than T_m^0 of the respective nBA gelators. This substantial difference is explained via FHM model, combining the theories of Flory-Huggins and Gibbs free energy of melting. FHM model fitting to the melting-dissolution curves of nBA gels includes the entropy of mixing term changing the level of order as the gelators transform from the solid state to the melted and dissolved state. Lower T_m^0 and ΔH of nBA gels compared to the nBA gelators is primarily caused by the entropy of mixing. The XRD patterns of the nBA gels (20 wt%) show $00l$ reflections matching with the respective pure gelators in the solid state, implying a regular structure. The similar reflections in 19–25 °(2θ) region of even nBA gels and gelators were observed which confirm the observation of SEM images: the sheet-like microstructures of even gels are in a reasonable agreement with the analogous lamellar spacing of the even gelators in the solid state. In contrast, the 20–25 °(2θ) region of odd nBA gels was quite different than the gelators in the solid

state, and also in comparison to each other. Apparently, the supramolecular arrangement of these molecules in the gel state is distinctly different for the odd and even nBA gelators but the complete analysis of this is outside of the scope of this study. It is worth noting the very close trends in the melting temperatures suggest that the differences might still be rather despite substantial changes in the XRD patterns. Concerning the observed mixed morphologies of woven fibers and spheres found in the SEM images of odd nBA gels this could indicate some polymorphism. The relation between the microstructure and rheological properties was explained using some inspiration from Halpin-Tsai model and indeed the results were also compared to foam mechanics. Here the nBA gels are considered as composite materials consisting of two components, the gel network crystals and the entrapped solvent with a certain degree of stiffness. The change of the storage modulus (G') with the shape factor of woven fibers and sheets in nBA gels (20wt%) indicates an odd-even effect. The G' of even and odd nBA gels are linearly proportional to ζ_e and ζ_o respectively which is in some agreement with the simplified Halpin-Tsai model, the difference in slope however seems unexplained as yet. Analogously, we found that foam mechanics substantially overestimates the moduli of the gels again indicating that more subtle approaches to bisamide organogelator mechanics are required. Once such a rheological model is established, it will allow for more rapid optimization of gel properties and will provide a solid theoretical framework to build on.

4.5 References

- [1] M. George and R. G. Weiss, "Molecular organogels. Soft matter comprised of low-molecular-mass organic gelators and organic liquids", *Acc. Chem. Res.*, 2006.
- [2] P. Terech and R. G. Weiss, "Low molecular mass gelators of organic liquids and the properties of their gels", *Chem. Rev.*, 1997.
- [3] M. M. Piepenbrock, G. O. Lloyd, N. Clarke, and J. W. Steed, "Metal-and anion-binding supramolecular gels", *Chem. Rev.*, 2010.
- [4] L. E. Buerkle and S. J. Rowan, "Supramolecular gels formed from multi-component low molecular weight species", *Chem. Soc. Rev.*, 2012.
- [5] L. Zhang, X. Wang, T. Wang, and M. Liu, "Tuning soft nanostructures in self-assembled supramolecular gels: from morphology control to morphology-dependent functions", *Small*, 2015.
- [6] B. O. Okesola and D. K. Smith, "Applying low-molecular weight supramolecular gelators in an environmental setting-self-assembled gels as smart materials for pollutant removal", *Chem. Soc. Rev.*, 2016.
- [7] S. S. Babu, V. K. Praveen, and A. Ajayaghosh, "Functional π -gelators and their applications", *Chem. Rev.*, 2014.
- [8] C. D. Jones and J. W. Steed, "Gels with sense: Supramolecular materials that respond to heat, light and sound", *Chem. Soc. Rev.*, 2016.
- [9] R. G. Weiss, "The past, present, and future of molecular gels. What is the status of the field, and where is it going?", *J. Am. Chem. Soc.*, 2014.
- [10] B. Escuder and J. F. Miravet, "Functional molecular gels", Royal Society of Chemistry, 2013.
- [11] K. Araki, "Low Molecular Mass Gelators: Design, Self-Assembly, Function", Springer Science & Business Media, 2005.
- [12] A. R. Hirst, B. Escuder, J. F. Miravet, and D. K. Smith, "High-tech applications of self-assembling supramolecular nanostructured gel-phase materials: From regenerative medicine to electronic devices", *Angew. Chemie - Int. Ed.*, 2008.
- [13] D. Wang et al., "Parenteral thermo-sensitive organogel for schizophrenia therapy, *in vitro* and *in vivo* evaluation", *Eur. J. Pharm. Sci.*, 2014.
- [14] E. Główka et al., "Polymeric nanoparticles-embedded organogel for roxithromycin delivery to hair follicles", *Eur. J. Pharm. Biopharm.*, 2014.

- [15] A. Vintiloiu and J.-C. C. Leroux, "Organogels and their use in drug delivery—A review", *J. Control. release*, 2008.
- [16] J. Song et al., "Multifunctional antimicrobial biometallohydrogels based on amino acid coordinated self-assembly", *Small*, 2020.
- [17] R. Xing et al., "An injectable self-assembling collagen–gold hybrid hydrogel for combinatorial antitumor photothermal/photodynamic therapy", *Adv. Mater.*, 2016.
- [18] J. Bai et al., "Biomineral calcium-ion-mediated conductive hydrogels with high stretchability and self-adhesiveness for sensitive iontronic sensors", *Cell Reports Phys. Sci.*, 2021.
- [19] S. Raut, S. S. Bhadoriya, V. Uplanchiwar, V. Mishra, A. Gahane, and S. K. Jain, "Lecithin organogel: A unique micellar system for the delivery of bioactive agents in the treatment of skin aging", *Acta Pharm. Sin. B*, 2012.
- [20] J. Puigmartí-Luis et al., "Supramolecular conducting nanowires from organogels", *Angew. Chemie*, 2007.
- [21] M. Pernetti, K. F. van Malssen, E. Flöter, and A. Bot, "Structuring of edible oils by alternatives to crystalline fat", *Curr. Opin. Colloid Interface Sci.*, 2007.
- [22] N. Zweep, A. Hopkinson, A. Meetsma, W. R. Browne, B. L. Feringa, and J. H. van Esch, "Balancing hydrogen bonding and van der Waals interactions in cyclohexane-based bisamide and bisurea organogelators", *Langmuir*, 2009.
- [23] O. Elvet, G. O. Lloyd, and J. W. Steed, "Anion-tuning of supramolecular gel properties", *Nat. Chem.*, 2009.
- [24] J.-M. M. Lehn, "Dynamers: dynamic molecular and supramolecular polymers", *Prog. Polym. Sci.*, 2005.
- [25] J.-W. W. Liu, J.-T. T. Ma, and C.-F. F. Chen, "Structure–property relationship of a class of efficient organogelators and their multistimuli responsiveness," *Tetrahedron*, vol. 67, no. 1, pp. 85–91, 2011.
- [26] K. Murata et al., "Thermal and light control of the sol–gel phase transition in cholesterol-based organic gels. Novel helical aggregation modes as detected by circular dichroism and electron microscopic observation", *J. Am. Chem. Soc.*, 1994.
- [27] M. Laupheimer, N. Preisig, and C. Stubenrauch, "The molecular organogel n-decane/12-hydroxyoctadecanoic acid: Sol–gel transition, rheology, and microstructure", *Colloids Surfaces A Physicochem. Eng. Asp.*, 2015.
- [28] M. A. Rogers, J. Hee, and J. J. H. J. Kim, "Rheological assessment of the sol–gel transition for self-assembling low molecular weight gelators", *Food Res. Int.*, 2011.

- [29] Y. Wang, L. Tang, and J. Yu, "Investigation of spontaneous transition from low-molecular-weight hydrogel into macroscopic crystals", *Cryst. Growth Des.*, 2008.
- [30] D. K. Kumar and J. W. Steed, "Supramolecular gel phase crystallization: orthogonal self-assembly under non-equilibrium conditions", *Chem. Soc. Rev.*, 2014.
- [31] T. H. Zhang and X. Y. Liu, "Experimental modelling of single-particle dynamic processes in crystallization by controlled colloidal assembly", *Chem. Soc. Rev.*, 2014.
- [32] A. R. Patel, M. Babaahmadi, A. Lesaffer, and K. Dewettinck, "Rheological Profiling of Organogels Prepared at Critical Gelling Concentrations of Natural Waxes in a Triacylglycerol Solvent", *J. Agric. Food Chem.*, 2015.
- [33] P. Terech, D. Pasquier, V. Bordas, and C. Rossat, "Rheological properties and structural correlations in molecular organogels", *Langmuir*, 2000.
- [34] A. Bui and N. Virgilio, "Tuning organogel properties by controlling the organic-phase composition", *Ind. Eng. Chem. Res.*, 2013.
- [35] C. Van Der Pol et al., "Orthogonal self-assembly of low molecular weight hydrogelators and surfactants", *J. Am. Chem. Soc.*, 2003.
- [36] M. Žinic, F. Vögtle, and F. Fages, "Cholesterol-based gelators", *Low Mol. Mass Gelator*, 2005.
- [37] A. Dawn and H. Kumari, "Low Molecular Weight Supramolecular Gels Under Shear: Rheology as the Tool for Elucidating Structure–Function Correlation", *Chem. - A Eur. J.*, 2018.
- [38] M. L. Muro-small, J. Chen, and A. J. McNeil, "Dissolution parameters reveal role of structure and solvent in molecular gelation", *Langmuir*, 2011.
- [39] M. Suzuki, Y. Nakajima, M. Yumoto, M. Kimura, H. Shirai, and K. Hanabusa, "Effects of hydrogen bonding and van der Waals interactions on organogelation using designed low-molecular-weight gelators and gel formation at room temperature", *Langmuir*, 2003.
- [40] L. Wang, Y. Jiang, Y. Lin, J. Pang, and X. Y. Liu, "Rheological properties and formation mechanism of DC electric fields induced konjac glucomannan-tungsten gels", *Carbohydr. Polym.*, 2016.
- [41] E. Ghanbari, A. Krishnamurthy, S. J. Picken, E. A. Klop, L. J. Bannenberg, and J. van Esch, "Molecular Arrangement and Thermal Properties of Bisamide Organogelators in the Solid State", *Langmuir*, 2022.
- [42] F. Cuomo, M. Cofelice, and F. Lopez, "Rheological characterization of hydrogels from alginate-based nanodispersion", *Polymers (Basel.)*, 2019.

- [43] H. H. Winter and F. Chambon, "Analysis of linear viscoelasticity of a crosslinking polymer at the gel point", *J. Rheol. (N. Y. N. Y.)*, 1986.
- [44] J. C. Halpin, "Stiffness and expansion estimates for oriented short fiber composites", *J. Compos. Mater.*, 1969.
- [45] W. Patterson, A. Force, J. C. H. Afdal, and J. L. Kardos, "The Halpin-Tsai equations: a review", *Polym. Eng. Sci.*, 1976.
- [46] O. D. O. Osoka Emmanuel, E. C. Osoka, and O. D. Onukwuli, "A modified Halpin-Tsai model for estimating the modulus of natural fiber reinforced composites", *Int. J. Eng. Sci. Inven.*, 2018.
- [47] C. L. Tucker III, E. Liang, C. L. Tucker, and E. Liang, "Stiffness predictions for unidirectional short-fiber composites: review and evaluation", *Compos. Sci. Technol.*, 1999.
- [48] U. K. Weber et al., "Role of interaction anisotropy in the formation and stability of molecular templates", *Phys. Rev. Lett.*, 2008.
- [49] W. Pabst, T. Uhliřová, E. Gregorová, and A. Wiegmann, "Young's modulus and thermal conductivity of closed-cell, open-cell and inverse ceramic foams—model-based predictions, cross-property predictions and numerical calculations", *J. Eur. Ceram. Soc.*, 2018.
- [50] W. Zhu, N. Blal, S. Cunsolo, and D. Baillis, "Micromechanical modeling of effective elastic properties of open-cell foam", *Int. J. Solids Struct.*, 2017.

4.6 Supplementary information

Here, more information about the methodologies and the analytical data for all nBA gels are provided.

4.6.1 DSC thermogram of 5BA gel (20 wt%)

The DSC thermogram of 5BA gel (20 wt%) is shown in Figure S4.1. The first heating trace shows two peaks for the melting-dissolution transition while the second heating trace (Figure S4.2) shows a single endothermic peak. To obtain T_m^0 , $DSC_N(T)$ was fitted to the normalized traces. The fit parameters are listed in Table S4.1.

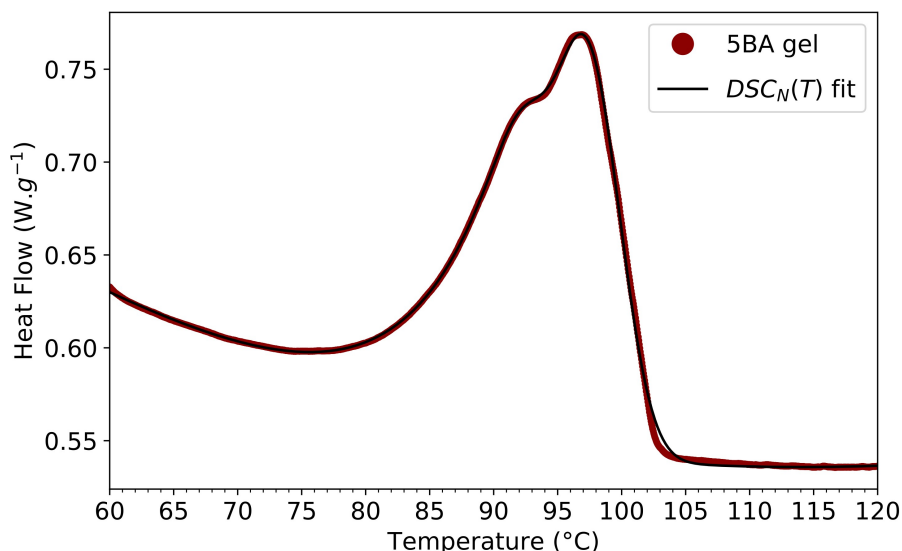


Figure S4.1 First heating DSC trace of 5BA gel (20 wt%) showing a double peak at the melting-dissolution transition.

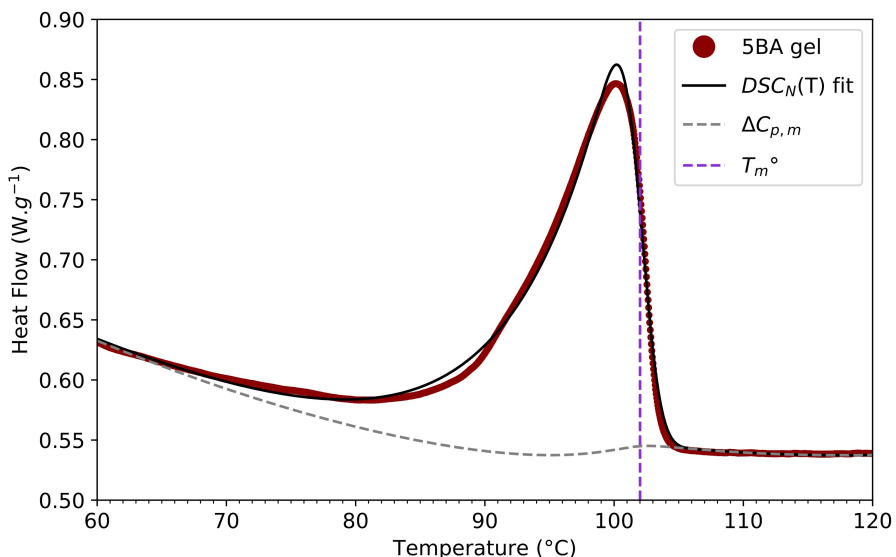


Figure S4.2 The second heating DSC trace, just as an example of a nBA gel, to show how T_m^0 and $\Delta C_{p,m}$ are obtained from the fitting of the $DSC_N(T)$ function to the experimental trace.

Table S4.1 Fitted parameters, standard deviations, and goodness of fit obtained from fitting $DSC_N(T)$ model to the second heating DSC traces of nBA gels (20 wt%)^[a].

nBA gels	5BA	6BA	7BA	8BA	9BA	10BA
$\Delta H (J.g^{-1})$	34.32 ± 0.02	53.88 ± 0.06	51.84 ± 0.01	52.44 ± 0.02	64.08 ± 0.01	47.64 ± 0.07
$T_m^0 (^\circ C)$	101.92 ± 0.02	111.49 ± 0.03	103.60 ± 0.01	112.71 ± 0.01	104.82 ± 0.01	108.42 ± 0.04
$\alpha (K^{-1})$	0.17 ± 0.00	0.15 ± 0.00	0.14 ± 0.00	0.11 ± 0.00	0.15 ± 0.00	0.16 ± 0.00
$\beta (K^{-2})$	0.31 ± 0.01	0.31 ± 0.02	0.31 ± 0.01	0.35 ± 0.01	0.44 ± 0.01	0.32 ± 0.03
$\Delta C_{p,m} (W.g^{-1}.K^{-1})$	0.01 ± 0.00	0.03 ± 0.01	0.03 ± 0.00	0.13 ± 0.00	0.04 ± 0.00	0.05 ± 0.01
$B (W.g^{-1})$	0.55 ± 0.00	0.20 ± 0.01	0.39 ± 0.00	0.39 ± 0.00	1.59 ± 0.00	0.44 ± 0.01
$C (mW.g^{-1}.K^{-1})$	-7.97 ± 0.03	-5.50 ± 0.02	-1.43 ± 0.03	-3.43 ± 0.07	0.09 ± 0.04	-4.40 ± 0.28
$D (mW.g^{-1}.K^{-2})$	0.03 ± 0.00	-0.02 ± 0.00	0.01 ± 0.00	0.01 ± 0.00	0.05 ± 0.00	0.00 ± 0.00
R^2	0.97	0.96	0.98	0.96	0.98	0.95

[a] All gels are 20 wt% and heated at $5 \text{ K}.\text{min}^{-1}$ after calibration at the onset for the given the sample weight and the scan rate (the error margins are exclusively the errors from the non-linear fitting itself).

4.6.2 FHM model development

The underlying principle of melting theory explains that the Gibbs free-energy (per volume) of the solid ($G_{s,v}$) and liquid state ($G_{l,v}$) at the equilibrium melting is the same,

therefore $\Delta G=0$ at the melting point (Equation S4.1). Thus, the melting point is obtained from Equation S4.2 where T_m is the equilibrium melting point and ΔS and ΔH are the change in entropy and enthalpy respectively.

$$\Delta G = G_{l,v} - G_{s,v} = \Delta H_v - T\Delta S_v \quad \text{Equation S4.1}$$

$$T_m = \frac{\Delta H_v}{\Delta S_v} \quad \text{Equation S4.2}$$

Flory-Huggins theory is frequently used for polymer solutions (Equation S4.3) where φ_1 and φ_2 are volume fractions of polymer (gelator in the case of LMWG gels) and solvent ($\varphi_1 = \frac{N_1}{N_1+x.N_2}$, $\varphi_2 = \frac{x.N_2}{N_1+x.N_2}$), N_1 and N_2 are the number of moles of polymer/gelator and solvent components respectively. The χ parameter is a free energy parameter thus including entropic component. Accordingly, W_{12} describes the enthalpy interaction between the solute and solvent ($W_{12} = \chi \cdot R \cdot T$). The parameter X_1 is the degree of polymerization or the degree of association of the gelator molecules in the solution (in the vicinity of the gel melting-dissolution transition).

$$\Delta G_m = R \cdot T \cdot (n_1 \cdot \ln \varphi_1 + n_2 \cdot \ln \varphi_2 + n_1 \cdot \varphi_2 \cdot \chi) \quad \text{Equation S4.3}$$

FHM model combines the free energy of melting with the free energy of dissolution into the same framework in Equation S4.4.

$$\begin{aligned} \Delta G = & \varphi(\Delta H_m - T \cdot \Delta S_m) + R \cdot T \cdot \left(\frac{\varphi}{X_1} \right) \cdot \ln \varphi \\ & + (1 - \varphi) \cdot \ln(1 - \varphi) + \varphi \cdot (1 - \varphi) \cdot W_{12} \end{aligned} \quad \text{Equation S4.4}$$

Upon dissolution, ΔG becomes 0 which ultimately yields Equation S4.5, where the $\frac{\varphi \cdot (1 - \varphi) \cdot W_{12}}{R \cdot (\varphi \cdot \ln(\varphi) + (1 - \varphi) \cdot \ln(1 - \varphi))}$ term is derived from Flory-Huggins, and the $\frac{\varphi \cdot \Delta H_m}{\varphi \cdot \Delta S_m}$ term is derived from the melting theory of the pure compounds.

$$T_{m,s} = \frac{\varphi \cdot \frac{\Delta H_m}{R} + \frac{\varphi \cdot (1 - \varphi) \cdot W_{12}}{R}}{\varphi \cdot \frac{\Delta S_m}{R} - \left(\frac{\varphi}{X_1} \cdot \ln \varphi + (1 - \varphi) \cdot \ln(1 - \varphi) \right)} \quad \text{Equation S4.5}$$

4.6.3 Solubility curves of nBA gels

4.6.3.1 First method based on T_m^0

The solubility curves for 5BA and 6BA gels, as representatives of odd and even gels, were plotted using T_m^0 of gels at different concentrations which were obtained from fitting DSC_N(T) model to the second heating trace of 5BA and 6BA gels at different

concentrations (Figure S4.3). It is worth to note that the DSC traces of 5BA gels at different concentrations show that the increase of both the melting temperature and enthalpy is proportional to the increase in the concentration of 5BA gels (Figure S4.3a). However, this is not the case for 6BA gels (Figure S4.3b). This could have been caused due to not scooping out homogeneous samples for DSC measurements, although gels looked uniform, or due to the solvent evaporation during sample preparation, although hermetically sealed pans were used for the measurements.

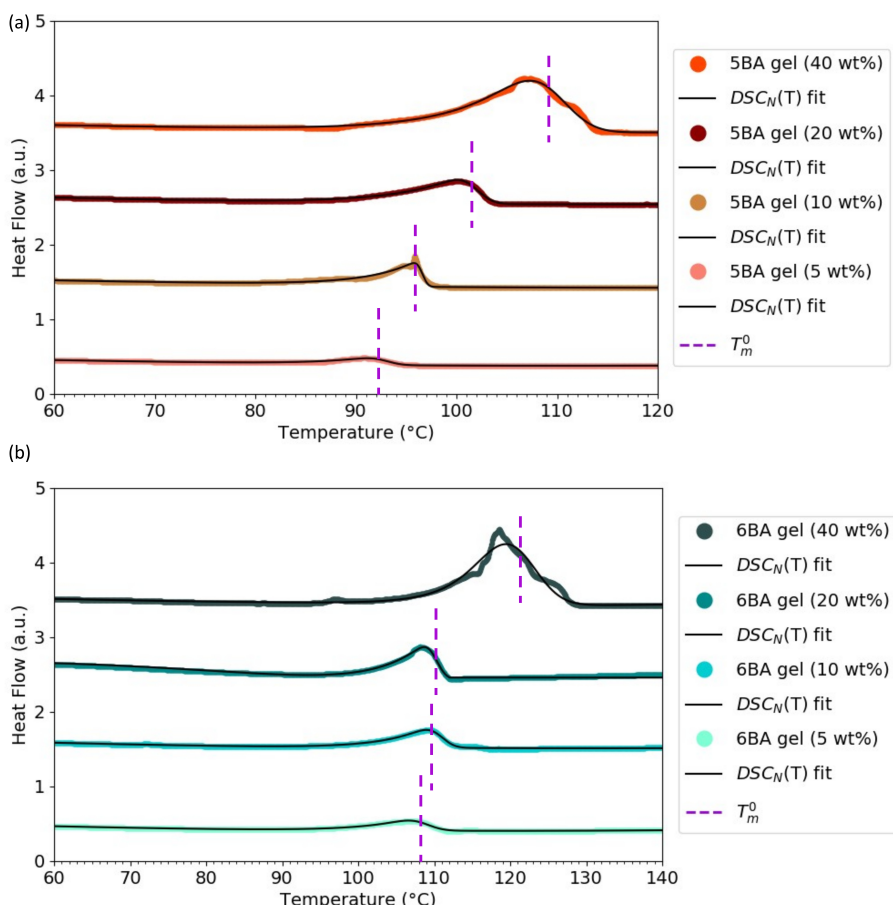


Figure S4.3 $DSC_N(T)$ model fitted to the second heating traces of: a) 5BA gels, b) 6BA gels at different concentrations yielding T_m^0 of the gels (curves were shifted vertically for clarity).

4.6.3.2 Second method based on the cumulative integration of DSC trace

The second approach that we implemented was to obtain the solubility curve based on the cumulative integration of the melting transition of the nBA gel (20 wt%). The underlying rationale of this method is that DSC technique measures the heat uptake for an endothermic transition while the temperature increases. The consumed heat in DSC corresponds to the necessary heat for dissolution of a fraction of the gel crystals. Evidently the total heat taken up in the DSC heating trace corresponds to the heat consumed during the dissolution process.

As Figure S4.3 shows, the nearly similar shape of the DSC curves for nBA gels at different concentrations allows to obtain the solubility curve of the gel from a single DSC trace. In this method, the cumulative integration of the peak area in the single DSC trace (20 wt%) up to the endpoint, the maximum concentration, is calculated. At low temperatures of the heating trace, the solubility of the gelator is assumed to be reasonably close to zero and at the end of the transition peak all gelator molecules are dissolved. By assuming that the uptake of the heat is linearly proportional to the concentration, as heat capacity hardly changes over a small temperature window (on average 20 °C), the solubility curve of 5BA as an example is obtained using the integration of the DSC trace (Figure S4.4a) and inversion of x and y axes (Figure S4.4b). The resulting solubility curve for 5BA is plotted in Figure S4.4c.

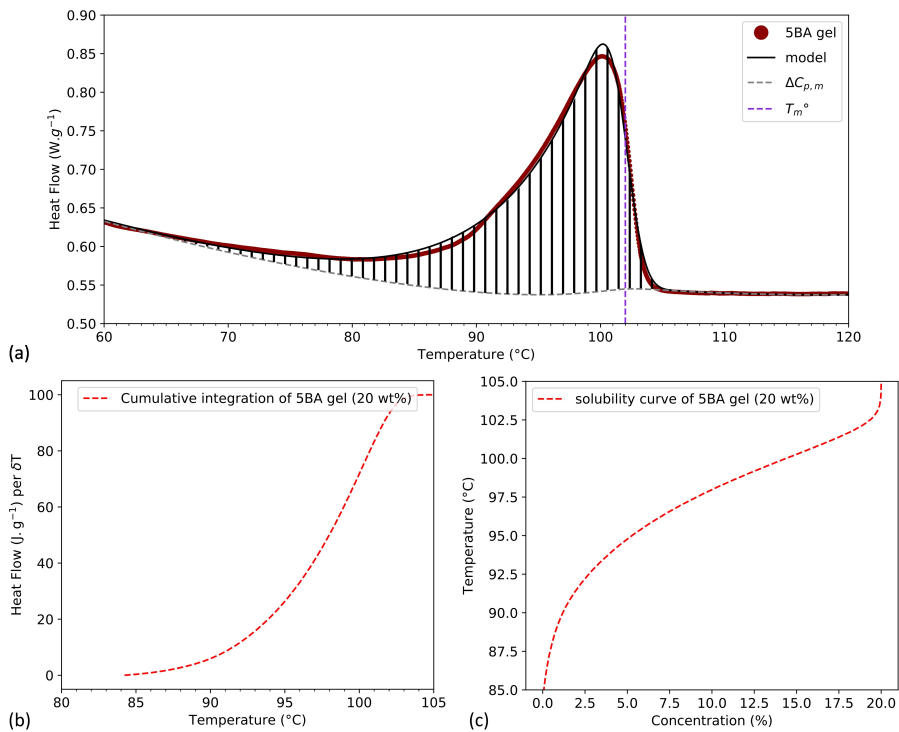


Figure S4.4 Cumulative integration method used to plot the solubility curve for 5BA gel as an example: a) the second heating DSC trace of 5BA gel (20 wt%) and the integration of the peak region, b) cumulative integration of 5BA DSC trace versus temperature, c) the solubility curve for 5BA gel showing temperature change with change in concentration.

4.6.4 Microstructure evolution of gels with change in the concentration

Increasing the concentration of 5BA gelators in xylene results in a microstructural evolution in the gel state; the woven structure at 5 wt% turns into the mixture of woven and spheres at 10 wt% and 20 wt%. The woven fibers change to sheet-like structure at 40 wt% (Figure S4.5). For 6BA gels at all concentrations, sheet-like structures are observed which are more densely aggregated at lower concentrations. At higher concentrations (20 wt% and 40 wt%), larger sheets have formed.

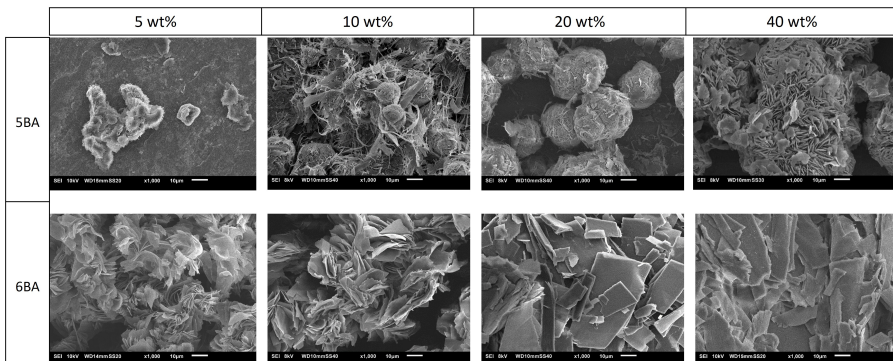


Figure S4.5 SEM images (at 1000x magnification) of 5BA and 6BA gels at different concentrations showing the microstructural evolution upon increasing the concentration from 5 wt% to 40 wt%.

4.6.5 FHM model fitted to the solubility curves of nBA gels (20 wt%)

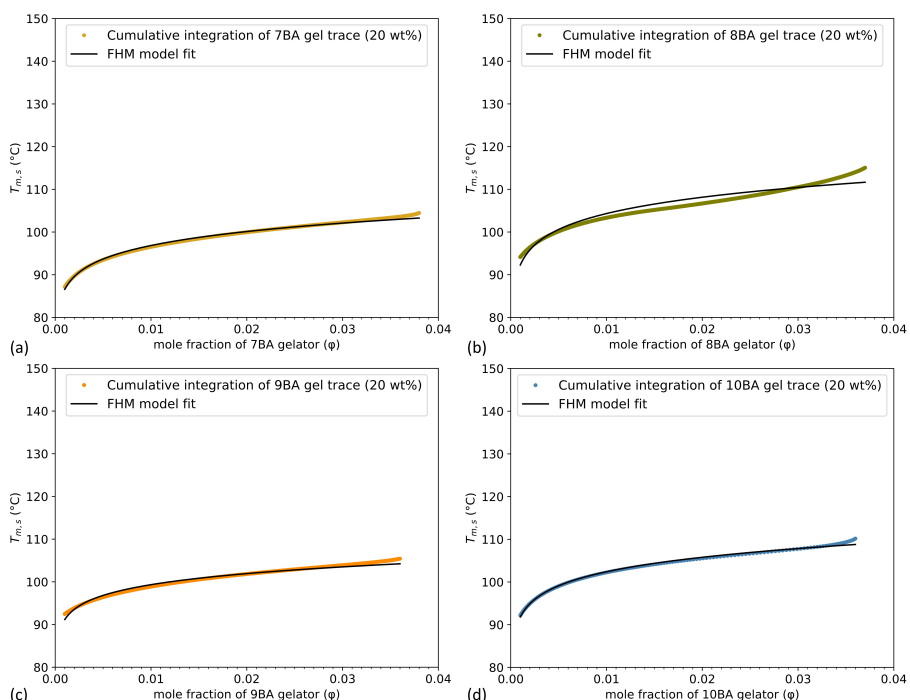


Figure S4.6 FHM model fitted to the solubility curves of gels (20 wt%): a) 7BA, b) 8BA, c) 9BA, and d) 10BA. These solubility curves were obtained from the cumulative integration of DSC traces from the onset up to the endpoint, where 100 % of the gels dissolve.

4.6.6 XRD patterns of nBA gels (20 wt%) in comparison with their gelators in the solid state

Using the indexing of the nBA gelators in the solid state (chapter 3)³⁷, the $00l$ reflections are present in both odd and even nBA gels (Figure S4.7) which indicate the regular layer spacing even though some higher order reflections have relatively lower intensities³⁷; the d-spacings of the peaks corresponding to $(00l)$ family of planes representing the lamellar structure of the molecules which is known as the one-dimensional array of molecules stacked on top of one another with a constant bilayer thickness^{1,2}. The c-axis length increases with increasing spacer length which leads to a low-angle shift of the $00l$ peaks. This similarity between the packing in the gel phase and the solid phase is seen in many bisamide and biscarbamate systems; the monocarbamates studied by Sundararajan et al. observed structural similarities between the gel phase and the solid state of the gelators³. Terech et al. reported similar X-Ray diffraction patterns in organogels, xerogels, and crystalline powder of 12-hydroxystearic acid⁴.

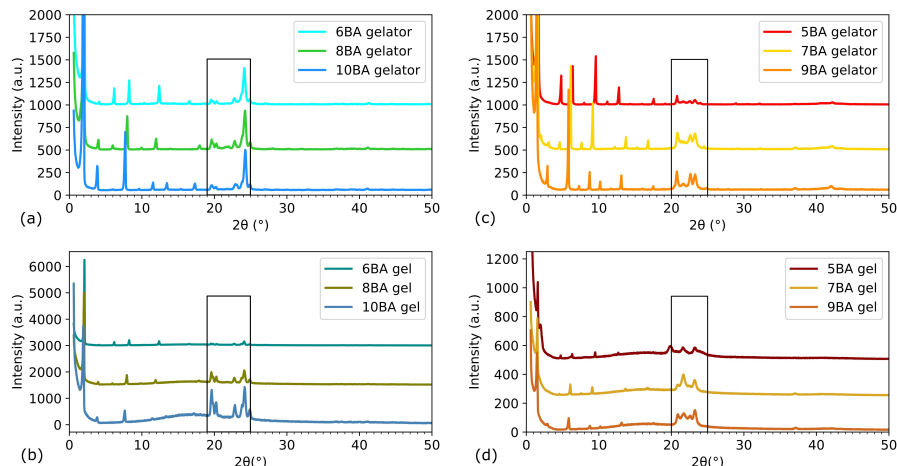


Figure S4.7 Observed XRD patterns of nBA gelators and gels, a) even nBA gelators in the solid state, b) even nBA gels (20 wt%), c) odd nBA gelators in the solid state, d) odd nBA gels (20 wt%). All curves were normalized to the highest intensity and shifted vertically for clarity (the boxes have been added to guide the eyes toward the similarities and differences between the characteristic reflections in the patterns of the solid and gel states).

Chapter 5

Analysis of differential scanning calorimetry (DSC): Determining the transition temperatures, and enthalpy and heat capacity changes in multi-component systems by analytical model fitting

Abstract

We have developed an analytical method to quantitatively analyze differential scanning calorimetry (DSC) experimental data. This method provides accurate determination of thermal properties such as equilibrium melting temperature, latent heat, and change of heat capacity which can be performed automatically without an intervention of a DSC operator. DSC is one of the best techniques to determine the thermal properties of materials. However, the accuracy of the transition temperature and enthalpy change can be affected by artefacts caused by the instrumentation, sampling, and the DSC analysis methods which are based on graphical constructions. In the present study, an analytical function ($DSC_N(T)$) has been developed based on an assumed Arrhenius crystal size distribution together with instrumental and sample-related peak broadening. The $DSC_N(T)$ function was successfully applied to fit the experimental data of a substantial number of calibration and new unknown samples, including samples with an obvious asymmetry of the melting peak, yielding the thermal characteristics such as melting and glass transition temperatures, and enthalpy and heat capacity change. It also allows very accurate analysis of binary systems with two distinct but severely overlapping peaks and samples that include a cold crystallization before melting.

5.1 Introduction

Differential scanning calorimetry (DSC) is a widely and commonly-used thermoanalytical technique to characterize the thermal properties of materials such as transition temperature (T°_t) and change in enthalpy (ΔH) ¹. There are different types of DSC technique such as heat flux and power compensation. In power compensation DSC, the heat flow in the form of electrical power as a function of time (isothermal experiments) or temperature (non-isothermal experiments), respectively, is measured by the instrument. The principle underlying the power compensating DSC is that during endothermic or exothermic chemical reactions or physical phase transitions occurring in the sample, a compensating power needs to be released or absorbed in a sample relative to the reference. In fact, the furnace is heated up or down at a constant rate to keep the temperature of the sample and reference the same. The difference in the heat flow is due to the difference in the heat capacity of the sample and the reference which appears as an endothermic or exothermic peak in the DSC trace ².

The DSC trace recorded for melting of an ideal sample, fully crystalline or 100% pure compound with low thermal resistance, is in theory an infinitely sharp precisely-defined temperature, which could be imagined as a delta function spike in the heat capacity (Figure 5.1a) ³. However, in practice DSC records the heat flow as a distribution, which for simplicity could be assumed to be a Gaussian bell-shaped curve (Figure 5.1a). The Gaussian broadening is a combination of some artefacts caused by sampling (such as mass and geometry), the sample quality itself (such as the presence of a distribution of crystal sizes and/or impurities), and the instrumentation which may cause the sharp symmetric DSC peak turning into an asymmetric distribution as schematically shown in Figure 5.1b. The instrumental artefacts may be due to imbalances in the instrument which can cause instrument baseline features that include (at least) an offset, slope, and curvature. It can also be due to the heat capacity effects caused by the different thermal resistance of different compartments, in other words, the thermal conductivity through the outer and inner interfaces (calorimeter/pan and pan/sample respectively) which can reduce the resolution of the recorded trace ⁴.

Recorded DSC traces are usually analyzed by an operator via the built-in software of the DSC equipment. The determination of the key elements, such as the peak positions and peak area are usually done manually for the further analysis which is typically as follows; the section of the curve between T_i , where the curve of measured values begins to deviate from the extrapolated initial baseline, and T_f , where it reaches again the extrapolated final baseline, is defined as the peak

(Figure 5.1). In practice, various methods are applied to interpolate the baseline between the initial and the final peak temperature. The linear extrapolations of the initial and final baseline are usually used to determine the extrapolated onset and endset temperature of the peak. The point where the auxiliary line through the rising edge of the peak intersects the linearly extrapolated baseline is usually considered as the onset of transition, which is taken as the transition temperature during calibration; taking a melting transition as an example, the temperature during the melting remains constant which is plausibly valid for reasonably uniform large crystalline materials with a high thermal conductivity such as metals⁵. The determination of the peak area with visual-manual examination is substantially subjective depending on the range of temperature selected by a data analyst for the integration of the area under the peak.

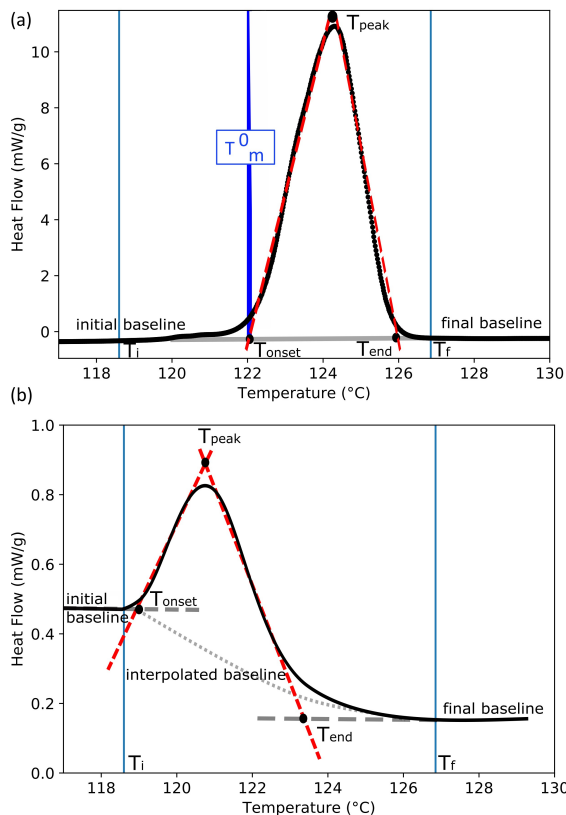


Figure 5.1 Schematic anatomy of DSC trace, the measured heat flow versus temperature: a) sharp spike (blue curve) versus Gaussian distribution (black curve) in the DSC trace with a flat baseline, T_{onset} is the temperature used as the calibration temperature (T_{cal}), b) asymmetric endothermic peak with a skewed baseline.

The possible errors due to the artefacts on top of the visual-manual examination of the DSC data necessitates a reliable method which can determine the main feature of the DSC trace by eliminating the possible variabilities, especially in the case of asymmetric and broad peaks. In this study, an analytical model, $DSC_N(T)$ function, has been developed to provide accurate and reproducible analysis of experimental DSC output data. $DSC_N(T)$ analytical model is based on thermodynamics concepts which takes the baseline features, limited instrumental resolution, and the sample-related effects into account to capture the key features of experimental DSC traces. It is based on the assumption that the sample crystalline structure develops via a rate-limited growth, for instance governed by the temperature-dependent viscosity which has been described by a simple Arrhenius activated process. This gives rise to a crystal size distribution which causes a distribution of melting points. Upon heating, the DSC trace will reflect this Arrhenius-like distribution of melting points. The model also includes the accuracy of the measurement which we assume is limited by a Gaussian smearing of the data which accounts for the shape of the peak.

5.2 Materials and methods

5.2.1 Differential Scanning Calorimetry (DSC) measurement

All the DSC measurements in this study were performed on Perkin Elmer-Pyris diamond Differential scanning calorimeter with two 1g- furnaces (working on the Power-compensation temperature null principle with accuracy/precision: $< \pm 1\% / < \pm 0.1\%$). Nitrogen (99.99% purity) was used to purge the thermal analysis system at a rate of $50 \text{ mL}\cdot\text{min}^{-1}$. Temperature and heat flow calibration were done by the heating scan of indium, a highly pure metal provided by Perkin Elmer with accurately known enthalpies of fusion and melting point, $\Delta H_{\text{fusion}}=6.80 \text{ cal}\cdot\text{g}^{-1}$ or $28.47 \text{ J}\cdot\text{g}^{-1}$ and $T_m^0=156.4 \text{ }^{\circ}\text{C}$, under the same condition as the to-be-measured samples before each measurement. The onset of melting transition (T_{onset} in Figure 5.1a) and the area under the peak from T_i to T_f were chosen respectively for the calibration of the melting temperature and enthalpy of fusion.

Samples were weighed in an aluminum sample pan on a microbalance and the sample pan and an identical empty pan as the reference. Both sample and reference pans were covered by identical aluminum lid and placed in the furnaces of the DSC apparatus. Heating and cooling scans were run at the given heating rate, annotated by R , ($R=dT/dt$). Both pans were heated over a certain temperature range where the transition temperature of the compound is expected (at least $30 \text{ }^{\circ}\text{C}$ below and above the temperature range of interest). A first isothermal/heating scan was run

followed by a fixed cooling cycle preceding a second heating cycle. The traces recorded for the second heating cycles were used for further analysis since the previous thermal histories of the compounds through the synthesis or sample preparation have been eliminated via the first two cycles. Moreover, the pre-heating and cooling scans could also eliminate the sample geometry effect and provide the measurement with a sample with more flat and uniform layer which has a proper contact with the bottom of the pan. The contact between the sample and the sample pan and the location of the pan in the crucible can affect the reproducibility of the extrapolated onset temperature of the melting peak. As the heat transfer between the sample and sample pan can change due to the fusion and this might influence the extrapolated peak onset temperature, each sample must be subjected to at least two subsequent measurements under the same condition. To validate the applicability of $DSC_N(T)$ model for different materials, DSC experiments on a variety of organic and inorganic compounds were conducted and $DSC_N(T)$ model was fitted to the experimental data sets; two sets of experiments were performed on indium: 1) variable heating rates, investigated between 2–50 $K \cdot min^{-1}$ for a small sample of 7 mg and variable sample mass with constant heating rate of 2 $K \cdot min^{-1}$, for different samples within 1–54 mg. To assess the level of errors associated with the experiment and the fitting procedure, three samples with nearly identical mass from the identical benzoic acid (99%, Metler Toledo) were heated at 2 $K \cdot min^{-1}$. The heating of stearic acid with two different degrees of purity (95% and 97%, Sigma-Aldrich), Poly((R)-3-hydroxybutyrate-co-(R)-3-hydroxyvalerate-co-(R)-3-hydroxyhexanoate), commonly known as PHBVH, with the composition of 3-Hydroxyhexanoic acid content, 4.1%, 3-Hydroxyvaleric acid content, 2.3%, PHH content, 4.1%, PHV content, 2.3% in powder form ($M_n=1,000,000$, Sigma-Aldrich), and 8OCB (4'-octyloxy-4- cyanobiphenyl), commercially available in the form of powder (crystalline phase) were performed under the above-mentioned conditions. Likewise, the bisamide gelators varying in the number of bridging carbons between amide groups (5, 6, 7, 8, 9, and 10) used in all the experimental studies were synthesized based on the protocol of our previous study ⁶. Binary bisamides of 5BA6BA have been prepared by mixing the single 5BA and 6BA at different molar ratios which were mechanically stirred in the molten state. The subscripts show the molar ratio of the individual compounds, for example (5BA)₁(6BA)₇ indicates that 5BA and 6BA were molecularly mixed in 1:7 molar ratio.

The initial estimation of the transition temperatures on the raw data of the DSC experiments were done by means of the built-in software of Diamond DSC machine, Pyris. Prior to the data collection for the analysis by Pyris or $DSC_N(T)$ analytical model,

the heat flow of the raw data (mW) was normalized per mass of the sample (mg) resulting in ‘normalized heat flows’ (W/g). The normalized data were transferred from the Perkin-Elmer computer into ASCII format. The data visualization has been done by Python and in all graphs the endothermic peaks were plotted in an upward direction. The non-linear curve fitting have been done by Python programming language. Non-linear least squares (NLLS) from `scipy.optimize.curve_fit` module has been used to fit the $DSC_N(T)$ function to the experimental data. It takes the independent variable and the function parameters and optimizes the parameters within a defined Lower and upper bounds to minimize the sum of squares of nonlinear functions. In some cases, a manual fitting was applied to improve the optimized parameters by finding the global minimum using the solver in Microsoft excel. The curve fitting consisted of the entire temperature range on the X-axis which is broad enough to cover the peak region and the precise baseline determination on the tails at both sides of the peak minimum. This improves the reproducibility of the fitting process and the precision of the fit statistics. For the purpose of improving the illustration resolution, the temperature ranges were further narrowed to the peak and baseline domain in all subsequent figures, although experimental data and fit are available over the entire experimental domain.

5.2.2 Theoretical principles and calculation of $DSC_N(T)$ analytical model

There are abundant models and theoretical methods explaining the thermodynamic of phase transitions in materials using DSC experimental data ⁷⁻¹⁶. However, the quantitative description of DSC which can deconvolute the superposition of the underlying thermal phenomena is missed. In DSC trace of heat flow versus temperature, the slope is representative of the heat capacity of the samples (Equation 5.1) (if the trace has been normalized with respect to the entire mass of the sample, then the slope is representative of the specific heat capacity) ¹⁷. The heat capacity itself at T_m^0 in an ideal DSC measurement (Figure 5.1a) would be infinite but in practice is a rather broad trace due to instrumental broadening, non-isothermal conditions, and impurity effects ¹⁸⁻²⁰.

$$C_p = \frac{dH}{dT} \quad \text{Equation 5.1}$$

In fact, the DSC instrument measures the differential heat flow absorbed or released by the sample with respect to the reference in terms of the power which is the heat exchange rate (Equation 5.2).

$$P(t) = \frac{dH}{dt}$$

Equation 5.2

By division of the fraction in Equation 5.2 with respect to Equation 5.1, Equation 5.3 is obtained where R is the heating rate imposed by the instrument.

$$P(t) = \frac{dH}{dt} = \frac{dH}{dT} \cdot \frac{dT}{dt} = C_p(T) \cdot R$$

According to the Equation 5.4, $C_p(T)$ can be directly measured by division of power to the rate of heating which for a semi-crystalline polymer is shown schematically in Figure 5.2.

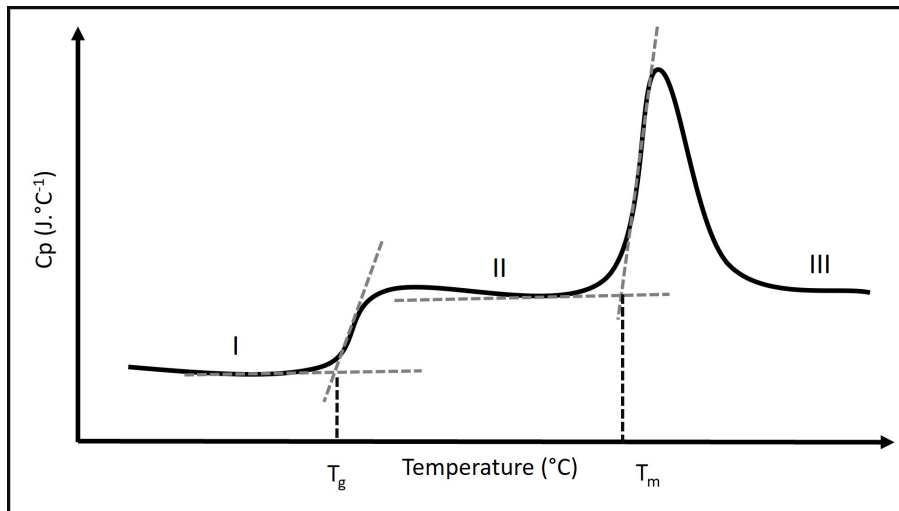


Figure 5.2 A schematic DSC (C_p versus Temperature) of semi-crystalline polymers over the range of temperature where glass transition and melting transition occur at T_g and T_m respectively.

$$C_p(T) = \frac{P(t)}{R}$$

Equation 5.4

The heat capacity of the sample in different states can be defined as following: below T_g where the amorphous and crystalline regions exist in semi-crystalline materials, the specific heat capacity can be calculated by Equation 5.5 where Φ_k is the fraction of the crystalline phase, accordingly $(1 - \Phi_k)$ is the fraction of an amorphous glassy state. The parameters, $C_{p,k}$ and $C_{p,g}$, are respectively the heat capacity of the crystalline and glassy phases of the partially melted material. In region II, between T_g and T_m^0 , C_p is defined as Equation 5.5:

$$C_p = \Phi_k \cdot C_{p,k} + (1 - \Phi_k) \cdot C_{p,g}$$

Equation 5.5

In region III, where the entire material has melted and is in the liquid state, C_p is defined as $C_{p,l}$. In practice, the melting transition spreads out as a Gaussian distribution trace due to the distribution of crystal size or lamellar domains giving rise to a melting point distribution, notated as $\rho(T)$. The latent heat of melting is driven by the transition of the crystalline state to the liquid state which therefore is $(1 - \Phi_k) \cdot \Delta H_m$.

The total heat capacity of a melted material is the summation of the heat capacity in the three regions, namely below (I), during (II), and above the melting transition or region (III) which is represented in Equation 5.6:

$$C_p(T) = \frac{P(T)}{R} = \frac{dH}{dT} = C_{p,k} + (C_{p,L} - C_{p,k}) \cdot \int_0^T \rho(T) dT \quad \text{Equation 5.6}$$

The normalized heat flow at a given temperature in the DSC endothermic curve is proportional to the mass fraction of the molten crystals at that temperature ¹⁴. The crystal size distribution $\rho(T)$ can be derived from the Arrhenius function¹ (Equation 5.7) which is linearized around the equilibrium melting point (T_m^0).

$$K = A \cdot e^{\frac{-E_a}{R \cdot T}} \quad \text{Equation 5.7}$$

The crystal size distribution, $\rho(T)$, is calculated by defining the Arrhenius Equation around T_m^0 with a small ΔT , the melting point distribution, where E_a is the activation energy of the T which is dependent of the viscosity around T_m^0 (Equation 5.8).

$$\rho(T) = e^{\frac{E_a}{R \cdot T_m^0}} \cdot e^{\frac{-E_a}{R \cdot T}} \quad \text{Equation 5.8}$$

Here, $\frac{E_a}{R}$ is the activation energy of the process per mole, therefore $e^{\frac{E_a}{R}}$ is a large constant value, notated as A , where linearizing around T_m^0 and $\alpha = \frac{E_a}{R \cdot (T_m^0)^2}$ with the unit of (K^{-1}) solves the Equation 5.9 to give Equation 5.10:

$$\rho(T) = e^{\alpha \cdot \Delta T} \quad \text{Equation 5.9}$$

The crystal size distribution, $\rho(T)$ calculated based on Equation 5.10 is not the normalized surface area since the area under the melting transition is associated to

¹ Arrhenius function describes the dependence of the rate constant of a chemical reaction or physical transition on the absolute temperature (Equation 5.7) where K is the rate constant, T is the absolute temperature (Kelvins), A is the pre-exponential factor, E_a is the activation energy for the reaction (in the same units as RT), and R is the universal gas constant).

the crystalline fraction of the material, therefore $\int \rho(T) dT = 1$. The surface under the melting transition trace (Z) is calculated by Equation 10 as follow:

$$Z = \int_0^{\infty} e^{\alpha x} dx = \frac{1}{\alpha} e^{\alpha x} \Big|_{-\infty}^0 = \frac{1}{\alpha} \quad \text{Equation 5.10}$$

The normalized $\rho(T)$ around T_m^0 where $\Delta T \leq 0$ is given in Equation 5.11 which yields in Equation 5.12 where $\alpha = \frac{T_a}{T_m^0}$ and the activation temperature is denoted as $T_a = \frac{E_a}{k}$.

$$\rho(T) = \rho(T_m^0 + \Delta T) = e^{\alpha \Delta T} \quad \text{Equation 5.11}$$

$$\rho_N(T) = \frac{1}{\alpha} e^{\alpha \Delta T} \quad \text{Equation 5.12}$$

The limited resolution of a DSC instrument and difference in the thermal conductivity, for example in the case of organic compounds, could cause a non-isothermal measurement which leads to a Gaussian distribution of the heat flow versus temperature where impurities may also influence the sharpness of the transition peak which gives rise to the additional broadening in Gaussian distribution explained by $\rho(T)$. The Gaussian function, $f_N(\Delta T)$, taking the broadening effect into account is defined as Equation 5.13.

$$f_N(\Delta T) = \frac{1}{\sigma \sqrt{2\pi}} e^{-\frac{1}{2} \left(\frac{\Delta T}{\sigma}\right)^2} \quad \text{Equation 5.13}$$

The convolution of $\rho_N(T)$ and $f_N(\Delta T)$ expressing how the shape of one function is modified by the other produces a third function defined as the integral of the product of the two functions after one is reversed and shifted. Therefore, the integral is evaluated for all values of the shift, producing the convolution function (Equation 5.14).

$$DSC_N(\Delta T) = \rho_N(T) * f_N(\Delta T) = \int_{-\infty}^0 \rho(p) f(\Delta T - p) dp \quad \text{Equation 5.14}$$

$$DSC(T) = \frac{A}{2\alpha} e^{\alpha(T-T_m^0)} \operatorname{erfc} \left(\sqrt{\beta} \left(T - T_m^0 + \frac{\alpha}{2\beta} \right) \right) \quad \text{Equation 5.15}$$

The normalization by dividing by $\frac{\alpha}{2} e^{\frac{\alpha^2}{4\beta}}$ gives $\Delta H = \frac{A}{\alpha^2} e^{-\frac{\alpha^2}{4\beta}}$ which with Equation 5.15 yield in Equation 5.16:

$$DSC(T) = \frac{\alpha}{2} e^{\frac{\alpha^2}{4\beta}} \left(e^{\alpha(T-T_m^0)} \operatorname{erfc} \left(\sqrt{\beta} \left(T - T_m^0 + \frac{\alpha}{2\beta} \right) \right) \right) \quad \text{Equation 5.16}$$

The DSC(T) in Equation 5.16 requires to be normalized, regardless of the peak shape, the total energy required to melt the same amount of material remains constant, i.e. the area under the melting trace is constant. Therefore, the total energy to melt the material, ΔH , which is obtained by integration of the DSC trace is equal to 1 ($\int_{-\infty}^{\infty} \frac{\alpha}{2} \cdot e^{\frac{\alpha^2}{4\beta}} \cdot (e^{\alpha(T-T_m^0)} \cdot \operatorname{erfc}(\sqrt{\beta}(T-T_m^0 + \frac{\alpha}{2\beta})) = 1$). By changing the variables as $z = \Delta T + \frac{\alpha}{2\beta}$ thus, $\Delta T = z - \frac{\alpha}{2\beta}$ and solving the integration, the cumulative function is obtained by Equation 5.17:

$$H(z) = \frac{\alpha}{2} \cdot e^{\frac{\alpha^2}{4\beta}} \cdot \frac{1}{\alpha} \cdot (e^{\alpha z} \cdot \operatorname{erfc}(\sqrt{\beta} \cdot z) + e^{\frac{\alpha^2}{4\beta}} \cdot (\operatorname{erf}(\sqrt{\beta} \left(z - \frac{\alpha}{2\beta} \right)) + 1) \quad \text{Equation 5.17}$$

Changing the variables with the original notations yields in Equation 5.18 where the second term represents $\Delta C_{p,m}(T)$ which can be given in the separate Equation, Equation 5.19:

$$\begin{aligned} & \text{DSC}_N(T) \\ &= \Delta H \cdot \frac{\alpha}{2} \cdot e^{\frac{\alpha^2}{4\beta}} \cdot e^{\alpha(T-T_m^0)} \cdot \operatorname{erfc}(\sqrt{\beta}(T-T_m^0 + \frac{\alpha}{2\beta})) \\ &+ \Delta C_{p,m} \cdot \frac{1}{2} \cdot e^{\frac{-\alpha^2}{4\beta}} \cdot (e^{\frac{\alpha^2}{2\beta}} \cdot e^{\alpha(T-T_m^0)} \cdot \operatorname{erfc}(\sqrt{\beta}(T-T_m^0 + \frac{\alpha}{2\beta})) \\ &+ e^{\frac{\alpha^2}{4\beta}} \cdot (\operatorname{erf}(\sqrt{\beta}(T-T_m^0)) + 1)) \end{aligned} \quad \text{Equation 5.18}$$

$$\begin{aligned} & \Delta C_p(T) \\ &= \Delta C_{p,m} \cdot \frac{1}{2} \cdot e^{\frac{-\alpha^2}{4\beta}} \cdot (e^{\frac{\alpha^2}{2\beta}} \cdot e^{\alpha(T-T_m^0)} \cdot \operatorname{erfc}(\sqrt{\beta}(T-T_m^0 + \frac{\alpha}{2\beta})) + \\ & e^{\frac{\alpha^2}{4\beta}} \cdot ((\operatorname{erf}(\sqrt{\beta}(T-T_m^0)) + 1)) \end{aligned} \quad \text{Equation 5.19}$$

5

Adding functions to adjust the fit for baseline and its shifting level gives rise to the equation below:

$$\begin{aligned} & \text{DSC}_N(T) = \Delta H \cdot \frac{\alpha}{2} \cdot e^{\frac{\alpha^2}{4\beta}} \cdot e^{\alpha(T-T_m^0)} \cdot \operatorname{erfc}(\sqrt{\beta}(T-T_m^0 + \frac{\alpha}{2\beta})) \\ &+ \Delta C_p(T) \\ &+ B + C(T - T_m^0) + D(T - T_m^0)^2 \end{aligned} \quad \text{Equation 5.20}$$

The analytical function (Equation 5.20) formulates the heat flow of the DSC trace for melting transition and extends to the other phenomena such as crystallization, glass transition, liquid-crystal phase transitions to calculate the equilibrium transition

temperature. The equilibrium melting temperature, T_m^0 , can be calculated by this function for crystals with infinite size irrespective of how fast or how slow the crystallites crystallize or melt. This function is based on two main functions; the convolution of the Arrhenius-like crystal size distribution function, $e^{\alpha(T-T_m^0)}$, and the Gaussian peak broadening ($e^{\beta(T-T_m^0)}$) as shown in Figure 5.3. The Arrhenius function can cause a negative skew at the low temperature side of the peak (negative asymmetry in peak shape) which is usually the case for a melting transition. Positive asymmetry can occur in the melting peak shape if there are serious thermal gradients caused by a (too) high rate of measurement or too thick sample. Positive asymmetry might also be observed upon crystallization and from thermal decomposition processes, however, this is outside the scope of this manuscript.

The α and β parameters are inversely proportional to the width of the peak, therefore they determine the peak shape in terms of the width and the asymmetry as shown schematically in Figure 5.3c-f. The mathematical terms and physical attributions of the fit parameters of $DSC_N(T)$ are summarized in Table 5.1.

The part of the DSC trace in pre- and post-transition, where no change occurs in the heat flow, is defined as the baseline (Figure 5.1). According to the Equation 5.7, at the end of the melting transition, the whole $C_p(T)$ term turns into $(C_{p,l} - C_{p,k})$ which is the summation of heat capacity during the transition and the post-transition in the liquid state. Above the melting transition in the DSC of heat-flow versus temperature, where the melting of all crystals has completed ($\rho(T)=0$), if the heat capacity of the solid and liquid state are equal ($\Delta C_p = C_{p,l} - C_{p,k} = 0$), the baseline becomes a horizontal flat line. As highlighted in Equation 5.19, in $DSC_N(T)$, $\Delta C_{p,m}$ as one of the fit parameters can be fitted (Table 5.1) and absolute C_p is very inaccurate. For transitions where $\Delta C_p > 1$ or $\Delta C_p < 1$, the baseline steps up or down respectively. This step has defined in the function by the partial adjustment of the slope which smoothly changes from pre- to post-transition, depending on how far the melting transition develops. In fact, $\int_0^T \rho(T) dT$ is the partial melting point which indicates that how much solid is still present in the system by subtracting the amount of the molten compound. On top of this theoretical equation, there is an instrumental calibration-related linear slope in the baseline or a quadratic curvature of the baseline.

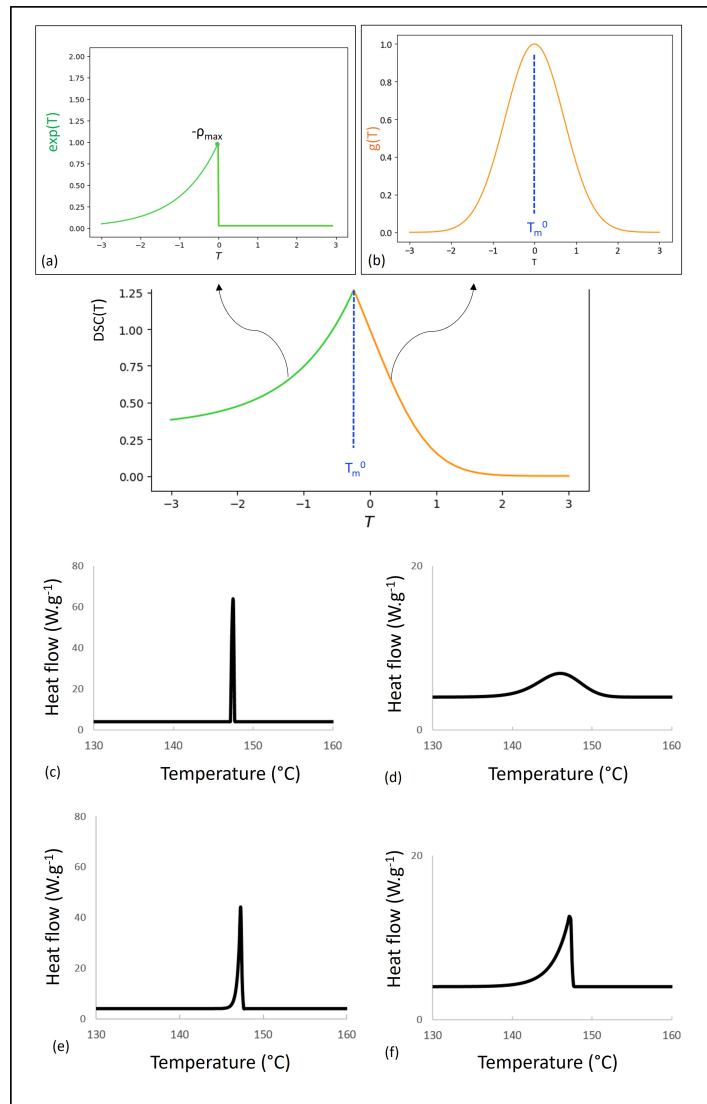


Figure 5.3 Schematic underlying mathematics representing the convolution of the analytical DSC function to two main functions and the effect of α and β on the peak shape, symmetry, and width; a) the Arrhenius function ($\Delta T < 0 : \rho(T).erfc(\Delta T/\omega)$), b) the first order guess of a step-wised function, complementary error function ($\Delta T > 0 : \rho_{\max}.erfc(\Delta T/\omega)$), c) symmetrical narrow peak by large α and β ($\alpha=50$, $\beta=100$), d) symmetrical broad peak by small α and β ($\alpha=0.5$, $\beta=0.1$), e) asymmetrical narrow peak by small α and large β ($\alpha=5$, $\beta=100$), f) asymmetrical broad peak by small α and large β ($\alpha=0.5$, $\beta=50$).

Table 5.1 The variables, functions, and the parameters of the $DSC_N(T)$.

parameter	power units	thermodynamic units	physical attributions and mathematical terms
T_m^0	°C	K	The equilibrium melting point of the phase transition
B	W.g ⁻¹	J.g ⁻¹ .K ⁻¹	Baseline offset
C	W.g ⁻¹ .K ⁻¹	J.g ⁻¹ .s ⁻¹	Linear baseline slope
D	W.g ⁻¹ .K ⁻²	J.g ⁻¹ .s ⁻¹ .K ⁻²	Second order baseline curvature
α	K ⁻¹	K ⁻¹	Strength of the linearized Arrhenius function ($\alpha = Ea/(R.(T_m^0)^2)$ describing the crystal size distribution.
β	K ⁻²	K ⁻²	The parameter in relation to the Gaussian distribution of the peak ($\beta = \frac{1}{2\sigma^2}$).
$\Delta C_{p,m}$	W.g ⁻¹ .K ⁻¹	J. K ⁻¹	The difference between the heat capacity of the solid and liquid state.
$e^{\alpha.(T-T_m^0)}$	-	-	The Arrhenius function determining the rising edge of the curve.
$erfc\left(\sqrt{\beta}(T-T_m^0+\frac{\alpha}{2\beta})\right)$	-	-	Erfc, the complementary error function, describes the falling edge of the peak as it returns to the baseline.
ΔH	W.g ⁻¹	J.g ⁻¹	The coefficient of $DSC_N(T)$ function representing the change in enthalpy associated with the phase transition.
R^2	-	-	The statistical measure for the goodness of a fit in a regression function.

5.2.3 Experimental error and fitting residuals

To extract accurate information from a raw DSC trace, three samples with nearly identical mass from the identical benzoic acid were heated under the same condition. The standard deviation of characteristic thermal properties such as T_m^0 and ΔH were obtained once by averaging the values from the raw data analyzed with the Pyris analyzer software which contain the experimental error and graphical examination error, depending on the selected temperature range. The standard deviation of function parameters were obtained by fitting the analytical model $DSC_N(T)$ to the three sets of raw data which contains the experimental error along with the fitting procedure error (Table 5.2). The fitting deviation for each parameter was obtained from the residuals of NLLS. The reported error margins of the fit parameters in this study are the residuals of NLLS rounded to two digits.

Table 5.2 Experimental versus fit errors for DSC measurements^[a].

characteristic parameters	measured with DSC (from the literature ²¹⁾	measured with DSC and analyzed with Pyris	measured with DSC and analyzed with $DSC_N(T)$	fitting deviation (residuals of NLLS)
$\Delta H (J.g^{-1})$	141.6	127.94 ± 2.39	147.50 ± 1.86	147.5022 ± 0.0018
$T_m^0 (^\circ C)$	121.4	122.23 ± 0.06	123.51 ± 0.07	123.5146 ± 0.0002
$\alpha (K^{-1})$	NA	NA	1.95 ± 0.18	1.9595 ± 0.0009
$\beta (K^{-2})$			10.84 ± 4.18	10.8491 ± 0.0529
$\Delta C_{p,m} (W.g^{-1}.K^{-1})$			0.12 ± 0.03	0.1184 ± 0.0006
$B (W.g^{-1})$			0.32 ± 0.13	0.3242 ± 0.0003
$C (W.g^{-1}.K^{-1})$			0.00 ± 0.00	-0.0007 ± 1.3804
$D (W.g^{-1}.K^{-2})$			0.00 ± 0.00	$(2.83 \pm 1.27) \times 10^{-5}$

[a] The values and the errors were obtained by measuring DSC traces of 3 samples of the same Benzoic acid under the same condition and analyzed using Pyris software and fitting of $DSC_N(T)$ to the raw data, NA stands for not available.

5.3 Validation of $DSC_N(T)$ analytical method for different types of materials

5.3.1 Indium as a metal calibration sample

To check the validity of the $DSC_N(T)$, the function was fitted to the experimental DSC curves of indium measured at different mass and heating rates. The traces in Figure 5.4 were measured by heating from 25 °C to 170 °C at different scanning rates after the temperature and heat calibration for each given condition and normalization per mass of the sample. As it is seen in Figure 5.4, the onset has remained constant due to the calibration of the melting temperature defined at the onset of the peak. However, upon increasing the rate of heating the peak and endset values shift to higher temperatures due to the non-isothermal heating at high rates which is a well-known feature of a DSC²².

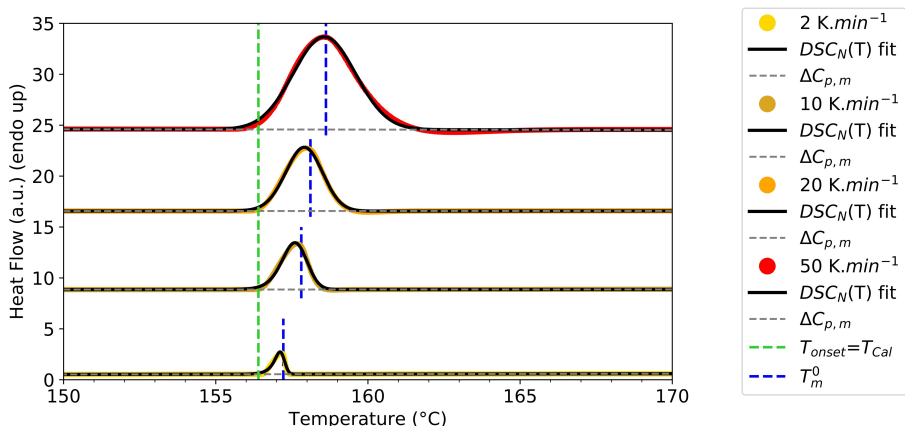


Figure 5.4 DSC of indium during heating from 25 °C to 170 °C at different scanning rates and $DSC_N(T)$ function fitted to the measured curves which were calibrated at the onset for the given rate, the heat flow has been normalized per mass of each sample, the unit of heat flow in each trace is (W.g⁻¹), curves were shifted vertically for clarity.

$DSC_N(T)$ analytical function was fitted to the normalized experimental curves with a good correlation coefficients ($R^2 > 0.99$) for all rates (Table S5.1). The T_m^0 obtained from $DSC_N(T)$ is 157.22 ± 0.00 °C which shifts to 158.62 ± 0.61 °C upon increasing the heating rate from 2 to 50 K·min⁻¹ due to the superimposition of the fit on the shifting peak (Table 5.3). At lower rates where the sample is at a better thermal equilibrium, T_m^0 obtained from the model, 157.22 ± 0.00 °C, is within less than 1 °C different from

156.59 °C reported by National Institute of Standards and Technology (NIST) for indium ²³.

Table 5.3 Fit parameters of the $DSC_N(T)$ for experimental curves of indium heated at different rates^[a].

parameters	literature values ²³	$R=2\text{ K}\cdot\text{min}^{-1}$	$R=10\text{ K}\cdot\text{min}^{-1}$	$R=20\text{ K}\cdot\text{min}^{-1}$	$R=50\text{ K}\cdot\text{min}^{-1}$
ΔH ($\text{J}\cdot\text{g}^{-1}$)	28.51	30.15 ± 0.00	29.37 ± 0.01	28.62 ± 0.01	27.98 ± 0.04
T_m^0 (°C)	156.60	157.22 ± 0.00	157.81 ± 0.00	158.11 ± 0.00	158.62 ± 0.61
α (K^{-1})	NA	4.88 ± 0.01	3.50 ± 0.03	4.44 ± 0.08	19.67^*
β (K^{-2})		37.44 ± 0.14	4.01 ± 0.02	1.54 ± 0.01	0.48 ± 0.03
$\Delta C_{p,m}$ ($\text{W}\cdot\text{g}^{-1}\cdot\text{K}^{-1}$)		0.01 ± 0.00	0.01 ± 0.00	-0.02 ± 0.00	0.00 ± 0.00

[a] The measurements were done using 7 mg of indium after calibration for the given rate (the error margins are from the nonlinear fitting), *nonlinear least squares error out of the bounds due to indeterminate high α value, NA stands for not available.

In the case of indium, the melting peaks measured at the all heating rates are symmetric. The width of the peak in the rising edge has been captured by α which decreases upon increasing the rate. In fact, α is in linear relationship with the activation energy (E_a), depending on the rate and mass of the sample ²⁴. The value of E_a determines the temperature sensitivity of the melting transition; the higher the α and the larger the E_a becomes, the stronger the melting rate changes per the same change in temperature, thus the steeper the slope of the rising edge becomes ²⁵. Although indium has a relatively good thermal conductivity, β decreases by increasing the heating rate, consequently the peaks become broader. The peak area gets larger due to the peak broadening and the incorporated heating rate in the heat flow, which is measured by the DSC instrument as power (mW) (Equation 5.3). The change in enthalpy of the fusion of indium varies from $27.98\pm0.04\text{ J}\cdot\text{g}^{-1}$ to $30.15\pm0.00\text{ J}\cdot\text{g}^{-1}$ which is comparable with the reported value by NIST $28.66\text{ J}\cdot\text{g}^{-1}$. The change in the heat capacity, $\Delta C_{p,m}$, at different rates has remained very close to zero as the baseline levels remains at the same level in pre- and post-transition states. Figure 5.5 presents the DSC curves measured and normalized per mass of the samples ($\text{W}\cdot\text{g}^{-1}$) for different sample mass 1-54 mg at the common heating rate of $2\text{ K}\cdot\text{min}^{-1}$ which is slow enough to keep the sample at the thermal equilibrium. The detected melting peak for 1 mg sample is extremely sharp and symmetric which turn to an asymmetric broad peak for the 54 mg sample where an overload effect causes a non-isothermal heat regime.

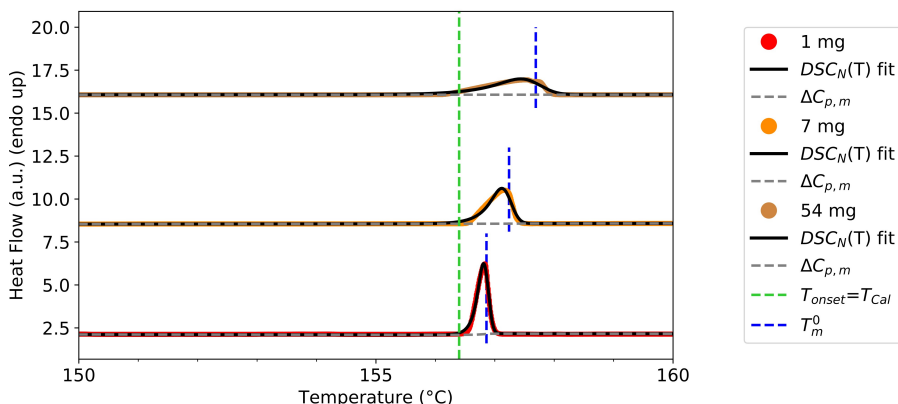


Figure 5.5 DSC of different mass of indium measured with heating from 25 °C to 170 °C at 2 K.min⁻¹ and DSC_N(T) function fitted to the experimental curves calibrated at the onset for the given mass, the heat flow has been normalized per mass of each sample, the unit of heat flow in each trace is (W.g⁻¹), curves were shifted vertically for clarity.

Similar to the rate effect, the onset values have remained constant due to the calibration at the onset while the peak and endset values have shifted toward the higher temperatures due to the increase in the thermal resistance of the samples at larger mass. As thermal transfer is much better across the contact zone between the solid indium and the aluminum pan, initial partial melting occurs with the formation of an interface liquid layer with different thermal properties than the solid indium. Therefore, the higher the mass of indium sample, the higher the thickness of sample, the larger the thermal gradient and temperature lag between these two parts.

The DSC_N(T) fits the DSC experimental traces (Figure 5.5) with a good correlation coefficients ($R^2 > 0.97$) for all rates (Table S5.2). T_m^0 obtained by fitting of the DSC_N(T) on the measurement with 1 mg of indium is 156.86 ± 0.00 °C, which is the closest to the melting point of indium reported by NIST. It slightly shifts to higher temperature for larger sample mass (Table 5.4). β decreases by increasing the mass of the sample due to the larger thermal gradient which makes the peak broader. Similarly, α decreases which leads to the decrease in the slope of the rising edge of the peak due to the higher thermal gradient caused by higher mass for 7 mg sample. Progressively, increasing the mass to 54 mg decreases the slope of the rising edge since α decreases due to the recrystallization of the molten crystals on the existing non-molten crystals which spreads the crystal size distribution. A dramatic increase in the width of the peak at 54 mg is indeed caused by the increase in the domain of

erfc at the decaying edge, the decrease in β and α , manifesting the width of the peak in the rising edge. ΔH obtained from the function fitted to the trace of 1 mg indium is the closest to the reported enthalpy for indium by NIST. The change in heat capacity, $\Delta C_{p,m}$, is zero which is manifested in the same baseline level of pre- and post-transition tails (Table 5.4).

Table 5.4 Fit parameters of the $DSC_N(T)$ for experimental curves of indium samples with different mass^[a].

parameters	literature values ²³	$m=1$ mg	$m=7$ mg	$m=54$ mg
ΔH (J g ⁻¹)	28.51	29.61±0.00	30.27±0.00	29.71±0.00
T_m^0 (°C)	156.60	156.86±0.00	157.24±0.00	157.69±0.00
α (K ⁻¹)	NA	10.25±0.03	4.43±0.01	1.87±0.00
β (K ⁻²)		98.60±0.27	34.49±0.11	8.34±0.03
$\Delta C_{p,m}$ (W.g ^{-1.K⁻¹)}		0.06±0.00	0.01±0.00	0.00±0.00

[a] all samples were heated at 2 K.min⁻¹ measured after calibration at the onset for the given mass (the error margins are from the nonlinear fitting), NA stands for not available.

5.3.2 Stearic acid as an organic compound

The DSC traces of 6 mg of stearic acid (SA) with two different purities (95% and 97%) were measured at 2 K.min⁻¹ after calibration of indium for the given rate and sample mass (Figure 5.6).

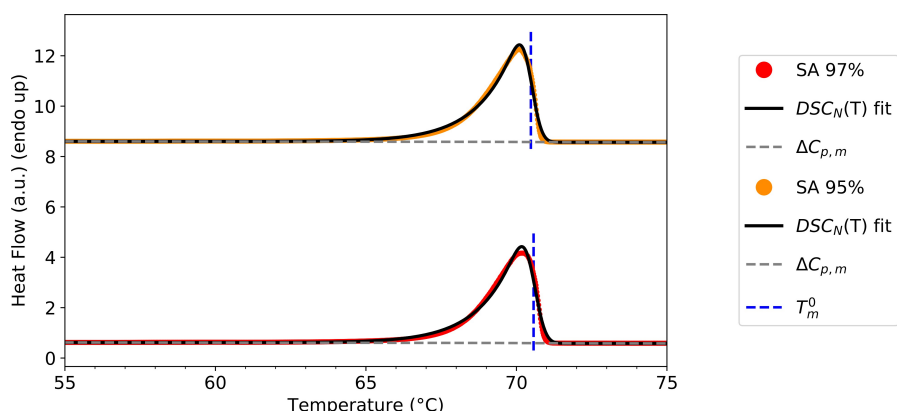


Figure 5.6 DSC of 6 mg SA with different purities heated at 2 K.min⁻¹ and $DSC_N(T)$

function fitted to the measured curves after calibration at the onset for the given mass and rate (curves were shifted vertically for clarity).

The $DSC_N(T)$ fits well to the both heating curves, $R^2=0.99$ (Table S5.6). T_m^0 obtained from the function is 70.5 °C for both SA samples which is in a good agreement with the reported T_m^0 in the literature ²⁶. The temperature shifts to the lower temperatures due to the presence of impurity. This shift is not significant enough to be detected by the DSC instrument due to its low resolution. However, it has affected the β values relating to the peak width; β increases for the SA (97%) which has shown the less broad peak (Figure 5.6). Compared to indium trace measured for nearly the same rate and mass, β of SA samples ($\beta_{SA\ 95\%}=6.08\pm0.07\ K^{-2}$ and $\beta_{SA\ 97\%}=7.05\pm0.08\ K^{-2}$) are significantly smaller than β of indium ($\beta_{indium}=34.49\pm0.11\ K^{-2}$). As a result the melting peaks of SA samples have become more asymmetric and broader at the declining edge of the peak due to its relatively lower thermal conductivity. Despite β , α has not changed significantly (Table 5.5); in fact, the presence of more impurity could lead to the faster crystallization but not necessarily narrower crystal size distribution. The latent heat obtained from $DSC_N(T)$ for SA (95%) and SA (97%) are in good agreement with the enthalpy of fusion of SA measured with DSC at 10 K.min⁻¹ by Xu et al ²⁷. The deviation can be due to the weighing accuracy. The negative $\Delta C_{p,m}$ for both samples ($-0.02\pm0.00\ W.g^{-1}.K^{-1}$) indicates the step-down in the baseline moving from pre- to the post-transition tail.

Table 5.5 Fit parameters of the $DSC_N(T)$ fitted to the experimental curves of stearic acid (SA) with different degrees of impurities^[a].

parameters	literature values	SA 95%	SA 97%
$\Delta H\ (J.g^{-1})$	216.5 ²⁶	215.73 ± 0.01	213.99 ± 0.01
$T_m^0\ (^{\circ}C)$	69.3 ²⁷	70.57 ± 0.00	70.48 ± 0.00
$\alpha\ (K^{-1})$	NA	0.82 ± 0.00	0.81 ± 0.00
$\beta\ (K^{-2})$		6.08 ± 0.07	7.05 ± 0.08
$\Delta C_{p,m}\ (W.g^{-1}.K^{-1})$		-0.02 ± 0.00	-0.02 ± 0.00

[a] The samples were heated at 2 K.min⁻¹ after calibration at the onset for the given mass and rate, NA stands for not available.

5.3.3 Phase transitions in a liquid crystal compound

Three endothermic peaks were observed in the DSC experimental trace of 8OCB (4'-octyloxy-4- cyanobiphenyl) heated from 0 °C to 100 °C at 2 K.min⁻¹ (Figure 5.7).

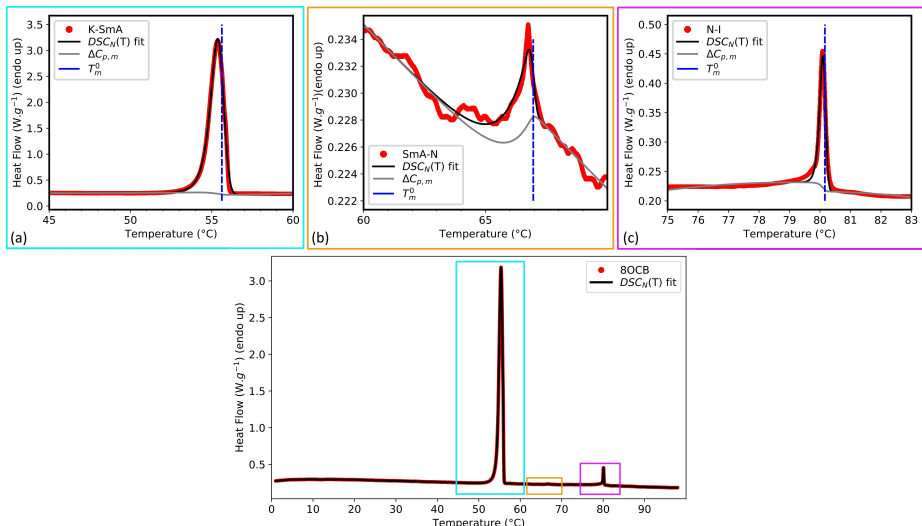


Figure 5.7 DSC of 8OCB and $DSC_N(T)$ function fitted to the measured curves for 6 mg of 8OCB heated at $2\text{ K}\cdot\text{min}^{-1}$ after calibration for the given mass and rate, $\Delta C_{p,t}$ is the change in heat capacity for different liquid crystal transitions: a) K to Sm-A, b) Sm-A to N, and c) N to I.

The $DSC_N(T)$ function fits to the first and third transition peaks with asymmetric shape very well ($R^2 > 0.99$) and ($R^2 = 0.97$) respectively (Table S5.7). The obtained temperature of each transition, T_t^0 , for these peaks are respectively at $55.62 \pm 0.00\text{ }^\circ\text{C}$, $66.96 \pm 0.00\text{ }^\circ\text{C}$, and $80.16 \pm 0.00\text{ }^\circ\text{C}$ which could be attributed to the transitions from crystalline to Smectic-A phase (K-SmA) at $53.54\text{ }^\circ\text{C}$, Smectic-A to Nematic (SmA-N) at $65.25\text{ }^\circ\text{C}$, and Nematic to isotropic (N-I) at $78.53\text{ }^\circ\text{C}$ respectively (Table 5.6). The enthalpy change of these transitions were obtained from the $DSC_N(T)$ were in good agreement with the values reported in literature²⁸⁻³⁰. The difference in the obtained enthalpy change and the reported values is due to different calibration approaches, setting peak value instead of the onset value.

Table 5.6 Fit parameters of the $DSC_N(T)$ for experimental curves of 6 mg of 8OCB (4'-octyloxy-4- cyanobiphenyl)^[a].

8OCB	1 st peak (K-SmA)	2 nd peak (SmA-N)	3 rd peak (N-I)
ΔH (J.g ⁻¹)	97.05±0.00	0.21±0.00	1.74±0.00
literature ΔH (J.g ⁻¹)	140.32 ²⁹	0.9±0.9 ³⁰	1.55±0.05 ³⁰
T_m^0 (°C)	55.62±0.00	66.96±0.00	80.16±0.00
literature T_m^0 (°C)	53.54 ²⁹	65.25 ²⁹	78.53 ²⁹
α (K ⁻¹)	2.31±0.00	1.01±0.01	10.36±0.12
β (K ⁻²)	5.72±0.02	36.21±2.16	91.10±1.15
$\Delta C_{p,t}$ (W.g ⁻¹ .K ⁻¹)	-0.06±0.00	0.01±0.00	-0.01±0.00

[a] The samples were heated at 2 K.min⁻¹ after temperature calibration of indium at the onset for the given mass and rate (the error margins are from the nonlinear fitting).

5.3.4 Low molecular weight bisamide gelators with different number of methylene spacers between the amide groups

As Figure 5.8 shows, the melting peaks of bisamide low molecular mass gelators, briefly nBA where n represents the odd and even spacer length between the amide groups, were observed upon heating at 10 K.min⁻¹. $DSC_N(T)$ function fits remarkably well to the experimental traces of all these nBA compounds, $R^2>0.98$ (Table S5.8). T_m^0 and the ΔH of fusion for our newly synthesized bisamide compounds (Table 5.7) were obtained more reliably from the $DSC_N(T)$ than the analyzing software⁶.

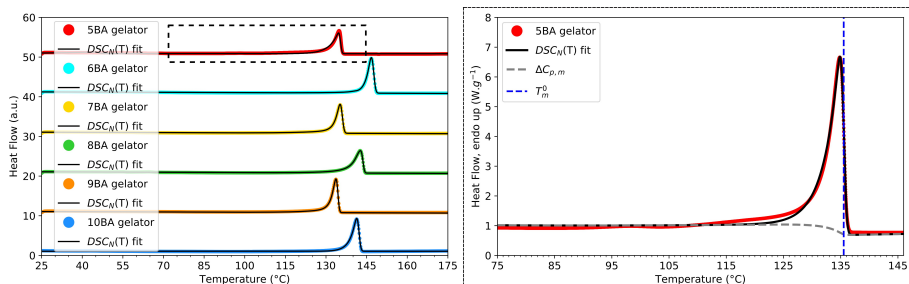


Figure 5.8 DSC experimental traces and $DSC_N(T)$ function fitted to the measured curves of nBA compounds (6 mg) heated at 10 K.min⁻¹ after temperature calibration of indium at the onset for the given mass and rate (curves were shifted vertically for clarity).

Table 5.7 Fit parameters of the $DSC_N(T)$ for experimental curves of 6 mg of odd and even bisamides^[a].

gelators	5BA	6BA	7BA	8BA	9BA	10BA
$\Delta H (J.g^{-1})$ from $DSC_N(T)$	126.18±0.04	168.66±0.07	140.88±0.09	155.12±0.12	149.21±0.08	172.20±0.06
$\Delta H (J.g^{-1})$ from Pyris	100.2±5.7	117.6±2.5	113.1±6.3	123.1±3.4	118.4±5.3	139.6±2.6
$T_m^0 (^{\circ}C)$ from $DSC_N(T)$	135.52±0.00	147.46±0.00	135.97±0.00	143.53±0.00	132.50±0.00	142.11±0.00
$T_m (^{\circ}C)$ from Pyris	135±1	147±1	135±1	143±1	134±1	141±1
$\alpha (K^{-1})$	0.39±0.00	0.63±0.00	0.52±0.00	0.31±0.00	0.52±0.00	0.48±0.00
$\beta (K^{-2})$	3.01±0.04	1.19±0.02	1.50±0.03	1.69±0.04	2.68±0.05	1.40±0.02
$\Delta C_{p,m} (W.g^{-1}.K^{-1})$	-0.44±0.01	-0.31±0.01	-0.40±0.01	-0.28±0.01	-0.35±0.01	-0.29±0.01

[a] The samples were heated at 10 K.min⁻¹ after calibration at the onset for the given mass and rate (the error margins are from the nonlinear fitting) and calculated T_m and ΔH from Pyris analyzing software, these compounds were newly synthesized and there is no data available in the literature for comparison.

$\Delta C_{p,m}$ of all the traces are negative which shows a downward step in the baseline from pre- to post-melting transition tail (Table 5.7). In crystals where the molecules are free to rattle in the crystal lattice, the heat capacity of the solid state will be higher than the heat capacity of the liquid state where the molecules cannot rattle anymore and they are sterically interacting. As a result, their freedom is lost to a great extent upon melting.

5.3.5 Binary systems (binary mixtures of low molecular weight gelators)

The $DSC_N(T)$ for binary compounds can be obtained based on the Equation 5.21, where T_r is the reference temperature for the overall curved baseline.

$$DSC_N(T) = (\Delta H_1 \cdot \frac{\alpha_1}{2} \cdot e^{\frac{\alpha_1^2}{4\beta_1}} \cdot e^{\alpha_1(T-T_{m,1}^0)} \cdot \operatorname{erfc}(\sqrt{\beta_1}(T-T_{m,1}^0 + \frac{\alpha_1}{2\beta_1})) + \Delta C_{p,1}(T)) + (\Delta H_2 \cdot \frac{\alpha_2}{2} \cdot e^{\frac{\alpha_2^2}{4\beta_2}} \cdot e^{\alpha_2(T-T_{m,2}^0)} \cdot \operatorname{erfc}(\sqrt{\beta_2}(T-T_{m,2}^0 + \frac{\alpha_2}{2\beta_2})) + \Delta C_{p,2}(T)) + B + C(T - T_r) + D(T - T_r)^2 \quad \text{Equation 5.21}$$

The $DSC_N(T)$ function fits to the heat flow curves of all binary mixtures of 5BA and 6BA in different ratios with $R^2=0.99$ (Table S5.9). As Figure 5.9a shows, except for $(5BA)_3(6BA)_1$, two distinct melting peaks were observed in the heating traces of all binary mixtures which indicates the tendency of these molecules for phase

separation. T_m^0 and ΔH for all compounds were obtained reliably from $DSC_N(T)$. For the overlapping peaks $\Delta C_{p,m}$ does not converge due to purely mathematical artefact. However, if the peaks are sufficiently apart with sufficient baseline tail on each side, the cumulative $\Delta C_{p,m}$ can be reliably determined via fitting the function to the DSC trace.

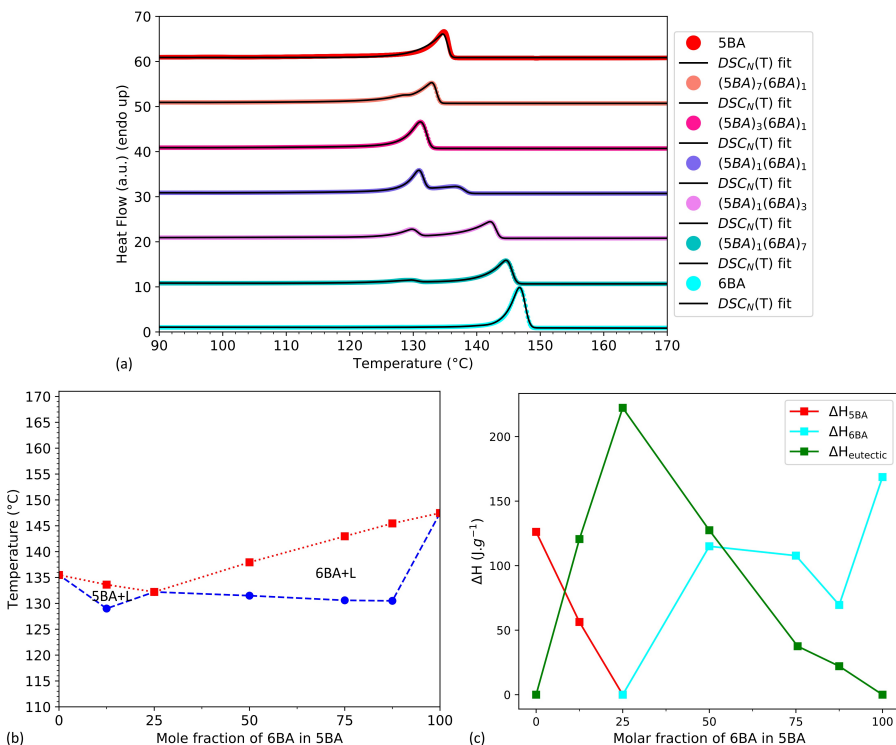


Figure 5.9 a) $DSC_N(T)$ function fitted to the experimental traces of 6 mg of molecularly mixed binary bisamides (blends of 5BA and 6BA in different molar ratios) heated at $10 \text{ K}\cdot\text{min}^{-1}$ after calibration at the onset for the given sample mass and rate, b) phase diagram of binary 5BA6BA, T_m^0 obtained from the $DSC_N(T)$ fitting the DSC traces of 5BA6BA blends at different molar ratios (the error bars from the nonlinear fitting are not visible since they are very small (Table S5.6)), c) enthalpy change of individual phases in 5BA6BA and the total enthalpy change of the compounds at different ratios were obtained from the $DSC_N(T)$ and plotted versus the mole fraction of 6BA in 5BA (the error bars from the nonlinear fitting are not visible since they are very small (Table S5.6)), the trend lines are to guide the eye.

As Figure 5.9b shows, the phase diagram of 5BA6BA mixture is plotted using the accurate T_m^0 obtained for each phase from the fitting of $DSC_N(T)$ to the DSC traces of 5BA6BA (Table 5.8). The mixture with $(5BA)_3(6BA)_1$ composition shows a single

melting transition with the lower melting point (132.21 ± 0.02 °C) compared to single 5BA and 6BA compounds. The occurrence of the mixture at the non-equimolar ratio can be due to the difference in H-bonding patterns of 5BA and 6BA compounds where 5BA has more freedom than 6BA to bond to an adjacent molecule⁶. The latent heat for each phase individually has been obtained from the DSC_N(T) (Table 5.8). As shown in the enthalpy diagram (Figure 5.9c), the mixture (5BA)₃(6BA)₁ has the highest latent heat (222.3 ± 7.07 J.g⁻¹).

Table 5.8 Fit parameters of the DSC_N(T) function fitted to the experimental DSC trace of 6 mg of molecularly mixed binary bisamides (5BA6BA in different ratios)^[a].

binary 5BA6BA	6BA	(5BA) ₁ (6BA) ₇	(5BA) ₁ (6BA) ₃	(5BA) ₁ (6BA) ₁	(5BA) ₃ (6BA) ₁	(5BA) ₇ (6BA) ₁	SBA	
First peak								
ΔH_1 (J.g ⁻¹)	Single peak	22.08±0.05	37.56±0.03	69.54±0.02	222.3±7.07	56.34±0.76	Single peak	
$T_{m,1}^0$ (°C)		130.49±0.03	130.59±0.00	131.49±0.00	132.21±0.02	129.00±0.02		
α_1 (K ⁻¹)		0.17±0.00	0.38±0.00	0.61±0.00	0.07±0.00	0.07±0.00		
β_1 (K ⁻²)		1.20±0.12	1.41±0.04	1.94±0.02	2.43±0.28	1.62±0.21		
$\Delta C_{p,m,1}$ (W.g ⁻¹ .K ⁻¹)	NA							
Second peak								
ΔH_2 (J.g ⁻¹)	168.66±0.07	127.44±0.06	107.76±0.11	115.02±0.12	Single peak	120.6±0.23	126.18±0.04	
$T_{m,2}^0$ (°C)	147.46±0.00	145.46±0.00	142.97±0.00	137.94±0.01		133.62±0.00	135.49±0.00	
α_2 (K ⁻¹)	0.63±0.00	0.36±0.00	0.27±0.00	0.09±0.00		0.30±0.00	0.39±0.00	
β_2 (K ⁻²)	1.19±0.02	1.50±0.02	1.89±0.03	1.11±0.02		2.65±0.04	3.01±0.04	
$\Delta C_{p,m,2}$ (W.g ⁻¹ .K ⁻¹)	NA							
R^2	0.99	0.99	0.99	0.99	0.99	0.99	0.99	

[a] The samples were heated at 10 K.min⁻¹ after calibration at the onset for the given mass and rate, in the case of (5BA)₃(6BA)₁, only one fitting peak is required due to the peak overlap (the error margins are from the nonlinear fitting), $\Delta C_{p,m}$ is not available (NA) due to purely mathematical artefact, if the peaks are sufficiently apart with sufficient baseline tail on each side, the cumulative $\Delta C_{p,m}$ can be reliably determined via the function.

5.3.6 Semi-crystalline polymer (PHBVH) with glass transition, cold crystallization, and melting peaks

The DSC of PHBVH upon heating (Figure 5.10) shows multiple transitions; a glass transition which is followed by a cold crystallization: the exothermic crystallization process which is observed on heating of a sample that has previously been cooled so quickly that has no time to crystallize. In fact, at temperature below the glass transition, the molecular mobility is restricted and cold crystallization does not occur

but above the glass transition, small crystals are formed at relatively low temperatures. In addition, two endothermal peaks were observed subsequently upon further heating. The glass transition was fitted by $DSC_N(T)$ function (Equation 5.20). The cold crystallization peak was fitted by using a negative ΔH as stated in Equation 5.22. The melting transition peaks were fitted by $DSC_N(T)$ for binary peaks (Equation 5.21). As Figure 5.10 shows $DSC_N(T)$ function fits all peaks remarkably well, $R^2 > 0.99$ (Table S5.10).

$$DSC_N(T) = -\Delta H \cdot \frac{\alpha}{2} \cdot e^{\frac{\alpha^2}{4\beta}} \cdot e^{\alpha(T-T_m^0)} \cdot \operatorname{erfc}\left(\sqrt{\beta}(T-T_m^0) \pm \frac{\alpha}{2\beta}\right) \pm \Delta C_p(T) \pm B \pm C(T - T_m^0) \pm D(T - T_m^0)^2 \quad \text{Equation 5.22}$$

The glass transition temperature, crystallization temperature, and melting points obtained from the corresponding $DSC_N(T)$ are $T_g^0 = 10.45 \pm 0.02$ °C, $T_c^0 = 68.01 \pm 0.01$ °C, and $T_{m,1}^0 = 138.88 \pm 0.03$ °C and $T_{m,2}^0 = 152.72 \pm 0.01$ °C^{31,32}. For the glass transition and melting transitions, the baselines step up from the pre-transition tail to the post transition state, $\Delta C_{p,g} = 1.82 \pm 0.03$ W.g⁻¹.K⁻¹ and $\Delta C_{p,c} = 2.46 \pm 0.04$ W.g⁻¹.K⁻¹. For the overlapping melting peaks, $\Delta C_{p,m}$ does not converge (NA) due to purely mathematical artefact. However, if the peaks are sufficiently apart with sufficient baseline tail on each side, the cumulative $\Delta C_{p,m}$ can be reliably determined via the function (Table 5.9).

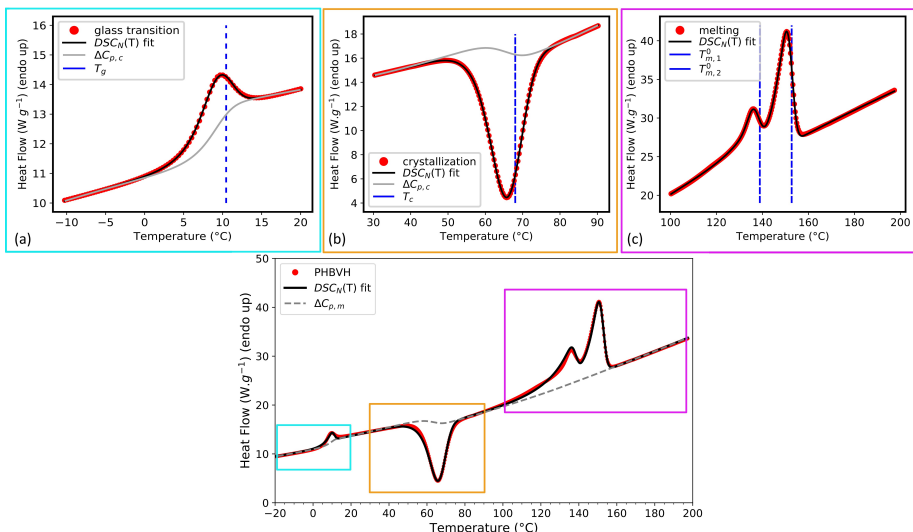


Figure 5.10 $DSC_N(T)$ function fitted to the experimental traces of 6 mg of PHBVH heated after calibration at the onset for the given sample mass and rate. For the

overlapping peaks, $\Delta C_{p,m}$ does not converge (Not available=NA) due to purely mathematical artefact.

Table 5.9 Fit parameters of the $DSC_N(T)$ for experimental curves of 6 mg of PHBVH^[a].

PHBVH	1 st peak glass transition (T_g)	2 nd peak Crystallization (T_c)	1 st melting peak ($T_{m,1}$)	2 nd melting peak ($T_{m,2}$)
ΔH (J.g ⁻¹)	13.54±0.08	201.90±0.24	75.57±1.35	136.31±0.75
T_t^0 (°C)	10.45±0.02	68.01±0.01	138.88±0.03	152.72±0.01
α (K ⁻¹)	0.45±0.01	0.28±0.00	6.77*	0.02±0.00
β (K ⁻²)	0.23±0.01	0.04±0.00	0.08±0.03	0.12±0.00
$\Delta C_{p,t}$ (W.g ⁻¹ .K ⁻¹)	1.82±0.03	2.46±0.04	NA	NA

[a] The samples were measured after calibration at the onset for the given sample mass and rate (the error margins are from the nonlinear fitting), *nonlinear least squares error out of the bounds due to indeterminate high α value.

5.4 Conclusion

$DSC_N(T)$ analytical function was developed to be fitted to the DSC experimental traces of different samples. It contains the equilibrium melting point (T_m^0), a parameter for the Arrhenius activation energy ($\alpha = Ea/(T_m^0)^2$), and a parameter for the Gaussian broadening (β). It is based on the assumption that the sample crystalline structure develops via a rate limited growth governed by a simple Arrhenius activated process. The function also includes the Gaussian broadening to account for instrumental accuracy. Non-isothermal conditions as governed by the rate of heating, sample mass, and thermal conductivity may additionally reflect the possible presence and inhomogeneous incorporation of impurities. It was found that the function is remarkably versatile in providing an excellent fit to the DSC experimental data. It enables a very accurate analysis of the DSC data yielding reliable transition temperatures such as melting, crystallization, and liquid crystal transitions. A distinct advantage of $DSC_N(T)$ to the conventional analysis methods is that it allows the analysis of mixtures showing multiple overlapping peaks which can differentiate the phases more accurately. In addition, changes in enthalpy are obtained which are in excellent agreement with the reference standards in the literature. Using the same function, the glass transition can also be analyzed. Here, we used the same procedure as for the melting point where the primary feature is

the step function and associated stepwise change of heat capacity ($\Delta C_{p,t}$). The value of $\Delta C_{p,m}$ although not very accurate, is a novel feature in $DSC_N(T)$ analytical model which is not usually available in the standard analysis methods relying on the linear baseline selected by a data analyst.

5.5 References

- [1] C. Demetzos, "Differential Scanning Calorimetry [DSC]: A tool to study the thermal behavior of lipid bilayers and liposomal stability", *J. Liposome Res.*, 2008.
- [2] S. Tanaka, "Theory of power-compensated DSC", *Thermochim. Acta*, 1992.
- [3] M. Raimo, "Kinetics of phase transformation of indium in the presence of polytetrafluoroethylene: implications for DSC measurements on polymers and their composites", 2015.
- [4] J. S. Crighton and F. W. Wilburn, "The role of heat transfer in the production of DSC curves", *Thermochim. Acta*, 1992.
- [5] L. Bouzidi, M. Boodhoo, K. L. Humphrey, and S. S. Narine, "Use of first and second derivatives to accurately determine key parameters of DSC thermographs in lipid crystallization studies", *Thermochim. Acta*, 2005.
- [6] E. Ghanbari, A. Krishnamurthy, S. J. Picken, E. A. Klop, L. J. Bannenberg, and J. van Esch, "Molecular Arrangement and Thermal Properties of Bisamide Organogelators in the Solid State", *Langmuir*, 2022.
- [7] A. K. Ahmed, M. Atiqullah, D. R. Pradhan, and M. A. Al-Harthi, "Crystallization and melting behavior of i-PP: a perspective from Flory's thermodynamic equilibrium theory and DSC experiment", *RSC Adv.* , 2017.
- [8] B. Coto, C. Martos, J. J. Espada, M. D. Robustillo, and J. L. Peña, "Analysis of paraffin precipitation from petroleum mixtures by means of DSC: iterative procedure considering solid–liquid equilibrium Equations", *Fuel*, 2010.
- [9] J. L. Martin and J. L. Martín, "Kinetic analysis of an asymmetrical DSC peak in the curing of an unsaturated polyester resin catalysed with MEKP and cobalt octoate", *Polymer*, 1999.
- [10] G. Wang and I. R. Harrison, "Polymer melting: heating rate effects on DSC melting peaks", *Thermochim. Acta*, 1994.
- [11] G. J. Davis and R. S. Porter, "Application of the differential scanning calorimeter to purity measurements", *J. Therm. Anal. Calorim.*, 1969.

- [12] T. Kousksou, A. Jamil, and Y. Zeraouli, "Enthalpy and apparent specific heat capacity of the binary solution during the melting process: DSC modeling", *Thermochim. Acta*, 2012.
- [13] A. Müller and W. Borchard. "Correlation between DSC curves and isobaric state diagrams. 3. Simulation of smeared DSC curves", *J. Phys. Chem. B*, 1997.
- [14] L. Feng and M. R. Kamal. "Distributions of crystal size from DSC melting traces for polyethylenes", *Can. J. Chem. Eng.*, 2004.
- [15] H. B. Dong and J. D. Hunt. "A numerical model for a heat flux DSC: Determining heat transfer coefficients within a DSC", *Mater. Sci. Eng. A*, 2005.
- [16] J. C. M. M. Torfs, L. Deij, A. J. Dorrepaal, and J. C. Heijens. "Determination of Arrhenius Kinetic Constants by Differential Scanning Calorimetry", *Anal. Chem.*, 1984.
- [17] G. Della Gatta, M. Józwiak, B. Brunetti, and L. Abate, "Enthalpies and entropies of fusion and of sublimation at the temperature 298.15 K of thiourea and seven N-alkylthioureas", *J. Chem. Thermodyn.*, 2000.
- [18] M. E. Brown, "Determination of purity by differential scanning calorimetry (DSC)", *J. Chem.*, 1979.
- [19] C. Demetzos, "Differential scanning calorimetry (DSC) a tool to study the thermal behavior of lipid bilayers and liposomal stability", *J. Liposome Res.*, 2008.
- [20] G. Widmann and O. Scherrer, "A new program for DSC purity analysis", *J. Therm. Anal.*, 1991.
- [21] B. L. Sharma, R. Jamwal, and R. Kant, "Thermodynamic and lamella models relationship for the eutectic system benzoic acid - Cinnamic acid", *Cryst. Res. Technol.*, 2004.
- [22] V. T. Popa and E. Segal, "Shape analysis of DSC ice melting endotherms. Towards an estimation of the instrumental profile", *J. Therm. Anal. Calorim.*, 2002.
- [23] D. G. Archer, "Enthalpy of fusion of bismuth: A certified reference material for differential scanning calorimetry", *J. Chem. Eng. Data*, 2004.
- [24] E. S. P. B. V. J. C. V. A. N. Miltenburg, and C. T. Group, "The influence of sample mass, heating rate and heat transfer coefficient on the form of dsc curves", *Thermochimica acta*, 1989.
- [25] S. Vyazovkin, "Activation Energies and Temperature Dependencies of the Rates of Crystallization and Melting of Polymers", *Polymers*, 2020.
- [26] J. K. Guillory, "Book Review of CRC Handbook of Chemistry and Physics. 90th Edition",

- J. Med. Chem., 2009.
- [27] L. Xu and R. Yang, "Stearic Acid / Inorganic Porous Matrix Phase Change", 2019.
 - [28] S. Ghosh and A. Roy, "Crystal polymorphism of 8OCB liquid crystal consisting of strongly polar rod-like molecules", RSC Adv., 2021.
 - [29] Ş. Özgan and M. Okumuş, "Thermal and Spectrophotometric Analysis of Liquid Crystal 8CB/8OCB Mixtures", Brazilian J. Phys., 2011.
 - [30] G. Cordoyiannis, C. S. P. Tripathi, C. Glorieux, and J. Thoen, "Order of phase transitions and tricriticality in mixtures of octyloxycyanobiphenyl and nonyloxycyanobiphenyl liquid crystals: A high-resolution study by adiabatic scanning calorimetry", Phys. Rev. E - Stat. Nonlinear. Soft Matter Phys., 2010.
 - [31] L. Shang, Q. Fei, Y. H. Zhang, X. Z. Wang, D. Di Fan, and H. N. Chang. "Thermal properties and biodegradability studies of poly (3-hydroxybutyrate-co-3-hydroxyvalerate)", J. Polym. Environ., 2012.
 - [32] B. Laycock et al., "Thermal properties and crystallization behavior of fractionated blocky and random polyhydroxyalkanoate copolymers from mixed microbial cultures", J. Appl. Polym. Sci., 2014.

5.6 Supplementary information

Here more information on the step by step calculation of $DSC_N(T)$ and all the parameters of $DSC_N(T)$ fit to the DSC experimental traces are provided.

The rout which was taken to develop $DSC_N(T)$ is as follows:

$$C_p = dH/dT$$

Equation S5.1

$$P(t) = dH/dT$$

Equation S5.2

$$P(t) = dH/dt = dH/dT \cdot dT/dt = C_p(T) \cdot R$$

Equation S5.3

$$C_p(T) = P(T)/R$$

Equation S5.4

$$C_p = \Phi_k \cdot C_{p,k} + (1 - \Phi_k) \cdot C_{p,G}$$

Equation S5.5

$$C_p = \Phi_k \cdot C_{p,k} + (1 - \Phi_k) \cdot C_{p,G}$$

Equation S5.6

$$C_p(T) = \frac{P(T)}{R} = \frac{dH}{dT} = C_{p,k} + (C_{p,L} - C_{p,k}) \cdot \int_0^T \rho(T) dT$$

Equation S5.7

$$K = A \cdot e^{-Ea/RT}$$

Equation S5.8

$$\rho(T) = e^{Ea/RT_m^0} \cdot e^{-Ea/RT}$$

Equation S5.9

$$\rho(T) = e^{\frac{Ea}{R} \left(\frac{1}{T_m^0} - \frac{1}{T} \right)} = e^{\frac{Ea}{T_m^0} \left(1 - \frac{T_m^0}{T} \right)} = \left(e^{\frac{Ea}{R}} \right)^{\left(1 - \frac{T_m^0}{T} \right)}$$

$$\rho(T) = (A)^{\left(1 - \frac{T_m^0}{T} \right)} = (A)^{\left(1 - \frac{T_m^0}{T_m^0 + \Delta T} \right)}$$

$$\rho(T) = (A)^{\left(1 - \frac{T_m^0/T_m^0}{(T_m^0 + \Delta T)/T_m^0} \right)} = (A)^{\left(1 - \frac{1}{1 + \Delta T/T_m^0} \right)}$$

$$\rho(T) = (A)^{\left(1 - \frac{\frac{\Delta T}{T_m^0}}{1} \right)} = (A)^{\frac{\Delta T}{T_m^0}} = \left(A^{\frac{1}{T_m^0}} \right)^{(\Delta T)}$$

$$= \left(\left(e^{\frac{Ea}{T_m^0}} \right)^{\frac{1}{T_m^0}} \right)^{(\Delta T)}$$

$$= \left(e^{\frac{Ea}{R} \cdot \frac{1}{T_m^0}} \right)^{(\Delta T)}$$

$$\rho(T) = \left(e^{\frac{Ea}{R \cdot (T_m^0)^2}} \right)^{(\Delta T)}$$

$$\rho(T) = e^{\alpha \Delta T}$$

Equation S5.10

$$z = \int_0^\infty e^{\alpha x} \cdot dx = \frac{1}{\alpha} e^{\alpha x} \Big|_{-\infty}^0 = \frac{1}{\alpha}$$

Equation S5.11

$$\rho_N(T) = \frac{1}{\alpha} \cdot e^{\alpha \Delta T}$$

Equation S5.12

$$f_N(\Delta T) = \frac{1}{\sigma\sqrt{2\pi}} \cdot e^{-\frac{1}{2}\left(\frac{\Delta T}{\sigma}\right)^2} \quad \text{Equation S5.13}$$

$$\rho_N(T) * f_N(\Delta T) = \int_{-\infty}^0 \rho(p) f(\Delta T - p) \cdot dp \quad \text{Equation S5.14}$$

Here $p < 0$, therefore:

$$\begin{aligned} DSC(\Delta T) &= (\rho_N * f_N)(\Delta T) = \\ &\int_{-\infty}^0 \frac{1}{\alpha} \cdot e^{\alpha p} \cdot \frac{1}{\sigma\sqrt{2\pi}} \cdot e^{-\frac{1}{2}\left(\frac{\Delta T-p}{\sigma}\right)^2} \cdot dp = \frac{1}{\alpha\sigma\sqrt{2\pi}} \\ &\int_{-\infty}^0 e^{-\frac{1}{2}\left(\frac{\Delta T-p}{\sigma}\right)^2 + \alpha p} \cdot dp \end{aligned}$$

Where A is $\frac{1}{\alpha\sigma\sqrt{2\pi}}$,

$$DSC(\Delta T) = e^{-\frac{1}{2}\left(\frac{\Delta T-p}{\sigma}\right)^2 + \alpha p} \cdot dp = A \int_{-\infty}^0 e^{-\frac{1}{2\sigma^2}(\Delta T-p)^2 + \alpha p} \cdot dp$$

$\Delta T = x$ and $\beta = \frac{1}{2\sigma^2}$, therefore β is the variance of distribution.

$$DSC(\Delta T) = A \int_{-\infty}^0 e^{-\beta(x-p)^2 + \alpha p} \cdot dp$$

$p' = x - p$ and consequently $dp' = -dp$,

$$DSC(x) = A \int_0^{+\infty} e^{-\beta(x^2 + 2p'x + p'^2) + \alpha p'} \cdot dp'$$

$$DSC(x) = Ae^{-\beta x^2} \int_0^{+\infty} e^{-\beta(p' + \frac{2\beta x + \alpha}{2\beta})^2 + \beta(\frac{2\beta x + \alpha}{2\beta})^2} \cdot dp'$$

$$= Ae^{-\beta x^2} e^{\beta(x + \frac{\alpha}{2\beta})^2} \int_0^{+\infty} e^{-\beta(p' + \frac{2\beta x + \alpha}{2\beta})^2} \cdot dp'$$

$$s = p' + x + \frac{\alpha}{2\beta}, \quad ds = dp'$$

$$DSC(x) = Ae^{\alpha x} \cdot e^{\beta(\frac{\alpha}{2\beta})^2} \cdot \int_{x + \frac{\alpha}{2\beta}}^{+\infty} e^{-\beta s^2} \cdot ds$$

$\int_{x + \frac{\alpha}{2\beta}}^{+\infty} e^{-\beta s^2} \cdot ds$ which is a complementary error function type of integral, in fact:

$$\text{erfc}(z) = 2 \int_z^{\infty} \frac{1}{\sqrt{\pi}} \exp(-u^2) du$$

$$x + \frac{\alpha}{2\beta} = z, \quad -(\beta^{1/2}s^2) = u, \quad dz = -2\beta s ds$$

$$DSC(x) = Ae^{\alpha x} \cdot e^{\frac{\alpha^2}{4\beta}} \cdot \frac{\sqrt{\pi}}{2} \cdot \text{erfc}(\beta^{\frac{1}{2}} \left(x + \frac{\alpha}{2\beta} \right)) \quad \text{Equation S5.15}$$

Normalization of the heat flow function gives the following equation:

$$DSC_N(T) = \frac{\sqrt{\pi}}{2} \cdot \frac{A}{\alpha^2} \cdot e^{-\frac{\alpha^2}{\beta}} \cdot e^{\alpha(T-T_m^0)} \cdot \operatorname{erfc}(\sqrt{\beta}(T - T_m^0 + \frac{\alpha}{2\beta})) + B \cdot (T - T_m^0) + C \quad \text{Equation S5.16}$$

$$H(z) = \frac{\alpha}{2} \cdot e^{\frac{\alpha^2}{4\beta}} \cdot \frac{1}{\alpha} \cdot (e^{\alpha z} \cdot \operatorname{erfc}(\sqrt{\beta} \cdot z) + e^{\frac{\alpha^2}{4\beta}} \cdot \operatorname{erf}\left(\sqrt{\beta} \left(z - \frac{\alpha}{2\beta}\right)\right) + 1) \quad \text{Equation S5.17}$$

$$DSC_N(T) = \Delta H \cdot \frac{\alpha}{2} \cdot e^{\frac{\alpha^2}{4\beta}} \cdot e^{\alpha(T-T_m^0)} \cdot \operatorname{erfc}\left(\sqrt{\beta}(T-T_m^0 + \frac{\alpha}{2\beta})\right) + \Delta C_{p,m} \cdot \frac{1}{2} \cdot e^{\frac{-\alpha^2}{4\beta}} \cdot (e^{\frac{\alpha^2}{2\beta}} \cdot e^{\alpha(T-T_m^0)} \cdot \operatorname{erfc}\left(\sqrt{\beta}(T-T_m^0 + \frac{\alpha}{2\beta})\right) + e^{\frac{\alpha^2}{4\beta}} \cdot (\operatorname{erf}(\sqrt{\beta}(T-T_m^0)) + 1)) \quad \text{Equation S5.18}$$

$$\Delta C_p(T) = \Delta C_{p,m} \cdot \frac{1}{2} \cdot e^{\frac{-\alpha^2}{4\beta}} \cdot (e^{\frac{\alpha^2}{2\beta}} \cdot e^{\alpha(T-T_m^0)} \cdot \operatorname{erfc}\left(\sqrt{\beta}(T-T_m^0 + \frac{\alpha}{2\beta})\right) + e^{\frac{\alpha^2}{4\beta}} \cdot ((\operatorname{erf}(\sqrt{\beta}(T-T_m^0)) + 1))) \quad \text{Equation S5.19}$$

$$DSC_N(T) = \Delta H \cdot \frac{\alpha}{2} \cdot e^{\frac{\alpha^2}{4\beta}} \cdot e^{\alpha(T-T_m^0)} \cdot \operatorname{erfc}\left(\sqrt{\beta}(T-T_m^0 + \frac{\alpha}{2\beta})\right) + \Delta C_p(T) + B + C(T - T_m^0) + D(T - T_m^0)^2 \quad \text{Equation S5.20}$$

Table S5.1 Fit parameter of $DSC_N(T)$ fitted to the experimental curves of indium heated at different rates^[a].

indium	R=2 K.min ⁻¹	R=10 K.min ⁻¹	R=20 K.min ⁻¹	R=50 K.min ⁻¹
ΔH (J.g ⁻¹)	30.15±0.00	29.37±0.01	28.62±0.01	27.98±0.04
T_m^0 (°C)	157.22±0.00	157.81±0.00	158.11±0.00	158.62±0.61
α (K ⁻¹)	4.88±0.01	3.50±0.03	4.44±0.08	19.67*
β (K ⁻²)	37.44±0.14	4.01±0.02	1.54±0.01	0.48±0.03
$\Delta C_{p,m}$ (W.g ⁻¹ .K ⁻¹)	0.01±0.00	0.01±0.00	-0.02±0.00	0.00±0.00
B (W.g ⁻¹)	0.54±0.00	0.86±0.00	0.58±0.00	0.57±0.01
C (W.g ⁻¹ .K ⁻¹)	0.00±0.00	0.00±0.00	0.00±0.00	0.00±0.00
D (W.g ⁻¹ .K ⁻²)	0.00±0.00	0.00±0.00	0.00±0.00	0.00±0.00
R^2	0.99	0.99	0.99	0.99

[a] The samples (7 mg) were measured after calibration for the given rate (the error margins are from the nonlinear fitting), *nonlinear least squares error out of the bounds due to indeterminate high α value.

Table S5.2 Fit parameters of $DSC_N(T)$ fitted to the experimental curves of indium with different weights^[a].

indium	w=1 mg	w=7 mg	w=54 mg
$\Delta H (J.g^{-1})$	29.61±0.00	30.27±0.00	29.71±0.00
$T_m^0 (^\circ C)$	156.86±0.00	157.24±0.00	157.69±0.00
$\alpha (K^{-1})$	11.86±0.03	4.43±0.01	1.87±0.00
$\beta (K^{-2})$	98.60±0.27	34.49±0.11	8.34±0.03
$\Delta C_{p,m} (W.g^{-1}.K^{-1})$	0.06±0.00	0.01±0.00	0.00±0.00
$B (W.g^{-1})$	2.09±0.00	0.56±0.00	0.07±0.00
$C (W.g^{-1}.K^{-1})$	0.00±0.00	0.00±0.00	0.00±0.00
$D (W.g^{-1}.K^{-2})$	0.00±0.00	0.00±0.00	0.00±0.00
R^2	0.99	0.99	0.99

[a] The samples were measured at $2 K.\min^{-1}$ after calibration at the onset for the given weight (the error margins are from the nonlinear fitting).

Table S5.3 Fit parameters of the $DSC_N(T)$ fitted to the experimental curves of stearic acid with different degrees of impurities^[a].

Stearic acid (SA)	SA 95%	SA 97%
$\Delta H (J.g^{-1})$	215.73±0.01	213.99±0.01
$T_m^0 (^\circ C)$	70.57±0.00	70.48±0.00
$\alpha (K^{-1})$	0.82±0.00	0.81±0.00
$\beta (K^{-2})$	6.08±0.07	7.05±0.08
$\Delta C_{p,m} (W.g^{-1}.K^{-1})$	-0.02±0.00	-0.02±0.00
$B (W.g^{-1})$	0.61±0.00	0.59±0.00
$C (W.g^{-1}.K^{-1})$	0.00±0.00	0.00±0.00
$D (W.g^{-1}.K^{-2})$	0.00±0.00	0.00±0.00
R^2	0.99	0.99

[a] The samples were heated at $2 K.\min^{-1}$ after calibration at the onset for the given weight and rate.

Table S5.4 Fit parameters of $DSC_N(T)$ fitted to the experimental curves of 8OCB (4'-octyloxy-4- cyanobiphenyl)^[a].

8OCB	1 st peak (K-SmA)	2 nd peak (SmA-N)	3 rd peak (N-I)
ΔH (J.g ⁻¹)	97.05±0.00	0.21±0.00	1.74±0.00
T_m^0 (°C)	55.62±0.00	66.96±0.00	80.16±0.00
α (K ⁻¹)	2.31±0.00	1.01±0.01	10.36±0.12
β (K ⁻²)	5.72±0.02	36.21±2.16	91.10±1.15
ΔC_p (W.g ⁻¹ .K ⁻¹)	-0.06±0.00	0.01±0.00	-0.01±0.00
B (W.g ⁻¹)	0.27±0.00	0.22±0.00	0.23±0.00
C (W.g ⁻¹ .K ⁻¹)	0.01±0.00	0.00±0.00	0.00±0.00
D (W.g ⁻¹ .K ⁻²)	0.00±0.00	0.00±0.00	0.00±0.00
R^2	0.99	0.97	0.98

[a] The samples (6 mg) were heated at 2 K.min⁻¹ after calibration at the onset for the given weight and rate (the error margins are from the nonlinear fitting).

Table S5.5 Fit parameters of $DSC_N(T)$ fitted to the experimental curves of odd and even bisamides^[a].

nBA	5BA	6BA	7BA	8BA	9BA	10BA
ΔH (J.g ⁻¹)	126.18±0.04	168.66±0.07	140.88±0.09	155.12±0.12	149.21±0.08	172.20±0.06
T_m^0 (°C)	135.52±0.00	147.46±0.00	135.97±0.00	143.53±0.00	132.50±0.00	142.11±0.00
α (K ⁻¹)	0.39±0.00	0.63±0.00	0.52±0.00	0.31±0.00	0.52±0.00	0.48±0.00
β (K ⁻²)	3.01±0.04	1.19±0.02	1.50±0.03	1.69±0.04	2.68±0.05	1.40±0.02
$\Delta C_{p,m}$ (W.g ⁻¹ .K ⁻¹)	-0.44±0.01	-0.31±0.01	-0.40±0.01	-0.28±0.01	-0.35±0.01	-0.29±0.01
B (W.g ⁻¹)	1.12±0.00	1.12±0.01	1.04±0.01	0.94±0.01	1.07±0.01	1.19±0.01
C (W.g ⁻¹ .K ⁻¹)	0.00±0.00	0.00±0.00	0.00±0.00	0.00±0.00	0.00±0.00	0.01±0.00
D (W.g ⁻¹ .K ⁻²)	0.00±0.00	0.00±0.00	0.00±0.00	0.00±0.00	0.00±0.00	0.00±0.00
R^2	0.99	0.99	0.99	0.99	0.99	0.99

[a] The samples (6 mg) were heated at 10 K.min⁻¹ after calibration at the onset for the given weight and rate (the error margins are from the nonlinear fitting).

Table S5.6 Fit parameters of $DSC_N(T)$ function fitted to the experimental DSC trace of molecularly mixed binary bisamides (5BA6BA in different ratios)^[a].

binary 5BA6BA	6BA	$(5BA)_1(6BA)_7$	$(5BA)_1(6BA)_3$	$(5BA)_1(6BA)_1$	$(5BA)_3(6BA)_1$	$(5BA)_7(6BA)_1$	5BA		
First peak									
$\Delta H_1 (J.g^{-1})$	Single peak	22.08 \pm 0.05	37.56 \pm 0.03	69.54 \pm 0.02	Single peak	56.34 \pm 0.76	Single peak		
$T_{m,1}^0 (^\circ C)$		130.49 \pm 0.03	130.59 \pm 0.00	131.49 \pm 0.00		129.00 \pm 0.02			
$\alpha_1 (K^{-1})$		0.17 \pm 0.00	0.38 \pm 0.00	0.61 \pm 0.00		0.07 \pm 0.00			
$\beta_1 (K^{-2})$		1.20 \pm 0.12	1.41 \pm 0.04	1.94 \pm 0.02		1.62 \pm 0.21			
$\Delta C_{p,m,1}$ (W.g $^{-1}$.K $^{-1}$)	NA								
Second peak									
$\Delta H_2 (J.g^{-1})$	168.66 \pm 0.07	127.44 \pm 0.06	107.76 \pm 0.11	115.02 \pm 0.12	222.3 \pm 7.07	120.6 \pm 0.23	126.18 \pm 0.04		
$T_{m,2}^0 (^\circ C)$	147.46 \pm 0.00	145.46 \pm 0.00	142.97 \pm 0.00	137.94 \pm 0.01	132.21 \pm 0.02	133.62 \pm 0.00	135.49 \pm 0.00		
$\alpha_2 (K^{-1})$	0.63 \pm 0.00	0.36 \pm 0.00	0.27 \pm 0.00	0.09 \pm 0.00	0.07 \pm 0.00	0.30 \pm 0.00	0.39 \pm 0.00		
$\beta_2 (K^{-2})$	1. 19 \pm 0.02	1.50 \pm 0.02	1.89 \pm 0.03	1.11 \pm 0.02	2.43 \pm 0.28	2.65 \pm 0.04	3.01 \pm 0.04		
$\Delta C_{p,m,2}$ (W.g $^{-1}$.K $^{-1}$)	NA								
B (W.g $^{-1}$)	1.12 \pm 0.01	0.38 \pm 0.00	0.51 \pm 0.00	0.38 \pm 0.00	0.38 \pm 0.00	0.39 \pm 0.00	1.12 \pm 0.00		
C (mW.g $^{-1}$)	0.00 \pm 0.00	-0.24 \pm 0.05	0.64 \pm 0.04	-0.45 \pm 0.03	-0.59 \pm 0.02	-0.54 \pm 0.04	0.00 \pm 0.00		
D (mW.g $^{-1}$.K $^{-2}$)	0.00 \pm 0.00	0.01 \pm 0.00	0.00 \pm 0.00						
R^2	0.99	0.99	0.99	0.99	0.99	0.99	0.99		

[a] The samples (6 mg) were heated at 10 K.min $^{-1}$ after calibration at the onset for the given weight and rate, in the case of $(5BA)_3(6BA)_1$, only one fitting peak is required due to the peak overlap (the error margins are from the nonlinear fitting), $\Delta C_{p,m}$ does not converge (Not available=NA) due to purely mathematical artefact, if the peaks are sufficiently apart with sufficient baseline tails on each side, the cumulative $\Delta C_{p,m}$ can be reliably determined via the $DSC_N(T)$ function for binary systems.

Table S5.7 Fit parameter of $DSC_N(T)$ function fitted to the experimental curves of PHBVH^[a].

PHBVH	1 st peak glass transition (T_g)	2 nd peak Crystallization (T_c)	1 st melting peak ($T^0_{m,1}$)	2 nd melting peak ($T^0_{m,2}$)
ΔH (J.g ⁻¹)	13.54±0.08	201.90±0.24	75.57±1.35	136.31±0.75
T_t^0 (°C)	10.45±0.02	68.01±0.01	138.88±8.03	152.72±0.01
α (K ⁻¹)	0.45±0.01	0.28±0.00	6.77*	0.02±0.00
β (K ⁻²)	0.23±0.01	0.04±0.00	0.08±0.03	0.12±0.00
$\Delta C_{p,t}$ (W.g ⁻¹ .K ⁻¹)	1.82±0.03	2.46±0.04	NA	NA
B (W.g ⁻¹)	11.50±0.02	-18.18±0.02	13.89±0.33	13.89±0.03
C (W.g ⁻¹ .K ⁻¹)	0.06±0.00	-0.12±0.00	0.08±0.00	0.08±0.00
D (W.g ⁻¹ .K ⁻²)	0.00±0.00	-0.12±0.00	0.00±0.00	0.00±0.00
R^2	0.99	0.99	0.99	0.99

[a] The samples (6 mg) were measured after calibration at the onset for the given sample weight and rate (the error margins are from the nonlinear fitting), *nonlinear least squares error out of the bounds due to indeterminate high α value.

Chapter 6

Design rules for binary bisamide gelators: towards gels with tailor-made structures and properties

Abstract

This study intends to develop design rules for binary mixture of gelators that govern their assembly behavior, and subsequently explore the impact of their supramolecular assembly patterns on the gels rheological properties. To achieve these goals, nBA gelators with odd and even parities (n-methylene spacers between the amide groups ($n = 5-10$) and 17 carbons at each end) were blended at different ratios. Such bisamides with the simple structures were selected to study because their different spacer lengths offer the possibility to have matching or non-matching hydrogen bonds.

The results show that the assembly behavior of binary mixtures of bisamide gelators is the same in the solid and gel states. Binary mixtures of gelators, which only differ two methylene moieties in spacer length, form compounds and co-assemble into fibers and sheets observed for $(5\text{BA})_1(7\text{BA})_1$ and $(6\text{BA})_1(8\text{BA})_1$ mixtures, respectively. Binary gelator mixtures of the same parity and a larger spacer length difference still lead to mixing for the odd parity couple $(5\text{BA})_1(9\text{BA})_1$, but to partial phase-separation for the even parity mixture $(6\text{BA})_1(10\text{BA})_1$. Binary mixtures of gelators of different parities gave complete phase-separation in the solid state, and self-sorted gels consisting of discrete fibers and sheets in the gels of $(5\text{BA})_3(6\text{BA})_1$ and $(5\text{BA})_3(10\text{BA})_1$. The even-even binary gels (20 wt%) consisting of co-assembled sheets show higher G' than odd-odd binary gels (20 wt%) consisting of co-assembled fibers. In general, the self-sorting of odd and even molecules into the separate primary structures results in a dramatic decrease of G' compared to the co-assembled gels (20 wt%), except for $(5\text{BA})_1(9\text{BA})_1$ gel (20 wt%). It might be due to

larger woven spheres in (5BA)₁(9BA)₁ gel (20 wt%), which probably have a less entangled gel network.

6.1 Introduction

Supramolecular gels are composed of two main components, a small molecule like low molecular weight gelators (LMWGs) and a solvent system. During the gelation process, gelator molecules respond to external stimuli such as temperatures. Many LMWGs depending on their chemical structures are thermally triggered ¹⁻⁶; the LMWGs are dissolved in a solvent upon heating to higher temperatures and usually self-assemble into primary structures by cooling the solution to below the gelation transition temperature.

In the course of cooling when sufficient undercooling has been reached, the gelator molecules assemble through non-covalent bonds to build primary structures such as tapes, rods, fibers, sheets, and cylinders ⁷. The properties of these gels are governed by both the primary structures and their interactions in a mesoscopic scale ^{8,9}. In fact, these primary structures are able to efficiently immobilize the solvent if they form a three-dimensional entangled network ⁹⁻¹¹.

Initially, structurally diverse LMWGs were developed based on saccharides ¹², peptides, ureas, amides ¹³⁻¹⁵, nucleobases ¹⁶, steroid derivatives ¹⁷, dendrimers ¹⁸, etc. to produce supramolecular gels for many potential applications ^{19,20,29,21-28}. In recent years, the field of single LMWGs was expanded from ab-initio synthesis of new gelators with new functionalities towards designing multicomponent systems to introduce more flexibility in gel systems for different purposes, generally aiming at controlling the assembly pattern and study its effect on the gel properties³⁰. For instance for biomedical applications, the main LMWGs in the system are used to develop the supporting network structure, while a second assembly moiety is added to improve the cell adhesion to the network matrix ³¹.

Primary structures in multicomponent gels can form either via the co-assembly of gelators with alternating order or random organizations or via their self-sorting into discrete structures ³²⁻³⁴. It is also likely that the final gel structure is the mixture of all these assembly modes ³⁵. Another advantage of using multicomponent gelator systems is the reinforcement in the mechanical properties of the final gel formulation by inducing co-assembly of the gelator molecules ³⁶ or via encouraging the self-sorting of gelator molecules in pH-triggered hydrogels where each gelator component responds to a certain pH ³⁷.

Here, the aim is to develop design rules for the binary mixture of gelators that govern the mixing or phase separation behavior, and subsequently explore its

impact on the phase behavior and their relation to the gel properties. For that purpose, the binary mixtures of bisamide gelators with odd-even spacer lengths were used. These gelators were chemically designed to have the simplest structure, n-methylene spacers between the amide groups ($n = 5-10$) and 17 carbons at each end, which makes them ideal model systems to tune mixing or phase separation behavior via hydrogen bond complementarity. Our hypothesis is that the systematic addition of a nBA gelator with different parities or spacer-lengths to the parent nBA gelator, inducing partial or matching complementary interactions between the gelator molecules, can determine their phase behavior.

To achieve the above-mentioned objectives, these systems were studied in multiple steps. In chapter 3, the molecular arrangement and hydrogen bonding pattern of a series of single bisamide gelators with different spacer lengths have been fully investigated³⁸. In chapter 4, their gelation behavior and the odd-even effect on their rheological properties have been addressed³⁹. In this chapter, binary mixtures of these bisamide gelators in the solid state and the gels were studied. The effect of differences in the spacer length and parity on the solid state phase behavior and the gel structure and thermal properties were studied. Finally, the rheological properties of the gels from the binary gelator mixtures have been studied in relation to the phase behavior as well as the rheological properties of the gels from the single bisamides.

6.2 Materials and methods

6.2.1 Binary mixtures of nBA gelators

The synthesis and characterization of single nBA gelators- with n-methylene spacers between the amide groups (n varies from 5 to 10) and 17 carbons at each end- were described in chapter 3³⁸. The single nBA gelators were notated according to the number of carbon atoms in the spacer between the amide groups (n) with “BA” as the suffix for “bisamide gelator”. The general chemical structure of nBA gelators is shown in Figure 6.1 for 5BA and 6BA as examples of odd and even nBA gelators, respectively³⁸.

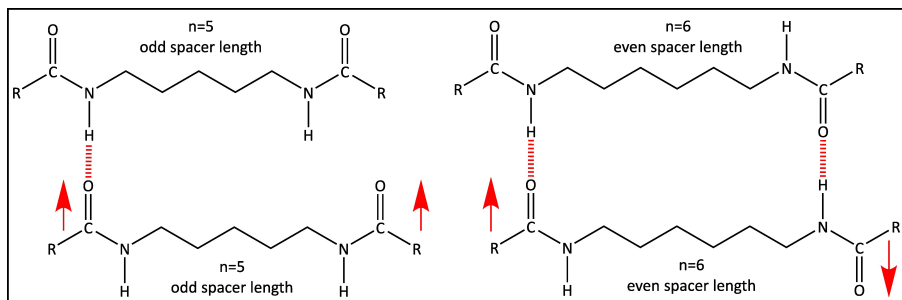


Figure 6.1 Chemical structure of single bisamide gelators (nBAs) with $(CH_2)_n$ spacer between the amide groups: a) 5BA with a parallel arrangement of amide groups, b) 6BA with an anti-parallel arrangement of amide groups.

The binary bisamides were prepared by systematic blending (odd-odd, even-even, and odd-even spacer length) of two single nBA gelators (Table 6.1). The single gelators were heated to their melting points and were stirred isothermally just above their melting points to ensure that the gelators are uniformly mixed. After mixing for 15 minutes, the mixtures were cooled down to room temperature. Binary gelators were prepared at five different mole ratios (1:7, 1:3, 1:1, 3:1, and 7:1). The binary gelators were named by taking the notation of their single nBA gelators with their assigned ratios as the subscript; for example, the blend of 5BA and 6BA in 1:7 ratio is notated as (5BA)₁(6BA)₇.

Table 6.1 Systematically blended bisamide gelators based on the parity of spacer length to produce binary BAs at five different ratios.

blending based on parity	directionality of amide groups	single components	difference in spacer length	molar ratio
odd-odd	parallel-parallel	5BA and 7BA	2	1:7
		5BA and 9BA	4	
even-even	antiparallel-antiparallel	6BA and 8BA	2	1:3
		6BA and 10BA	4	
odd-even	parallel-antiparallel	5BA and 6BA	1	3:1
		5BA and 10BA	5	

6.2.2 Gel preparation

The gelation behavior of single nBA gelators was investigated in our chapter 4³⁹. To prepare the gels from binary BA gelators, binary gelators were first ground into powders. Then, they were weighed (20 wt%) and dispersed in xylene as the solvent. The gelator-solvent mixtures were heated to 120 °C using a heating block while

stirring using magnetic bars at 500 rpm. Once the mixtures became transparent, the vials were taken out and cooled down to the ambient temperature. A tube inversion test ⁴⁰ was conducted as a quick assessment of gel formation immediately after cooling down to the room temperature and after 72 h.

6.2.3 Differential Scanning Calorimetry (DSC)

The melting transition of gelators and gel-sol transition temperatures of gel samples were measured using Perkin Elmer-Pyris Diamond differential scanning calorimeter with two 1(g)-furnaces (working on the Power-compensation temperature null principle with temperature accuracy/precision of $\pm 0.1\text{ }^{\circ}\text{C}/\pm 0.01\text{ }^{\circ}\text{C}$ and calorimetry accuracy/precision of $<\pm 1\%/\pm 0.1\%$). Nitrogen (99.99% purity) was used to purge the interior system at a rate of 50 ($\text{mL}\cdot\text{min}^{-1}$). Temperature and heat flow calibration were done before each measurement under the same condition as the measurement of the samples.

For the solid binary gelator mixtures, about $6 \pm 1\text{ mg}$ of binary bisamide gelator was placed in a $40\text{ }\mu\text{L}$ aluminum sample pan with an ambient maximum pressure. The sample pan and the identical reference pan were both covered by aluminum lids. The sealed pans were placed in the furnaces of the DSC apparatus. Both pans were heated from room temperature to at least $30\text{ }^{\circ}\text{C}$ above the temperature range of interest. Isothermal melting was followed by a fixed cooling cycle preceding a second heating cycle, all scans were done at the rate of $10\text{ K}\cdot\text{min}^{-1}$.

A similar procedure was followed for the gel samples: a gel sample ($8 \pm 1\text{ mg}$) in a $40\text{ }\mu\text{L}$ stainless steel sample pan and an identical empty pan as reference- both covered by stainless steel lids- were heated at $5\text{ K}\cdot\text{min}^{-1}$ from $25\text{ }^{\circ}\text{C}$ to $130\text{ }^{\circ}\text{C}$. The first heating cycle to eliminate the sample thermal history was followed by a cooling cycle from $130\text{ }^{\circ}\text{C}$ to $25\text{ }^{\circ}\text{C}$ at $5\text{ K}\cdot\text{min}^{-1}$. Finally, a second heating cycle was run at $5\text{ K}\cdot\text{min}^{-1}$ from $25\text{ }^{\circ}\text{C}$ to $130\text{ }^{\circ}\text{C}$ to study the thermal properties of the samples. To assure the thermal equilibrium of the sample, the samples were kept isothermally for 2 min at the end of each temperature scan.

6.2.4 $\text{DSC}_N(T)$ analytical model and curve fitting

$\text{DSC}_N(T)$ function has been developed in our research group ⁴¹ and was extended for binary gelators which show two endothermic peaks in their second heating DSC traces (Equation 6.1).

$$DSC_N(T) \quad \text{Equation 6.1}$$

$$\begin{aligned}
 &= (\Delta H_1 \cdot \frac{\alpha_1}{2} \cdot e^{\frac{\alpha_1^2}{4\beta_1}} \cdot e^{\alpha_1(T-T_{m,1}^0)} \cdot \operatorname{erfc}\left(\sqrt{\beta_1}(T-T_{m,1}^0 + \frac{\alpha_1}{2\beta_1})\right) \\
 &+ \Delta C_{p,1}(T)) \\
 &+ (\Delta H_2 \cdot \frac{\alpha_2}{2} \cdot e^{\frac{\alpha_2^2}{4\beta_2}} \cdot e^{\alpha_2(T-T_{m,2}^0)} \cdot \operatorname{erfc}\left(\sqrt{\beta_2}(T-T_{m,2}^0 + \frac{\alpha_2}{2\beta_2})\right) \\
 &+ \Delta C_{p,2}(T)) + B + C(T - T_r) + D(T - T_r)^2
 \end{aligned}$$

$$\begin{aligned}
 \Delta C_p(T) &= \Delta C_{p,m} \cdot \frac{1}{2} \cdot e^{\frac{-\alpha^2}{4\beta}} \cdot (e^{\frac{\alpha^2}{2\beta}} \cdot e^{\alpha(T-T_m^0)} \cdot \operatorname{erfc}\left(\sqrt{\beta}(T-T_m^0 + \frac{\alpha}{2\beta})\right) \\
 &+ e^{\frac{\alpha^2}{4\beta}} \cdot ((\operatorname{erf}(\sqrt{\beta}(T-T_m^0)) + 1))
 \end{aligned} \quad \text{Equation 6.2}$$

$DSC_N(T)$ is based on an assumed Arrhenius function taking the crystal size distribution into account together with instrumental and sample-related peak broadening. Relying on $DSC_N(T)$, melting point (T_m^0) and enthalpy of fusion (ΔH) of each phase in binary gelators can be obtained much more accurately. In Equation 6.1, ΔH_1 and ΔH_2 are the coefficients representing the change in enthalpy associated with the phase transition of each peak, $T_{m,1}^0$ and $T_{m,2}^0$ are the equilibrium temperatures of the phase transitions. The strength of the linearized Arrhenius function (α) is related to the crystal size distribution. The parameter β describes the Gaussian peak broadening distribution of the peak due to the peak broadening, related to the peak width in the declining edge. The difference between the heat capacity of the pre- and post-transition states is represented by $\Delta C_{p,m}$. The parameters B, C, and D correct for the baseline features; the offset, linear slope, and second order curvature, respectively. This model captures the shape of experimental DSC peaks of binary bisamides, where T_r is a reference temperature for the overall curved baseline. The non-linear curve fitting of $DSC_N(T)$ to the experimental DSC traces of binary compounds was done using the Python 3 programming language which has been described comprehensively in chapter 5⁴¹. To assure the accuracy of thermal properties obtained from DSC measurements, at least three samples with similar weights were measured under the same condition and the data were analyzed after normalization per weight of the sample. The standard deviation of the thermal properties, melting temperature, enthalpy of fusion, heat capacity change, and the other fit parameters were obtained by fitting the analytical model $DSC_N(T)$ to the three sets of raw data which contain the experimental error along with the fitting procedure error. The fitting deviation for each parameter was obtained from the residuals of non-linear least squares (NLLS).

The reported error margins of the fit parameters in Table S6.1-S6.12 are the residuals of NLLS rounded to two digits.

6.2.5 X-ray diffraction (XRD)

To compare the crystal structures of single gelators and their gels with binary BA systems, X-ray diffraction (XRD) patterns of these gels were studied. A dab of sample was placed onto the standard PMMA sample holders. The measurement on binary systems was conducted under the same condition as single nBA gelators and gels^{38,39}: a Bruker D8 ADVANCE ECO diffractometer in Bragg-Brentano geometry equipped with a Cu X-ray source ($K_{\alpha 1}=1.54060$ Å and $K_{\alpha 2}=1.54439$ Å) and LYNXEYE-XE-T position sensitive detector was operated at room temperature. A knife-edge was embedded to reduce the background due to the scattering of the primary beam. The diffraction patterns were recorded from 0.6 ° to 50 ° (2θ) with a step size of 0.01 ° and measuring time of 0.5 s per step.

6.2.6 Scanning Electron Microscopy (SEM)

Samples for scanning electron microscopy (SEM) were prepared by placing a small amount of freshly prepared gels on an aluminum foil covering a microscope glass. To get rid of the solvent, the samples were dried in a VT6025 vacuum oven (Thermo Electron Corporation) for 3 h at 60 °C. Due to the low volatility of xylene, applying this temperature in addition to the vacuum drying is essential. The temperature 60 °C has been chosen safely below the melting point of the gel sample and its constituents to avoid any morphological changes. To improve conductivity for better image quality, the samples were placed in a benchtop SEM sputter coater to be coated with a thin layer of gold particles at 20 mA for 30 s. The morphology of the binary gels was observed by using a JEOL JSM 6010LA scanning electron microscope with an accelerating voltage of 8 kV. The images were recorded at different magnifications (500x, 1000x and 2500x) in the secondary electron image (SEI) mode, WD10 mm, and SS40.

6.2.7 Rheology

Rheological measurements were carried out on a DISCOVERY HR-3 hybrid rheometer (TA Instrument). Parallel steel plates (with diameter of 40 mm) and Peltier plate steel-999580 were used. Geometry gap between the plates was set at 500 µm. Zero gap was determined after calibration of inertia, friction, and rotational mapping. A freshly prepared gel sample (1.0 ± 0.2 g) was placed evenly on the bottom

plate, and then the parallel plate was lowered to the set geometry gap. All the measurements were performed at 25 °C. To avoid solvent evaporation during the measurement, a few drops of Xylene were added on a solvent trap covering the gap prior to each measurement. Before frequency sweep, an amplitude sweep test from 0.001 s⁻¹ to 1 s⁻¹ strain rate at 1 Hz was conducted on each sample to find the linear viscoelastic region. The strain rate was set to 0.01 s⁻¹ selected from the linear viscoelastic region. Frequency sweep measurement was carried out setting angular frequency from 0.1 rad·s⁻¹ to 100 rad·s⁻¹ and the strain 0.01 was applied to measure the storage modulus (G') and loss modulus (G''). To compare the modulus of binary and single nBA gels, the values of G' at a constant frequency ($\omega = 10$ rad·s⁻¹) for all gels were chosen. The final G' values are the average of the G' from the measurement of three independent samples. To compare the rheological properties of the single and binary gels, the binary gel samples were prepared and measured under the same conditions as the single nBA gels ³⁹.

6.3 Results and discussion

Here, in section 6.3.1, the molecular arrangement of binary bisamide gelators in the solid will be discussed and subsequently the supramolecular assembly in the gel state will be explained in section 6.3.2. Finally, the effect of complementarity of hydrogen bonding on the rheological properties will be described in section 6.3.3.

6.3.1 Binary gelators in the solid state

To investigate the effect of the addition of the second nBA gelator on the thermal properties of the parent gelator, melting transitions of single gelators and their binary compositions were studied by DSC. The experimental DSC traces were fitted using the $DSC_N(T)$ function for single ³⁸ and binary systems (Equation 6.1) to obtain the melting point (T_m^0) and enthalpy of fusion (ΔH) for each phase accurately. The fit parameters for all gelators and their binary compounds are listed in the tables in the supplementary information file.

6.3.1.1 Odd-odd binary gelators

The DSC traces and $DSC_N(T)$ fits of 5BA, 7BA, and their binary compositions at different ratios are shown in Figure 6.2a. At all non-equimolar binary compositions, two separate peaks are observed while the equimolar mixture (5BA)₁(7BA)₁ shows a single peak. The T_m^0 of both phases in binary 5BA7BA gelators are at lower temperatures (Table S6.1) compared to the single gelators 5BA and 7BA gelators,

with T_m^0 of 135.5 °C and 136.1 °C, respectively. However, T_m^0 of (5BA)₁(7BA)₁ has increased to 136.1 °C, close to the T_m^0 of single 5BA and 7BA. The seemingly single melting transition of (5BA)₁(7BA)₁ could be due to either two single overlapping peaks or the formation of a new compound. To find out, the XRD pattern of (5BA)₁(7BA)₁ was compared to the diffraction patterns of the corresponding single compounds, 5BA and 7BA, as previously studied in chapter 3 ³⁸. Figure 6.2b shows that the first-order reflection of (5BA)₁(7BA)₁ is a single reflection at 1.55° (2θ) at different 2θ positions from the 001 reflection of 5BA, at 1.63° (2θ), but at the same position as the 001 reflection of 7BA, at 1.55° (2θ). At higher angles (20°-25° (2θ)), the reflections of (5BA)₁(7BA)₁ do not correspond to the reflections of single 5BA and single 7BA and have shifted towards lower angles. This indicates the formation of a single phase with a supramolecular arrangement very similar to the crystal structure of 7BA.

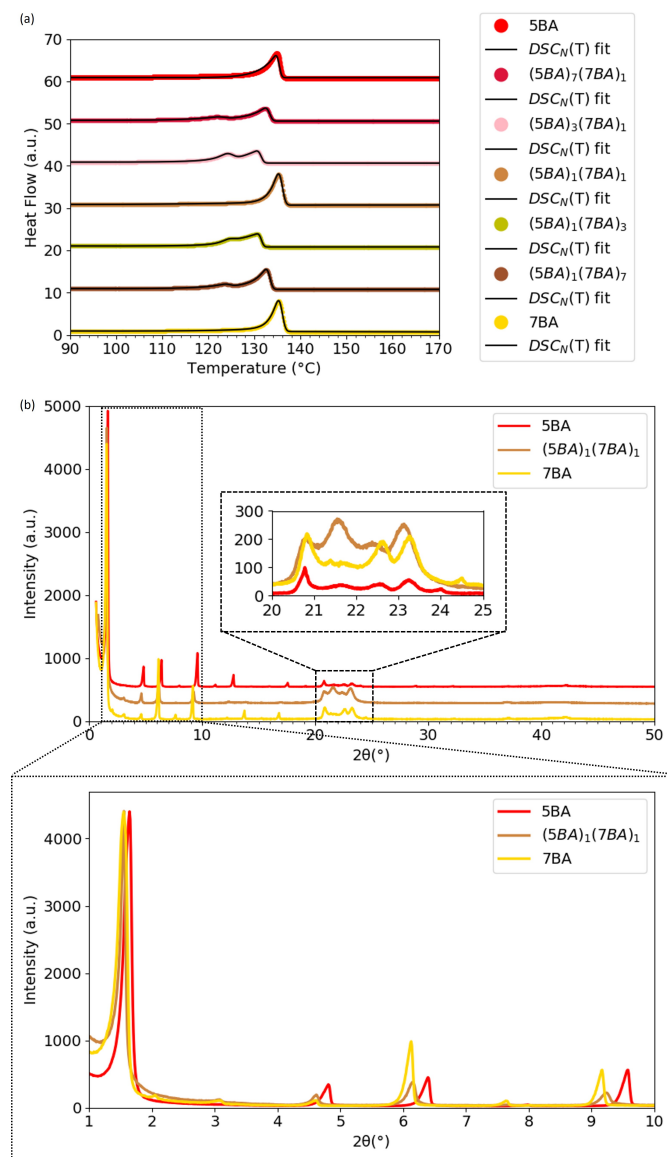


Figure 6.2 Phase behavior of 5BA7BA gelators: a) $DSC_N(T)$ fit to the second heating DSC traces of 5BA7BA at different mixing ratios (the traces and fits were shifted vertically for clarity), b) XRD patterns of $(5BA)_1(7BA)_1$ mixtures in comparison to single 5BA and 7BA gelators (curves were normalized to the highest intensity), the insets magnify high-angle (20° - 25° (2θ)) and low-angle (0° - 10° (2θ)) regions.

Increasing the difference between the spacer length of binary odd-odd gelators from 2 (in 5BA7BA) to 4 (in 5BA9BA) shows the similar trend of DSC traces as 5BA7BA compositions (Figure S6.1a): two separate melting peaks for non-equimolar ratios while a single melting peak for $(5\text{BA})_1(9\text{BA})_1$. However, on the contrary to $(5\text{BA})_1(7\text{BA})_1$, the single melting transition of $(5\text{BA})_1(9\text{BA})_1$ has shifted to the lower temperature (126.5°C) compared to its corresponding single gelators, 5BA (135.5°C) and 9BA (132.50°C). As shown in Figure S6.1b, the single 001 reflection of $(5\text{BA})_1(9\text{BA})_1$ is a broad peak at $1.55^\circ(2\theta)$ between the reflections of single 5BA ($1.63^\circ(2\theta)$) and 9BA ($1.46^\circ(2\theta)$) implying that they have formed the compound $(5\text{BA})_1(9\text{BA})_1$ ³⁸.

6.3.1.2 Even-even binary gelators

For binary gelators of 6BA8BA, where 6BA and 8BA are two spacer lengths apart and have the same parity, the general trend of the DSC thermogram is very similar to 5BA7BA with the same above-mentioned characteristics (Figure S6.2a); at non-stoichiometric ratios, two melting peaks are observed but they appear to merge into a single melting transition at 1:1 ratio. This single melting transition is observed for $(6\text{BA})_1(8\text{BA})_1$ at 143.5°C , which is lower than the T_m^0 of the parent gelators, single 6BA (147.5°C) and 8BA (143.5°C) but higher than the T_m^0 of the mixtures. Similar to the XRD pattern of $(5\text{BA})_1(7\text{BA})_1$ where the first-order reflection occurs at the same position as 001 reflection of 7BA, the XRD pattern of $(6\text{BA})_1(8\text{BA})_1$ in Figure S6.2b shows a single reflection at $2.00^\circ(2\theta)$, which is at the exact same position as the 001 reflection of 8BA. The similar T_m^0 and XRD 001 reflection of $(6\text{BA})_1(8\text{BA})_1$ to the those of single 8BA indicates that a compound has formed at 1:1 ratio, which has a similar crystal structure to 8BA.

Keeping the parity the same and increasing the difference in the spacer length to 6BA10BA, all compositions of 6BA10BA including the equimolar composition show two melting peaks in the DSC thermogram (Figure 6.3a) implying that 6BA and 10BA have less tendency to mix compared to 6BA8BA. As Figure 6.3b shows, the first two reflections of $(6\text{BA})_1(10\text{BA})_1$ at 1.97° and $2.08^\circ(2\theta)$ are comparable to the 001 reflections of single 6BA at $2.08^\circ(2\theta)$ and 10BA at $1.91^\circ(2\theta)$. The XRD pattern of $(6\text{BA})_1(10\text{BA})_1$ is approximately a linear superposition of the single 6BA and single 10BA XRD patterns, which confirms that these molecules have mostly phase separated. This can be due to the larger difference in the spacer length of 6BA and 10BA causing a mismatch of molecules for the paired hydrogen bonding observed for single even bisamide gelators³⁸.

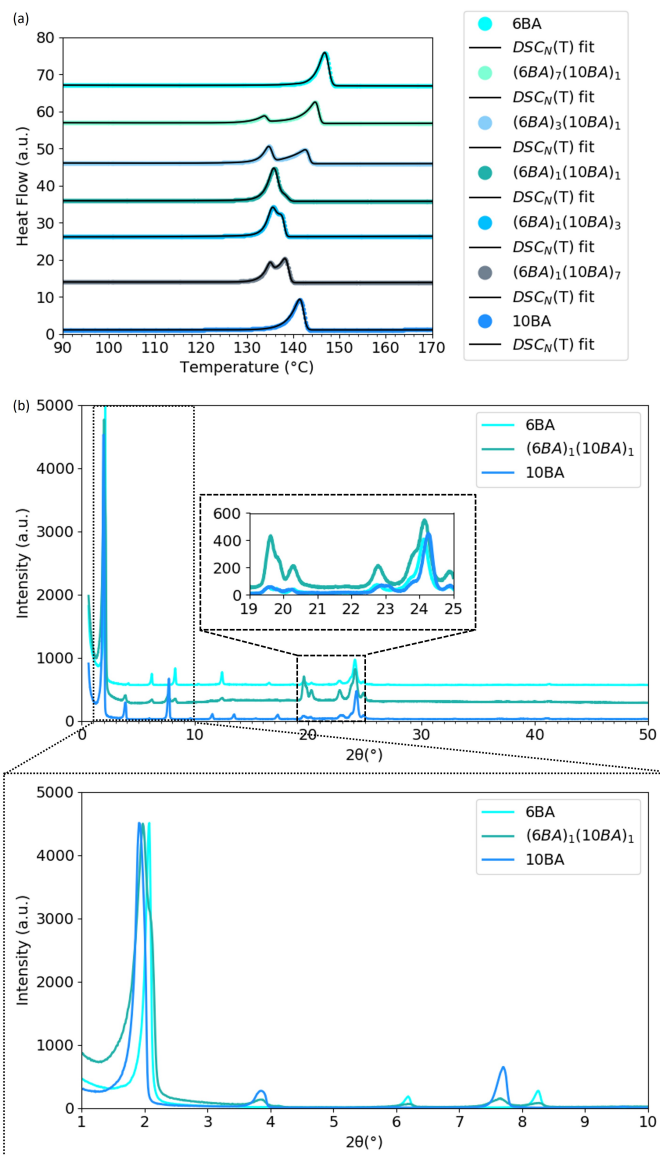


Figure 6.3 Phase behavior of 6BA10BA gelators: a) the second heating traces for various mixing ratios 6BA and 10BA. $DSC_N(T)$ fits to the experimental traces (the traces and fits were shifted vertically for clarity), b) XRD patterns of $(5BA)_1(6BA)_1$ in comparison to single 6BA and 10BA gelators (curves were normalized to the highest intensity), the insets magnify high-angle (20° - 25° (2θ)) and low-angle (0° - 10° (2θ)) regions.

6.3.1.3 Odd-even binary gelators

The DSC thermogram of 5BA and 6BA mixtures at different compositions (Figure 6.4a) shows double melting transitions for all compositions except for $(5BA)_3(6BA)_1$. $(5BA)_3(6BA)_1$ melts at 131.0 °C which is lower than single 5BA and 6BA (Table S6.5). The seemingly single melting transition of $(5BA)_3(6BA)_1$ at 132.2 °C could be due to either two single overlapping peaks or the formation of a new phase. To find out, the XRD pattern of $(5BA)_3(6BA)_1$ was compared with the patterns of 5BA, 6BA, and $(5BA)_1(6BA)_1$. Figure 6.4b shows the splitting of the first-order reflection both for $(5BA)_3(6BA)_1$ -with single melting peak- and $(5BA)_1(6BA)_1$ -with double peaks. The first and second reflections of $(5BA)_3(6BA)_1$ have shifted to lower positions of 1.61° (2θ) and 1.99° (2θ) with respect to the first-order reflections of 5BA (at 1.64° (2θ)) and single 6BA (at 2.07° (2θ)). These two reflections are at the same angles as the two first reflections of $(5BA)_1(6BA)_1$. This demonstrates that the single melting transition is the result of two overlapping yet separated phases.

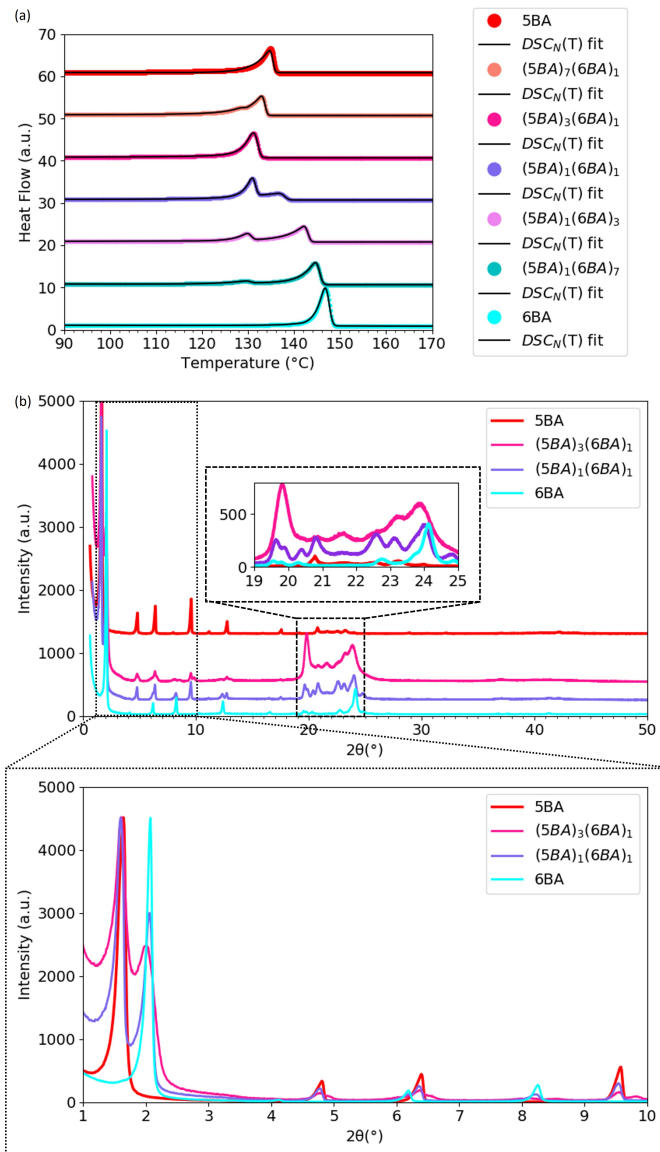


Figure 6.4 Phase behavior of 5BA6BA gelators: a) the second heating traces for various mixing ratios 5BA and 6BA. $DSC_N(T)$ fits to the experimental traces (the traces and fits were shifted vertically for clarity), b) XRD patterns of $(5BA)_3(6BA)_1$ in comparison to single 5BA and 6BA gelators and binary $(5BA)_1(6BA)_1$ which has two distinct melting peaks and shows split first order reflections (curves were normalized to the highest intensity), the insets magnify high-angle (20° - 25° (2θ)) and low-angle (0° - 10° (2θ)) regions.

Although 5BA10BA has a larger difference in the spacer length than 5BA6BA, its DSC thermogram shows a similar trend to 5BA6BA (Figure S6.3a): all binary compositions show two distinct melting peaks. The presence of two completely distinct peak is less obvious for $(5BA)_3(10BA)_1$ due to two peaks which are mostly overlapping. The first reflection of $(5BA)_3(10BA)_1$ is at $1.64^\circ (2\theta)$, at the same position as the 001 reflection of single 5BA, and the second reflection has shifted to a lower angle ($1.86^\circ (2\theta)$) than the 001 reflection of 10BA at $1.90^\circ (2\theta)$. These two reflections are at the exact angles as the two reflections of $(5BA)_1(10BA)_1$, where two distinct melting peaks are observed in Figure S6.3a. Similar to $(5BA)_3(6BA)_1$, phase separation occurs for $(5BA)_3(10BA)_1$.

6.3.2 Phase diagram

To gain more insights on how the addition of the second nBA affects the T_m^0 of the parent nBA, the phase diagrams of all nBA gelators (temperature vs. composition) are constructed and shown in Figure 6.5a-f. The T_m^0 of all phases at different compositions were obtained from the fitting of $DSC_N(T)$ to their DSC experimental traces.

6.3.2.1 Odd-odd binary gelators

The phase diagram of 5BA7BA (Figure 6.5a) shows that 5BA and 7BA form a compound, $(5BA)_1(7BA)_1$ with nearly the same T_m^0 as the single gelators (Table S6.1). The compound formation of 5BA and 7BA with the same parity and close spacer length can be due to their similar crystal structure ³⁸. A closer look into the phase diagram of 5BA7BA shows that $(5BA)_1(7BA)_1$ forms eutectic mixtures with single 5BA and single 7BA, respectively, at around 12.5% and 87.5% of 7BA in 5BA.

As shown in Figure 6.5b, 5BA and 9BA gelators form a single phase at the 1:1 ratio, $(5BA)_1(9BA)_1$ which shows lower T_m^0 at 127.0°C compared to single 5BA and 9BA (Table S6.2).

6.3.2.2 Even-even binary gelators

The phase diagram of even-even binary systems (Figure 6.5c,d) follows the same trend as odd-odd gelators (Figure 6.5a,b): 6BA and 8BA form the compound $(6BA)_1(8BA)_1$ with very close melting point to the single 8BA gelators (Table S6.3). Similarly, $(6BA)_1(8BA)_1$ forms eutectic mixtures with 6BA and 8BA respectively at approximately 12.5% and 87.5% of 8BA in 6BA.

6BA and 10BA gelators mostly phase separate at 1:1 $(6BA)_1(10BA)_1$, melting at 138.7 °C, lower than single 6BA and 10BA (Table S6.4).

6.3.2.3 Odd-even binary gelators

Mixtures of 5BA with 6BA at the non-equimolar ratio of 3:1 show a dramatically lower melting temperature than single 5BA and 6BA gelators. The same trend is seen for $(5BA)_3(10BA)_1$ however with the presence of two different phases. The phase diagrams of these odd-even binary systems (Figure 6.5e,f) suggest that these two compositions still form eutectic mixtures.

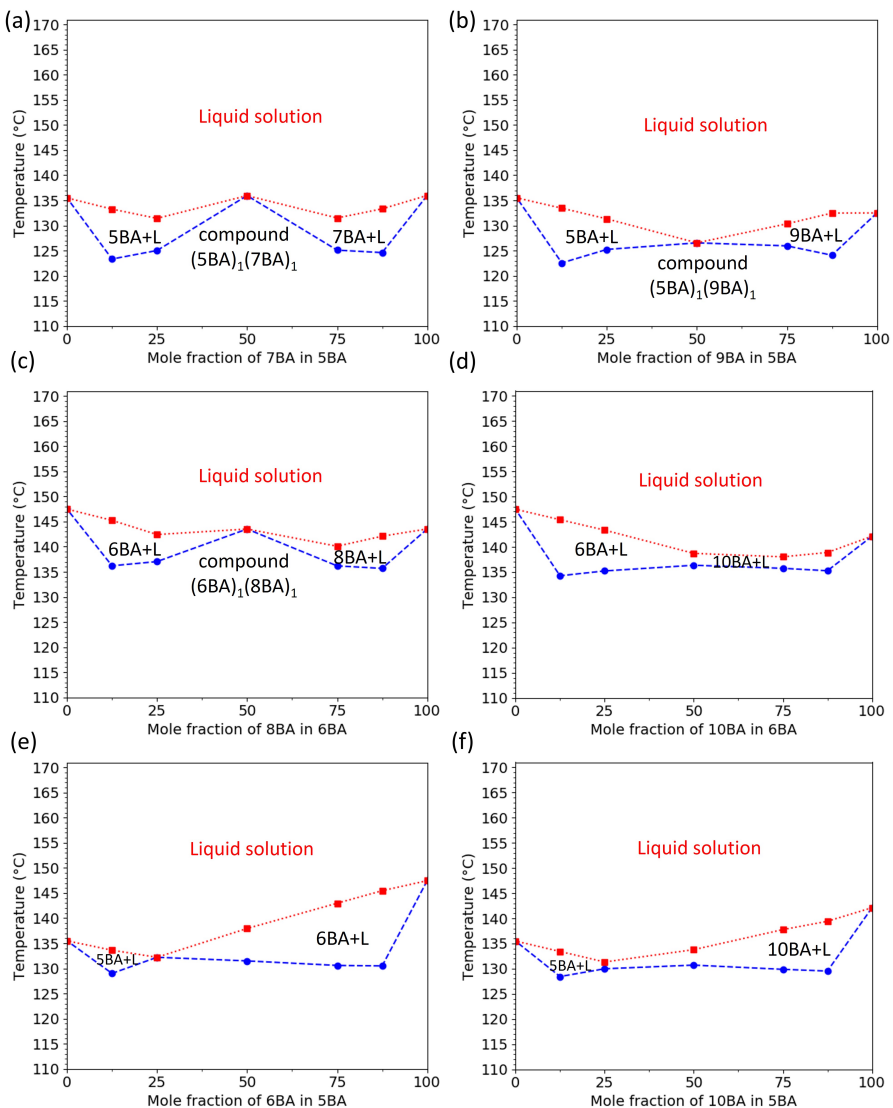


Figure 6.5 Temperature-composition phase diagrams of binary BAs constructed from T_m^0 obtained from the fitting of $DSC_N(T)$ to the experimental traces of single nBA gelators and their binary blends at different compositions (the blue and red curves are the T_m^0 of the first and second phases respectively): a) 5BA7BA, b) 5BA9BA, c) 6BA8BA, d) 6BA10BA, e) 5BA6BA, and f) 5BA10BA showing compound formation for 5BA7BA and 6BA8BA and mixtures with lower T_m^0 for $(5BA)_1(9BA)_1$ and $(6BA)_1(10BA)_1$.

An overview of the phase behavior in binary bisamides in the solid state has been given in Table 6.2.

Table 6.2 Molecular assembly behavior for binary bisamide gelators in the solid state, X represents the unstudied mixtures.

gelators	5BA	6BA	7BA	8BA	9BA	10BA
5BA	x	phase separation	compound	x	compound	phase separation
6BA	-	x	x	compound	x	mostly phase separation
7BA	-	x	x	x	x	x
8BA	x	-	x	x	x	x
9BA	-	x	x	x	x	x
10BA	-	-	x	x	x	x

6.3.3 Binary bisamides in the gel state

To assess the gelation behavior of the binary compounds and mixtures compared to their single gelators, their gels were produced. To compare the characteristics of the binary gels with their single nBA gels from chapter 4³⁸, all gels were prepared at 20 (wt %) concentration of the binary BAs under the same condition as single nBA gels (20 wt %). The gels made of binary gelators are called binary gels for simplicity. As assessed by the tube inversion test, all binary gels resisted flow by gravity except (5BA)₁(9BA)₁ (Figure 6.6).

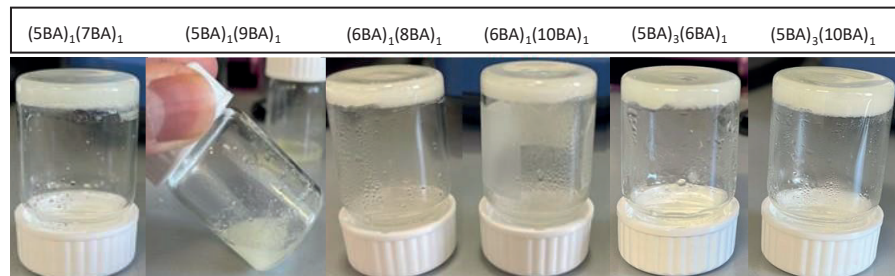


Figure 6.6 Binary gels (20 wt%) prepared from the mixtures and compound binary gelators.

To understand the assembly behavior of binary gelator molecules in the gel state, whether they mix (co-assemble) or phase separate (self-sort), the phase behavior and morphology of the binary gels were compared with their single nBA gels. The DSC thermograms of all nBA single gels and the underlying thermodynamics of their melting-dissolution transition were fully discussed in chapter 4³⁹.

6

6.3.3.1 Odd binary gels

The DSC thermogram of (5BA)₁(7BA)₁ gel (Figure 6.7a) shows a main melting-dissolution transitions with a minor residual transition on top where the T_m^0 is 10 °C

lower than the T_m^0 of single 5BA gel and single 7BA gel (Table S6.7). To understand whether 5BA and 7BA molecules in $(5BA)_1(7BA)_1$ compound have co-assembled or self-sorted in the gel state, the XRD pattern of $(5BA)_1(7BA)_1$ gel was compared with the respective single gels, as shown in Figure 6.7b. Similar to the low-angle XRD pattern of 5BA gel, the first-order reflection of $(5BA)_1(7BA)_1$ gel shows a clear splitting, where the first peak is at 1.52° (2θ), between the first-order reflection of 7BA gel and of 5BA gel, and the second peak is at 1.97° (2θ). Together with the fact that no further splitting is observed in any of the higher-order reflections, as seen for 5BA gel, these observations indicate the tendency of these molecules for co-assembly. The microstructure of $(5BA)_1(7BA)_1$ gel in the SEM images (Figure 6.7d) displays common morphological features that this binary gel shares with single 5BA and 7BA gels³⁸; similar to single 5BA and 7BA gels, almost entirely a single morphology of spheres consisting of woven fibers are observed for $(5BA)_1(7BA)_1$ gel, however with much thinner fibers, which suggests the co-assembly of 5BA and 7BA molecules in the gel state. Co-assembly in the $(5BA)_1(7BA)_1$ gel state was observed in the solid state where molecules formed the $(5BA)_1(7BA)_1$ compound. A small fraction of coarser fibers explains the minor DSC peak which is assigned to the small deviation from the stoichiometric ratio.

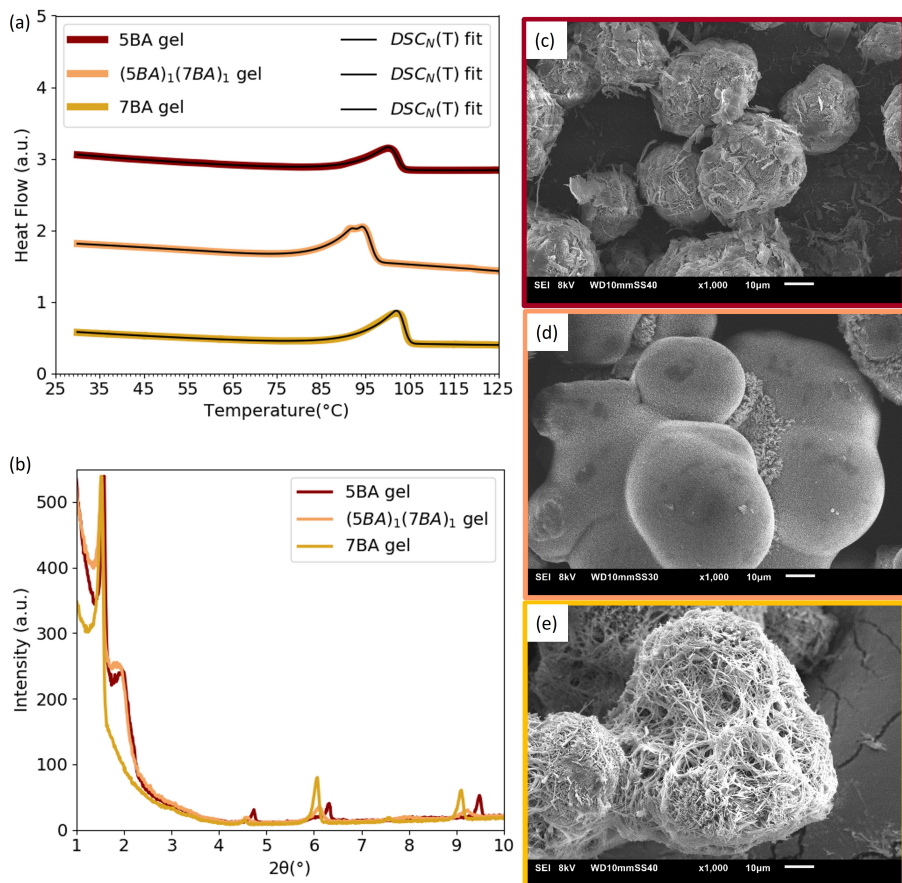


Figure 6.7 Phase behavior of 5BA, 7BA, and (5BA)₁(7BA)₁ gels (20 wt%): a) DSC_N(T) fits to the second heating traces (curves are shifted vertically for clarity), b) diffraction patterns of single and binary 5BA7BA gels (curves were normalized to the highest intensity), SEM images of gels (20 wt%): c) single 5BA, d) (5BA)₁(7BA)₁, and e) single 7BA at 1000x magnification.

The melting-dissolution of (5BA)₁(9BA)₁ gel occurs as a single phase transition (Figure S6.4a). Compared to single 5BA and 9BA gels, the melting-dissolution temperature of (5BA)₁(9BA)₁ gel shifts towards the lower temperature at 103.0 °C (Table S6.8). As Figure S6.4b shows, none of the characteristic reflections in the low-angle XRD pattern of (5BA)₁(9BA)₁ gel shows splitting. Moreover, the first-order reflection of (5BA)₁(9BA)₁ gel appears at 1.40° (2θ) which is at the lower angle than that of 5BA gel (1.47° (2θ)) and 9BA gel (1.58° (2θ)). In a reasonable agreement with molecular arrangement in the solid state, 5BA and 9BA molecules in Figure S6.4d

have co-assembled into a woven fibrous structure in the (5BA)₁(9BA)₁ gel with a new distinct morphology from single 5BA gel and 9BA gel (Figure S6.4c,e) ³⁸.

6.3.3.2 Even binary gels

The melting-dissolution transition of the even-even binary gels from (6BA)₁(8BA)₁ and (6BA)₁(10BA)₁ are shifted towards lower temperatures compared to their single parent gels (Table S6.9 and S6.10). The low-angle XRD pattern (Figure 6.8b) shows that the first-order reflection of (6BA)₁(8BA)₁ gel shifted to 1.91° (2θ) which is significantly lower than 6BA gel (2.07° (2θ)) and 8BA gels (2.01° (2θ)).

Similarly for (6BA)₁(10BA)₁ (Figure S6.5b), the first-order reflection shifted to the lower angle at 1.86° (2θ) compared to that of 6BA gel at 2.07° (2θ) and that of 10BA gel at 1.91° (2θ). However, a small wedge is observed at 1.99° (2θ) which can refer to a partial phase-separation. Even-even gelator molecules co-assemble to form sheets in the (6BA)₁(8BA)₁ and (6BA)₁(10BA)₁ gels (Figure 6.8d and S6.5d) which is in line with the single melting-dissolution transition and the single first-order XRD reflection for (6BA)₁(8BA)₁ and (6BA)₁(10BA)₁ gels at different angles than their respective parent gels. However, the sheet-like structure of (6BA)₁(8BA)₁ is uniform than (6BA)₁(10BA)₁ where a mixture of sheets with higher size distribution is observed. Investigating the molecular arrangement of single even gelators in chapter 3 has shown that the even gelator molecules are tilted at an angle with respect to the layer normal ³⁸ and assemble into sheets in the gel state (Figure 6.8c,e and S6.5c,e) ³⁹. The shift towards the lower angles in the first-order reflection in the XRD pattern of binary gels with respect to that of single parent gels indicates the tilt is changing.

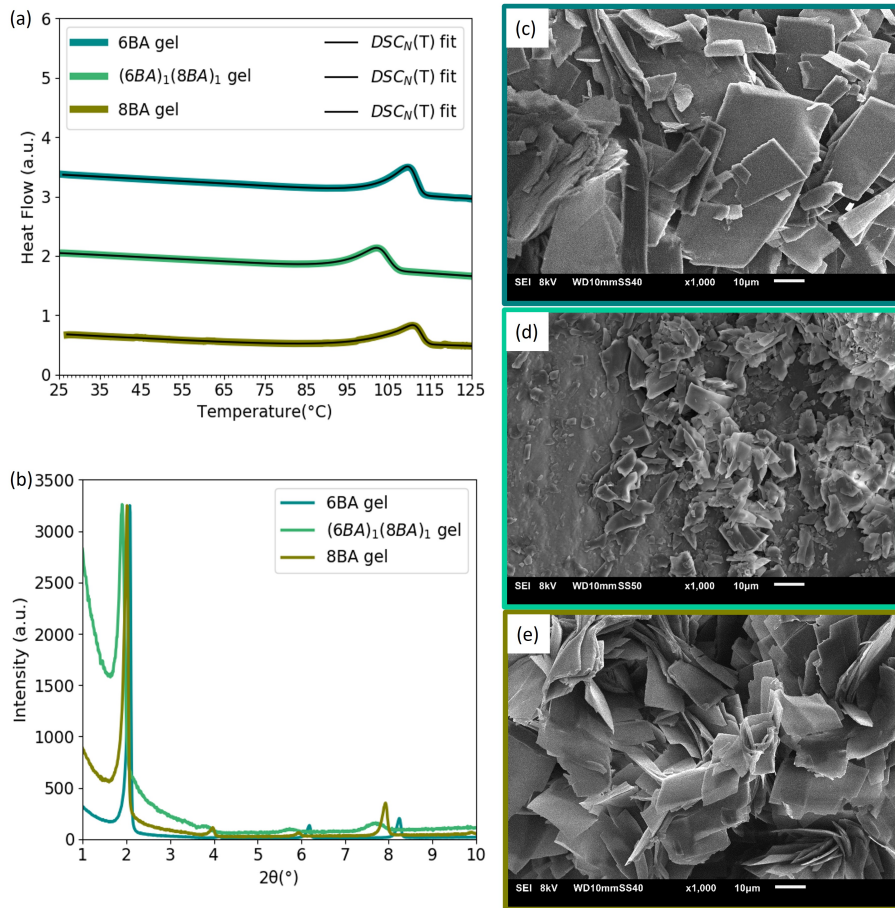


Figure 6.8 Phase behavior of 6BA, 8BA, and (6BA)₁(8BA)₁ gels (20 wt%): a) DSC_N(T) fits to the second heating traces (curves are shifted vertically for clarity), b) diffraction patterns (curves were normalized to the highest intensity). SEM images of gels (20 wt%): c) single 6BA, d) (6BA)₁(8BA)₁ gel, and e) single 8BA gel at 1000x magnification.

6.3.3.3 Odd-even binary gels

The binary gel from (5BA)₃(6BA)₁ mixture shows a double melting-dissolution peak in the DSC thermogram in Figure 6.9a. Both peaks shifted to lower temperatures compared to the single peak of 5BA and 6BA gels (Table S6.11). The presence of two phases, likewise odd-odd and even-even binary gels, is evident from the split first-order and higher order reflections of (5BA)₃(6BA)₁ gel in their low-angle XRD patterns (Figure 6.9b). It is controversial to deduce a full self-sorting of 5BA and 6BA molecules in the binary gel because on the one hand the first-order reflection of 5BA

gel is already split as discussed earlier. On the other hand, the split reflections in the XRD pattern of $(5\text{BA})_3(6\text{BA})_1$ gel do not identically correspond to the reflections of a single 5BA gel or to those of a 6BA gel. Despite this, the SEM images of $(5\text{BA})_3(6\text{BA})_1$ gel in Figure 6.9d show that the microstructure is the combination of woven spheres characteristic of a 5BA gel (Figure 6.9c) and sheets of a 6BA gel (Figure 6.9e). Altogether, these observations indicate that in the gel state these molecules tend to self-sort.

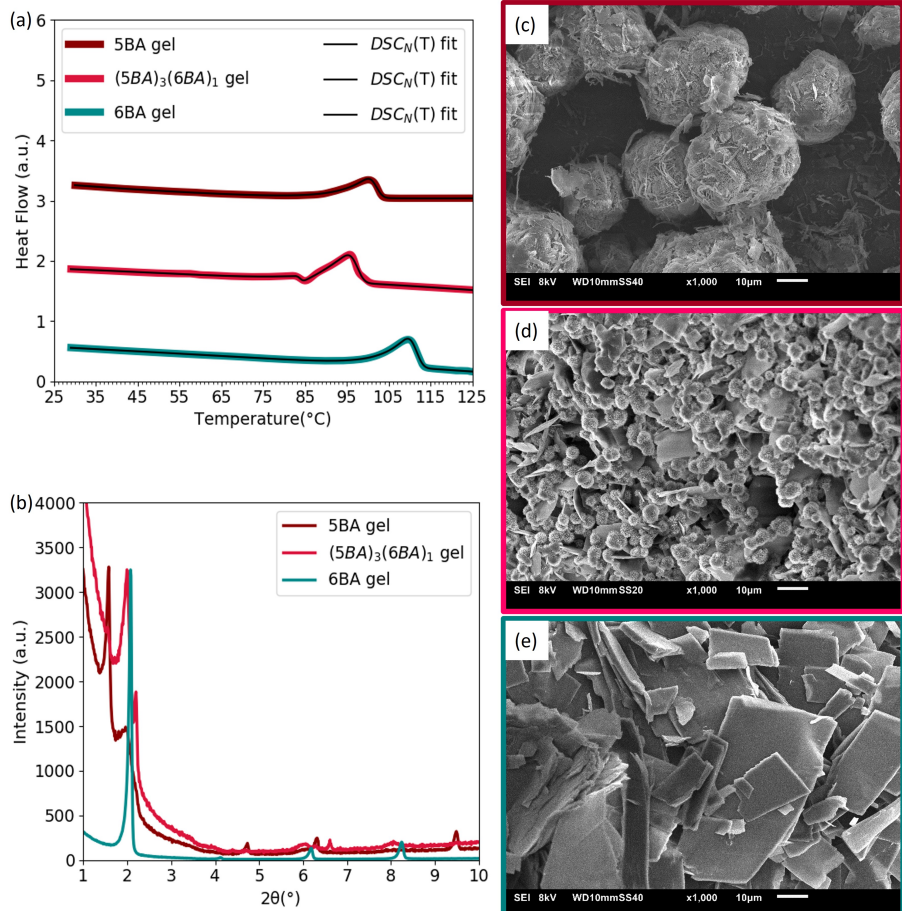


Figure 6.9 Phase behavior of 5BA, 6BA, and $(5\text{BA})_3(6\text{BA})_1$ gels (20 wt%): a) DSC_N(T) fits to the second heating traces (curves are shifted vertically for clarity), b) diffraction patterns (curves were normalized to the highest intensity). SEM images of gels: (20 wt%) c) single 5BA, d) $(5\text{BA})_3(6\text{BA})_1$ gel, and e) single 6BA gel at 1000x magnification.

Comparable observations are made for $(5\text{BA})_3(10\text{BA})_1$ gel, having a similar ratio as $(5\text{BA})_3(10\text{BA})_1$ gelator (Figure S6.6). However, the low-angle XRD pattern of $(5\text{BA})_3(10\text{BA})_1$ gel is the linear superposition of the patterns of single 5BA gel and 10BA gel as seen in (Figure S6.6b). Therefore, the self-sorting of 5BA and 10BA molecules in the $(5\text{BA})_3(10\text{BA})_1$ gel is more obvious than 5BA and 6BA in $(5\text{BA})_3(6\text{BA})_1$. This is probably due to the larger difference in their spacer length impeding their co-assembly via slightly intermixing. The assembly pattern of BA gelators in the gel state is summarized in Table 6.3.

Table 6.3 Assembly behavior of molecules in binary bisamides in the gel state, X represents the unstudied mixtures.

gels	5BA	6BA	7BA	8BA	9BA	10BA
5BA	X	self-sorting (sheet-fiber)	co-assembly (thin fiber)	X	co-assembly (woven fibers)	self-sorting (sheet-fiber)
6BA	-	X	X	co-assembly (sheet)	X	partial self-sorting (mixture of sheets)
7BA	-	X	X	X	X	X
8BA	X	-	X	X	X	X
9BA	-	X	X	X	X	X
10BA	-	-	X	X	X	X

6.3.4 Rheological properties

To understand how the assembly behavior of molecules in the binary gels affects the rheological properties, the rheological properties of the binary gels are compared to those of their single parent gels which were measured under the same condition ³⁹. For a more objective comparison, all gels were measured at the same concentration of 20 w%, and the storage modulus (G') of binary gels were compared with G' of their parent nBA gels (20 w%) at a constant frequency ($\omega=10 \text{ rad}\cdot\text{s}^{-1}$, which is in the linear viscoelastic region of all these gels at this concentration).

As shown in Figure 6.10a, the value of G' for all binary gels is lower than their respective single parent gels except for $(6\text{BA})_1(10\text{BA})_1$ where G' is approximately the average storage modulus of single 6BA and 10BA gels. Increasing the difference in the spacer length of the nBA components in both odd-odd (Figure 6.10a,b) and

even-even (Figure 6.10c,d) binary gels has caused a more dramatic drop in the G' of binary gels.

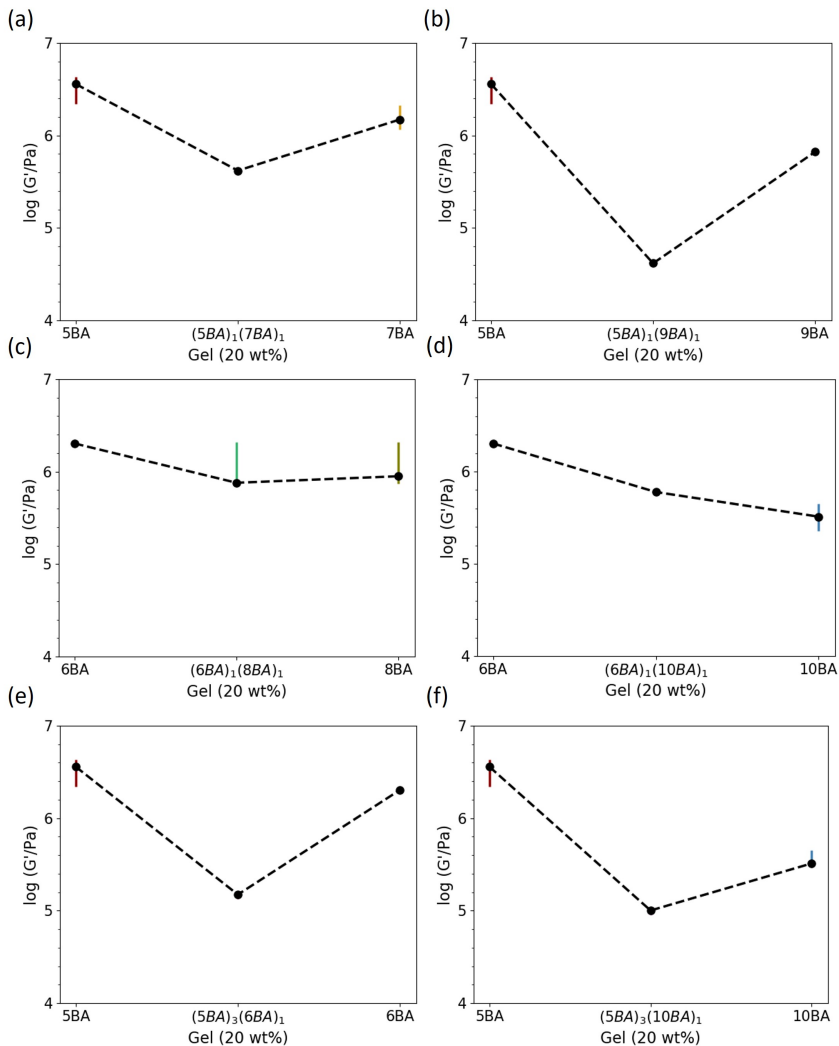


Figure 6.10 Storage modulus (G') of binary gels (20 wt%) compared to their single parent gels (20 wt%) showing how the mechanical properties can be tailored by the addition of the second bisamide to the parent bisamide gelator: a, b) odd-odd gels, c, d) even-even gels, e, and f) odd-even gels.

Co-assembly of even nBA molecules into sheets in even-even binary gels has endowed higher G' to their gels than the co-assembly of odd molecules into fibrous

structures in odd-odd binary gels. The $(5\text{BA})_1(9\text{BA})_1$ gel has the lowest G' among all binary gels which is in line with the table-top inversion test (Table 6.4). The self-sorted gels with both sheets and woven spheres in their morphologies (Figure 6.9d and Figure S6.6d) generally display a lower G' than the co-assembled gels (except for the $(5\text{BA})_1(9\text{BA})_1$ gel). Increasing the difference between the spacer length of the even-even BAs has decreased the G' dramatically, which can be due to the presence of self-sorted 10BA molecules into sheets, which have shown the lowest G' among all single nBA gels ³⁹.

Table 6.4 The effect of assembly behavior in binary gels (20 wt%) on their storage moduli (G') ^[a].

gels	5BA	6BA	7BA	8BA	9BA	10BA
5BA	6.56+0.21/-0.08	5.22+0.04/-0.05	5.63+0.01/-0.01	x	4.63+0.02/-0.02	5.04+0.04/-0.04
	woven fibers and spherical structures	sheet-fiber	thin fibers		woven fibers	sheet-fiber
6BA	-	6.30+0.02/-0.02	x	6.32+0.44/-0.02	x	5.78+0.00/-0.00
		sheet		sheet		mixture of sheets
7BA	-	x	6.1+0.11/-0.16	x	x	x
			woven fibers			
8BA	x	-	x	5.95+0.08/-0.37	x	x
				sheet		
9BA	-	x	x	x	5.82±0.00	x
					woven fibers	
10BA	-	-	x	x	x	5.51+0.15/-0.14
						sheet

[a] All samples were measured at the certain frequency ($\omega=10 \text{ rad}\cdot\text{s}^{-1}$), X represents the unstudied mixtures, the data for single gels are from chapter 4 ³⁹.

6.4 Conclusions

This study on model binary nBA gelators aimed to establish design rules for binary mixture of gelators that govern the mixing or phase separation in the solid and gel states, to investigate the effect of the phase behavior on the gel rheological properties.

From studying the arrangement of molecules in the solid state, the molecular self-recognition in binary bisamides with the same parity and close spacer lengths is not strong which results in the formation of compounds ((5BA)₁(7BA)₁ and (6BA)₁(8BA)₁) with a close crystal structure and melting points to their single parent gelators. A larger difference in the spacer length leads to the partial phase-separation of these molecules in (6BA)₁(10BA)₁. Although 5BA and 9BA are also four spacer lengths apart, these molecules still tend to mix in (5BA)₁(9BA)₁ which could be due to their unpaired hydrogen bonding pattern which gives them more freedom compared to (6BA)₁(10BA)₁. Different parities of BA molecules leads to the phase-separation of these molecules in (5BA)₃(6BA)₁ and (5BA)₃(10BA)₁.

The gel architectures imply that in binary gels from binary compounds or (partially-mixed) mixtures, molecules with the same parity co-assemble into fibers of the woven spheres (odd-odd gels) and into sheets (even-even gels). In binary gels from odd-even gelators, (5BA)₃(6BA)₁ and (5BA)₃(10BA)₁, the molecules self-sort to the separate woven spheres from sheets.

Comparing the supramolecular arrangement in the solid and gel states, the assembly pattern of molecules in the solid and gel states is the same for all binary bisamides; the solvent is indifferent to the interaction with the molecules and does not change their assembly patterns.

Studying the rheological properties in correlation with morphological characteristics, all binary gels have lower G' compared to their single parent gels except (6BA)₁(10BA)₁, where the G' is nearly the average G' of single 6BA and single 10BA gels. The decrease in the G' of binary gels is more dramatic when the parity of the gelators is different or the difference in the spacer length increases. The rheological properties of the binary gels depend on the morphology of their gels, which can be primarily controlled using the odd-even symmetry of the molecules, where binary compounds or mixtures can lead to a variety of assembly behavior: from co-assembly of even-even molecules into more homogeneous sheets to the co-assembly of odd-odd molecules into fibers in the woven spheres with less uniformity and ultimately the self-sorting of odd and even molecules into separate primary structures of spheres and sheets, which results in the least elastic gel behavior. In fact, although odd-odd molecules also show co-assembly, the microstructures of their gels are the combination of woven spheres which apparently shows less entanglement than even-even sheets, and consequently lower storage modulus G'. It is in a reasonable agreement with the table-top inversion test where all binary gels (20 wt%) from mixtures and compounds could form stable gels with more flow resistance than the (5BA)₁(9BA)₁ gel (20 wt%).

6.5 References

- [1] J. R. Moffat and D. K. Smith, "Controlled self-sorting in the assembly of 'multi-gelator'gels", *Chem. Commun.*, 2009.
- [2] K. Sugiyasu, S. Kawano, N. Fujita, S. Shinkai, and R. V January, "Self-sorting organogels with p- n heterojunction points", *Chem. Mater.*, 2008.
- [3] M. M. Smith and D. K. Smith, "Self-sorting multi-gelator gels - Mixing and ageing effects in thermally addressable supramolecular soft nanomaterials", 2011.
- [4] D. García, R. Luque, D. G. Velázquez, and R. Luque, "Spontaneous Orthogonal Self-Assembly of a Synergetic Gelator System", *Chem. Eur. J.*, 2011.
- [5] A. Das and S. Ghosh, "A generalized supramolecular strategy for self-sorted assembly between donor and acceptor gelators", *Chem. Commun.*, 2011.
- [6] M. D. Segarra-Maset et al., "Control of H-and J-type π stacking by peripheral alkyl chains and self-sorting phenomena in perylene bisimide homo-and heteroaggregates", *Chem. Eur. J.*, 2008.
- [7] J. H. van Esch and B. L. Feringa, "New functional materials based on self-assembling organogels: from serendipity towards design", *Angew. Chemie Int. Ed.*, 2000.
- [8] J. S. Foster, A. W. Prentice, R. S. Forgan, M. J. Paterson, and G. O. Lloyd, "Targetable Mechanical Properties by Switching between Self-Sorting and Co-assembly with In Situ Formed Tripodal Ketoamine Supramolecular Hydrogels", *ChemNanoMat*, 2018.
- [9] E. R. Cross, S. Sproules, R. Schweins, E. R. Draper, and D. J. Adams, "Controlled tuning of the properties in optoelectronic self-sorted gels", *J. Am. Chem. Soc.*, 2018.
- [10] K. Tao, A. Levin, L. Adler-Abramovich, and E. Gazit, "Fmoc-modified amino acids and short peptides: simple bio-inspired building blocks for the fabrication of functional materials", *Chem. Soc. Rev.*, 2016.
- [11] A. Y.-Y. Y. Tam and V. W.-W. W. Yam, "Recent advances in metallogels", *Chem. Soc. Rev.*, 2013.
- [12] S. Kiyonaka, K. Sugiyasu, S. Shinkai, and I. Hamachi, "First thermally responsive supramolecular polymer based on glycosylated amino acid", *J. Am. Chem. Soc.*, 2002.
- [13] N. Zweep, A. Hopkinson, A. Meetsma, W. R. Browne, B. L. Feringa, and J. H. Van Esch, "Balancing hydrogen bonding and van der waals interactions in cyclohexane-based bisamide and bisurea organogelators", *Langmuir*, 2009.

- [14] F. Fages, F. Vögtle, and M. Žinić, “Systematic design of amide-and urea-type gelators with tailored properties”, *Top. Curr. Chem.*, 2005.
- [15] B. C. Baker, A. L. Acton, G. C. Stevens, and W. Hayes, “Bis amide-aromatic-ureas—highly effective hydro- and organogelator systems”, *Tetrahedron*, 2014.
- [16] K. Araki and I. Yoshikawa, “Nucleobase-containing gelators”, *Low Mol. Mass Gelator*, 2005.
- [17] M. Žinic, F. Vögtle, and F. Fages, “Cholesterol-based gelators”, *Low Mol. Mass Gelator*, 2005.
- [18] D. K. Smith, “Dendritic gels—many arms make light work”, *Adv. Mater.*, 2006.
- [19] M. Sangeetha and U. Maitra, “Supramolecular gels: Functions and uses”, *Chem. Soc. Rev.*, 2005.
- [20] R. G. Ellis-Behnke et al., “Nano neuro knitting: peptide nanofiber scaffold for brain repair and axon regeneration with functional return of vision”, *Proc. Natl. Acad. Sci.*, 2006.
- [21] G. A. Silva et al., “Selective differentiation of neural progenitor cells by high-epitope density nanofibers”, *Science*, 2004.
- [22] G. Liang et al., “Supramolecular hydrogel of a D-amino acid dipeptide for controlled drug release in vivo”, *Langmuir*, 2009.
- [23] K. J. C. C. Van Bommel, A. Friggeri, and S. Shinkai, “Organic templates for the generation of inorganic materials”, *Angew. Chemie Int. Ed.*, 2003.
- [24] K. Sada, M. Takeuchi, N. Fujita, M. Numata, and S. Shinkai, “Post-polymerization of preorganized assemblies for creating shape-controlled functional materials”, *Chem. Soc. Rev.*, 2007.
- [25] J. Puigmartí-Luis et al., “Supramolecular Conducting Nanowires from Organogels”, *Angew. Chemie*, 2007.
- [26] P. Varelis, L. Melton, and F. Shahidi, “Encyclopedia of food chemistry”, Elsevier, 2018.
- [27] G. Weiss, “The past, present, and future of molecular gels. What is the status of the field, and where is it going?”, *J. Am. Chem. Soc.*, 2014.
- [28] M. Tena-Solsona, S. Alonso-de Castro, J. F. Miravet, and B. Escuder, “Co-assembly of tetrapeptides into complex pH-responsive molecular hydrogel networks”, *J. Mater. Chem. B*, 2014.
- [29] M. D. Segarra-Maset, V. J. Nebot, J. F. Miravet, and B. Escuder, “Control of molecular gelation by chemical stimuli”, *Chem. Soc. Rev.*, 2013.

- [30] M. M. Smith and D. K. Smith, "Self-sorting multi-gelator gels - Mixing and ageing effects in thermally addressable supramolecular soft nanomaterials", *Soft Matter*, 2011.
- [31] M. Zhou et al., "Self-assembled peptide-based hydrogels as scaffolds for anchorage-dependent cells", *Biomaterials*, 2009.
- [32] E. R. Draper and D. J. Adams, "How should multicomponent supramolecular gels be characterised?", *Chem. Soc. Rev.*, 2018.
- [33] . Kar and S. Ghosh, "Self-Sorting in Supramolecular Assembly of π -Systems", *Isr. J. Chem.*, 2019.
- [34] A. S. W. W. Chan and P. R. Sundararajan, "Co-Assembly and Self-Sorting Effects in Gels of Blends of Polyurethane Model Compounds", *ChemistrySelect*, 2017.
- [35] E. R. Draper and D. J. Adams, "How should multicomponent supramolecular gels be characterised?", *Chem. Soc. Rev.*, 2018.
- [36] D. Li, Y. Shi, and L. Wang, "Mechanical Reinforcement of Molecular Hydrogel by Co-assembly of Short Peptide-based Gelators with Different Aromatic Capping Groups", *Chinese J. Chem.*, 2014.
- [37] C. Colquhoun et al., "The effect of self-sorting and co-assembly on the mechanical properties of low molecular weight hydrogels", *Nanoscale*, 2014.
- [38] E. Ghanbari, A. Krishnamurthy, S. J. Picken, E. A. Klop, L. J. Bannenberg, and J. van Esch, "Molecular Arrangement and Thermal Properties of Bisamide Organogelators in the Solid State", *Langmuir*, 2022.
- [39] A. E. Ghanbari, Z. Chen, P. Padmanabhan, S. J. Picken, and J. Van Esch, "Supramolecular arrangement and rheological properties of bisamide gels", *Langmuir*, 2023.
- [40] P. T. Weiss, Richard G., "Molecular gels: Materials with Self-Assembled Fibrillar Networks", Springer, 2006. .
- [41] A. E. Ghanbari, S. J. Picken, and J. Van Esch, "Analysis of differential scanning calorimetry (DSC): Determining the transition temperatures , enthalpy and heat capacity changes in multicomponent systems by analytical model fitting", *J. Therm. Anal. Calorim*, 2023.

6.6 Supplementary Information

Here, the phase behavior of binary gelators and gels and more analytical data from fitting of $DSC_N(T)$ model to the second heating traces of single and binary systems are provided.

Table S6.1 Fit parameters of $DSC_N(T)$ function fitted to the experimental DSC trace of molecularly mixed binary 5BA7BA at different ratios ^[a].

binary 5BA7BA	5BA	(5BA) ₁ (7BA) ₇	(5BA) ₁ (7BA) ₃	(5BA) ₁ (7BA) ₁	(5BA) ₃ (7BA) ₁	(5BA) ₇ (7BA) ₁	7BA		
First peak									
$\Delta H_1 (J.g^{-1})$	Single peak	25.20±0.16	11.88±0.10	Single peak	28.62±0.04	26.04±0.08	Single peak		
$T_{m,1}^0 (^{\circ}C)$		124.60±0.05	125.09±0.06		125.02±0.01	123.32±0.03			
$\alpha_1 (K^{-1})$		0.19±0.00	0.64±0.05		0.59±0.01	0.17±0.00			
$\beta_1 (K^{-2})$		0.88±0.13	0.54±0.08		0.52±0.01	0.41±0.02			
$\Delta C_{p,m,1}$ (W.g ⁻¹ .K ⁻¹)	NA								
Second peak									
$\Delta H_2 (J.g^{-1})$	126.18±0.04	104.52±0.23	116.64±0.29	131.82±0.12	120.96±0.09	82.98±0.13	140.88±0.09		
$T_{m,2}^0 (^{\circ}C)$	135.49±0.00	133.31±0.00	131.49±0.01	135.94±0.00	131.41±0.00	133.25±0.00	135.97±0.00		
$\alpha_2 (K^{-1})$	0.39±0.00	0.39±0.01	0.19±0.00	0.59±0.00	0.18±0.00	0.30±0.00	0.52±0.00		
$\beta_2 (K^{-2})$	3.01±0.04	1.84±0.04	2.47±0.09	1.41±0.01	1.88±0.02	1.76±0.02	1.50±0.03		
$\Delta C_{p,m,2}$ (W.g ⁻¹ .K ⁻¹)	-0.44±0.01	NA		-0.62±0.02	NA		-0.40±0.01		
$B (W.g^{-1})$	1.12±0.00	0.45±0.00	0.18±0.05	1.31±0.40	0.43±0.00	0.38±0.00	1.04±0.01		
C (mW.g ⁻¹ .K ⁻¹)	0.00±0.00	-0.27±0.01	-0.01±0.00	-0.01±0.00	-0.13±0.03	-0.68±0.02	0.00±0.00		
D (mW.g ⁻¹ .K ⁻²)	0.00±0.00	0.00±0.00	0.12±0.03	0.12±0.03	0.00±0.00	0.00±0.00	0.00±0.00		
R^2	0.99	0.99	0.99	0.99	0.99	0.99	0.99		

[a] The samples (6 mg) were heated at 10 K.min⁻¹ after calibration at the onset for the given weight and rate, in the case of (5BA)₁(7BA)₇, only one fitting peak is required due to the peak overlap (the error margins are from the nonlinear fitting), $\Delta C_{p,m}$ does not converge (Not available=NA) due to purely mathematical artefact, if the peaks are sufficiently apart with sufficient baseline tail on each side, the cumulative $\Delta C_{p,m}$ can be reliably determined via the $DSC_N(T)$ function for binary systems.

Table S6.2 Fit parameters of $DSC_N(T)$ function fitted to the experimental DSC trace of 6mg of molecularly mixed binary 5BA9BA at different ratios ^[a].

binary 5BA9BA	5BA	$(5BA)_1(9BA)_7$	$(5BA)_1(9BA)_3$	$(5BA)_1(9BA)_1$	$(5BA)_3(9BA)_1$	$(5BA)_7(9BA)_1$	9BA		
First peak									
$\Delta H_1 (J.g^{-1})$	Single peak	18.06±0.09	39.78±0.03	Single peak	59.52±0.17	3.35±0.15	Single peak		
$T_{m,1}^0 (^{\circ}C)$		124.08±3.17	125.94±0.01		125.23±0.01	122.55±7.80			
$\alpha_1 (K^{-1})$		9.66±300.42	0.74±0.01		0.27±0.00	8.3±0.80			
$\beta_1 (K^{-2})$		0.27±0.09	1.12±0.02		2.41±0.16	0.15±0.08			
$\Delta C_{p,m,1}$ (W.g ⁻¹ .K ⁻¹)	NA								
Second peak									
$\Delta H_2 (J.g^{-1})$	126.18±0.04	189.06±0.13	138.78±0.08	150.12±0.14	49.26±0.83	184.44±0.18	149.21±0.08		
$T_{m,2}^0 (^{\circ}C)$	135.49±0.00	132.47±0.00	130.33±0.00	126.54±0.00	131.31±0.02	133.44±0.01	132.50±0.00		
$\alpha_2 (K^{-1})$	0.39±0.00	0.21±0.00	0.17±0.00	0.44±0.00	0.41±0.05	0.14±0.00	0.52±0.00		
$\beta_2 (K^{-2})$	3.01±0.04	3.91±0.07	3.46±0.06	2.02±0.04	1.80±0.10	2.46±0.07	2.68±0.05		
$\Delta C_{p,m,2}$ (W.g ⁻¹ .K ⁻¹)	-0.44±0.01	NA		0.00±0.04	NA		-0.35±0.01		
$B (W.g^{-1})$	1.12±0.00	0.45±0.00	0.44±0.00	0.46±0.26	0.45±0.00	0.44±0.00	1.07±0.01		
C (mW.g ⁻¹ .K ⁻¹)	0.00±0.00	-0.37±0.01	-0.43±0.02	1.32±0.08	0.02±0.06	-0.41±0.00	0.00±0.00		
D (mW.g ⁻¹ .K ⁻²)	0.00±0.00	0.01±0.00	0.01±0.00	0.02±0.00	0.01±0.00	0.01±0.00	0.00±0.00		
R^2	0.99	0.99	0.99	0.99	0.99	0.99	0.99		

[a] The samples (6 mg) were heated at 10 K.min⁻¹ after calibration at the onset for the given weight and rate, in the case of $(5BA)_1(9BA)_1$, only one fitting peak is required due to the peak overlap (the error margins are from the nonlinear fitting), $\Delta C_{p,m}$ does not converge (Not available=NA) due to purely mathematical artefact, if the peaks are sufficiently apart with sufficient baseline tail on each side, the cumulative $\Delta C_{p,m}$ can be reliably determined via the $DSC_N(T)$ function for binary systems.

Table S6.3 Fit parameters of $DSC_N(T)$ function fitted to the experimental DSC trace of 6mg of molecularly mixed binary 6BA8BA at different ratios^[a].

binary 6BA8BA	6BA	$(6BA)_1(8BA)_7$	$(6BA)_1(8BA)_3$	$(6BA)_3(8BA)_1$	$(6BA)_3(8BA)_1$	$(6BA)_7(8BA)_1$	8BA
First peak							
$\Delta H_1 (J.g^{-1})$		36.96 \pm 1.05	34.02 \pm 0.09		49.38 \pm 0.05	32.46 \pm 0.07	
$T_{m,1}^0 (^\circ C)$	Single peak	135.68 \pm 0.06	136.18 \pm 0.02	Single peak	137.04 \pm 0.01	136.20 \pm 0.02	Single peak
$\alpha_1 (K^{-1})$		0.09 \pm 0.01	0.50 \pm 0.01		0.59 \pm 0.01	0.28 \pm 0.00	
$\beta_1 (K^{-2})$		0.71 \pm 0.12	0.84 \pm 0.05		0.88 \pm 0.02	1.28 \pm 0.07	
$\Delta C_{p,m,1}$ (W.g $^{-1}$.K $^{-1}$)		NA					
Second peak							
$\Delta H_2 (J.g^{-1})$	168.66 \pm 0.07	142.26 \pm 1.14	149.04 \pm 0.29	162.30 \pm 1.91	127.02 \pm 0.11	120.66 \pm 0.18	155.12 \pm 0.12
$T_{m,2}^0 (^\circ C)$	147.46 \pm 0.00	142.09 \pm 0.01	140.09 \pm 0.01	143.51 \pm 0.00	142.42 \pm 0.00	145.24 \pm 0.00	143.53 \pm 0.00
$\alpha_2 (K^{-1})$	0.63 \pm 0.00	0.23 \pm 0.01	0.15 \pm 0.00	0.30 \pm 0.02	0.18 \pm 0.00	0.36 \pm 0.00	0.31 \pm 0.00
$\beta_2 (K^{-2})$	1.19 \pm 0.02	1.24 \pm 0.02	1.77 \pm 0.05	1.67 \pm 0.04	1.61 \pm 0.03	1.14 \pm 0.02	1.69 \pm 0.04
$\Delta C_{p,m,2}$ (W.g $^{-1}$.K $^{-1}$)	-0.28 \pm 0.01	NA		0.27 \pm 0.52	NA		-0.28 \pm 0.01
$B (W.g^{-1})$	1.12 \pm 0.01	0.42 \pm 0.00	0.44 \pm 0.00	0.38 \pm 0.00	0.44 \pm 0.00	0.43 \pm 0.00	0.94 \pm 0.01
$C (mW.g^{-1}.K^{-1})$	0.00 \pm 0.00	-0.29 \pm 0.06	-0.25 \pm 0.05	-0.26 \pm 0.09	0.03 \pm 0.04	0.31 \pm 0.05	0.00 \pm 0.00
$D (mW.g^{-1}.K^{-2})$	0.00 \pm 0.00	0.01 \pm 0.00	0.00 \pm 0.00				
R^2	0.99	0.99	0.99	0.99	0.99	0.99	0.99

[a] The samples (6 mg) were heated at 10 K.min $^{-1}$ after calibration at the onset for the given weight and rate, in the case of $(6BA)_1(8BA)_1$, only one fitting peak is required due to the peak overlap (the error margins are from the nonlinear fitting), $\Delta C_{p,m}$ does not converge (Not available=NA) due to purely mathematical artefact, if the peaks are sufficiently apart with sufficient baseline tail on each side, the cumulative $\Delta C_{p,m}$ can be reliably determined via the $DSC_N(T)$ function for binary systems.

Table S6.4 Fit parameters of $DSC_N(T)$ function fitted to the experimental DSC trace of 6mg of molecularly mixed binary 6BA10BA at different ratios^[a].

binary 6BA10BA	6BA	$(6BA)_1(10BA)_7$	$(6BA)_3(10BA)_3$	$(6BA)_1(10BA)_1$	$(6BA)_3(10BA)_1$	$(6BA)_7(10BA)_1$	10BA	
First peak								
ΔH_1 (J.g ⁻¹)	Single peak	34.56±0.13	49.32±0.03	125.16±0.07	58.56±0.04	31.74±0.04	Single peak	
$T_{m,1}^0$ (°C)		135.26±0.01	135.74±0.00	136.35±0.00	135.22±0.00	134.26±0.01		
α_1 (K ⁻¹)		1.21±0.00	0.84±0.00	0.73±0.00	0.80±0.01	0.41±0.00		
β_1 (K ⁻²)		1.85±0.15	1.81±0.02	1.21±0.01	1.64±0.02	3.24±0.15		
$\Delta C_{p,m,1}$ (W.g ⁻¹ .K ⁻¹)	NA							
Second peak								
ΔH_2 (J.g ⁻¹)	168.66±0.07	148.38±0.01	310.08±1.17	164.52±1.49	136.98±0.14	122.40±0.07	172.20±0.06	
$T_{m,2}^0$ (°C)	147.46±0.00	138.89±0.07	138.02±0.00	138.71±0.01	143.33±0.00	145.40±0.00	142.11±0.00	
α_2 (K ⁻¹)	0.63±0.00	0.35±0.07	0.12±0.00	0.08±0.00	0.20±0.00	0.40±0.00	0.48±0.00	
β_2 (K ⁻²)	1.19±0.02	2.22±0.04	3.45±0.02	1.50±0.06	2.62±0.05	2.21±0.03	1.40±0.02	
$\Delta C_{p,m,2}$ (W.g ⁻¹ .K ⁻¹)	- 0.28±0.01	NA		-1.72±0.03	NA		- 0.29±0.01	
B (W.g ⁻¹)	1.12±0.01	0.46±0.00	0.62±0.00	0.39±0.00	0.00±0.00	0.44±0.00	1.19±0.01	
C (mW.g ⁻¹ .K ⁻¹)	0.00±0.00	0.38±5.08	1.63±0.02	-0.39±0.04	-0.14±0.05	0.29±0.05	0.01±0.00	
D (mW.g ⁻¹ .K ⁻²)	0.00±0.00	0.01±0.00	0.01±0.00	0.01±0.00	0.01±0.00	0.01±0.00	0.00±0.00	
R^2	0.99	0.99	0.99	0.99	0.99	0.99	0.99	

[a] The samples (6 mg) were heated at 10 K.min⁻¹ after calibration at the onset for the given weight and rate, in the case of $(6BA)_1(10BA)_1$, only one fitting peak is required due to the peak overlap (the error margins are from the nonlinear fitting), $\Delta C_{p,m}$ does not converge (Not available=NA) due to purely mathematical artefact, if the peaks are sufficiently apart with sufficient baseline tail on each side, the cumulative $\Delta C_{p,m}$ can be reliably determined via the $DSC_N(T)$ function for binary systems.

Table S6.5 Fit parameters of $DSC_N(T)$ function fitted to the experimental DSC trace of 6mg of molecularly mixed binary 5BA6BA at different ratios^[a].

binary 5BA6BA	5BA	(5BA) ₁ (6BA) ₇	(5BA) ₁ (6BA) ₃	(5BA) ₁ (6BA) ₁	(5BA) ₃ (6BA) ₁	(5BA) ₇ (6BA) ₁	6BA		
First peak									
$\Delta H_1 (J.g^{-1})$	Single peak	22.08±0.05	37.56±0.03	69.54±0.02	Single peak	56.34±0.76	Single peak		
$T_{m,1}^0 (^\circ C)$		130.49±0.03	130.59±0.00	131.49±0.00		129.00±0.02			
$\alpha_1 (K^{-1})$		0.17±0.00	0.38±0.00	0.61±0.00		0.07±0.00			
$\beta_1 (K^{-2})$		1.20±0.12	1.41±0.04	1.94±0.02		1.62±0.21			
$\Delta C_{p,m,1}$ (W.g ⁻¹ .K ⁻¹)	NA								
Second peak									
$\Delta H_2 (J.g^{-1})$	126.18±0.04	127.44±0.06	107.76±0.11	115.02±0.12	222.3±7.07	120.6±0.23	168.66±0.07		
$T_{m,2}^0 (^\circ C)$	135.49±0.00	145.46±0.00	142.97±0.00	137.94±0.01	132.21±0.02	133.62±0.00	147.46±0.00		
$\alpha_2 (K^{-1})$	0.39±0.00	0.36±0.00	0.27±0.00	0.09±0.00	0.07±0.00	0.30±0.00	0.63±0.00		
$\beta_2 (K^{-2})$	3.01±0.04	1.50±0.02	1.89±0.03	1.11±0.02	2.43±0.28	2.65±0.04	1.19±0.02		
$\Delta C_{p,m,2}$ (W.g ⁻¹ .K ⁻¹)	-0.44±0.01	NA			-1.85±0.52	NA	-0.28±0.01		
B (W.g ⁻¹)	1.12±0.00	0.38±0.00	0.51±0.00	0.38±0.00	0.38±0.00	0.39±0.00	1.12±0.01		
C (mW.g ⁻¹ .K ⁻¹)	0.00±0.00	-0.24±0.05	0.64±0.04	-0.45±0.03	-0.59±0.02	-0.54±0.04	0.00±0.00		
D (mW.g ⁻¹ .K ⁻²)	0.00±0.00	0.01±0.00	0.01±0.00	0.01±0.00	0.01±0.00	0.01±0.00	0.00±0.00		
R^2	0.99	0.99	0.99	0.99	0.99	0.99	0.99		

[a] The samples (6 mg) were heated at 10 K.min⁻¹ after calibration at the onset for the given weight and rate, in the case of (5BA)₃(6BA)₁, only one fitting peak is required due to the peak overlap (the error margins are from the nonlinear fitting), $\Delta C_{p,m}$ does not converge (Not available=NA) due to purely mathematical artefact, if the peaks are sufficiently apart with sufficient baseline tail on each side, the cumulative $\Delta C_{p,m}$ can be reliably determined via the $DSC_N(T)$ function for binary systems.

Table S6.6 Fit parameters of $DSC_N(T)$ function fitted to the experimental DSC trace of 6mg of molecularly mixed binary 5BA10BA at different ratios^[a].

binary 5BA10BA	SBA	(5BA),(10BA), 1	(5BA),(10BA), 3	(5BA),(10BA), 1	(5BA),(10BA), 1	(5BA),(10BA), 1	10BA	
First peak								
$\Delta H_1 (J.g^{-1})$	Single peak	22.62±0.00	33.36±0.05	76.38±0.03	62.28±0.14	18.12±0.06	Single peak	
$T_{m,1}^0 (^\circ C)$		0.00±0.00	129.87±0.01	130.71±0.00	129.98±0.01	128.44±0.02		
$\alpha_1 (K^{-1})$		0.00±0.00	0.85±0.02	0.64±0.00	0.60±0.00	1.21±0.08		
$\beta_1 (K^{-2})$		0.99	1.41±0.04	1.29±0.01	2.08±0.05	1.16±0.07		
$\Delta C_{p,m,1} (W.g^{-1}.K^{-1})$	NA							
Second peak								
$\Delta H_2 (J.g^{-1})$	126.18±0.04	24.57±0.07	169.32±0.13	169.26±0.40	250.98±0.90	147.30±0.09	172.20±0.06	
$T_{m,2}^0 (^\circ C)$	135.49±0.00	139.42±0.00	137.76±0.00	133.78±0.00	131.33±0.01	133.42±0.00	142.11±0.00	
$\alpha_2 (K^{-1})$	0.39±0.00	0.40±0.01	0.21±0.00	0.11±0.00	0.09±0.00	0.19±0.00	0.48±0.00	
$\beta_2 (K^{-2})$	3.01±0.04	1.87±0.01	2.87±0.04	1.17±0.02	3.03±0.08	2.80±0.07	1.40±0.02	
$\Delta C_{p,m,2} (W.g^{-1}.K^{-1})$	-0.44±0.01	NA			-2.61±0.05	NA	-0.29±0.01	
$B (W.g^{-1})$	1.12±0.00	0.42±0.00	0.44±0.00	0.43±0.00	0.36±0.00	0.58±0.03	1.19±0.01	
$C (mW.g^{-1}.K^{-1})$	0.00±0.00	-0.15±0.03	-0.11±0.04	-0.47±0.00	-0.46±0.02	-0.12±0.04	0.01±0.00	
$D (mW.g^{-1}.K^{-2})$	0.00±0.00	0.01±0.00	0.01±0.00	1.44±1.91	0.01±0.00	0.01±0.00	0.00±0.00	
R^2	0.99	0.99	0.99	0.99	0.99	0.99	0.99	

[a] The samples (6 mg) were heated at 10 K.min⁻¹ after calibration at the onset for the given weight and rate, in the case of (5BA)₃(10BA)₁, only one fitting peak is required due to the peak overlap (the error margins are from the nonlinear fitting), $\Delta C_{p,m}$ does not converge (Not available=NA) due to purely mathematical artefact, if the peaks are sufficiently apart with sufficient baseline tail on each side, the cumulative $\Delta C_{p,m}$ can be reliably determined via the $DSC_N(T)$ function for binary systems.

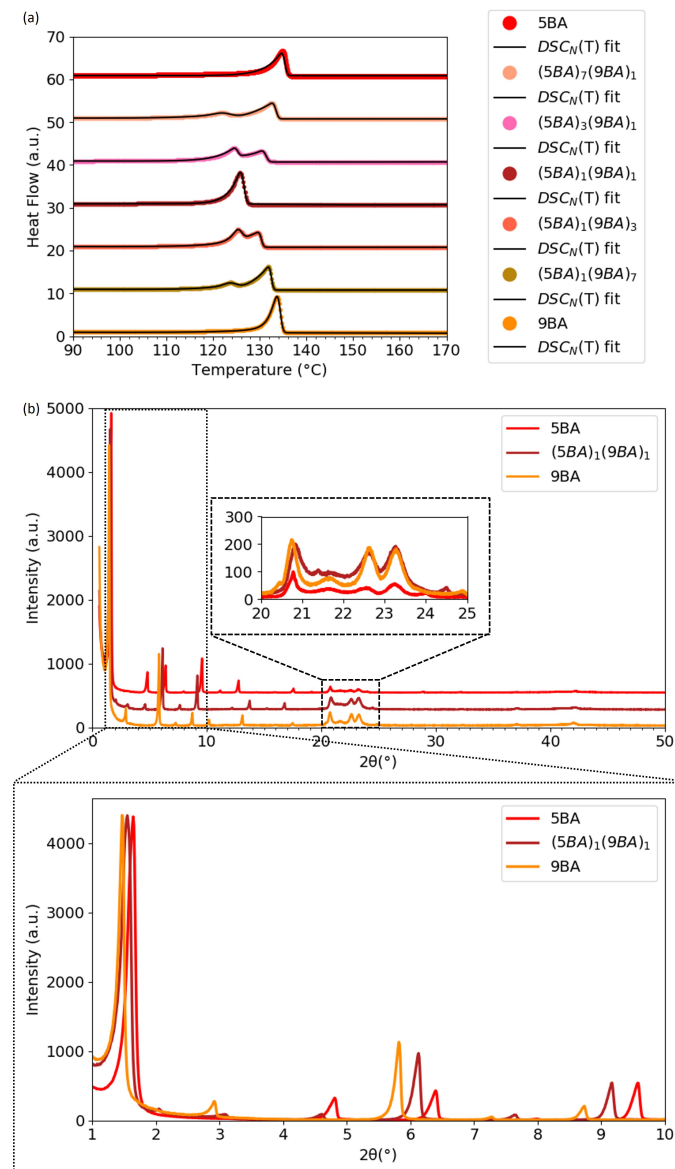


Figure S6.1 Phase behavior of 5BA9BA gelators: a) $DSC_N(T)$ fit to the second heating DSC traces of 5BA9BA at different mixing ratios (the traces and fits were shifted vertically for clarity), b) XRD patterns of $(5BA)_1(9BA)_1$ in comparison to single 5BA and 9BA gelators (curves were normalized to the highest intensity), the insets magnify high-angle (20° – 25° (2θ)) and low-angle (0° – 10° (2θ)) regions.

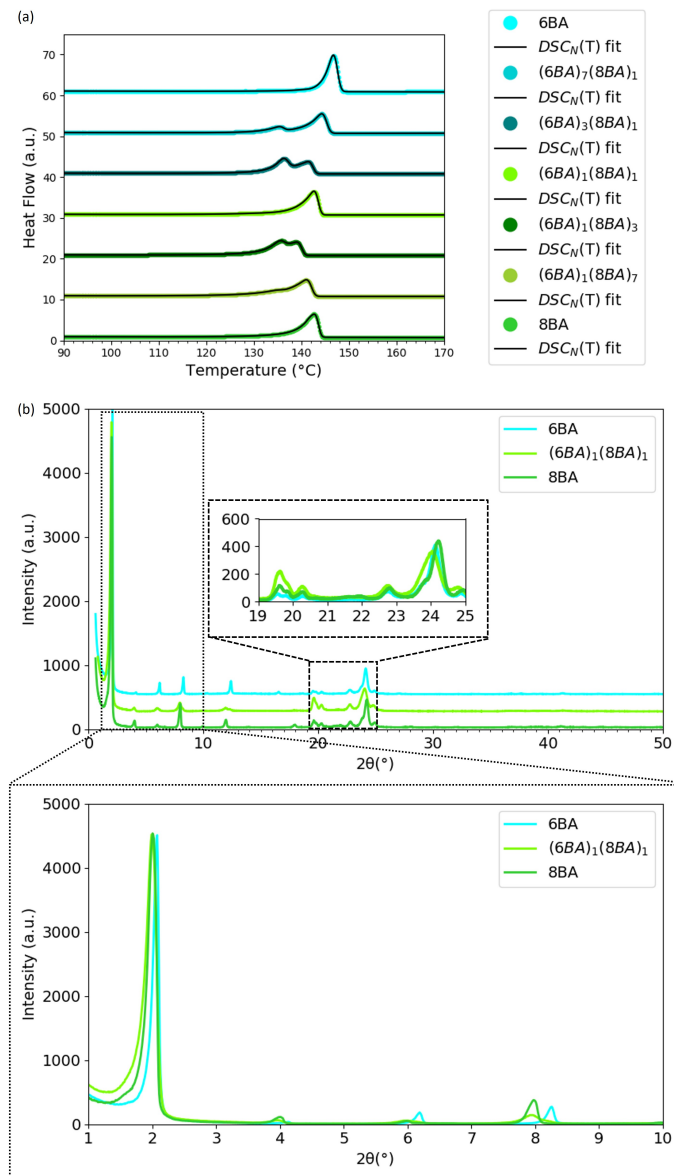


Figure S6.2 Phase behavior of 6BA8BA gelators: a) the second heating traces for various mixing ratios 6BA and 8BA. $DSC_N(T)$ fits to the experimental traces (the traces and fits were shifted vertically for clarity), b) XRD patterns of $(6BA)_1(8BA)_1$ in comparison to single 6BA and 8BA gelators (curves were normalized to the highest intensity), the insets magnify high-angle (20°-25° (2θ)) and low-angle (0°-10° (2θ)) regions.

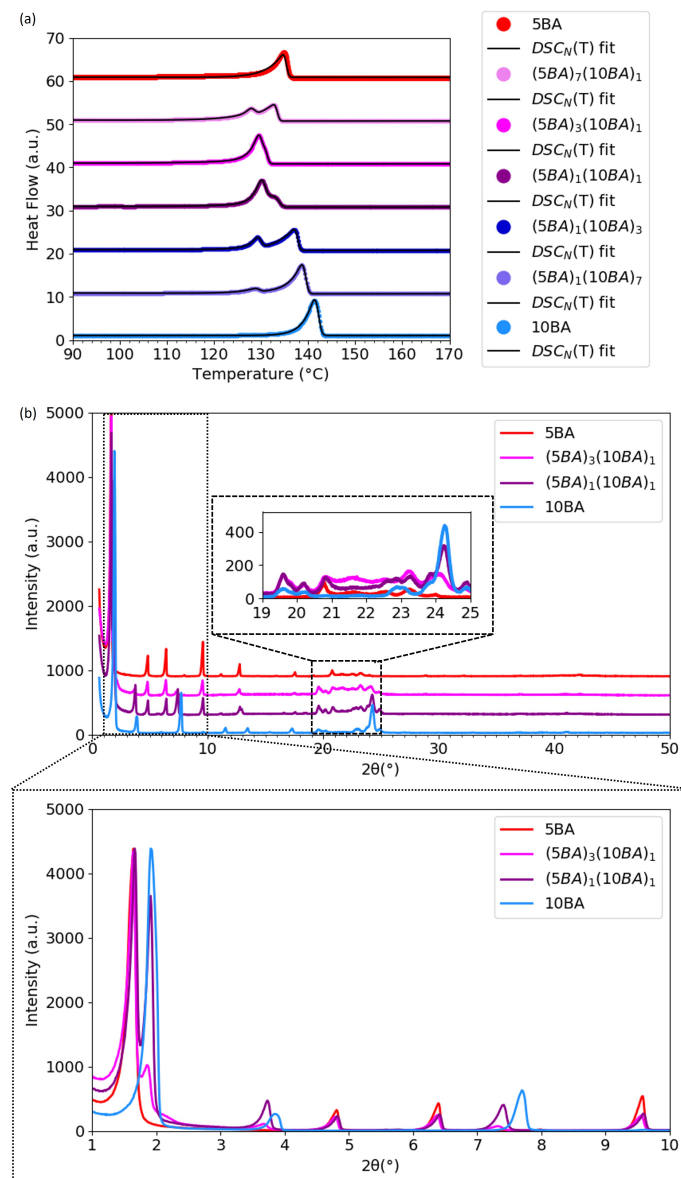


Figure S6.3 Phase behavior of 5BA10BA gelators: a) the second heating traces for various mixing ratios 5BA and 10BA. $DSC_N(T)$ fits to the experimental traces (the traces and fits were shifted vertically for clarity), b) XRD patterns of $(5BA)_3(10BA)_1$ in comparison to single 5BA and 10BA gelators and binary $(5BA)_1(10BA)_1$ which also shows two DSC peaks and two distinct first-order reflections (curves were normalized to the highest intensity), the insets magnify high-angle (20°-25° (2θ)) and low-angle (0°-10° (2θ)) regions.

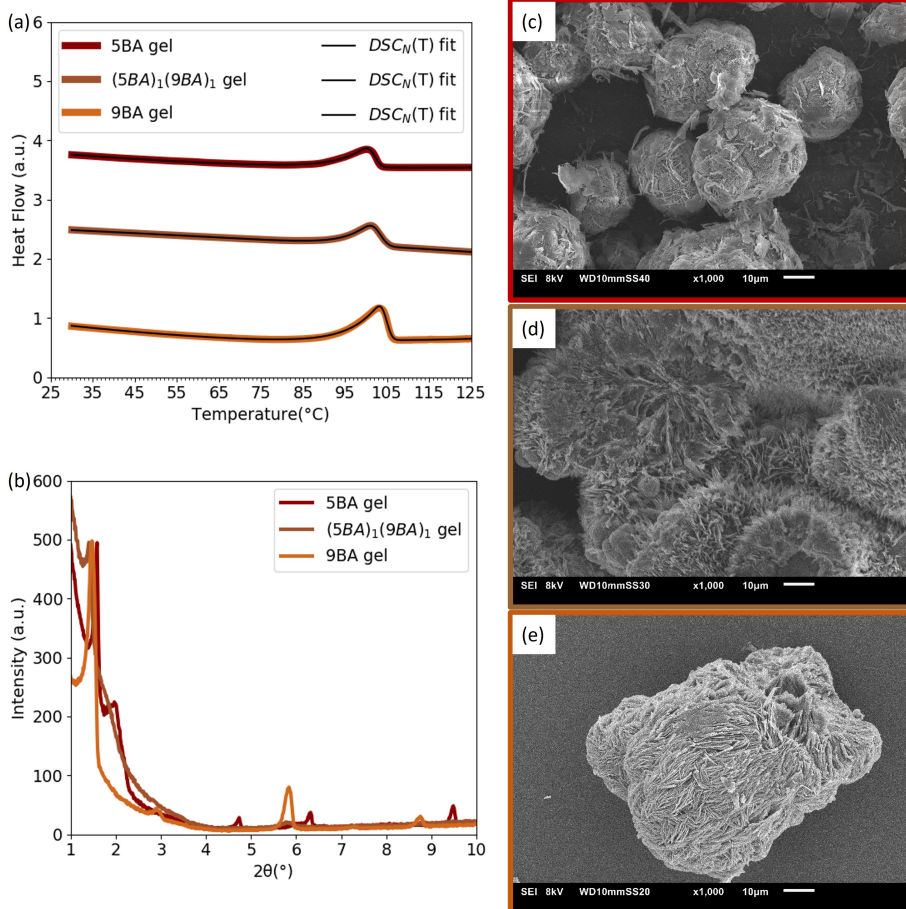


Figure S6.4 Phase behavior of 5BA, 9BA, and $(5BA)_1(9BA)_1$ gels (20 wt%): a) $DSC_N(T)$ fits to the second heating traces (curves are shifted vertically for clarity), b) diffraction patterns of 5BA, 9BA, and $(5BA)_1(9BA)_1$ gels (curves were normalized to the highest intensity). SEM images of gels (20 wt%) c) single 5BA, d) $(5BA)_1(9BA)_1$ gel, e) single 9BA gel at 1000x magnification.

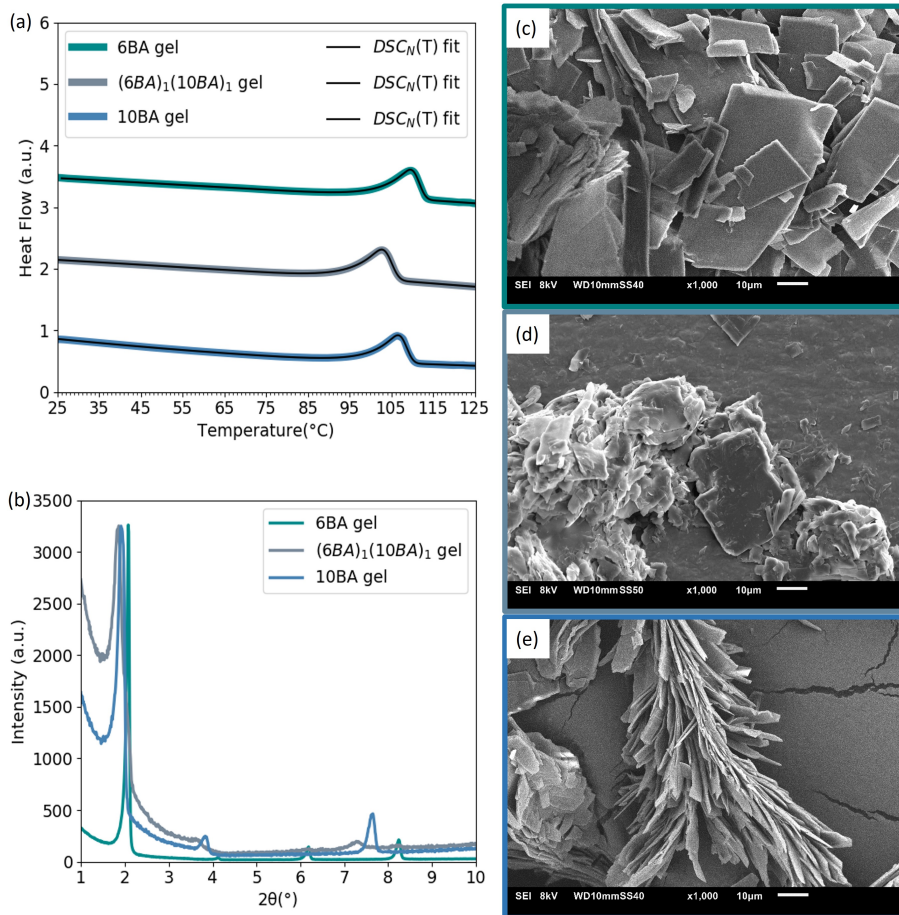


Figure S6.5 Phase behavior of 6BA, 10BA, and $(6BA)_1(10BA)_1$ gels (20 wt%): a) $DSC_N(T)$ fits to the second heating traces (curves are shifted vertically for clarity), b) diffraction patterns (curves were normalized to the highest intensity). SEM images of gels (20 wt%) c) single 6BA, d) $(6BA)_1(10BA)_1$ gel, e) single 10BA gel at 1000x magnification.

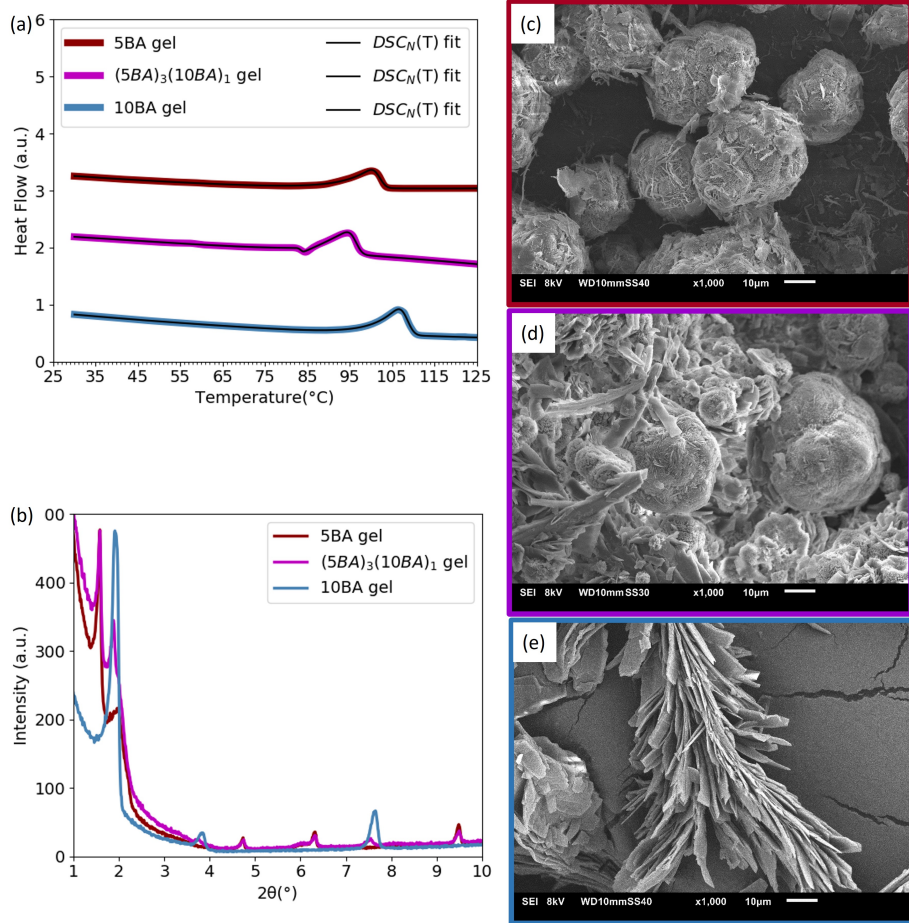


Figure S6.6 Phase behavior of 5BA, 10BA, and $(5BA)_3(10BA)_1$ gels (20 wt%): a) $DSC_N(T)$ fits to the second heating traces (curves are shifted vertically for clarity), b) diffraction patterns (curves were normalized to the highest intensity). SEM images of gels (20 wt%) c) single 5BA, d) $(5BA)_1(10BA)_1$ gel, e) single 10BA gel at 1000x magnification.

Table S6.7 Fit parameters of $DSC_N(T)$ function fitted to the experimental DSC trace of 8mg of 5BA, 7BA, and $(5BA)_1(7BA)_1$ gels (20 wt%)^[a].

5BA7BA gels	5BA gel	$(5BA)_1(7BA)_1$ gel	7BA gel
ΔH_1 (J.g ⁻¹)	Single peak	93.36±0.01	Single peak
$T_{m,1}^0$ (°C)		92.51±0.01	
α_1 (K ⁻¹)		0.00±0.00	
β_1 (K ⁻²)		1.45±0.07	
$\Delta C_{p,m,1}$ (W.g ⁻¹ .K ⁻¹)		NA	
ΔH_2 (J.g ⁻¹)	36.12±0.01	59.64±0.02	53.16±0.01
$T_{m,2}^0$ (°C)	101.96±0.01	95.96±0.00	103.63±0.00
α_2 (K ⁻¹)	0.15±0.00	0.15±0.00	0.14±0.00
β_2 (K ⁻²)	0.33±0.00	0.34±0.00	0.52±0.00
$\Delta C_{p,m,2}$ (W.g ⁻¹ .K ⁻¹)	0.01±0.00	NA	0.03±0.00
B (W.g ⁻¹)	0.54±0.00	5.05±1.74	0.39±0.00
C (mW.g ⁻¹ .K ⁻¹)	-0.86±0.01	-1.92±0.03	-1.30±0.02
D (mW.g ⁻¹ .K ⁻²)	0.03±0.00	-0.01±0.00	0.02±0.00
R ²	0.99	0.99	0.99

[a] The samples were heated at 5 K.min⁻¹ after calibration at the onset for the given weight and rate, in the case of single gels only one fitting peak is required (the error margins are from the nonlinear fitting), $\Delta C_{p,m}$ does not converge (Not available=NA) due to purely mathematical artefact, if the peaks are sufficiently apart with sufficient baseline tail on each side, the cumulative $\Delta C_{p,m}$ can be reliably determined via the $DSC_N(T)$ function for binary systems.

Table S6.8 Fit parameters of $DSC_N(T)$ function fitted to the experimental DSC trace of 8mg of 5BA, 9BA, and $(5BA)_1(9BA)_1$ gels (20 wt%)^[a].

5BA9BA gels	5BA gel	$(5BA)_1(9BA)_1$ gel	9BA gel
$\Delta H_1 (J.g^{-1})$	36.12 ± 0.01	37.56 ± 0.00	64.08 ± 0.00
$T_{m,1}^0 (^\circ C)$	101.96 ± 0.01	103.13 ± 0.00	104.82 ± 0.00
$\alpha_1 (K^{-1})$	0.15 ± 0.00	0.18 ± 0.00	0.15 ± 0.00
$\beta_1 (K^{-2})$	0.33 ± 0.00	0.19 ± 0.00	0.44 ± 0.00
$\Delta C_{p,m,1} (W.g^{-1}.K^{-1})$	0.01 ± 0.00	0.08 ± 0.00	0.04 ± 0.00
$B (W.g^{-1})$	0.54 ± 0.00	0.20 ± 0.00	1.59 ± 0.00
$C (mW.g^{-1}.K^{-1})$	-0.86 ± 0.01	-4.20 ± 0.01	1.02 ± 0.01
$D (mW.g^{-1}.K^{-2})$	0.03 ± 0.00	-0.01 ± 0.00	0.05 ± 0.00
R^2	0.99	0.99	0.99

[a] The samples were heated at $5 K.\min^{-1}$ after calibration at the onset for the given weight and rate, in the case of single gels only one fitting peak is required (the error margins are from the nonlinear fitting).

Table S6.9 Fit parameters of $DSC_N(T)$ function fitted to the experimental DSC trace of 8mg of 6BA, 8BA, and $(6BA)_1(8BA)_1$ gels (20 wt%)^[a].

6BA8BA gels	6BA gel	$(6BA)_1(8BA)_1$ gel	8BA gel
$\Delta H_1 (J.g^{-1})$	53.04 ± 0.01	49.56 ± 0.00	53.88 ± 0.01
$T_{m,1}^0 (^\circ C)$	111.50 ± 0.00	104.51 ± 0.00	112.77 ± 0.00
$\alpha_1 (K^{-1})$	0.16 ± 0.00	0.15 ± 0.00	0.11 ± 0.00
$\beta_1 (K^{-2})$	0.28 ± 0.00	0.15 ± 0.00	0.33 ± 0.00
$\Delta C_{p,m,1} (W.g^{-1}.K^{-1})$	0.00 ± 0.00	0.01 ± 0.00	0.01 ± 0.00
$B (W.g^{-1})$	0.22 ± 0.00	0.24 ± 0.00	0.41 ± 0.00
$C (mW.g^{-1}.K^{-1})$	-4.45 ± 0.03	-4.49 ± 0.01	-2.48 ± 0.02
$D (mW.g^{-1}.K^{-2})$	0.01 ± 0.00	-0.01 ± 0.00	0.01 ± 0.00
R^2	0.99	0.99	0.99

[a] The samples were heated at $5 K.\min^{-1}$ after calibration at the onset for the given weight and rate, in the case of single gels only one fitting peak is required (the error margins are from the nonlinear fitting).

Table S6.10 Fit parameters of $DSC_N(T)$ function fitted to the experimental DSC trace of 8mg of 6BA, 10BA, and $(6BA)_1(10BA)_1$ gels (20 wt%)^[a].

6BA10BA gels	6BA gel	$(6BA)_1(10BA)_1$ gel	10BA gel
$\Delta H_1 (J.g^{-1})$	53.04 \pm 0.01	59.16 \pm 0.00	47.88 \pm 0.01
$T_{m,1}^0 (^\circ C)$	111.50 \pm 0.00	104.84 \pm 0.00	108.48 \pm 0.00
$\alpha_1 (K^{-1})$	0.16 \pm 0.00	0.15 \pm 0.00	0.17 \pm 0.00
$\beta_1 (K^{-2})$	0.28 \pm 0.00	0.21 \pm 0.00	0.28 \pm 0.00
$\Delta C_{p,m,1} (W.g^{-1}.K^{-1})$	0.00 \pm 0.00	0.02 \pm 0.00	0.00 \pm 0.00
$B (W.g^{-1})$	0.22 \pm 0.00	0.29 \pm 0.00	0.46 \pm 0.00
$C (mW.g^{-1}.K^{-1})$	-4.45 \pm 0.03	-5.03 \pm 0.01	-2.79 \pm 0.02
$D (mW.g^{-1}.K^{-2})$	0.01 \pm 0.00	-0.01 \pm 0.00	0.02 \pm 0.00
R^2	0.99	0.99	0.99

[a] The samples were heated at 5 K.min⁻¹ after calibration at the onset for the given weight and rate, in the case of single gels only one fitting peak is required (the error margins are from the nonlinear fitting).

Table S6.11 Fit parameters of $DSC_N(T)$ function fitted to the experimental DSC trace of 8mg of 5BA, 6BA, and $(5BA)_3(6BA)_1$ gels (20 wt%)^[a].

5BA6BA gels	5BA gel	$(5BA)_3(6BA)_1$ gel	6BA gel
$\Delta H_1 (J.g^{-1})$	Single peak	25.44 \pm 0.18	Single peak
$T_{m,1}^0 (^\circ C)$		83.30 \pm 0.03	
$\alpha_1 (K^{-1})$		0.04 \pm 0.00	
$\beta_1 (K^{-2})$		2.14 \pm 0.29	
$\Delta C_{p,m,1} (W.g^{-1}.K^{-1})$		NA	
$\Delta H_2 (J.g^{-1})$		119.88 \pm 0.49	53.04 \pm 0.01
$T_{m,2}^0 (^\circ C)$	101.96 \pm 0.01	96.34 \pm 0.01	111.50 \pm 0.00
$\alpha_2 (K^{-1})$	0.15 \pm 0.00	0.05 \pm 0.00	0.16 \pm 0.00
$\beta_2 (K^{-2})$	0.33 \pm 0.00	0.31 \pm 0.00	0.28 \pm 0.00
$\Delta C_{p,m,2} (W.g^{-1}.K^{-1})$	0.01 \pm 0.00	NA	0.00 \pm 0.00
$B (W.g^{-1})$	0.54 \pm 0.00	0.23 \pm 0.01	0.22 \pm 0.00
$C (mW.g^{-1}.K^{-1})$	-0.86 \pm 0.01	-2.64 \pm 0.03	-4.45 \pm 0.03
$D (mW.g^{-1}.K^{-2})$	0.03 \pm 0.00	-0.01 \pm 0.00	0.01 \pm 0.00
R^2	0.99	0.99	0.99

[a] The samples were heated at 5 K.min⁻¹ after calibration at the onset for the given weight and rate, in the case of single gels only one fitting peak is required (the error margins are from the nonlinear fitting), $\Delta C_{p,m}$ does not converge (Not available=NA) due to purely mathematical artefact, if the peaks are sufficiently apart with sufficient baseline tail on each side, the cumulative $\Delta C_{p,m}$ can be reliably determined via the $DSC_N(T)$ function for binary systems.

Table S6.12 Fit parameters of $DSC_N(T)$ function fitted to the experimental DSC trace of 8mg of 5BA, 10BA, and $(5BA)_3(10BA)_1$ gels (20 wt%)^[a].

5BA10BA gels	5BA gel	(5BA) ₃ (10BA) ₁ gel	10BA gel
$\Delta H_1 (J.g^{-1})$	Single peak	39.84±0.31	Single peak
$T_{m,1}^0 (^\circ C)$		83.91±0.03	
$\alpha_1 (K^{-1})$		0.03±0.00	
$\beta_1 (K^2)$		1.46±0.17	
$\Delta C_{p,m,1} (W.g^{-1}.K^{-1})$		NA	
$\Delta H_2 (J.g^{-1})$		163.20±0.78	47.88±0.01
$T_{m,2}^0 (^\circ C)$	36.12±0.01	97.39±0.01	101.96±0.01
$\alpha_2 (K^{-1})$	0.15±0.00	0.05±0.00	0.17±0.00
$\beta_2 (K^2)$	0.33±0.00	0.27±0.00	0.28±0.00
$\Delta C_{p,m,2} (W.g^{-1}.K^{-1})$	0.01±0.00	NA	0.00±0.00
$B (W.g^{-1})$	0.54±0.00	0.13±0.02	0.46±0.00
$C (mW.g^{-1}.K^{-1})$	-0.86±0.01	1.81±0.05	-2.79±0.02
$D (mW.g^{-1}.K^{-2})$	0.03±0.00	-0.01±0.00	0.02±0.00
R^2	0.99	0.99	0.99

[a] The samples were heated at 5 K.min⁻¹ after calibration at the onset for the given weight and rate, in the case of single gels only one fitting peak is required (the error margins are from the nonlinear fitting), $\Delta C_{p,m}$ does not converge (Not available=NA) due to purely mathematical artefact, if the peaks are sufficiently apart with sufficient baseline tail on each side, the cumulative $\Delta C_{p,m}$ can be reliably determined via the $DSC_N(T)$ function for binary systems.

Summary

All gels like the well-known **jello** have a liquid component, a solvent, and a solid component, a gelator. Supramolecular gels form if gelator molecules in a minor portion self-assemble into primary structures constructing a continuous three-dimensional network which can permeate the major liquid portion. From the discovery of the first generation of gelators by serendipity, different gelators have been designed to produce diverse gels for different applications. In this research, we aim at alternative approaches to tune the gel properties: via the addition of another gelator to the main gelator system to create more freedom of formulation to the original system. To achieve this goal, we blend a homologous series of bisamide gelators, as model systems, to investigate their mixing behavior in the solid and gel state and to assess the subsequent impact of their assembly on the final gel properties.

The thesis starts with a brief overview of the field of molecular gelators and the objectives of this research project in **chapter 1** followed by the systematic study of single and binary systems in different steps, which are explained in the subsequent chapters.

In **chapter 2**, we present a relevant part of our tutorial review on different mechanisms of molecular assembly and supramolecular gel formation: this chapter focuses primarily on how supramolecular gels form via crystallization which is the dominant mechanism of microphase separation in bisamide gelator systems.

Chapter 3 describes a systematic study on the structure-property relationships of a homologous series of bisamide gelators (nBAs) with $(CH_2)_n$ spacer between two amide groups, where n varies from 5 to 10, and with two symmetric C17 alkyl tails. With increasing the spacer length, the thermal properties of the gelators obtained from analytical model $DSC_N(T)$ – namely the melting transition, enthalpy of fusion, and the change in heat capacity – show a clear odd-even effect.

The gelation behavior of the nBA gelators in xylene is studied in **chapter 4**. It was found that the melting temperature (T_m^0) of nBA gels are about 35 °C lower than T_m^0 of the pure nBA gelators. These melting temperatures (T_m^0) in both solid and gel states are obtained from fitting our $DSC_N(T)$ model to the experimental DSC data.

Application of the FHM model, combining theories of Flory-Huggins (FH) and Gibbs free energy of melting (M), explains how this depression in T_m^0 is attributed to an increase in entropy upon melting of the gel due to mixing with the solvent.

In **chapter 5**, we explain how the $DSC_N(T)$ model was developed to quantitatively analyse differential scanning calorimetry (DSC) experimental data. The model was validated by fitting the $DSC_N(T)$ function to the DSC thermogram of different single and multi-component systems. The success of the model and the quality of the fit were evaluated by comparing the obtained transition temperatures and enthalpy with the values from the literature. This model was used throughout this research to reliably analyse the phase behavior of bisamide molecules in the solid state (chapter 3), gel state (chapter 4), and binary systems in the solid and gel state (chapter 6).

Striving for the development of design rules to control the supramolecular assembly pattern in the solid and gel state of multi-component nBA systems, in **chapter 6**, we blend odd and even nBA gelators with different parities and spacer lengths at different ratios to produce binary mixtures of these gelators. Ultimately, to understand the role of matching or non-matching hydrogen bonds as design tools, the effect of supramolecular assembly patterns on the gelation and the gel rheological properties was studied.

In **conclusion**, it was found that the assembly behavior of binary mixtures of bisamide gelators is similar to their gels: the self-recognition of nBA gelators depends on the compatibility of the spacer length parity: binary mixtures of gelators with different parities gave complete phase separation in the solid state, and self-sorted gels consisting of discrete fibers and sheets in the gels of $(5BA)_3(6BA)_1$ and $(5BA)_3(10BA)_1$.

The rheological properties of binary gels can be controlled by tuning their morphological characteristics: the storage modulus G' of all binary gels is lower than their single parent gels, except $(6BA)_1(10BA)_1$ gel whose G' is nearly the average G' of single 6BA and 10BA gels. Different parities of the gelators or larger difference in the spacer lengths decreases G' of binary gels more dramatically.

Samenvatting

Alle gels, zoals de bekende jello, hebben een vloeibaar bestanddeel, een oplosmiddel, en een vast bestanddeel, een gelator. Supramoleculaire gels ontstaan als een kleine fractie gelatormoleculen zichzelf assembleren tot primaire structuren die een continu driedimensionaal netwerk vormen dat de grote meerderheid aan vloeistof kan samenbinden. Sinds de ontdekking – bij toeval – van de eerste generatie gelatoren zijn er verschillende gelatoren ontworpen om diverse gels voor verschillende toepassingen te produceren. In dit onderzoek richten we ons op alternatieve benaderingen om de gel eigenschappen te beheersen: via de toevoeging van een andere gelator aan het gelatorsysteem om een vrijere formulering te creëren dan in het originele systeem. Om dit doel te bereiken, mengen we een homologe reeks bisamide gelatoren, als modelsystemen, om hun menggedrag in vaste en in de gel vorm te onderzoeken en om het effect van hun assemblage patronen op de uiteindelijke geleigenschappen te beoordelen.

Dit proefschrift begint met een kort overzicht van het onderzoeksgebied van de moleculaire gelatoren en de doelstelling van dit onderzoeksproject in **hoofdstuk 1** gevolgd door de systematische studie van enkelvoudige en binaire systemen in verschillende stappen die in de volgende hoofdstukken worden uitgelegd. In **hoofdstuk 2** presenteren we een relevant deel van ons overzicht van verschillende mechanismen van moleculaire assemblage en supramoleculaire gevorming: dit hoofdstuk richt zich met name op hoe supramoleculaire gels zich vormen via kristallisatie, het dominante mechanisme van microfasenscheiding in bisamide systemen. **Hoofdstuk 3** beschrijft een systematisch onderzoek naar de structuur-eigenschap relaties van een homologe serie bisamide gelatoren (nBA's) met een $(\text{CH}_2)_n$ -verbindingsketen tussen twee amidegroepen, waarbij n varieert van 5 tot 10, en met twee eindstandige C17-alkylketens. Met toenemende lengte van de verbindingsketen vertonen de thermische eigenschappen van de gelatoren, verkregen uit het analytische model $\text{DSC}_N(T)$ – namelijk het smeltpunt, de smeltwarmte en de verandering in warmtecapaciteit – een duidelijk even-oneven effect. Het geleergedrag van de nBA-gelatoren in xyleen is bestudeerd in **hoofdstuk 4**. Het bleek dat de smelttemperatuur (T_m^0) van nBA gels ongeveer 35 °C lager ligt dan T_m^0 van de pure nBA-gelatoren. De smelttemperaturen (T_m^0) in zowel vaste als geltoestanden zijn verkregen door de experimentele DSC data te

beschrijven met ons $DSC_N(T)$ model. Het FHM-model, een combinatie van de theorieën van Flory-Huggins (FH) en de Gibbs vrije energie van smelten (M), verklapt hoe deze verlaging van T_m^0 wordt toegeschreven aan een toename van de entropie bij het smelten van de gel als gevolg van vermindering met het oplosmiddel.

In **hoofdstuk 5** leggen we uit hoe het $DSC_N(T)$ -model is ontwikkeld om experimentele gegevens van differentiële scanning calorimetrie (DSC) kwantitatief te analyseren. Het model werd gevalideerd door de $DSC_N(T)$ -functie toe te passen op het DSC-thermogram van verschillende enkele en meer-componentensystemen. Het succes van het model en de kwaliteit van de beschrijving van de experimentele data werden geëvalueerd door de verkregen overgangstemperaturen en smeltwarmtes te vergelijken met de waarden uit de literatuur. Dit model werd gedurende dit onderzoek gebruikt om het fasegedrag van bisamide-moleculen in de vaste toestand (hoofdstuk 3), de gel toestand (hoofdstuk 4) en binaire systemen in vaste en gel toestand (hoofdstuk 6) op betrouwbare wijze te analyseren.

In het streven naar de ontwikkeling van ontwerpregels om het supramoleculaire assemblagepatroon in de vaste en geltoestand van multi-component nBA-systemen te beheersen, mengen we in **hoofdstuk 6** oneven en even nBA-gelatoren met verschillende pariteit en lengtes van de verbindingsketen in verschillende verhoudingen met elkaar om binaire mengsels van deze gelatoren te produceren. Uiteindelijk werd het effect van supramoleculaire assemblagepatronen op de gelvorming en de reologische eigenschappen van de gel bestudeerd om de rol van overeenkomende of niet-overeenkomende waterstofbruggen als ontwerpgeredschap te begrijpen.

Concluderend bleek dat het assemblagegedrag van binaire mengsels van bisamide-gelatoren vergelijkbaar is met hun gels: De zelfherkenning van nBA-gelatoren hangt af van de compatibiliteit van de pariteit van de verbindingsketen: binaire mengsels van gelatoren met verschillende pariteit gaven volledige fasescheiding in de vaste toestand, en zelfgesorteerde gels bestaande uit discrete vezels en vellen in de gels van $(5BA)_3(6BA)_1$ en $(5BA)_3(10BA)_1$. De reologische eigenschappen van binaire gels kunnen worden geregeld door hun morfologische eigenschappen af te stemmen: de opslagmodulus G' van alle binaire gels is lager dan hun enkele moedergels, behalve $(6BA)_1(10BA)_1$ gel waarvan de G' bijna gelijk is aan het gemiddelde G' van de afzonderlijke 6BA- en 10BA-gels. Verschillende pariteit of een groter verschil in de lengte van de verbindingsketen in de gelatoren geven een sterkere verlaging van de G' van binaire gels.

Acknowledgment

I would like to express my gratitude to people who contributed to this thesis and paved the path to my growth, both scientifically and personally.

I am deeply grateful to my supervisors **Jan H. van Esch** and **Stephen J. Picken**. Our scientific discussions taught me a lot. Your feedback were mainly scientifically oriented but I took them to understand how my mind works. The entire journey of this PhD program made me face the problems that I have been fleeing from in my entire life. For me, acquiring this PhD degree indeed means beyond a degree to be an independent researcher in this field and how to live researching while keeping the balance between interaction and independence.

Also, I would like to express my gratitude to our collaborators at Arkema company: **Antony Nogues**, **Michael Bernard**, **Carine Fouillart**, and **Gaelle Mellot**. Being part of this industrial project gave me the opportunity to solve industrial issues while I could approach them from scientific perspective learnt in academia. Working with you has been a great pleasure and rewarding experience to me.

Throughout my PhD, I had the pleasure to collaborate with **Enno A. Klop** and **Lars J. Bannenberg**. Your scientific input, insightful comments, and constructive suggestions contributed immensely to my scientific development reflected in this thesis.

I would like to thank the **committee members** for taking their time to evaluate this thesis.

Behrouz, my genuine friend, you are always there for me to reach out. You always enlighten me with your brilliant scientific insights and your endless compassion during our mutual-psychoanalysis conversations.

My students, **Pooja**, **Aravind**, **Zian**, **Wanyu**, **Isabelle**, **Nneoma**, **Bing**, and **Marise**, our progress in a mutual learning process kept me motivated throughout my PhD journey and working with you on your MEP and BEP projects has greatly contributed to this piece of work.

Ardeshir, you are the brother that I always wish I could have. Sharing our work office, the review paper, and our information in different realms were the true moments

of this journey at TUDelft. I will always remember our laughter to our common struggles and the defense mechanisms that we developed to cope.

Benni, you are one of the most influential scientists to me. I learned from you how to dive into the most threatening matters in my life and apply my knowledge to improve my health and life-style. Friendship with you tastes like Jasmin Green Fossa chocolate to me.

Hendrik, you dropping in my office, giving me a tight hug, and sharing a piece of biological yummy snack accompanied with your unique humor was your magical recipe to cheer me up. Friendship with you is organic, sustainable, and a fair trade.

All colleagues and friends in TNW building and ASM group; **Jelmer, Suellen, Anand, Reece, Anastacia, Jacqueline, Irene, Tamar, Sarah, Guotai, Mark, Deepka**, I had a great time in this small community with you and I enjoyed your company in those four years.

Duco, you are a gift to TNW. Thank you for all your sense of responsibility and availability to help all of us around in the lab.

Ben, you were officially retired long time ago but never retired in practice for us. You have always been available for any help from the beginning of my PhD to the end. Your hospitality along with **Mieneke**'s have been always heart-warming for me.

Xiaohui, your help with XRD measurements and analysis was a huge contribution to this piece of work which remained hidden due to your humbleness, I am very thankful to you.

Veby, thank you for your support from the first day of my arrival to the Netherlands for my interview. Your cheerful personality and open heart have been always inspiring to me.

Sietse, Alexandra, Marcel, Bart, Else, thank you for your help whenever I reached you. **Stephen**, your passion for learning Farsi is very inspiring. Thanks for the wonderful photos that you are going to make for my defense.

Eduardo, Wolter, Rienk, Marcel, Laura thank you for your contributions to our ASM science meetings.

Shokufeh, from the first moment that I wanted to accept this offer you have been sincerely supportive. I am very grateful that I had your company in those though days.

Parisa, Elmira, Sanam, Mehrnoush, Ali, Rasool, Reza, Nick, Vladimir, Sabine, Rezvan, Niloofar, Mohsen, Richard, Laura, and Joost, you are my amazing friends and I am thankful for what you have been sharing with me throughout these years.

Hans en Mathilde, bedankt voor jullie gastvrijheid en hulp om mijn Nederlands te verbeteren en jullie steun toen ik worstelde met eenzaamheid in Nederland.

Afsaneh joon, in jedem Moment, in dem ich meine Verletzlichkeit zum Ausdruck brachte, wandelst du sie auf meinen Fingerspitzen in Stärke um.

I would like to express my deepest gratitude to my **family** members supporting me from all around this world:

مامان، تو برای من زندگی خلق کرده و برای بیشمار زن دیگه در ایران با سخت ترین شرایط کارآفریدی و به همه ما یاد دادی چطور در مسیر استقلال هر روز توانمندتر بشویم. این تر تقدیم به توست، قویتین و در عین حال لطیف ترین زنی که میشناسم.

بابا، از مهاجرتم و هر آنچه تا امروز خواستم با تمام توانت حمایت کرده. تمام عشقم به جستجوی حقیقت، تاریخ، منطق ریاضی، و پیدا کردن طنز در دل تلخی ها رو از تو دارم.

یگی، فرزانه، مریم، مرجان، مینا، شیدا، مامان مهری، دایی سعید، آرمان، عرفان، فربد، فوزان، فایدیم، سورنا، ماهان از لحظه ای که راهی هلنند شدم لحظه به لحظه در تمام وجودم با من بودید و خواهید بود.

Sana, Emma, Hanie, you are my sisters by choice. Your incredible support is the magic power helping me rise after every fall. Wherever your journey leads on this earth, our bond will always remain covalent.

Jannie en Fetze, jullie omhelzen me altijd met warme knuffels en ontvangen me als jullie dochter. Jullie zijn voor mij de reden om mijn Nederlands te verbeteren om jullie en Auke steeds beter te leren kennen.

Mijn lieve Auke joon, azizam, among all the unknowns in this world, you are the most interesting one to me to discover. You are my genius curious scientist who deserves a PhD in almost every subject. Your constant passion to dive into every matter inspires me to explore every corner of this life further with you. I am sincerely grateful for your support throughout the most though days of my life in the Netherlands.

Curriculum Vitae

Elmira Ghanbari was born on December 27th 1990. She received her bachelor degree in metallurgy engineering and materials science from University of Tehran, including 6 months of internship at Shahryar Co., Heavy Machinery, Iran. She worked one year as a material surface engineer at Sadeghi block machinery plant, understanding wear mechanisms and friction properties of bearing surfaces to improve the lifetime of the bearing components. She received her master degree in biomedical engineering-biomaterials from Amirkabir University of Technology, including 6 months of internship at Tehran Heart Center, Iran. She spent one year working as a junior researcher at the medical research center of Pasteur Institute of Iran, developing drug delivery systems based on niosomes which are loaded with angiogenesis stimulator for myocardial infarction (MI).

She started her doctoral studies at Delft University of Technology in 2018 under supervision of Jan H. van Esch and Stephen J. Picken resulting in this thesis consisting of 5 articles and a patent. After 4 years of PhD studies, she worked as a postdoctoral researcher at TUDelft in collaboration with Arkema company with Jan H. van Esch and Stephen Picken.

List of publications

1. **E. Ghanbari¹**, Ardesir Roshanasan, S. J. Picken, and J. H. van Esch, "From molecular assembly to gel formation: what is going on behind the scenes of supramolecular gel formation", under submission, 2023 (**chapter 2**).
2. **E. Ghanbari¹**, A. Krishnamurthy, S. J. Picken, E. A. Klop, L. J. Bannenberg, and J. H. van Esch, "Molecular Arrangement and Thermal Properties of Bisamide Organogelators in the Solid State", *Langmuir*, 2022 (**chapter 3**).
3. **E. Ghanbari¹**, Zian Chen, Pooja Padmanabhan, S. J. Picken, and J. H. van Esch, "Supramolecular arrangement and rheological properties of bisamide gels", *Langmuir*, 2023 (**chapter 4**).
4. **E. Ghanbari¹**, S. J. Picken, and J. H. van Esch, "Analysis of differential scanning calorimetry (DSC): Determining the transition temperatures, enthalpy and heat capacity changes in multi-component systems by analytical model fitting", *J. Therm. Anal. Calorim*, 2023 (**chapter 5**).
5. **E. Ghanbari¹**, S. J. Picken, and J. H. van Esch, "Design rules for binary bisamide gelators: towards gels with tailor-made structures and properties", *Langmuir*, 2023 (**chapter 6**).
6. B. van Straten, P. D. Robertson, H. Oussoren, S. Pereira Espindola, **E. Ghanbari**, J. Dankelman, S. Picken, T. Horeman, "Can sterilization of disposable face masks be an alternative for imported face masks? A nationwide field study including 19 sterilization departments and 471 imported brand types during COVID-19 shortages", *J. PLOS ONE*, 2021.

Patent

Analysis of differential scanning calorimetry (DSC): Determining the transition temperatures, enthalpy and heat capacity changes in multi-component systems by analytical model fitting.

